High Accuracy Nonlinear Control and Estimation for Machine Tool Systems

Papageorgiou, Dimitrios

Publication date:
2017

Document Version
Publisher's PDF, also known as Version of record

Technical University of Denmark

Dimitrios Papageorgiou

High Accuracy Nonlinear Control and Estimation for Machine Tool Systems

PhD Thesis, August 2017

DTU Electrical Engineering
Department of Electrical Engineering

SIEMENS

High Accuracy Nonlinear Control and Estimation for Machine Tool Systems

Dimitrios Papageorgiou

Technical University of Denmark
Kgs. Lyngby, Denmark, 2017

Technical University of Denmark
Automation and Control (AUT)
Elektrovej Building 326
DK-2800, Kgs. Lyngby
Denmark
Phone: (+45) 45 25 35 73
Email: info@elektro.dtu.dk
www.elektro.dtu.dk

Summary

Component mass production has been the backbone of industry since the second industrial revolution, and machine tools are producing parts of widely varying size and design complexity. The ever-increasing level of automation in modern manufacturing processes necessitates the use of more sophisticated machine tool systems that are adaptable to different workspace conditions, while at the same time being able to maintain very narrow workpiece tolerances. The main topic of this thesis is to suggest control methods that can maintain required manufacturing tolerances, despite moderate wear and tear. The purpose is to ensure that full accuracy is maintained between service intervals and to advice when overhaul is needed.

The thesis argues that quality of manufactured components is directly related to the positioning accuracy of the machine tool axes, and it shows which low level control architectures are used to position the machining tool relatively to the material being processed. While existing algorithms provide sufficient accuracy after commissioning of the machine by experts, the thesis shows how they fall short in keeping required tolerances in the presence of equipment wear, unless they are re-tuned by experts.

The goal of this research has therefore been investigation and development of advanced control and estimation algorithms, which facilitate high-accuracy machine-tool axis positioning, and are robust to equipment degradation and wear.

This thesis presents the findings of the research conducted during the three years of the PhD program at the Technical University of Denmark. The research has been carried out in close collaboration with Siemens AG in Nuremberg, who sponsored the research. Siemens also provided state-of-the-art industrial equipment to facilitate experimental testing and validation. DTU added mechanical components to test the development of friction and backlash. The scientific-technical contributions of the research fall into three parts, which also constitute the structure of the thesis.

The first part concerns the development of an efficient description of a generic machine-tool axis system. A detailed mathematical model is derived that captures the most important axis dynamics. Positioning degrading phenomena, such as

friction and backlash, are expressed as nonlinear axis torques. Identification of the test rig parameters and sensitivity analysis is carried out, to highlight the significance of individual model parameters.

The second contribution of this research pertains to the investigation of different nonlinear control strategies and architectures for the positioning of the axis. Eight position controllers based on sliding-mode and adaptive principles are designed, implemented and tested on the experimental setup. A set of quantitative and qualitative criteria is used for the systematic comparison of the methods. The evaluation results show that four out of the eight designs provide superior positioning accuracy and resilience to unknown and varying friction, in comparison to the state-of-the-art proportional-integral control solutions.

The third part of the research relates to the development of online backlash estimation algorithms for machine-tools. The proposed method utilizes position and velocity measurements in a cascaded scheme consisting of a sliding-mode velocity observer and an adaptive deadzone angle estimator. A series of experiments is conducted for testing the algorithm in various operation scenarios under different levels of uncertainty. The results show that the estimator identifies the unknown deadzone angle and changes in it with sufficient accuracy and can, therefore, facilitate backlash compensation, as well as equipment wear assessment and prognosis.

The scientific results of this research have been summarized in three journal articles, which have been submitted, and an article presented at the IFAC World Congress 2017 that has been published.

Resumé

Masseproduktion af komponenter har været en hjørnesten i industrien siden den anden industrielle revolution med maskiner der fremstiller emner af meget varierende størrelse og kompleksitet. Med automatiseret fremstilling af stadig mere diversificerede og komplekse emner er der både behov for at kunne tilpasse styringen af en maskine til nye emner og for at opretholde høje krav til fremstillingstolerancer. Kravet om præcision gælder både når en maskine er helt ny og over tid, når maskindele påvirkes af slidtage.

Hovedemnet for dette forskningsarbejde er at anvise styrings- og reguleringsmetoder, som kan sikre at en høj fremstillingsnøjagtighed opretholdes, uanset begyndende mekanisk slidtage. Hensigten er at sikre, at der arbejdes med fuld præcision imellem serviceeftersyn, samt at kunne anvise hvornår næste vedligehold bliver nødvendigt. Afhandlingen tager udgangspunkt i at tolerancer i maskinel bearbejdning hænger direkte sammen med nøjagtigheden hvormed et skærende værktøj kan positioneres i forhold til det emne der bearbejdes. Når en maskine er ny, og dens nummeriske styring er indjusteret, har den fuldt tilfredsstillende præcision.

Afhandlingen viser at eksisterende styringer mister præcision, når slidtage indfinder sig, med mindre regulatorparametre gen-justeres af eksperter. Formålet med forskningsarbejdet har derfor været at undersøge og foreslå avancerede metoder til styring og estimering, som kan tilbyde højpræcisions styring der ikke er følsom overfor mekanisk slidtage.

Afhandlingen præsenterer resultaterne af et tre-årigt phd program på Danmarks Tekniske Universitet. Forskningen er foregået i samarbejde med Siemens AG, Nürnberg, som har sponsoreret projektet og også har stillet state-of-art udstyr til rådighed for laboratorietest og validering.

Afhandlingen er opdelt i tre dele med hver deres teknisk-videnskabelige bidrag. I første del udarbejdes en generel matematisk beskrivelse af en enkelt akse i en fremstillingsmaskine. Modellen omfatter den nødvendige dynamik og inkluderer slidtage, i form af friktion og slør, som ikkelineære elementer i modellen. Parametre i modellen fastlægges teoretisk og eksperimentelt, bl.a. med anvendelse af system identifikation. De enkelte parametres betydning vurderes udfra den virkning på

præcision der kan iagtages, når de ændres.

I anden del undersøges udvalgte ikkelineære reguleringsmetoder, der er baseret på *sliding mode* og *adaptive* principper. Afhandlingen beskriver hvordan arkitektur og parametre bestemmes for de valgte metoder. Konvergens bevises teoretisk, hvor det er relevant, og afhandlingen vurderer styringskvalitet i form af resultater fra simuleringer og fra eksperimenter i laboratoriet. Reguleringsmetodernes kvalitet vurderes samlet udfra et sæt af indikatorer, der udtrykker reguleringskvalitet på en måde som er relevant for den industrielle anvendelse. Resultaterne viser at fire af otte ikkelineære styringsalgoritmer opnår bedre præcision og robusthed overfor ukendt og langsomt øget friktion end den eksisterende konventionelle regulering.

I tredie del undersøges hvordan mekanisk slør kan estimeres for en nummerisk styret maskine medens den udfører normal produktion. Der foreslås en ny metode til estimering af slør. Den anvender en kombination af en *sliding mode* observer og en adaptiv estimator til at at opnå en høj følsomhed. Estimationsalgoritmen er valideret under forskellige realistiske servo bevægelser, og for forskellige niveauer af mekanisk slør. Den eksperimentelle validering viser at den nye algoritme vil kunne anvendes både til kompensering af slør og til prognose af hvornår vedligehold skal foretages.

De videnskabelige resultater af dette arbejde er sammenfattet i tre tidsskrifts-artikler, som er indsendt, og i en artikel til IFAC World Congress i 2017, som er publiceret.

Preface

This project was prepared as a collaboration between the Automation and Control group in the Department of Electrical Engineering of the Technical University of Denmark (DTU) and Siemens AG in the context of the DTU PhD program. The industrial partner was the exclusive sponsor of the project.

The project advisors were:

- Professor Mogens Blanke (principal supervisor), Department of Electrical Engineering, Automation and Control group, DTU.
- Associate professor Hans Henrik Niemann (co-supervisor), Department of Electrical Engineering, Automation and Control group, DTU.
- Dr.-Ing. Jan H. Richter (company supervisor), Digital Factory Division, Technology and Innovations, Siemens AG.

This thesis consists of a summary report of all research findings gathered as a collection of submitted articles in peer reviewed scientific journals and published in conference proceedings in the period 2014-2017.

Kongens Lyngby, August 2017
Dimitrios Papageorgiou

List of Publications

Publications included in the thesis

(A) D. Papageorgiou, M. Blanke, H. H. Niemann, and J. H. Richter. “Friction resilience of machine tool controls - Classic, sliding mode and nonlinear adaptive techniques compared”. *Control Engineering Practice* (2017). : Submitted paper under review.

(B) D. Papageorgiou, M. Blanke, H. H. Niemann, and J. H. Richter. “Friction-resilient position control for machine tools - Adaptive and sliding-mode methods compared”. *Control Engineering Practice* (2017). : Submitted paper under review.

(C) D. Papageorgiou, M. Blanke, H. H. Niemann, and J. H. Richter. “Robust backlash estimation for industrial drive-train systems - theory and validation”. *Transactions on Control Systems Technology* (2017). : Submitted paper under review.

(D) D. Papageorgiou, M. Blanke, H. H. Niemann, and J. H. Richter. “Backlash estimation for industrial drive-train systems” (July 2017). : To appear in IFAC-PapersOnLine.

Publications not included in the thesis

(E) D. Papageorgiou, M. Blanke, H. H. Niemann, and J. H. Richter. “Fault tolerance for industrial actuators in absence of accurate models and hardware redundancy”. *2015 IEEE Conference on Control Applications (CCA)*. Sept. 2015, pp. 1887–1894. DOI: 10.1109/CCA.2015.7320885.

Acknowledgments

> "Πᾶσα τὲ ἐπιστήμη χωριζομένη δικαιοσύνης καὶ τῆς ἄλλης ἀρετής πανουργία οὐ σοφία φαίνεται."
> *Every science departing from justice and other virtue reveals cunningness and not wisdom.*
>
> — Plato*, Menexenus 247a*

During my PhD studies I enjoyed the privilege of having three charismatic researchers and accomplished professionals as supervisors. Professor Mogens Blanke has been my main advisor and academic mentor. Conducting research under his wing made it possible for small ideas to transform into high-quality results. His continuous guidance and support, irrespectively of the clock index position, have been catalytic in my development as a researcher, for which I am deeply grateful. I would like to thank my co-supervisor Associate Professor Hans-Henrik Niemann, for always being available for questions and for advising me on topics on classic control, frequency domain analysis and system identification. During the entire project, my advisor from Siemens Dr. Jan H. Richter had been sharing his expertise in control design and planning. Through his meticulous and dedicated supervision he taught me how to project academic research ideas onto real industrial applications. I take the chance here to thank my supervisors, as well as the general manager of the project Dr. Jörg Neidig, for believing in me and providing me with the opportunity of working on such an exciting research project.

During the second year of my project I had a short stay at Siemens AG facilities in Nuremberg, where I presented my research ideas and received training on Siemens drives commissioning. I would like to thank the Siemens team from the Digital Factory division for their valuable comments, as well as the interesting discussions on the project. Special thanks to Siemens motion control experts Dr. Hans-Georg Koepkin and Dr. Carsten Hamm, who shared their knowledge and experience with me, regarding several technical topics in modelling and control. It was Dr. Hamm's tireless efforts and expertise that made the integration of my control designs into the test rig possible.

Many times during my project did I knock on Associate Prof. Roberto Galeazzi's office door for a "five-minute" question and I always came out of his office with answers and good ideas. For that I full-heartedly thank him. I would also like to thank Dr. Konstantinos Poulios, Kristian Sloth Lauszus and Dr. Moises Pacheho for their help in designing and manufacturing the various extensions for the project's experimental setup.

Working at the Automation and Control Group in DTU has been truly inspiring. During these past three years I have had the pleasure of cooperating and socializing with people of excellent quality, whose company I cherish. I especially want to thank my treasured friends Mikkel Cornelius Nielsen, Dr. Remus Michail Prunescu, Nicholas Peter Hansen and Leon Nagel for all these "science-plus-coffee" sessions, where we all used to share our thoughts and ideas on our projects. I would also like to thank Dr. Andreas Søndergaard Pedersen, André Krabdrup Sekunda, Emil Krabbe Nielsen, Robert Miklos and the rest fellow-researchers from the AUT group.

My trajectory during my PhD studies would have been much less smooth had I not had the endless support of my two closest friends Konsantinos Goulas and Alexandros Meletis, for which I am deeply grateful. I would also like to thank my friend and teacher Dimitrios Metzikof Papadakis for his guidance and all the philosophical discussions we had on science ethics and virtue.

Finally, I would like to express my utmost gratitude to my father Epameinondas, mother Sotiria, sister Kalomoira and uncle Evaggelos for their love and support during all these years. Their moral paedeia has constantly been an example to me for pursuing a life of virtue. I thank them, as well as my grandparents and the rest of my family for always believing in me.

Table of Contents

List of Abbreviations

L_1AC $\mathcal{L}_1$ Adaptive Control. 13, 14

ABSC Adaptive Backstepping Controller. 12, 14, 63, 65, 66, 69, 72, 74, 72, 79, 80, 113, 156, 164, 174, 176, 178, 179, 181, 182, 183, 185, 182, 185

ACC Adaptive Control with Constraints. 118

ACO Adaptive Control with Optimization. 118

ASTSMC Adaptive Super-Twisting Sliding-Mode Controller. 68, 69, 74, 72, 74, 77, 80, 156, 170, 172, 174, 176, 178, 180, 181, 182, 183, 185, 182

BIBO Bounded Input-Bounded Output. 89, 241

CAM Computer Aided Manufacturing. 3

CCC Cross-Coupling Control. 7, 118

CI Complexity Index. 72

CIT Circular Interpolation Test. 72, 142, 176

CNC Computerized Numerical Control. 1, 3, 4, 192, 222

CP Control Power. 70, 141, 176

CU control unit. 22

ECP Error-Control Power product. 70, 141, 144, 149, 145, 149, 176, 181, 182

EKF Extended Kalman Filter. 10, 192, 222

ES Exponentially Stable. 67, 171

GAC Geometry Adaptive Control. 118

I&I-AC Immersion and Invariance Adaptive Control. 13, 14, 61, 62, 66, 69, 72, 74, 72, 79, 80, 113, 129, 133, 137, 140, 143, 144, 145, 147, 149, 151, 145, 185

IAC Individual Axis Control. 7, 8

ISE Integral Square Error. 70, 140, 176

ISS Input-to-State Stable. 137, 169, 204, 205, 208, 239, 240, 241

ITSE Integral Timed Square Error. 70, 141, 176

LMI Linear Matrix Inequality. 59, 128

LTI Linear Time-Invariant. 171, 172

MAE Maximum Absolute Error. 72, 70, 72, 74, 72, 74, 80, 86, 92, 140, 143, 144, 145, 149, 150, 149, 176, 178, 179, 181, 182, 181, 184, 182, 184, 189

MAEE Maximum Absolute Estimation Error. 106, 107, 109, 212, 214, 215

MAPE Maximum Absolute Phase Error. 70, 72, 70, 74, 141, 142, 145, 176, 181, 182

MRAC Model Reference Adaptive Control. 12, 13, 55, 128

NAC Nonlinear Adaptive Control. 12, 14, 59, 60, 61, 63, 66, 69, 72, 74, 72, 79, 80, 113, 128, 129, 130, 133, 135, 136, 137, 140, 143, 144, 145, 147, 149, 151, 145, 185

NCSTSMC Nested Continuous Singular Terminal Sliding-Mode Controller. 85, 86

OSTSMC Output Super-Twisting Sliding-Mode Controller. 66, 68, 69, 74, 72, 74, 77, 80, 156, 170, 172, 173, 174, 176, 178, 180, 181, 182, 183, 185, 182

P Proportional. 4, 5, 7, 8, 15, 16, 51, 56, 58, 69, 72, 74, 72, 74, 77, 80, 86, 87, 90, 92, 94, 113, 117, 118, 119, 124, 127, 128, 129, 130, 139, 140, 149, 150, 155, 156, 161, 162, 176, 178, 183, 184, 182, 189, 193

PDE Partial Differential Equation. 147

PDEs Partial Differential Equations. 61

PE Persistence of Excitation. 206, 230, 236

PI Proportional-Integral. 4, 5, 7, 8, 15, 16, 29, 51, 54, 55, 56, 57, 72, 74, 72, 74, 80, 86, 92, 94, 104, 113, 117, 118, 119, 124, 137, 139, 140, 143, 144, 145, 147, 149, 150, 145, 155, 156, 161, 176, 178, 179, 182, 183, 185, 182, 189, 193, 231

PID Proportional-Integral-Differential. 7

PMSM permanent magnet synchronous motor. 20, 22, 23, 25, 29, 120, 127, 129, 164, 193

PMSMs permanent magnet synchronous motors. 157, 174, 235

SFL_1 State-Feedback $\mathcal{L}_1$ adaptive controller. 85, 87, 92

SMC Sliding-Mode Control. 8, 11, 12, 53, 54, 58, 63, 72, 74, 77, 85, 119, 127, 151, 156, 169

SMO Sliding-Mode Observer. 11, 12, 102, 199, 200, 212, 215, 219, 228, 229

STSMC Super-Twisting Sliding-Mode Controller. 11, 12, 58, 59, 66, 67, 69, 72, 74, 72, 74, 77, 80, 113, 127, 128, 137, 140, 143, 144, 145, 147, 150, 151, 145, 169, 170, 172, 184, 185, 189

STSMO Super-Twisting Sliding-Mode Observer. 102, 103, 105, 109, 114, 199, 205, 206, 208, 209, 212, 222, 228, 230, 231, 233

UB Uniformly Bounded. 204

UGAS Uniformly Globally Asymptotically Stable. 103, 137, 169, 201, 202, 205, 207, 219

UGB Uniformly Globally Bounded. 103, 208, 209, 219

ULES Uniformly Locally Exponentially Stable. 103, 202, 204, 205, 206

Notation Convention

The following notation convention applies to the entire thesis report:

Table 1: Notation convention.

Notation rule	**Explanation**	**Example**
Lower/Upper-case normal font	Scalar variable, function or constant	δ, Σ
Lower-case bold font	Vector variable or function	$\boldsymbol{\vartheta}, \boldsymbol{\phi_1}(\boldsymbol{x})$
Upper-case bold font	Matrix	$\boldsymbol{A}$
Upper-case calligraphic font	Set	$\mathcal{M}$
Single-bar brackets	Norm of scalar or matrix	$\lvert\omega_r\rvert_{\mathcal{L}_\infty}, \lvert\boldsymbol{B}\rvert$
Double-bar brackets	Norm of vector	$\lVert\boldsymbol{x}\rVert$
"hat" symbol	Estimate of variable	$\hat{\delta}$
"tilde" symbol	Estimation error	$\tilde{\delta}$
"dot" symbol	Time-derivative of variable	$\dot{\boldsymbol{\vartheta}}$
diag$(\cdot)$	Diagonal of square matrix	diag$(\boldsymbol{\Gamma})$
Dimension superscript	Set of $n \times m$ real matrices	$\boldsymbol{\Gamma} \in \mathbb{R}_{>0}^{2\times 2}$
$\mathcal{C}^n$	Set of $n-$times differentiable functions	$\mathcal{C}^3$
$f^{(n)}$	n^{th} time derivative of $f(t)$	$\theta_r^{(3)}$

Chapter 1

Introduction

1.1 Background

Automated manufacturing is one of the pillars of modern industry. From aerospace and auto-mobile applications to medical equipment and small-scale electronic devices, the ability for fast mass production of a wide range of components has fuelled the technological advances, boosting the global economy during the past decades. According to the World Bank Database [6] manufacturing constitutes approximately 54% of the global industrial economy, while the value-added during 2014 was $12.165 trillion, which amounts to 14.9% of the world GDP in that year. Figure 1.1 shows the increase of the value-added in manufacturing industries during the period 2000-2014.

The advances in Computerized Numerical Control (CNC) in machine-tool systems within the last decades have facilitated the increase of the automation level in manufacturing, allowing faster and larger production of various components for nearly all industrial applications. The increasing demand for faster prototyping and product development [7] has also led to more sophisticated machine tool designs that allow for uninterrupted workpiece processing at smaller times.

Modern CNC machine tools vary in size, number of axes and tools, depending on the application and the tasks they are used for (e.g. milling, boring, grinding, turning, plasma cutting). The processing of the workpieces takes place in a secured cabinet, next to which there is an operating panel (see Figure 1.2). The basic parts of a machine tool include the spindle, which is the main rotary axis of the machine, the table, i.e. the platform where the workpiece is placed, several moving axes and the tool. Fully automated machine tools have an integrated tool-exchanging mechanism and a collection of different processing tools that add task flexibility to the machine.

All the moving parts of the machine, i.e. the spindle, the axes and the table, are

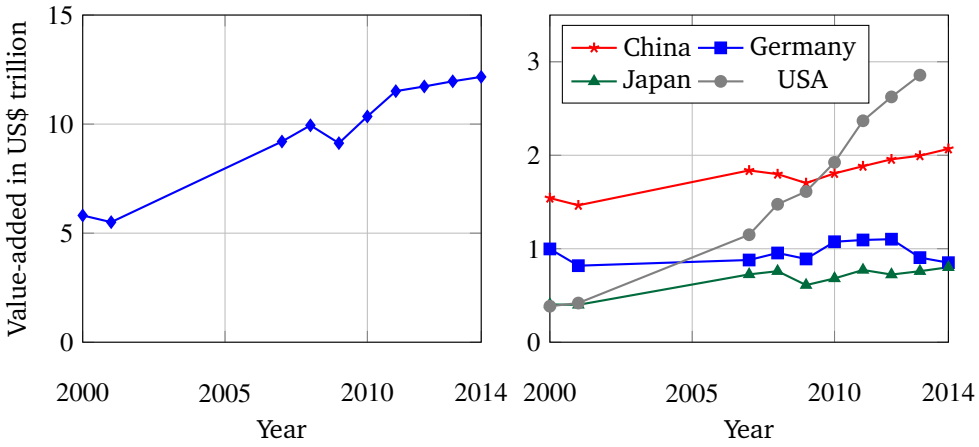

Figure 1.1: Manufacturing, value added for world economy (left) and for the industrial "leading" countries (right) in US$ trillion. The data was taken from the World Bank Database [6].

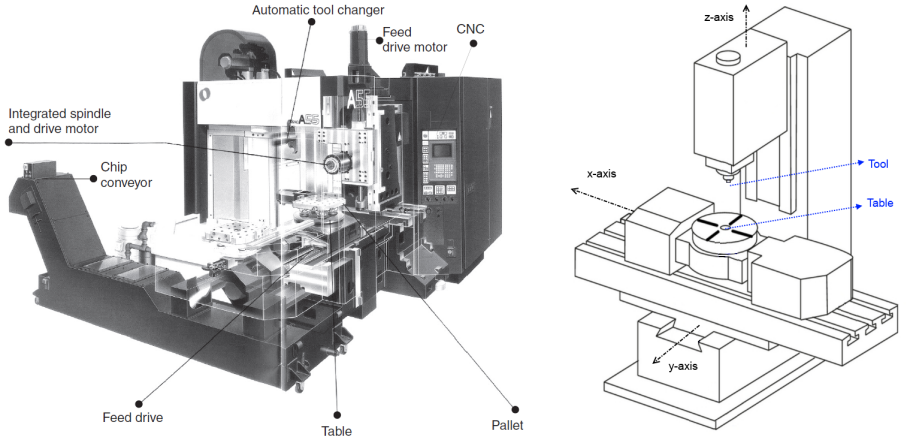

Figure 1.2: (Left): Interior of a machining cabinet with operating panel. (Right): Machine tool with three linear axes. Sources: [8, 9].

actuated by electrical drives, each of which has a dedicated control system. The combination of all the motions results in a predefined configuration between the processing tool and the workpiece that is machined. The quality of the manufactured component, reflected in the correct dimensioning, surface finishing and consistency to the component design, is directly related to the accurate tool-workpiece relative positioning during the entire process.

The ever-increasing complexity of mechanical designs requires high-accuracy tool positioning in machine-tool systems at the order of $10\mu\mathrm{m}$ or lower [10]. Achieving such tolerances assumes not only the availability of high-resolution measuring equipment but also the detailed and fine tuning of all the procedures in each stage of the machining. A typical automated manufacturing process consists of three basic levels [11] (see also Figure 1.3):

- **CNC programming**: With the mechanical design of the component as input the Computer Aided Manufacturing (CAM) software produces a sequence of motion directives for the axes of the machine tool, through which the machining of the workpiece can be made.

- **Trajectory generation**: The CAM translator feeds the program to an interpolator, which takes the machine characteristics (e.g. tool dimensions and geometry, spindle feed rate etc.) as input. Typically, machine tools are overdimensioned, such that deformations during machining have little influence on the product quality [8]. The interpolator generates position setpoints for each axis of the machine.

- **Axis control**: A closed-loop control system ensures that each axis is positioned according to the setpoints commanded by the trajectory generator.

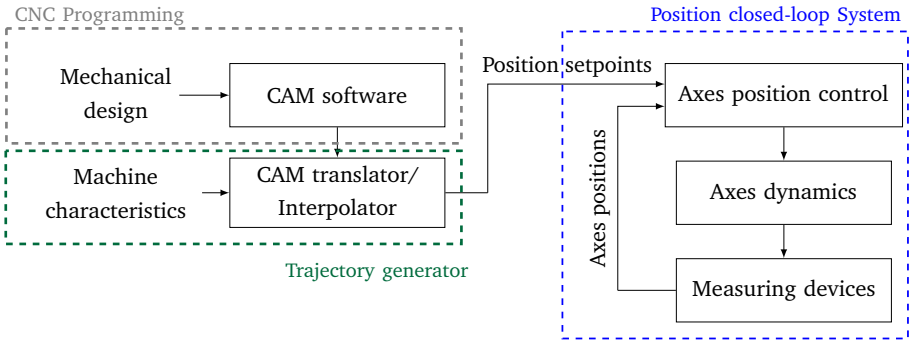

Figure 1.3: Automated component manufacturing chain.

Workpiece tolerances can be compromised by a number of different machining errors. Such errors can be related to the geometry of the machine and the tool (misalignment of the machine parts or the workpiece, tool deflection and wear, thermal expansion, etc.) or to measuring faults (e.g. uncertainty of the reference position, different measured position during reversal of motion) [11]. Although these errors are usually compensated for by recalibration of the machine and trajectory path correction, additional mechanical phenomena, such as variable friction, backlash and changing load inertias, show up during workpiece processing. These phenomena further complicate the machining process and will compromise the workpiece tolerances, unless properly handled by closed-loop control algorithms. Consequently, the most significant contribution to maintain workpiece tolerances, comes from the low-level axis control, the lowest process layer.

1.2 Motivation, Goals and Scope of the Project

High-accuracy relative positioning between tool and workpiece is essential for ensuring proper manufacturing of machined components. Counteracting complex accuracy-degrading phenomena in CNC machine tools, such as friction and backlash, necessitates the use of appropriate compensating algorithms at the level of axis position control. These closed-loop strategies can ensure confinement of the positioning errors within the tolerances only when the degrading phenomena are accurately described. In cases of varying friction and load parameters, or developing deadzones due to wear, conventional axis position controllers - typically based on Proportional (P) and Proportional-Integral (PI) principles - often fail to keep the workpiece tolerances. This compromises the quality of the end product. To compensate for this loss of positioning accuracy the axes' closed-loop control parameters have to be retuned to match the new degrading phenomena each time quality loss is observed. This inevitably leads to increased maintenance cost and, therefore, decrease of the overall efficiency of a production line.

In the light of the emerging Industrie 4.0 [12], future fully-automated CNC machine tools that can adapt [13] to varying workspace conditions, and are robust to equipment wear, may facilitate a wide penetration in the manufacturing market, offering larger competitive advantage. As a direct consequence of this, current axis-positioning solutions will have to be modified or completely redesigned such that they include the desirable robustness and adaptability features. This motivates the investigation of low-level control strategies taken from the arsenal of advanced nonlinear control theory. As outlined, focus should be on their applicability to the positioning problem in machine tools, as well as to robustness and adaptive features.

An additional aspect of the future self-healing manufacturing systems relates to wear assessment and prognosis. Estimating unknown or varying parameters that fully describe degrading phenomena not only may enhance error-compensation mechanisms in the position control loops, but could also be used to assess equipment degradation and provide prognosis of component lifetime. Such feature, by extension, would facilitate more efficient maintenance scheduling.

To this end, the current research project, fully funded by SIEMENS AG, and in the context of the PhD program at the Technical University of Denmark, focuses on developing advanced control and estimation strategies for robust, high-accuracy positioning in machine tools. The goals of the project were defined as follows:

1. To investigate the possibilities of employing nonlinear control strategies that provide high-accuracy positioning in machine tool systems in the presence of wear.

2. To establish an experimental setup with state-of-the-art industrial equipment, on which the developed methods can be tested. The physical hardware should facilitate validation of the theoretical findings and highlight design and applicability challenges of the methods.

3. To research estimation methods that can be used in machine tool control loops for compensating various degrading phenomena and for equipment wear assessment.

Based on these general goals, the project scope includes:

- Derivation of an appropriately detailed mathematical model of a single-axis drive train, to be used as the test bench for evaluation of high-accuracy control methods. The drive-train system serves as an abstraction of a single axis in a real machine-tool. Critical degrading phenomena, namely friction and backlash, should be effectively described and integrated into the drive-train model.

- Design, implementation and testing of various nonlinear control strategies for high-accuracy positioning in machine tools.

- Systematic comparison of the derived methods' accuracy and robustness features to those of the conventional P-PI solutions. The controllers should be evaluated with respect to their friction resilience by employing quantitative and qualitative performance criteria, similar to the evaluation methods used in the industry.

- Development of an algorithm for online accurate estimation of deadzones occurring in coupling components between the different mechanical parts of a drive train. This estimation scheme could be used to describe developing backlash, and the size of the deadzone could facilitate more effective backlash compensation in the control loops. Additionally, it could serve as a means of assessing wear in the coupling equipment.

1.3 Thesis Outline

The structure of the thesis follows the scheme of a collection of articles, where main results are submitted to journals and per-reviewed conferences in the course of study. The main body of the dissertation offers a comprehensive summary of the results obtained throughout the entire project, while technical details are analytically given in the appended articles. The only exception is Chapter 4, the results in which were not included in any of the listed publications.

After the introductory Chapter 1, the thesis continues with the presentation of state-of-the-art methods in control and backlash estimation for machine-tools, given in Chapter 2. Chapter 3 lists the main contributions of this research.

The detailed derivation of a drive-train mathematical model and the test rig are presented in Chapter 4. The relevance of the model to the experimental system and to the real machine tool axes is discussed along with the considered modelling assumptions. Sensitivity analysis and estimation of system unknown parameters are also presented.

Chapter 5 discusses the detailed design, implementation and performance of six nonlinear position control methods based on sliding-mode and adaptive principles. The experimental results are interpreted and juxtaposed to the specific assumption made for each method. An overall ranking of the controllers is provided. Two additional designs that did not meet the performance requirements are discussed and reasons to their lack of performance are addressed.

Online estimation of the deadzone angle between the two parts of the drive train is presented in Chapter 6. A new model of the backlash phenomenon is first suggested. It is based on a varying shaft stiffness approach to overcome mathematical requirements to smoothness of nonlinearities when applying certain nonlinear design methods. The design of the deadzone estimator is presented next, followed by a discussion on the robustness of the method against model and parameter uncertainties. The performance of the estimation scheme is assessed through experiments.

Finally, Chapter 7 gives a retrospective evaluation of the findings in the entire project along with directions on future research possibilities.

Chapter 2

State Of The Art

This chapter provides a summary of the most fundamental and recent advances on the theories and methodologies used in this project. The review starts with a report of the conventional machine tool control techniques and continues with results on friction description and compensation. The modelling and estimation of backlash in mechanical systems are discussed next. The last two sections of the chapter give a general overview of nonlinear control and estimation methods that are later employed in this project.

2.1 Machine Tool Position Control

Detailed presentation of different machine tool-positioning strategies was provided in [14]. State-of-the-art positioning solutions follow two main approaches. The first one is referred to as Cross-Coupling Control (CCC) [15], where the control loops of all machine's axes are considered simultaneously, and the control objective is expressed as a contour-error regulation problem [16, 17]. In the second approach, called Individual Axis Control (IAC), each axis is handled separately. The effects of dynamics of other axes are treated as disturbances, and the control design reduces to that of individual axes [18]. Results in high-accuracy machine tool position control from both these categories use P-PI control loops and assume accurate knowledge of the system parameters.

Several methods that employ adaptation schemes have been used to address parameter uncertainty in machine tool systems. These control strategies rely on adjusting either the machine operating parameters (feed rate, spindle speed etc.) [19] or the tool geometry [20], such that the contouring error is sufficiently small and certain constraints (eg. regarding cutting forces) are satisfied. Online optimization has also been used to account for vibrations during cutting and tool wear

[21]. Apart from few exceptions (see [22] for a varying-gain Proportional-Integral-Differential (PID) machine tool controller and [23] for adaptive CCC that accounts for unknown inertial matrix), the majority of machine-tool adaptive techniques do not utilize parameter estimation in the system dynamics. Such feature could provide information of the wear level in the machine equipment. This could be achieved through the use of nonlinear and adaptive control algorithms in IAC architectures, because the problem of nonlinear position control for flexible axes is well explored.

Indeed, a number of relevant studies that employ techniques from nonlinear control theory, such as the Sliding-Mode Control (SMC) and the nonlinear Adaptive Control, have been reported in the literature regarding axis positioning. A general framework for nonlinear adaptive control for flexible joint manipulators was presented in [24]. A position tracking controller with global uniform asymptotic stability properties for a 2-link manipulator with no friction was designed in [25]. The tracking problem of a flexible joint manipulator with time-varying mechanical stiffness was addressed in [26] via the design of an *Immersion and Invariance* adaptive controller. General robust control designs for electromechanical systems based on SMC principles were presented in [27]. The application of a second-order SMC in more general motion control systems, including robotic manipulators with flexible links, was illustrated in [28].

Although the afore-mentioned techniques facilitate robust position control with respect model and parameter uncertainties, they mainly focus on stability of the closed-loop dynamics without emphasizing high-accuracy positioning. Integration of such designs into IAC architectures could provide solutions that ensure high-performance in machine tools both in nominal conditions and in the presence of incipient wear.

2.2 Friction Modelling and Compensation

The friction that develops between the contacting surfaces along the machine axes can severely affect the tool positioning accuracy. In order to alleviate the effects of frictional torques on the machining process, state-of-the-art axis position control solutions utilize friction-compensation algorithms by integrating appropriate feedforward terms into the P-PI cascades [18]. The majority of these algorithms are model-based and require an accurate description of the friction phenomenon.

Over the last decades several models of the friction in mechanical systems have been proposed. A detailed presentation of various friction models was given in [29]. Apart from the well known Coulomb and viscous friction [30], several dynamic models for friction have been developed to describe the nonlinear friction behaviour,

especially at low relative speeds of the contacting surfaces. The Dahl model [31] captures the presliding or Stribeck phenomenon, i.e. the quasi-linear decrease of the static friction before the motion starts. The authors in [32] introduced the LuGre model, where the average displacement of the contacting surfaces asperities (bristles) was represented as a state equation. A physical interpretation of the Dahl and LuGre models parameters was provided in [33]. The elasto-plastic model [34] was developed as an upgrade of the LuGre model to also include the Stiction. The Maxwell-slip [35] and Generalized Maxwell-slip models [36] also extended the LuGre model by including presliding hysteresis with nonlocal memory [37]. Sufficiently accurate friction description and estimation facilitates effective compensation of the phenomenon.

An overview of the different friction models and the corresponding compensation techniques in machines was given in [38]. The work in [39] explicitly focused on the frictional phenomena appearing in several parts of machine tool feed drives. Different models were associated to the various friction types in the system and were used in the design of feedforward terms in the control loops. The Extended Kalman-Bucy Filter was employed in [40] for estimation and compensation of the unknown friction torque in a mechanical system. The proposed method was compared to other friction compensation schemes. The adaptive backstepping controller with LuGre friction compensation [41], was extended in [42] to address the positioning of a double-motor drive servo system. The unknown friction dynamics were estimated by a double adaptive observer system and the estimate was fed to the control law. An adaptive controller for global tracking with LuGre friction compensation was designed in [43] for an n-degrees of freedom robotic manipulator.

Nonlinear control techniques for friction compensation have been sparsely used in machine tools (see [44] for a comparison of an adaptive friction-compensating controller with a fuzzy controller based on Takagi–Sugeno systems). Systematic nonlinear adaptive designs that exclusively focus on positioning accuracy could provide robust friction disturbance rejection in machine tools, while at the same time indicate increasing friction levels, and by extension, wear in the machine.

2.3 Backlash Modelling and Estimation

Backlash is a common positioning-degrading phenomenon in machine tools systems. It is the effect of loss of contact and sudden impacts of two connected components in a drive train, which occurs due to developing gaps (deadzones) in the coupling mechanisms of the machine axes. A substantial number of studies have been carried out regarding the description of the backlash phenomenon. The

deazone model [45] describes the backlash in terms of loss of engagement between the two coupled parts. The interconnecting torque, which was modelled after a restoring torque with damping, becomes zero inside the deadzone, while outside of it the position difference between the coupling components is offset by the width of the deadzone. The authors in [46] followed a similar approach in describing backlash, where the ratio of the position differences between the coupled parts over the deadzone width was used to determine whether the components are engaged or not. The backlash torque was modelled after a "contact" and "non-contact" part in [47], where the latter was a differentiable function of the deadzone width.

The previous descriptions employ static models for backlash and provide information on whether the interconnecting torque that transmits the motion between the coupled parts (e.g. drive motor to load) actually acts on the components or not. However, they do not describe the impact torques that occur up engagement of the parts after exiting the deadzone. Dynamical models have been developed to include this aspect of backlash as well. Specifically, the backlash torque was expressed in [48] as a sudden impact. The restoring-damping torque description was again used but the elastic linear relative deformation of the two colliding coupling parts had its own stiff dynamics. A different model was described in [49], where the deadzone dynamics were used for calculating the impact torque for control design. A collective presentation of the most common static and dynamic models for backlash was provided in [50]. As with friction, model-based backlash compensation algorithms require accurate description of the phenomenon.

Indirect backlash estimation relates to identifying torques and accelerations of the coupled mechanical parts to extract information on the width of the deadzones. A characteristic example is the method presented in [51], where backlash estimation in a gearing system was done via calculation of the sudden speed change (bounce) of the driving part of the gear. The Extended Kalman Filter (EKF) was employed in [52] for estimation of the backlash torque in a two-mass motor arm. The backlash parameters were identified offline, based on the estimated interconnecting torques. A method based on a switching Kalman filter was used in [53] for estimating the backlash parameters in an automotive powertrain. The deadzone width was expressed in terms of positive and negative position offsets, which were included in the filter as unmeasured states. Describing functions were used for modelling the effect of backlash in a closed loop motion system in [54]. A static relation between the functions parameters and the controller gains was used. Offline identification of backlash torque in cascaded linear systems was presented in [55]. The backlash estimation was cast as a quasi-linear optimization problem.

Direct methods for backlash identification utilize observers for estimating the

deadzone width. Position, velocity and torque measurements were used by [56] for backlash estimation in a vehicle drive-line system. Identification of the deadzone position offsets was done offline by minimizing the square of the prediction error. A sliding-mode observer was employed in [57] for estimating the "non-contact" torque introduced in [47]. The backlash amplitude was directly calculated from the estimation of the backlash torque.

Most of the above-mentioned methods often lack in accuracy due to insufficient description of the phenomenon. Whenever detailed backlash models are used, their complexity due to heavy nonlinearities and discontinuities makes the methods unsuitable for fast online estimation that could be used in control loops. Additionally, the majority of the methods considered for direct online estimation of backlash are only valid around a linearisation point of the system, thus providing only local solutions. Combining adaptive estimation principles (see [57]) with smooth low-complexity models for backlash could enable fast and robust online estimation of developing clearances in the machine axes. This, in turn, could facilitate more effective backlash compensation, as well as condition-based maintenance of the machine.

2.4 Sliding-Mode Controllers and Observers

Sliding-mode methods were first introduced in [58] and were elaborated through specific controller and observer architectures in [59]. The basic principle in designs with sliding modes is the use of high-theoretically infinite-frequency switching terms in the control signals. The resulting control laws are discontinuous and apart from robust disturbance rejection, they can provide finite-time stabilization and tracking of a reference signal, under certain disturbance boundedness conditions.

A detailed overview of the basic SMC and Sliding-Mode Observer (SMO) design principles was presented in [60] and [61], where control and observation schemes were proposed for uncertain linear and nonlinear systems with bounded perturbations. Application of SMOs for fault detection and reconstruction were detailed in [62, 63], while [64] focus was on actuator additive and multiplicative faults. An extension of these results for uncertain nonlinear systems was presented in [65, 66], where fault reconstruction was achieved under certain matching conditions. The assumptions for fault matching were relaxed in [67] through the use of multiple cascaded SMOs. A collective presentation of the fault-reconstruction and disturbance rejection properties of sliding-mode algorithms was given in [68].

Finite-time convergence in the sliding-mode algorithms requires infinite switching frequency in the control and estimation signals, which is practically not implementa-

ble due to hardware limitations. This introduces a chattering effect in the control commands, which can be damaging for the system actuators and compromises the tracking accuracy. Alleviation of the induced chatter was the main reason that motivated the research on high-order sliding-mode algorithms. The attenuation of the chattering effect was further discussed by [69] in connection to the second-order sliding-mode algorithms. The general design principles of higher-order SMCs were provided in [70], where the order of the sliding-mode algorithm was associated to the relative degree of the system. Second-order SMCs were discussed in more detail in [71, 72], where a specific design, namely the Super-Twisting Sliding-Mode Controller (STSMC), was presented. Strict Lyapunov functions for proving finite time convergence and asymptotic stability of the STSMC were suggested in [73]. The design of arbitrary-order SMCs using robust differentiators was suggested in [74].

Adaptive SMC designs were presented in [75, 76], where the controller gains were dynamically adjusted. A different approach in adaptive STSMC was discussed in [77], where, instead of the controller gains, the structure of the sliding manifold was dynamically modified based on the tracking error magnitude. A collective presentation of the most recent sliding-mode control designs was provided in [78, 79, 80], where implementation and application topics were also discussed.

The robustness features of high-order SMCs, such as the ones presented in [71, 72, 77], could be essential for designing machine tool wear-resilient positioning algorithms without detailed knowledge of the degrading phenomena. Moreover, finite-time convergent SMOs [61, 74] could be used for fast online identification of degrdations, such as friction and backlash.

2.5 Adaptive control

Adaptive control methodologies for regulation, tracking and disturbance rejection have been extensively researched during the past seven decades. The main philosophy in such designs pertains to representing the system in terms of a known, desired part of the dynamics (reference model dynamics) perturbed by an uncertain part (the regressor function) that depends on unknown parameters. The discrepancy between the desired and measured system output is used to dynamically update the parameter estimates, which are then used in the control signal applied to the system. This basic design principle, referred to as Model Reference Adaptive Control (MRAC), was discussed in great detail in [81, 82], along with topics related to online parameter and state estimation. The majority of the adaptive control and estimation schemes introduced in these works concerned linear systems.

The problem of adaptive control for a wide class of nonlinear systems was extensively studied in [83], where general design principles for Nonlinear Adaptive Control (NAC) were presented. One of the most significant contributions of this work was the systematic description of the Adaptive Backstepping Controller (ABSC) scheme. The development of this family of adaptive controllers was primarily motivated by the problem of regulating systems with relative degrees larger than 1, where the concept of virtual inputs was introduced. The designs also included solutions for systems with uncertain input gains, as well as several methods for ensuring parameter boundedness, such as the *parameter projection*. Similar approaches for addressing the problem of position and velocity control in mechanical systems were followed in [84, 85], who proved different stability properties of the closed-loop system dynamics. These methods primarily concerned systems with linear parametrization.

To account for perturbations with nonlinear parametrization, adaptive control solutions employed discontinuous adaptation schemes, such as the min-max algorithm [86, 87]. These approaches required specific convexity and boundedness properties of the regressor functions [88] or special system structure [89]. Whenever such assumptions did not hold, re-parametrization of the system was utilized to ensure convexity/concavity of the regressor function [90, 91]. Alternative approaches included smooth adaptive control laws that relied on dominating over the uncertain parameters rather than cancelling their effect [92].

A different approach of the adaptive control and estimation problem through a differential geometry prism was made in [93], which presented the main principles of the Immersion and Invariance Adaptive Control (I&I-AC) theory. These results, elaborated in [94], suggested a control design that requires finding an invariant manifold on which the emerging system dynamics has the required properties (stability, tracking, etc.). A robust velocity I&I controller for a permanent magnet synchronous motor was designed in [95]. The stabilization of underactuated mechanical systems was achieved in [96] through an I&I controller formulated in a port-Hamiltonian framework. The problem of global exponential position and velocity tracking for mechanical systems without velocity measurements was addressed via an I&I-AC design in [97]. Results for tracking control in nonlinearly parametrized systems with monotone regressor functions were reported in [98].

The trade-off between closed-loop stability and fast parameter estimation can be limiting in terms of performance of adaptive control schemes. $\mathcal{L}_1$ Adaptive Control (L_1AC) techniques, discussed extensively in [99], combine MRAC [81, 82] principles with appropriate control input filtering. Like in MRAC, the systems are parametrized with respect to a target (reference) system, while the unknown parameters are estimated by appropriate adaptation schemes. The key element of L_1AC architecture

is a lowpass filter applied in the controller output, which decouples the adaptation problem from the control law. This decoupling allows very fast adaptation without compromising the robustness of the closed-loop system [99]. The design of L_1AC was extended for nonlinear uncertain systems in [100, 101], while [102] provided an $\mathcal{L}_1$ adaptive controller for nonlinear reference systems. Guidelines for systematic design of the lowpass input filter for state-feedback and output feedback $\mathcal{L}_1$ adaptive controllers were provided in [103] and [104].

Adaptive control principles could be used for high-accuracy machine-tool positioning in the presence of unknown disturbances due to equipment wear or workspace changes. Estimation of the degrading phenomena parameters could enable exact cancellation of their effect on the axis positioning and at the same time provide information on the wear level. Designs based on the ABSC methodologies facilitate compensation of disturbances at every level of the machine (both the drive and the load) without utilizing cascaded architectures that may be sensitive to poor transient responses of the different subsystems. On the other hand, NAC, I&I-AC [94] and L_1AC [100] could combine robust machine tool positioning with detection of wear, using simpler and modular designs.

Chapter 3

Summary of Main Contributions

Journal Articles

The contributions of the research reported in this dissertation cover two main topics. The first relates to the design, implementation and evaluation of high-accuracy nonlinear tool position control methods with friction-resilience features. The second concerns fast, accurate online estimation of the deadzone in drive-train systems with backlash, as a means of wear assessment and for use in backlash compensation. The results of this research have been submitted as three journal articles:

(A) D. Papageorgiou, M. Blanke, H. H. Niemann, and J. H. Richter. "Friction resilience of machine tool controls - Classic, sliding mode and nonlinear adaptive techniques compared". *Control Engineering Practice* (2017). : Submitted paper under review.

Needs for high-precision tool positioning and accurate trajectory following have renewed the focus on controller design for machine tools in the Industry 4.0 digital factory. State-of-the-art controllers are based on P and PI principles; while these achieve sufficient nominal performance and are easy to implement and understand, their performance quickly deteriorates in the presence of equipment wear, tear, and general degradation. Moreover, their good performance assumes tuning by experts when a machine is commissioned. This paper presents design and experimental validation of nonlinear controllers for a machine tool. Based on adaptive and sliding-mode principles, the nonlinear control strategies are designed to cope with unknown and increasing friction phenomena, and comparison is made with standard linear control. Experimental results from a single-axis test setup equipped with a Siemens SINAMICS S120 drive controller show the performance in nominal condition and under

circumstances with increased-friction.

(B) D. Papageorgiou, M. Blanke, H. H. Niemann, and J. H. Richter. "Friction-resilient position control for machine tools - Adaptive and sliding-mode methods compared". *Control Engineering Practice* (2017). : Submitted paper under review.

Robust trajectory tracking and increasing demand for high-accuracy tool positioning have motivated research in advanced control design for machine tools. State-of-the-art solutions employ cascades of P and PI controllers for closed loop servo control of position and velocity of the tool. Although these schemes provide the required positioning accuracy in nominal conditions, performance is shown to deteriorate in the presence of degrading phenomena such as increased friction and wear. With conventional control, re-tuning would be necessarily during the lifetime of a computer controlled machine if specified accuracy should be maintained. This paper analyses the design and performance of selected direct-position controllers. Conventional solutions are compared to model-based adaptive and sliding-mode control principles, with focus on resilience to unknown and increasing friction. A single-axis test setup is used to assess the performance of different controllers.

(C) D. Papageorgiou, M. Blanke, H. H. Niemann, and J. H. Richter. "Robust backlash estimation for industrial drive-train systems - theory and validation". *Transactions on Control Systems Technology* (2017). : Submitted paper under review.

Backlash compensation is used in modern machine tool controls to ensure high-accuracy positioning. When wear of a machine causes deadzone width to increase, high-accuracy control may be maintained if the deadzone is accurately estimated. Deadzone estimation is also an important parameter to indicate the level of wear in a machine transmission, and tracking its development is essential for condition-based maintenance. This paper addresses the backlash estimation problem using sliding-mode and adaptive estimation principles and shows that prognosis of the development of wear is possible in both theory and practice. The paper provides proof of asymptotic convergence of the suggested estimator and it shows how position offset between motor and load is efficiently utilized in the design of a very efficient estimator. The algorithm is experimentally tested on a drive-train system with state-of-the-art Siemens equipment. The experiments validate the theory and shows that expected performance and robustness to parameter uncertainties are both achieved.

Peer Reviewed Conference Proceedings

The results on backlash modelling and simulation for deadzone change detection were disseminated in a peer-reviewed IEEE conference paper[1]:

(D) D. Papageorgiou, M. Blanke, H. H. Niemann, and J. H. Richter. "Backlash estimation for industrial drive-train systems" (July 2017). : To appear in IFAC-PapersOnLine.

Backlash in gearing and other transmission components is a common positioning-degrading phenomenon that develops over time in industrial machines. High-performance machine tool controls use backlash compensation algorithms to maintain accurate positioning of the tool to cope with such deadzone phenomena. As such, estimation of the magnitude of deadzones is essential. This paper addresses the generic problem of accurately estimating the width of the deadzone in a single-axis mechanical drive train. The paper suggests a scheme to estimate backlash between motor and load, employing a sliding-mode observer and a nonlinear adaptive estimator. The efficacy of the approach is illustrated via simulations.

Unpublished Work

There are two unpublished contributions included in the following thesis sections:

(4.4) Single-axis system parameter sensitivity and identifiability analysis:

This section presents the sensitivity and identifiability analysis for the single-axis friction and shaft coefficients and provides a quantified ranking of the parameters and the quality of their estimated values. Obtaining an accurate calibration of the developed mathematical model for the single-axis drive-train system is essential for the design and performance assessment of model-based control and estimation algorithms. The credibility of each parameter estimate depends not only on the excitation content of the input signals during the identification process but also on the sensitivity of the system outputs to the parameter. Even in the cases where this sensitivity is substantial, the identification algorithms may deliver poor results due to strong parameter correlation.

(5.5) State-feedback $\mathcal{L}_1$ adaptive control for machine-tool axis positioning:

[1]The content of this paper was filed as an invention disclosure at the European Patent Office with registration number 16195975.4.

This section discusses the design and applicability challenges of a state-feedback $\mathcal{L}_1$ adaptive controller for the drive-motor velocity in a machine-tool axis. This nonlinear controller is connected serially to a proportional controller that outputs appropriate velocity setpoints with the purpose of regulating the load position. The procedure of selecting and tuning both the parameter estimator and the input lowpass filter is elaborated and the theoretical assumptions that are necessary for the design of the controller are juxtaposed to the system properties. Experimental evaluation of the controller performance with respect to the load positioning task is provided in comparison to the state-of-the-art P-PI solutions.

Publications not included in the thesis

During the PhD program the following peer-reviewed conference paper was published. It is not included in this thesis:

- D. Papageorgiou, M. Blanke, H. H. Niemann, and J. H. Richter. "Fault tolerance for industrial actuators in absence of accurate models and hardware redundancy". *2015 IEEE Conference on Control Applications (CCA)*. Sept. 2015, pp. 1887–1894. DOI: 10.1109/CCA.2015.7320885.

Chapter 4

System Modelling

4.1 Introduction

A machine tool axis can be sufficiently described by the interconnection of a drive motor to a generalized load with friction through a flexible shaft. The topic of this chapter concerns the modelling and identification of this drive-train system, which is used as a test bench through the entire project. In general, the characteristics of the load friction and the shaft coefficients are unknown or uncertain. Therefore, parameter estimation is an important first step in developing robust model-based algorithms for axis position control.

The chapter starts with a description of the machining process, highlighting the equivalence between the single-axis system accurate positioning and the manufacturing quality of the machined components. A discussion on the required workpiece tolerances and the phenomena that degrade the positioning accuracy follows, along with the description of the physical system used in the project for emulating a machine axis. The mathematical model of the single-axis is detailed and some assumptions regarding model reduction are discussed. The parameters of the model are identified using regression and optimization techniques and sensitivity analysis is performed to rank the parameters with respect to their significance in the system's outputs. Finally, the chapter is concluded with a discussion on the parameter estimation results and on possible future extensions.

4.2 System Description

As already mentioned in Chapter 1, the relative positioning between tool and workpiece in a machine tool can be reduced to the problem of controlling each axis of the machine separately. These axes contribute to the positioning of the table base,

on which the workpiece is, or to the placing of the tool itself. An axis in a machine tool, which in this thesis will be referred to as the *single-axis system*, typically consists of a drive motor, a lead screw (or ball-screw) linear axis and a coupling mechanism, usually with gearing.

The most common choice for a drive motor in machine tool systems is the permanent magnet synchronous motor (PMSM). This is due to the fact that this type of motors can generate very high torques with relatively simple control architectures [105], which makes them suitable for applications that demand highly-dynamic performance. The rotor shaft of the drive motor is connected to the main shaft of the linear axis via a number of coupling clutches and gearing mechanisms. The rotational motion of the drive motor shaft is transformed into linear motion through the lead/ball-screw mechanism of the linear axis, which, in turn, positions the tool relatively to the workpiece (or the table base bearing the workpiece with respect to the tool).

Looking from the drive motor side, the combined elasticity of all the mechanical components that connect to the rotor shaft can be represented as a series of interconnected torsional springs and dampers [18]. The masses of the linear axis, the couplers, the table and the workpiece can be lumped into a single inertia, which is accelerated by the torque produced by the drive motor. The total friction coming from the various contacting surfaces of the axis, along with the effects of the external cutting forces on the workpiece, constitute the decelerating torques at the shaft. This considerations allow the description of a single-axis system as a mechanical drive-train consisting of the drive motor, a flexible shaft with damping and a generalized load with friction and possibly backlash. This abstraction is illustrated in Figure 4.1, which shows the correspondence between the single-axis system and the drive train system.

4.2.1 Positioning Accuracy and Degradation

High accuracy is essential in automated manufacturing processes. The tolerances of a machined workpiece are required to be in the order of $1 - 10\ \mu\mathrm{m}$. Typical lead-screw linear axes used in machine tool applications have a lead pitch that ranges from $2\ \mathrm{mm}$ to $10\ \mathrm{mm}$. This translates the accuracy requirement to an angular positioning tolerance between $5\ \mathrm{mrad}$ and $20\ \mathrm{mrad}$ [18]. The accuracy requirement for the positioning of the generalized load considered in this study is chosen to be $10\ \mathrm{mrad}$.

In order for the workpiece tolerances to be maintained, i.e. the load angular positioning error be kept smaller than $10\ \mathrm{mrad}$, appropriate control algorithms are used to regulate the positioning of the machine axis. However, several phenomena,

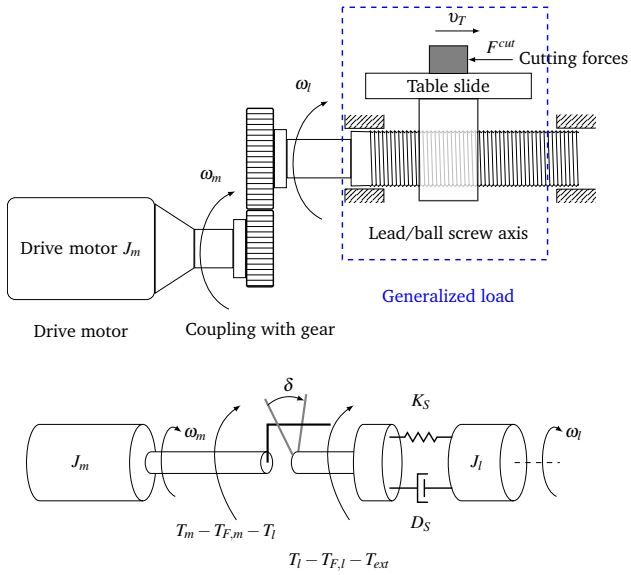

Figure 4.1: Correspondence between mechanical drive-train and machine-tool axis, where ω_m, ω_l are the motor and load angular velocities, respectively, υ_T is the linear velocity of the table (or of the tool) and F^{cut} are external cutting forces. In the bottom plot, J_m, J_l are the drive motor and generalized load inertias, respectively, δ is the width of the deadzone in the coupling, T_m is the torque generated by the drive motor, T_l is the interconnecting spring-damping torque, K_S, D_S are the spring constant and damping coefficient of the flexible shaft, respectively, $T_{F,m}, T_{F,l}$ are the friction torques acting on the motor and the load and T_{ext} is the torque-equivalent of the external cutting forces.

such as friction and backlash, may compromise the positioning accuracy and, by extension, the quality of the machined product. For this reason fiction and backlash compensation solutions are typically integrated in state-of-the-art machine tool controllers. These compensation schemes require knowledge of the friction and backlash characteristics, which are available after the commissioning of each machine. These characteristics, however, may change over time due to wear and varying environmental conditions. Characteristic examples include increased Coulomb friction between contacting surfaces of the machine due to small deformations and lubrication film failures, increased viscosity due to workspace temperature raise [39], as well as, developing clearances in the coupling components.

The effects of friction, backlash and other degrading phenomena, such as varying load inertia and eddy currents, are reflected on the deviation of the actual load position from the commanded motion profiles coming from the trajectory generator. This, in turn, leads not only to tool-positioning degradation but also to geometrical

errors, such as radial or axial contour distortions [18]. Moreover, backlash may compromise the machine's repeatability [10]. Figure 4.2 shows four common geometric errors in a two-axis machine tool system while performing a circular contouring task.

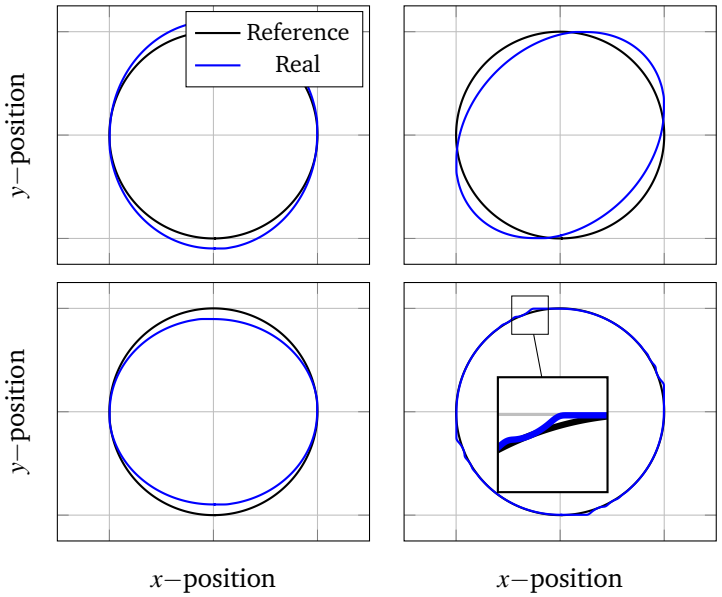

Figure 4.2: Four types of geometric (contouring) errors in a two-axis machine tool: (Left top and bottom) Scale mismatch due to amplitude error. (Right top) Squareness error due to phase lag or lack of synchronization between the axes. (Right bottom): Backlash.

4.2.2 Experimental Apparatus

The physical system considered in this research is a drive train consisting of two motors connected through a steel shaft. All the experimental equipment was provided by Siemens AG and included the following components:

1. Two Siemens 1FT7042-5AF70 PMSMs [106], one acting as the drive motor and the other as the load. The second motor can exert various torque profiles to emulate the effect of cutting forces and other external disturbances. Throughout the entire project it is considered as pure inertia. Each motor is equipped with an 11-bit absolute position encoder. The motors velocities readings are obtained by numerical differentiation of the position values and are inflicted with zero-mean white Gaussian noise with standard deviation approximately $\sigma_{meas} = 9 \cdot 10^{-3} \mathrm{rad\,s^{-1}}$ (see Figure 4.3).

2. A Siemens Sinamics S120 drive converter [107], which includes two power modules 340 with a CUA31 control unit (CU) adapter attached to each one of them (their combination correspond to two motor modules) and an external sensor module SMC20. The latter enables the communication between the control unit of the converter and the position encoders. The CU processor manages all the input/output signals and the control loops with sampling time $T_s = 125\ \mu$s. The signal values are recorded for offline processing with sampling frequency up to 500 Hz.
3. Two laser plates mounted on each motor for vibration detection.
4. Two chucks for mounting the connecting shaft on the motors.
5. A TB15 operator box that provides additional analogue and digital inputs.
6. Two aluminium strut profiles that serve as a base for the motors, along with the corresponding mounting components.

The experimental setup also includes a cylindrical Vari-tork 279.25.22 adjustable-friction clutch [108], which houses the interconnecting shaft (see Figure 4.4). The friction is developed between the inner cylinder housing the shaft, and the outer bearing of the component. A ring adjusts the friction between these two surfaces, increasing it as it turns clockwise. Finally, a number of components were designed and manufactured for the needs of the experiments. These include the friction component mounting base and three jaw couplings with different clearance sizes for emulating the backlash phenomenon. Figures 4.4 and 4.5 show the front and top view of the physical system and the experimental equipment.

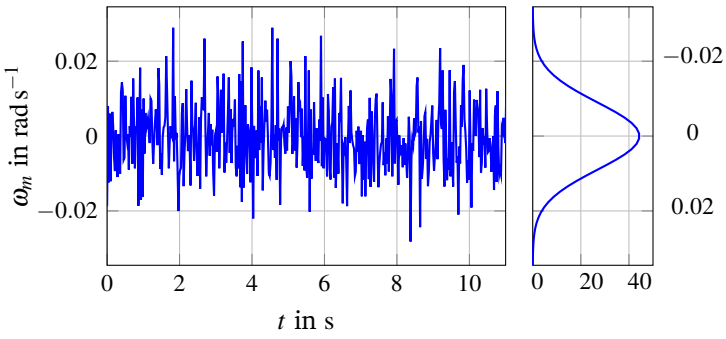

Figure 4.3: (Left) Drive motor zero velocity measurement. (Right) Probability distribution of velocity measurement noise.

The parametrization of the control algorithms as well as the initialization and termination of the experiments is done through the Siemens drive commissioning

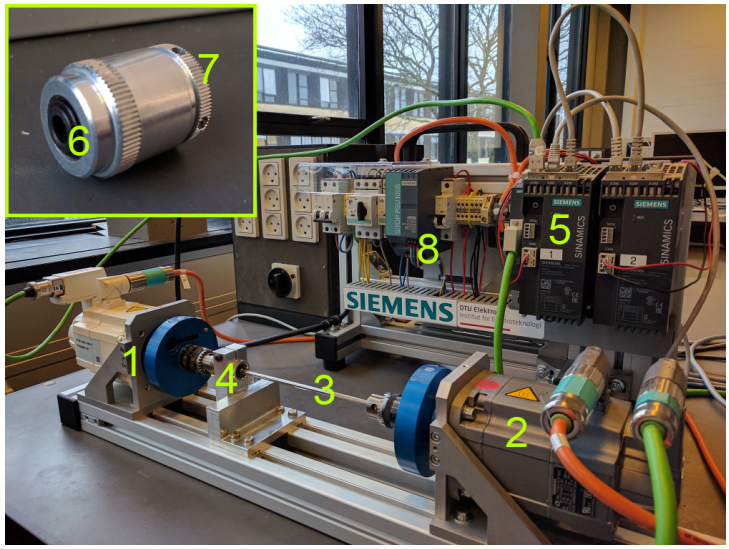

Figure 4.4: Front view of the experimental setup: (1) 1FT7 drive PMSM, (2) 1FT7 load PMSM, (3) steel shaft, (4) friction component base, (5) CUA31 control unit adapter, (6) shaft housing, (7) friction adjustment ring, (8) power safety.

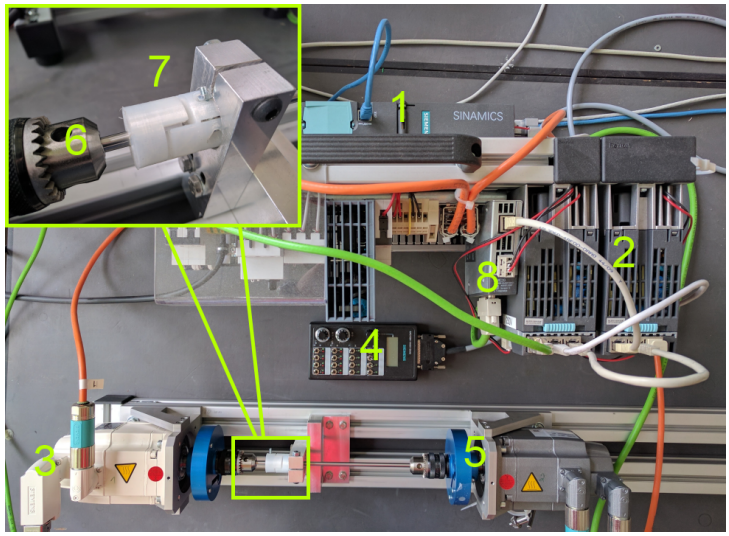

Figure 4.5: Top view of the experimental setup: (1) Sinamics S120 control unit, (2) power modules 340, (3) position encoder, (4) TB15 operator box, (5) lase plate, (6) chuck, (7) jaw coupling, (8) SMC20 external sensor module.

software STARTER. A schematic of the operational architecture of the experimental setup is provided in Figure 4.6.

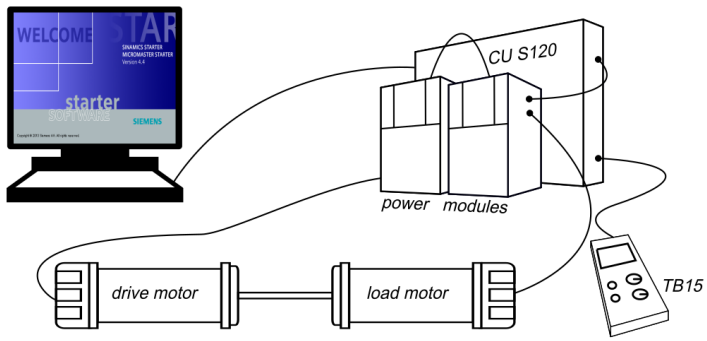

Figure 4.6: Operation interconnection of the experimental hardware.

4.3 Mathematical Model

A first-principle mathematical model is developed for the single-axis system. The quantities that describe the dynamics of the system are the drive motor stator currents (one in each of the three phases) and the angular position and velocity both of the rotor shaft on the motor and of the load. The equations describing the system dynamics are derived from the analysis of the electromagnetic equivalent circuit of the drive motor and Newton's laws for rotational motion. A complete explanation of the most important variables and notation used in the single-axis model is provided in Table 4.1.

4.3.1 Electrical Dynamics

The voltage equations from Kirchoff's law for the three-phase PMSM in the stator frame are given by [109]

$$v_{a,s} = r_s i_{a,s} + \frac{d\lambda_{a,s}}{dt} \tag{4.1}$$

$$v_{b,s} = r_s i_{b,s} + \frac{d\lambda_{b,s}}{dt} \tag{4.2}$$

$$v_{c,s} = r_s i_{c,s} + \frac{d\lambda_{c,s}}{dt} \tag{4.3}$$

or in matrix form

$$\boldsymbol{v_{abc,s}} = \boldsymbol{R_s i_{abc,s}} + \frac{d\boldsymbol{\lambda_{abc,s}}}{dt} \tag{4.4}$$

Table 4.1: System model nomenclature.

Symbol	Description	Units
States and Outputs		
i_d	Direct axis current	A
i_q	Quadrature axis current	A
ω_m	Motor angular velocity	$\mathrm{rad\,s^{-1}}$
θ_m	Motor angular position	rad
ω_l	Load angular velocity	$\mathrm{rad\,s^{-1}}$
θ_l	Load angular position	rad
Inputs		
θ_r	Load position reference	rad
ω_r	Motor velocity reference	$\mathrm{rad\,s^{-1}}$
V_d	Direct axis voltage	V
V_q	Quadrature axis voltage	V
u	Torque command	$\mathrm{N\,m}$
Constant parameters		
r_s	Stator total windings resistance	Ω
L_d	Direct axis inductance	mH
L_q	Quadrature axis inductance	mH
λ_m	Amplitude of flux linkages	$\mathrm{V\,s\,rad^{-1}}$
P_m	Number of drive motor poles	$-$
N	Gearing ratio	$-$
J_m	Motor inertia	$\mathrm{kg\,m^2}$
J_l	Load inertia	$\mathrm{kg\,m^2}$
K_S	Shaft stiffness	$\mathrm{N\,m\,rad^{-1}}$
D_S	Shaft damping coefficient	$\mathrm{N\,m\,s\,rad^{-1}}$
$T_{C,m}$	Coulomb friction on the motor	$\mathrm{N\,m}$
$T_{C,l}$	Coulomb friction on the load	$\mathrm{N\,m}$
$T_{S,m}$	Static friction on the motor	$\mathrm{N\,m}$
$T_{S,l}$	Static friction on the load	$\mathrm{N\,m}$
ω_S	Stribeck velocity	$\mathrm{rad\,s^{-1}}$
β_m	Motor viscous friction coefficient	$\mathrm{N\,m\,s\,rad^{-1}}$
β_l	Load viscous friction coefficient	$\mathrm{N\,m\,s\,rad^{-1}}$
Internal torques and disturbances		
d_e	Input torque ripples and harmonics	$\mathrm{N\,m}$
$T_{F,m}$	Motor friction	$\mathrm{N\,m}$
$T_{F,l}$	Load friction	$\mathrm{N\,m}$
T_m	Motor torque	$\mathrm{N\,m}$
T_l	Interconnecting torque	$\mathrm{N\,m}$

with

$$\boldsymbol{\lambda_{abc,s}} = \boldsymbol{L_s i_{abc,s}} + \boldsymbol{\lambda_m} \tag{4.5}$$

and

$$\boldsymbol{R_s} = \begin{bmatrix} r_s & 0 & 0 \\ 0 & r_s & 0 \\ 0 & 0 & r_s \end{bmatrix} \tag{4.6}$$

$$\boldsymbol{L_s} = \begin{bmatrix} L_{l,s} + L_{m,s} & -\frac{1}{2}L_{m,s} & -\frac{1}{2}L_{m,s} \\ -\frac{1}{2}L_{m,s} & L_{l,s} + L_{m,s} & -\frac{1}{2}L_{m,s} \\ -\frac{1}{2}L_{m,s} & -\frac{1}{2}L_{m,s} & L_{l,s} + L_{m,s} \end{bmatrix} \tag{4.7}$$

$$\boldsymbol{\lambda_m} = \lambda_m \begin{bmatrix} \sin(\theta_r) \\ \sin\left(\theta_r - \frac{2\pi}{3}\right) \\ \sin\left(\theta_r + \frac{2\pi}{3}\right) \end{bmatrix} \tag{4.8}$$

where v, i, λ are voltages, currents and magnetic fluxes of the stator in the dq-frame, r_s is the windings' resistances, $L_{l,s}$ and $L_{m,s}$ represent the leakage and magnetizing inductances, respectively and λ_m is the amplitude of the flux linkages established by the permanent magnet as viewed from the stator phase windings.

Differentiating Equation (4.5) and applying the *dq0-transformation* defined in (I.1) leads to the electrical dynamics of the drive motor:

$$\frac{di_d}{dt} = -\frac{r_s}{L_d} i_d + \frac{L_q}{L_d} i_q \omega_m + \frac{1}{L_d} V_d \tag{4.9a}$$

$$\frac{di_q}{dt} = -\frac{r_s}{L_q} i_q - \frac{L_d}{L_q} i_d \omega_m - \frac{\lambda_m}{L_q} \omega_m + \frac{1}{L_q} V_q \ . \tag{4.9b}$$

4.3.2 Mechanical Dynamics

The accelerating torque generated by the drive motor is given by [109]:

$$T_m = \frac{3P_m}{4} \left[\lambda_m i_q + (L_q - L_d) i_d i_q\right] \tag{4.10}$$

The mechanical part of the single-axis system can be viewed as the two-mass spring-damper system shown in the bottom diagram of Figure 4.1. Its dynamics are derived by applying Newton's law for rotational motion:

$$\frac{d\omega_m}{dt} = \frac{1}{J_m}(T_m - T_{F,m} - \frac{1}{N} T_l) \tag{4.11a}$$

$$\frac{d\theta_m}{dt} = \omega_m \tag{4.11b}$$

$$\frac{d\omega_l}{dt} = \frac{1}{J_l}(T_l - T_{F,l}) \tag{4.11c}$$

$$\frac{d\theta_l}{dt} = \omega_l \ , \tag{4.11d}$$

where the effect of the external cutting forces on the load has not be taken into consideration. In absence of any clearances in the coupling equipment between motor and load, the interconnecting torque T_l is given by:

$$T_l = K_S \left(\frac{1}{N}\theta_m - \theta_l \right) + D_S \left(\frac{1}{N}\omega_m - \omega_l \right). \tag{4.12}$$

In the case that deadzones are present in various places of the linear axis, the expression of T_l in (4.12) is modified in order to include the description of backlash. This description often utilizes discontinuous models for T_l, such as the deadzone model [45], which are difficult to use for control and estimation purposes. The backlash model proposed in this research is based on a variable-stiffness approach. The main consideration in this model is that the connecting shaft stiffness is zero inside the deadzone, as there is no contact between motor and load, and it assumes its nominal value K_S outside the deadzone. The interconnecting torque T_l is then given by:

$$K_{BL} = \frac{K_S}{\pi} \left[\pi + \arctan(\alpha(\Delta\theta - \delta + \delta_1)) - \arctan(\alpha(\Delta\theta + \delta_1)) \right] \tag{4.13}$$

$$T_l(\boldsymbol{x}, \delta) = \left[\Delta\theta + \delta_1 - \frac{\delta}{2} \cdot (1 + \text{sgn}(\Delta\theta)) + \frac{D_S}{K_S}\Delta\omega \right] \cdot K_{BL}(\Delta\theta, \delta)\ , \tag{4.14}$$

where δ is the width of the clearance in rad, δ_1 is the initial motor-load angular position offset, $\Delta\theta, \Delta\omega$ are the angular position and velocity differences between motor and load, respectively, and the signum function $\text{sgn}(\cdot)$ is defined in (II.1). The varying-stiffness model for backlash was introduced in [3, 4] and it is elaborated in Chapter 6 in relation to the deadzone angle estimation.

The friction torques T_m, T_l acting on the motor and load, respectively, in a machine tool axis are typically different. The friction on the motor side comes from the contacting surfaces of the motor bearings. Additionally, heat losses due to parasitic eddy currents can also be lumped into the viscous damping of the motor [105]. The load friction is a combination of all frictional forces that develop between any contact surface from the coupling mechanism to the end of the axis. Consequently, there can be used not only different parameter values but also different models for describing these two frictional torques $T_{F,m}, T_{F,l}$.

However, since in the physical system of this study the drive and the load are actually two identical motors, the same friction model is adopted for both of them. This consideration is valid on the basis that the friction sources on both sides are the same. For the cases where the operation speed of the machine is very low (lower than $0.5\ \text{rad}\,\text{s}^{-1}$), the Coulomb-viscous-Stribeck friction model [30] is used:

$$T_{F,i} = \left[T_{C,i} + (T_{S,i} - T_{C,i}) e^{-\left(\frac{\omega_i}{\omega_S}\right)^2} \right] \text{sgn}(\omega_i) + \beta_i \omega_i,\ i \in \{m, l\}, \tag{4.15}$$

where, $T_{C,i}, T_{S,i}, \beta_i$ are the Coulomb, static and viscous friction coefficients and ω_S is the Stribeck stick-slip velocity, typically very small (lower than $0.05\ \mathrm{rad\,s^{-1}}$) [29]. If the axis is moving with higher speeds, then the Coulomb and viscous friction are the dominant frictional phenomena, in which case the friction torques are given by:

$$T_{F,i} = T_{C,i}\mathrm{sgn}(\omega_i) + \beta_i\omega_i,\ i \in \{m, l\}. \tag{4.16}$$

It can easily be seen from (4.15), (4.16) that as the angular velocity (of the motor or the load) increases in amplitude with respect to ω_S, the Coulomb-viscous-Stribeck model converges to the Coulomb-viscous firction model of (4.16).

4.3.3 Model Reduction

The main positioning-degrading phenomena considered in this research, namely friction and backlash, appear as decelerating torques, i.e. in the mechanical dynamics of the system. This motivates focusing the control and estimation design on the position and velocity loops, rather than on the current control loops. The decoupling of the electrical from the mechanical dynamics of the system is also based on the fact that the former are much faster than the latter. For appropriate tuning of the current controllers, typically PI, any torque command which complies to the acceleration and jerk limitations of the motor can be generated. The torque commands, multiplied by the torque constant of the motor $k_T = \frac{3P_m}{4}$, are translated to current reference points and fed to the current controllers. These, in turn, produce the necessary voltage values for the motor, such that the desired torque profile is generated, as shown in the top diagram of Figure 4.7.

The actual torque T_m generated by the motor is the torque command u plus an input disturbance d_e, which describes any deviation between commanded and produced torque. The input disturbance d_e, which also includes any parasitic harmonics from the controlled current dynamics, is approximately no larger than $0.1 - 0.5\%$ of the maximum torque that can be generated by the motor and the torque harmonics appear within the frequency range $10 - 100$ Hz. This can be experimentally validated for the 1FT7042 PMSM, which has maximum torque value $T_m^{max} = 13\ \mathrm{N\,m}$ [106]. Figure 4.8 shows two different torque commands with the associated generated torques, as well as their difference. It can be seen that the disturbance d_e is confined in a $\pm 0.02\ \mathrm{N\,m}$ zone, which corresponds to approximately 0.15% of the maximum torque value. Figure 4.9 shows the torque response of the motor for a series of step commands along with the power spectral density plot for d_e. As it can be seen, the dominant torque harmonics are located below 40 Hz. It should be noted that part of the observed disturbance d_e is related to the measurement

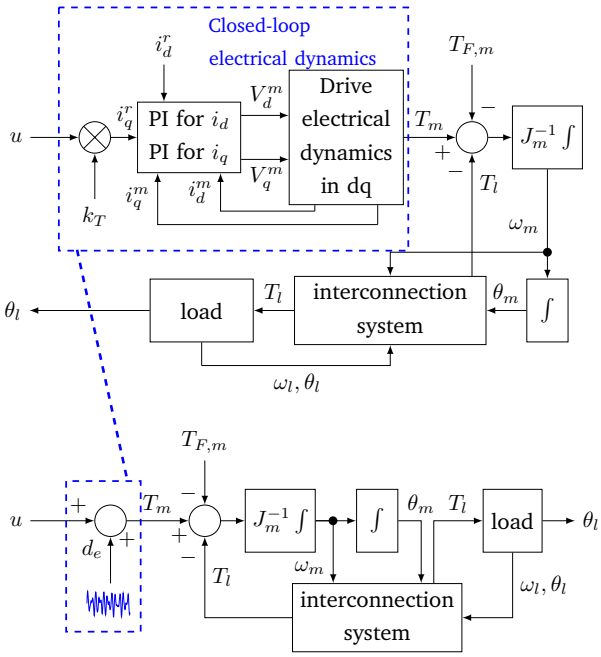

Figure 4.7: (Top) Single axis system with closed-loop electrical dynamics. The torque command u is translated into the current reference signal i_q^r through the torque constant $k_T = \frac{3P_m}{4}$. (Bottom) Reduced-order single-axis system.

noise and ripples in the current transducers that provide an indirect measurement of the generated torque.

These considerations lead to the following assumption pertaining to the model reduction for the single-axis system:

Assumption 4.3.1. *The closed-loop electrical dynamics of the single-axis system can be considered as a unit gain perturbed by a finite number of torque ripples, i.e. the torque produced by the motor is the torque command plus a deviation which is no larger than* 0.5% *of the maximum allowable torque:*

$$T_m = u + d_e \ , \ |d_e| \leq 0.005 \cdot T_m^{max} \ . \tag{4.17}$$

The reduced model of the single-axis system, which is shown in the bottom

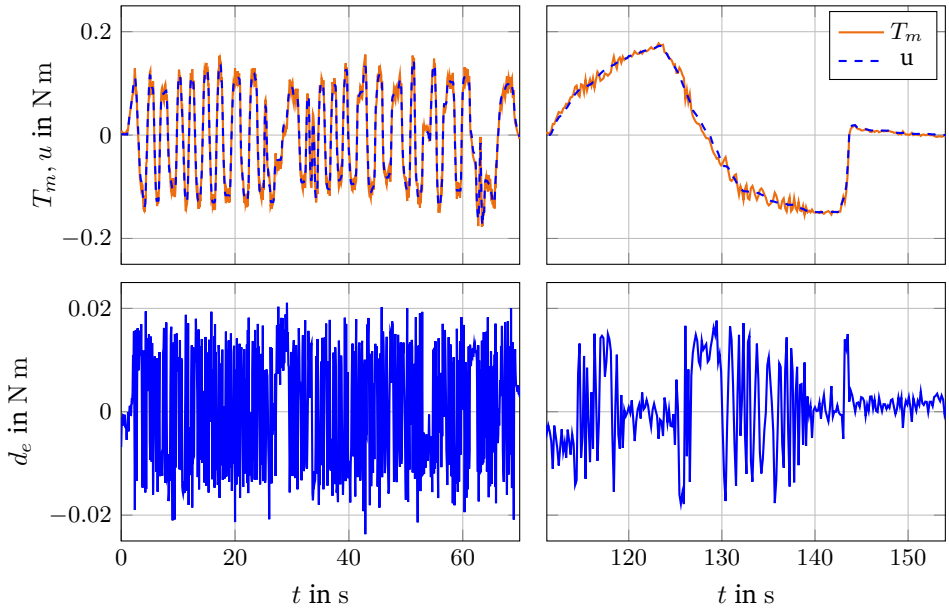

Figure 4.8: Two different torque profiles. (Top) Torque command u and actual motor torque T_m. (Bottom) Input torque errors.

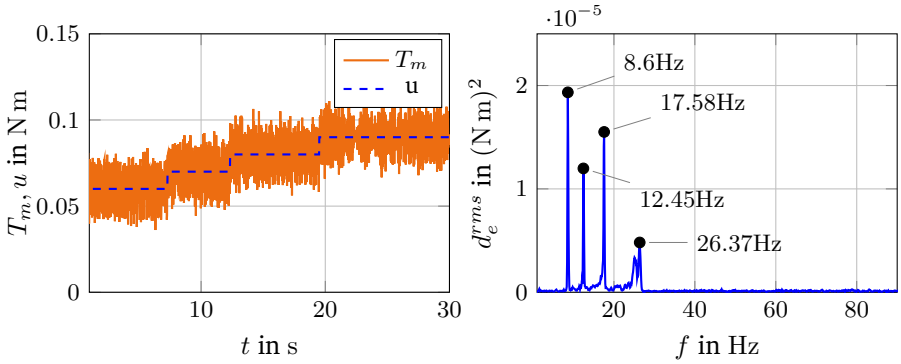

Figure 4.9: (Left): Step torque commands and actual torque. (Right): Power spectral density and frequency locations of torque ripples.

diagram of Figure 4.7, is now described by the following dynamics:

$$\dot{\omega}_m = \frac{1}{J_m}(u + d_e) - \frac{1}{J_m}\left(T_{F,m} + \frac{1}{N}T_l\right) \tag{4.18a}$$

$$\dot{\theta}_m = \omega_m \tag{4.18b}$$

$$\dot{\omega}_l = \frac{1}{J_l}\left(T_l - T_{F,l}\right) \tag{4.18c}$$

$$\dot{\theta}_l = \omega_l \ , \tag{4.18d}$$

where u is the torque command and $T_{F,m}, T_{F,l}, T_l$ have been defined in Equations (4.15), (4.16), (4.12).

4.4 Parameter Sensitivity Analysis and Identification

The single-axis system contains six unknown parameters, namely the connecting shaft stiffness K_S and damping coefficient D_S and the friction Coulomb and viscous characteristics $T_{C,m}, \beta_m, T_{C,l}, \beta_l$ for the motor and load, respectively. If the Coulomb-viscous-Stribeck friction model in (4.15) is used, then the unknown parameters are increased by four, including the static friction coefficients $T_{S,m}, T_{S,l}$ and Stribeck velocities $\omega_{S,m}, \omega_{S,l}$. Identifying ten parameters can, in general, be challenging and requires extensive efforts in designing appropriate excitation signals, which is out of the scope of this research. However, sufficient calibration of the model such that it fits the physical system is necessary for evaluating the parameter estimation features of the adaptive control schemes presented in Chapter 5.

To this end an initial calculation of the shaft parameters is carried through based on the system geometry and physical properties. Additional steady-state experiments are performed such that some of the friction parameters are obtained. A sensitivity analysis follows, indicating the identifiability and correlation of the parameters, which, in turn, are separated into smaller subsets. Finally, estimation of the parameters in each of these subsets is performed using regressive least square methods.

4.4.1 Calculation of Friction Parameters

For the calculation of the viscous friction coefficients, the two motors of the experimental setup are decoupled and each of them is run in various constant speed profiles. The friction torque applied on each of the motors is calculated as the difference between the torque generated by the motor and its acceleration scaled by its inertia:

$$T_{F,i} = T_{m,i} - J_i\dot{\hat{\omega}}_i \ , \ i \in \{m, l\}. \tag{4.19}$$

The accelerations $\dot{\hat{\omega}}_i$ are estimated by using a linear velocity observer

$$\dot{\hat{\omega}}_i = \hat{\omega}_i + L\tilde{\omega}_i \ , \ L > 0 \ , \tag{4.20}$$

where $\hat{\omega}_i$ are the estimated velocities and $\tilde{\omega}_i \triangleq \omega_i - \hat{\omega}_i$ are the associated estimation errors. The observer gain is chosen $L = 154$.

For a given constant speed $\omega_F \gg \omega_S$, the friction torque is given by

$$T_{F,i} = T_{C,i}\text{sgn}(\omega_F) + \beta_i\omega_F \tag{4.21}$$

where the sign of ω_F is known and constant. Calculating the slope of the line $T_F = T_F(\omega_F)$ provides an estimate of the viscous friction coefficient. Table 4.2 shows the estimated values for β_m and β_l obtained from 14 different constant-speed experiments (7 for each motor) through linear regression. As the velocity setpoints increase in magnitude, both viscous friction coefficients converge to a constant value close to $0.0016\ \mathrm{N\,m\,s\,rad^{-1}}$. This is due to the fact that in large speeds the viscous friction dominates over the other friction phenomena making the calculation of the corresponding coefficients easier. This can be clearly seen in Figure 4.10, where β_m and β_l are plotted as functions of the velocity setpoint. Figure 4.11 shows the estimated slopes β_m, β_l fitted into the recorded velocity-friction data during four of the experiments.

Table 4.2: Calculation of viscous friction coefficients β_m, β_l from constant speed experiments.

Experiment	**Velocity setpoint**	**Viscous coefficient**
No	ω_m in $\mathrm{rad\,s^{-1}}$	β_m in $\mathrm{N\,m\,s\,rad^{-1}}$
1	3.45	0.0092
2	6	0.0060
3	11	0.0041
4	13	0.0037
5	19	0.0029
6	28	0.0024
7	33	0.0021
No	ω_l in $\mathrm{rad\,s^{-1}}$	β_l in $\mathrm{N\,m\,s\,rad^{-1}}$
8	1.5	0.0178
9	8	0.0050
10	11	0.0041
11	16	0.0034
12	19	0.0030
13	24	0.0026
14	39	0.0019

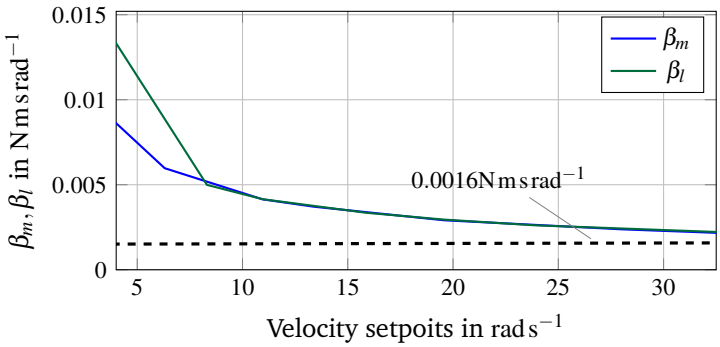

Figure 4.10: Viscous friction coefficients for the motor and the load as functions of the velocity setpoint. As the velocity increases, the coefficients asymptotically approach a constant value close to $0.0016\ \mathrm{N\,m\,s\,rad^{-1}}$.

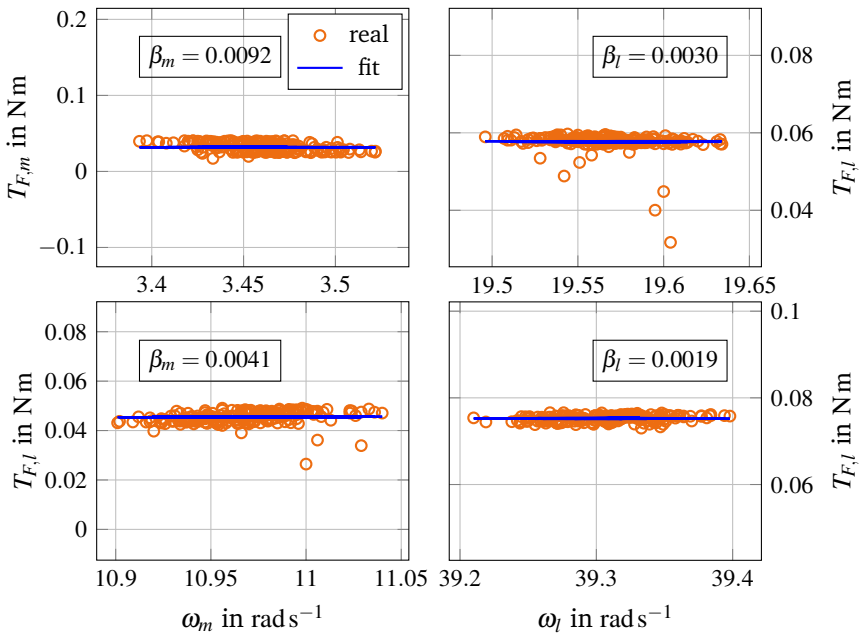

Figure 4.11: Viscous friction coefficients calculation via linear regression: Velocity-friction plots during different constant drive motor (left plots) and load (right plots) velocities.

The estimation of β_m, β_l allows the isolation of the term $T_{C,i}\text{sgn}(\omega_i)$ in the friction equation (4.16), where $T_{F,i}$ is again estimated by the linear observer described in Equation (4.20). Consequently, the Coulomb friction coefficients $T_{C,i},\ i \in \{m, l\}$ can be calculated using linear regression methods, i.e. by solving the over-constrained linear systems

$$\underbrace{\begin{bmatrix} T_{F,i}(t_0+T_s) \\ T_{F,i}(t_0+2T_s) \\ \vdots \\ T_{F,i}(t_0+n_sT_s) \end{bmatrix} - \beta_i \begin{bmatrix} \omega_i(t_0+T_s) \\ \omega_i(t_0+2T_s) \\ \vdots \\ \omega_i(t_0+n_sT_s) \end{bmatrix}}_{\boldsymbol{A_{F,i}}} = \underbrace{\begin{bmatrix} \text{sgn}(\omega_i(t_0+T_s)) \\ \text{sgn}(\omega_i(t_0+2T_s)) \\ \vdots \\ \text{sgn}(\omega_i(t_0+n_sT_s)) \end{bmatrix}}_{\boldsymbol{B_{F,i}}} T_{C,i}\ , \tag{4.22}$$

where t_0 is the time at which the recording of the data began, n_s is the number of samples and T_s is the sampling period. The solutions of (4.22) are given from:

$$T_{C,i} = \boldsymbol{B_{F,i}}^{+}\boldsymbol{A_{F,i}}\ ,\ i \in \{m, l\}\ , \tag{4.23}$$

where $\boldsymbol{B_{F,i}}^{+}$ is the left pseudoinverse of $\boldsymbol{B_{F,i}}$ defined in (II.2). By allowing $\beta_m = \beta_l = 0.0016\ \text{N m s rad}^{-1}$, the Coulomb friction coefficients for the motor and the load are found $T_{C,m} = 0.0223\ \text{N m}$ and $T_{C,l} = 0.0232\ \text{N m}$, respectively. Repeating the same procedure but with the Coulomb friction coefficients also fixed to their calculated values, allows for estimating the stiction coefficients $T_{S,m}, T_{S,l}$. In this case the matrices $\boldsymbol{A_{F,i}}, \boldsymbol{B_{F,i}}$ are defined as:

$$\begin{aligned}
\boldsymbol{A_{F,i}} &= [a_{ij}] \\
a_{ij} &= T_{F,i}(t_0+jT_s) - \left(1 - e^{-\left(\frac{\omega_i(t_0+jT_s)}{\omega_S}\right)^2}\right)\text{sgn}(\omega_i(t_0+jT_s)) - \beta_i\omega_i(t_0+jT_s) \\
\boldsymbol{B_{F,i}} &= [b_{ij}] \\
b_{ij} &= e^{-\left(\frac{\omega_i(t_0+jT_s)}{\omega_S}\right)^2}\text{sgn}(\omega_i(t_0+jT_s))\ ,
\end{aligned}$$

with $i \in \{m, l\}$ and $j \in \{1, 2, 3, \ldots, n_s\}$. The calculated stiction values are $T_{S,m} = 0.0441\ \text{N m}$ and $T_{S,l} = 0.0453\ \text{N m}$. The fit of the calculated friction parameters to the measured data is illustrated in Figure 4.12, where the velocity-torque plots are shown during two different experiments (one for the motor and one for the load), along with the measured and estimated velocities from the linear observer.

4.4.2 Shaft Coefficients Calculation

The shaft stiffness K_S and damping coefficient D_S can be calculated from the shaft physical properties and geometry and by examining the natural frequencies of the single-axis system. The connecting shaft is a cold-rolled steel cylinder with

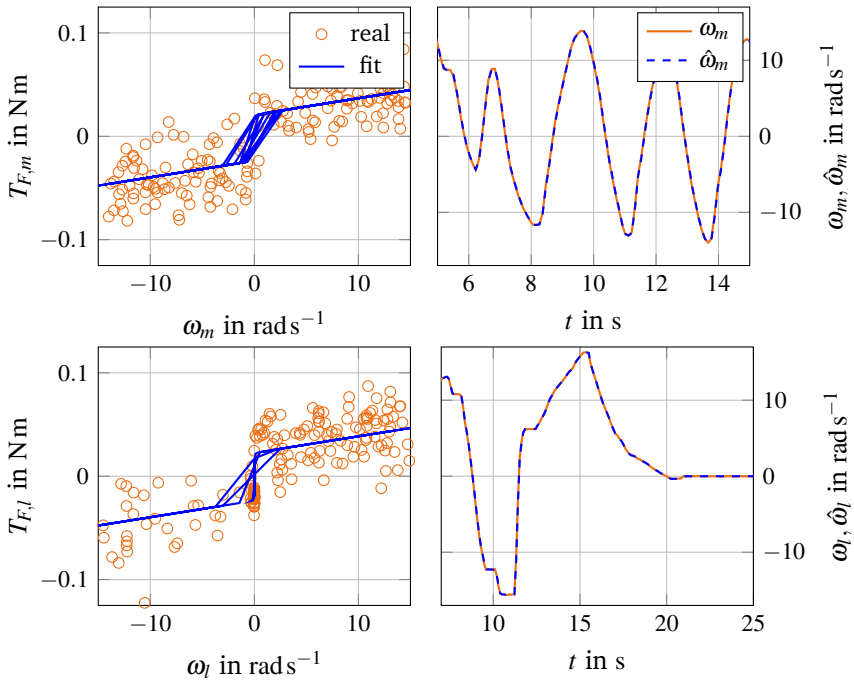

Figure 4.12: Coulomb friction and stiction calculation via linear regression with $\beta_m = \beta_l = 0.0016\ \mathrm{N\,m\,s\,rad^{-1}}$. On the left: Real and predicted velocity-friction plot for the drive motor (top) and the load (bottom). On the right: Real and estimated drive motor (top) and load (bottom) velocity from the linear observer.

diameter $D = 5.5\ \mathrm{mm}$ and length $l_S = 210\ \mathrm{mm}$. Its stiffness can be calculated by [110]:

$$K_S = \frac{J_p G}{l_S} \tag{4.24}$$

where $G = 75\ \mathrm{GPa}$ is the shear modulus for the cold-rolled steel and J_p is the polar moment of inertia (second moment of area) of the shaft given by

$$J_p = \frac{\pi D^4}{32} = \frac{\pi (5.5 \cdot 10^{-3})^4}{32} = 8.98 \cdot 10^{-11}\ \mathrm{m}^4\ . \tag{4.25}$$

Inserting the numerical values of G, l_S and J_p in (4.24) gives the shaft stiffness

$$K_S = 32.94\ \mathrm{N\,m\,rad^{-1}}. \tag{4.26}$$

The single-axis system can be described as a two-mass oscillator with the position and velocity differences

$$\Delta\theta \triangleq \theta_m - \theta_l \tag{4.27a}$$

$$\Delta\omega \triangleq \omega_m - \omega_l = \frac{d}{dt}\Delta\theta \tag{4.27b}$$

as states, where the gearing ratio $N = 1$ has been substituted in the equations. The unforced ($T_m = 0$) dynamics of the system can be written as:

$$\frac{d^2}{dt^2}\Delta\theta + D_S\left(\frac{1}{J_m} + \frac{1}{J_l}\right)\frac{d}{dt}\Delta\theta + K_S\left(\frac{1}{J_m} + \frac{1}{J_l}\right)\Delta\theta = 0\ , \tag{4.28}$$

where the effect of the frictional torques has been neglected since both motor and load have equal inertias and almost identical friction parameters. Comparing (4.28) to the standard mass-spring-damper dynamics equation

$$\ddot{\xi} + 2\zeta\omega_0\dot{\xi} + \omega_0^2\xi = 0\ , \tag{4.29}$$

where ξ is the mass displacement, ζ is the damping ratio and ω_0 is the angular natural frequency, it can be easily seen that the natural angular frequency of the two-mass oscillator denoted by $\omega_{0,2}$ is given by

$$\omega_{0,2} = \sqrt{K_S\left(\frac{1}{J_m} + \frac{1}{J_l}\right)} \tag{4.30}$$

and the corresponding damping ratio can be calculated from

$$\zeta_2 = \frac{D_S}{2}\sqrt{\frac{\frac{1}{J_m} + \frac{1}{J_l}}{K_S}}\ . \tag{4.31}$$

The natural frequency $f_{0,2}$ of the single-axis system is found by substituting (4.26) into (4.30):

$$f_{0,2} = \frac{\omega_{0,2}}{2\pi} = 44.8121\ \text{Hz}\ . \tag{4.32}$$

Performing a power spectral analysis on the position difference $\Delta\theta$, after having excited the system with a pure feedforward torque input, reveals the damped frequency $f_{d,2}$ of the single-axis system, which, as can be seen in Figure 4.13, is equal to

$$f_{d,2} = 44.75\ \text{Hz}. \tag{4.33}$$

The fact that the damped frequency is approximately equal to the natural frequency of the system suggests that the damping ratio ζ_2 cannot be larger than 0.3 [18].

The natural angular frequency and damping ratio of the one-mass oscillator associated to the single-axis system are given by

$$\omega_{0,1} = \sqrt{\frac{K_S}{J_l}} \tag{4.34a}$$

$$\zeta_1 = \frac{D_S}{2J_l\omega_{0,1}}\ . \tag{4.34b}$$

When the motor is locked into a fixed position, then after any excitation, the load will freely oscillate at the frequency $f_{0,1} = 2\pi\omega_{0,1}$ if the system is completely undamped

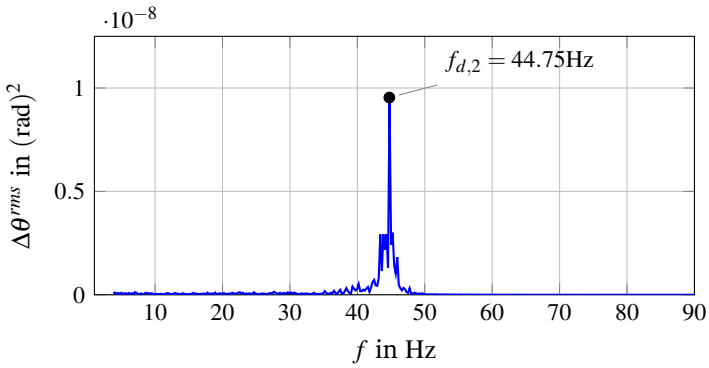

Figure 4.13: Power spectral density of the position difference $\Delta\theta$ between motor and load. The damped frequency $f_{d,2} = 44.75\text{Hz}$ of the double-mass oscillator is approximately equal to its natural frequency $f_{0,2}$, which is indicative of the shaft damping coefficient D_S magnitude.

or at $f_{d,1} = \frac{\omega_{d,1}}{2\pi}$ when there is damping. The damped angular frequency of the one-mass oscillator $\omega_{d,1}$ (also referred to as *locked rotor angular frequency* [18]), is related to the damping ratio ζ_1 and the angular natural frequency $\omega_{0,1}$ through the equation

$$\omega_{d,1} = \omega_{0,1}\sqrt{1-\zeta_1^2}\,. \tag{4.35}$$

For the determination of the damping coefficient D_S, the single-axis system is excited such that the motor position tracks a sinusoidal profile for 1.88 s, at which time it stops and maintains its position. The load is freely oscillating at the locked rotor frequency $f_{d,1}$ until it also stops, as it can be seen in Figure 4.14. By examining

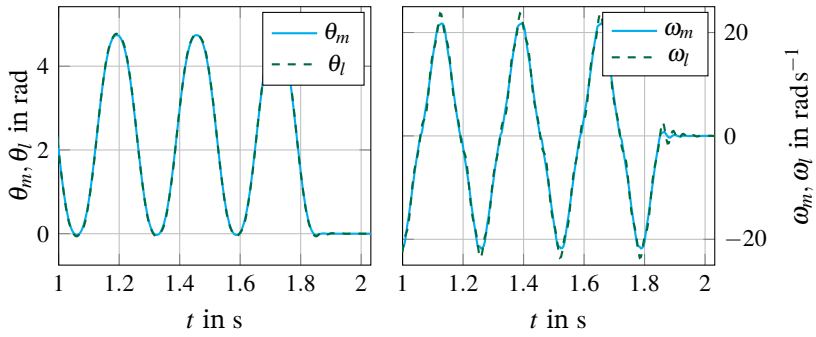

Figure 4.14: Motor and load positions (left) and velocities (right). The free oscillation of the load can be seen after $t = 1.88$ s.

the time differences between the several peak amplitudes of the decaying oscillation

of the load, the damped angular frequency is found to be

$$\omega_{d,1} = 2\pi f_{d,1} = 2\pi \cdot 32.25 \text{ rad s}^{-1} = 196.3495 \text{ rad s}^{-1} . \tag{4.36}$$

Figure 4.15 shows the response of the velocities difference[1] $\Delta\omega$, after the stopping time $t_S = 1.88$ s. By combining (4.34a) with (4.35) and substituting the numerical values, the damping ratio is calculated equal to

$$\zeta_1 = 0.1655 .$$

Lastly, solving (4.34b) with respect to D_S and substituting ζ_1 yields

$$D_S = 0.0548 \text{ N m s rad}^{-1}. \tag{4.37}$$

The decaying oscillation of $\Delta\omega$ is contained in an exponential envelope $\pm A_S e^{-B_S(t-t_S)}$, where

$$A_S = \Delta\omega(t_S) \tag{4.38a}$$

$$B_S = \zeta_1 \omega_{0,1} . \tag{4.38b}$$

Figure 4.15 shows the exponential envelope obtained by using the calculated values for $\zeta_1, \omega_{0,1}$. The calculated friction and shaft parameters of the single-axis system

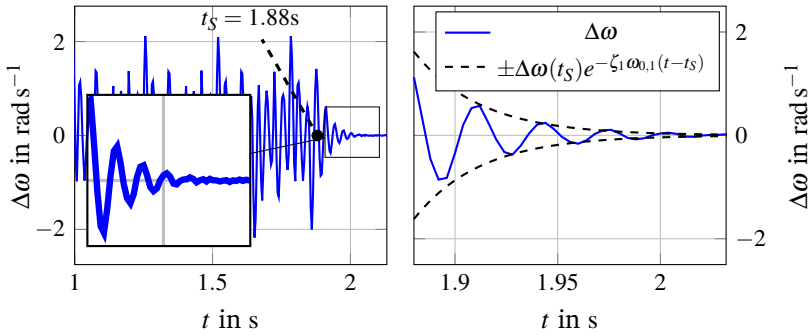

Figure 4.15: (Left): Zoomed plot of the velocities difference $\Delta\omega$. (Right): Envelopes of the exponential decay of the velocities difference. The rate of decay is equal to $\zeta_1\omega_{0,1}$.

are summarised in Table 4.3.

4.4.3 Sensitivity and Identifiability Analysis

The methods used in the previous section to calculate the system parameters provide a sufficient fit of the model to the experimental data but offer no indication

[1] It should be noted that since the motor position and velocity are locked, the load position, velocity and their differences $\Delta\theta, \Delta\omega$ from the motor position and velocity, respectively contain the same information regarding the frequency and damping ratio of the oscillating load.

Table 4.3: Summary of calculated friction and shaft parameters.

Parameter	Value	Unit	Method
K_S	32.94	$\mathrm{N\,m\,rad^{-1}}$	shaft physical properties
D_S	0.0548	$\mathrm{N\,m\,s\,rad^{-1}}$	system natural modes
$T_{C,m}$	0.0223	$\mathrm{N\,m}$	linear regression
$T_{C,l}$	0.0232	$\mathrm{N\,m}$	linear regression
$T_{S,m}$	0.0441	$\mathrm{N\,m}$	linear regression
$T_{S,l}$	0.0453	$\mathrm{N\,m}$	linear regression
β_m	0.0016	$\mathrm{N\,m\,s\,rad^{-1}}$	velocity-torque slope
β_l	0.0016	$\mathrm{N\,m\,s\,rad^{-1}}$	velocity-torque slope

of the parameter uncertainty since no optimization techniques were used. Standard system identification algorithms, such as the nonlinear least squares regression [111], facilitate (locally) optimal estimation of the system parameters along with their 5%-95% confidence intervals, providing, thus, a metric of the quality of the estimates. Such methods require that the design of the input signals excite all the system dynamics that contain the contribution of each of the parameters to the system outputs. Depending on the parametrization approach, it may not be possible to estimate all parameters at the same time and it is often necessary to separate the parameters into different groups, each of which can be identified separately. This is mainly due the fact that some parameters are highly correlated to each other and their individual effect on the system outputs cannot be identified from the other parameters.

For systems with large parameter sets this over-parametrization problem can be overcome by reduction of the parameter number, based on the sensitivity of the system outputs to each of the parameters [112]. In systems such as the single-axis drive train it is desirable to maintain the physical interpretation of the model parameters because of their direct association with the equipment wear levels. This means that, although reparametrization of the system is not an option, ranking the parameters' significance for the system's outputs and grouping them into different subsets may facilitate more accurate identification of the system.

Sensitivity analysis is performed on the single-axis system in order to quantify the contribution of each of the parameter to the system's outputs. Let

$$\boldsymbol{\vartheta} \triangleq \begin{bmatrix} K_S & D_S & T_{C,m} & T_{S,m} & \beta_m & T_{C,l} & T_{S,l} & \beta_l \end{bmatrix}^T$$
$$\boldsymbol{y} \triangleq \begin{bmatrix} \omega_m & \theta_m & \omega_l & \theta_l \end{bmatrix}^T$$

be the system parameters and output vectors, respectively and denote the calculated

parameter values from the previous section by $\boldsymbol{\vartheta}^*$. The *absolute sensitivity* of the output y_i to the parameter ϑ_j at a time instant is defined as the variation of the output to a small perturbation of the parameter [113]:

$$s_{ij} = \frac{\partial y_i}{\partial \vartheta_j}\Big|_{\vartheta_j=\vartheta_j^*} . \tag{4.39}$$

This quantity can be scaled by a suitable factor to become the non-dimensional sensitivity defined by:

$$s_{nd,ij} = \frac{\partial y_i}{\partial \vartheta_j}\frac{\vartheta_j^*}{sc_i} , \tag{4.40}$$

where sc_i has chosen to be the mean value of output y_i over n_s number of samples:

$$sc_i = \frac{1}{n_s}\sum_{k=1}^{n_s} y_i(kT_s) .$$

The system is simulated 8 times with each of the parameters being perturbed one at a time by 0.1% of its initially estimated value. The inputs used for calculation of the parameters are also used in the simulation for exciting the system. The $\delta-$mean square index δ_{ij}^{msqr} defined by [114]

$$\delta_{ij}^{msqr} \triangleq \sqrt{\frac{1}{n_s}\boldsymbol{s}_{nd,ij}^T\boldsymbol{s}_{nd,ij}} , \tag{4.41}$$

where the vector $\boldsymbol{s}_{nd,ij}$ contains all the $s_{nd,ij}$ values calculated at each sample, is used to rank the parameters for each system output according to their contribution to it. Figure 4.16 shows the ranked parameters with respect to each outputs sensitivity to them. The height of each bar in the histograms is equal to the corresponding δ_{ij}^{msqr} index. These plots show that the Coulomb and viscous friction coefficients are the ones that affect the system dynamics the most. The system outputs are not particularly sensitive to neither the stiction constants $T_{S,m}, T_{S,l}$ nor the shaft parameters. This indicates that only parameters $T_{C,m}, \beta_m, T_{C,l}, \beta_l$ can be accurately estimated with the available data. This conclusion can be also reached by examining the cumulative δ-mean square index defined for each parameter as:

$$\delta_j^{msqr} \triangleq \sum_{i=1}^{4} \delta_{ij}^{msqr} . \tag{4.42}$$

Parameters with cumulative δ-mean square index smaller than a threshold, usually defined as a percentage of the maximum δ_j^{msqr} [114], are deemed not significant for identification. Figure 4.17 shows the ranking of the single-axis system parameters based on the corresponding cumulative δ-mean square indices. The threshold is defined as 2% of the maximum δ^{msqr}.

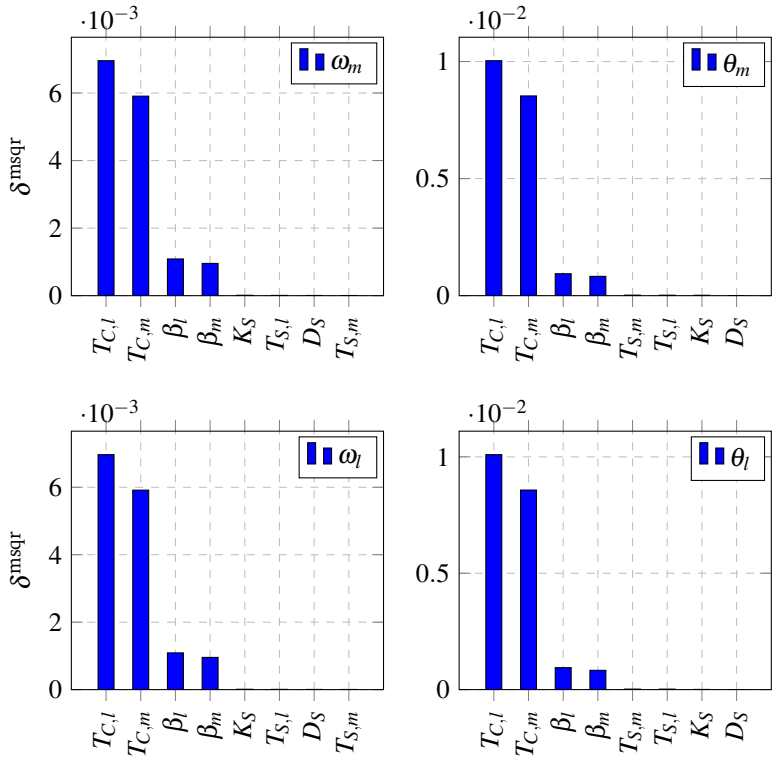

Figure 4.16: Sensitivity $\delta-$mean square index of the parameters with respect to the motor and load velocities and positions. All outputs are sensitive to the Coulomb and viscous friction coefficient, while the shaft and stiction parameters do not significantly contribute to the output dynamics.

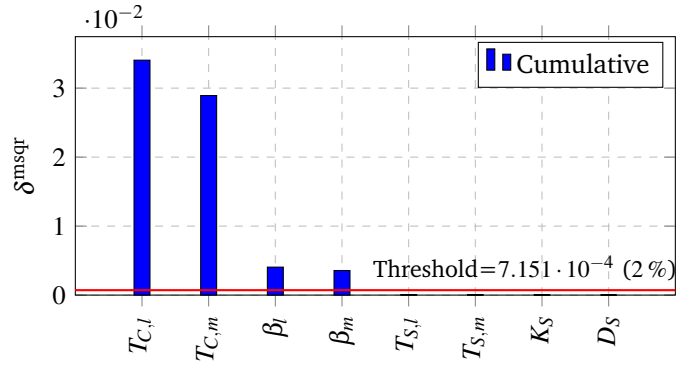

Figure 4.17: Cumulative $\delta-$mean square indices of the system parameters in descending order. The stiction and shaft coefficients are below the chosen threshold and, as such, are considered not significant for identification with the specific datasets.

The last part in the sensitivity analysis of the drive-train model is the calculation of the *collinearity index* γ_k of each possible subset of parameters. The idea behind this is to investigate and assess the near-linear dependency between parameters [114]. The collinearity index is calculated by

$$\gamma_k = \frac{1}{\sigma_{min,k}} , \tag{4.43}$$

where $\sigma_{min,k}$ is the smallest singular value of matrix $\boldsymbol{S}_{norm,k}$, which is defined for the parameter subset k as

$$\boldsymbol{S}_{norm,k} = \left[\frac{\boldsymbol{s}_{nd,1j}}{\|\boldsymbol{s}_{nd,1j}\|} \cdots \frac{\boldsymbol{s}_{nd,4j}}{\|\boldsymbol{s}_{nd,4j}\|} \right]_k .$$

and the column vectors $\boldsymbol{s}_{nd,1j}, \ldots, \boldsymbol{s}_{nd,4j}$ contain the non-dimensional sensitivities $s_{nd,ij}$ defined in (4.40) (j is the parameter index). When γ_k has low value, e.g. 2-5 or less, then the parameters in the subset k can be identified. When the collinearity index is very big (approaches ∞), then some parameters are almost linearly depended to each other and, hence, the number of the parameters for estimation must be reduced.

Since there are 8 parameters in total, there can be combinations of 2, 3, 4, 5, 6 and 7 parameters. For all these combinations the collinearity index has been calculated and the parameter subsets with $\gamma_k \leq 2$ are presented in Table 4.4. As it can be seen, the maximum number of parameters that can be simultaneously estimated without risking strong correlation to each other is 3 and the corresponding subsets always contain the most significant parameters for the outputs, i.e. $T_{C,m}$ and $T_{C,l}$.

Table 4.4: Identifiable parameter subsets and corresponding collinearity indexes.

$T_{C,l}$, $T_{C,m}$	$T_{C,l}$, β_l	$T_{C,l}$, β_m	$T_{C,l}$, $T_{S,l}$	$T_{C,l}$, $T_{S,m}$
1.3987	1.2216	1.2753	1.0180	1.2215
$T_{C,l}$, K_S	$T_{C,l}$, D_S	$T_{C,m}$, β_l	$T_{C,m}$, β_m	$T_{C,m}$, $T_{S,l}$
1.4770	1.0173	1.9203	1.7862	1.5454
$T_{C,m}$, $T_{S,m}$	$T_{C,m}$, K_S	$T_{C,m}$, D_S	$T_{C,l}$, $T_{C,m}$, β_l	$T_{C,l}$, $T_{C,m}$, β_m
1.9207	2.1897	1.5407	2.0113	1.8235
$T_{C,l}$, $T_{C,m}$, $T_{S,l}$	$T_{C,l}$, $T_{C,m}$, $T_{S,m}$	$T_{C,l}$, $T_{C,m}$, K_S	$T_{C,l}$, $T_{C,m}$, D_S	
1.9707	2.0119	2.2058	1.9656	

4.4.4 Parameter Identification

Taking into consideration the conclusions reached in the previous section, regarding the significance of the parameters on the system outputs and their identifiability,

suggests performing the parameter estimation in two steps. First the Coulomb and viscous friction coefficients for the motor and load are identified with two separate experiments. The stiction coefficients are no included in the estimation problem since they do not significantly affect the model outputs. The method used for the identification is the nonlinear square regression for grey-box models [115]. The estimated parameter vector $\hat{\boldsymbol{\vartheta}}$ is such that it minimizes the sum of squares of the output prediction error

$$J = \boldsymbol{e}^T \boldsymbol{e} \tag{4.44}$$

where $\boldsymbol{e}$ is a column vector that contains all the n_s past errors $e(iT_s) \triangleq y(iT_s) - \hat{y}(iT_s)$ between the real (measured) output y and the one predicted by the model $\hat{y}$. In the two experiments for the identification of the friction coefficients the real output is the friction torque for the motor and the load, obtained from Equations (4.19), (4.20). The predicted output is given by:

$$\hat{y}_i = \hat{T}_{C,i}\text{sgn}(\omega_i) + \hat{\beta}_i \omega_i \ , \ i \in \{m, l\} \ . \tag{4.45}$$

The results of the identification for the motor and the load are shown in Tables 4.5 and 4.6, respectively and are visualised in 4.18.

Table 4.5: Identified values for the motor friction parameters, with standard deviation σ, 95% confidence intervals and correlation matrix.

Estimation		**Deviation**		**95% confidence intervals**		**Correlation matrix**	
$\boldsymbol{\vartheta}$	Value	σ	%	Lower bound	Upper bound	$T_{C,m}$	β_m
$T_{C,m}$	0.0265	0.00025	0.94%	0.0260	0.0270	1.00	
β_m	0.0010	0.00051	51%	-0.0001	0.0025	$\mathbf{-0.97}$	1.00

Table 4.6: Identified values for the load friction parameters, with standard deviation σ, 95% confidence intervals and correlation matrix.

Estimation		**Deviation**		**95% confidence intervals**		**Correlation matrix**	
$\boldsymbol{\vartheta}$	Value	σ	%	Lower bound	Upper bound	$T_{C,l}$	β_l
$T_{C,l}$	0.0282	0.00052	1.84%	0.0271	0.0292	1.00	
β_l	0.0010	0.00078	78%	-0.0005	0.0025	$\mathbf{-0.92}$	1.00

As it can be seen, in both cases the Coulomb friction and viscous coefficients are strongly correlated to each other. Moreover, the relative estimation error of the viscous coefficient is very large (51% for the motor and 78% for the load), which indicates that the estimated values for β_m, β_l obtained from this dataset are not credible. In general, however, the friction parameters are found to be very close to

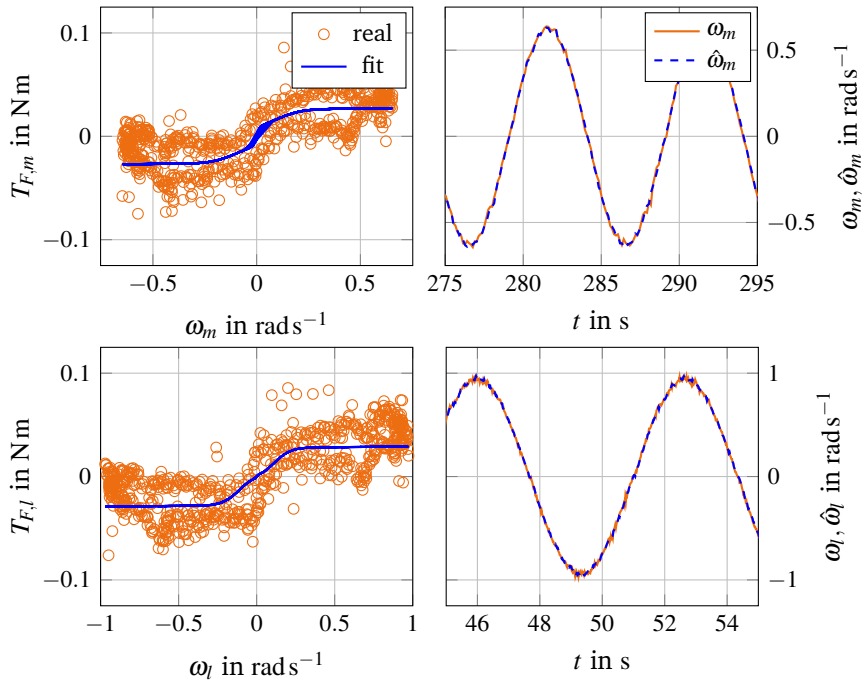

Figure 4.18: Friction parameters estimation. On the left: Real and predicted velocity-friction plot for the drive motor (top) and the load (bottom). On the right: Real and estimated drive motor (top) and load (bottom) velocity from the linear observer.

the values calculated in Table 4.3. Figure 4.19 shows the validation of the identified friction model on a different dataset.

Next, the shaft parameters K_S, D_S are identified. The real output is the interconnecting torque calculated by

$$y = T_m - T_{F,m} - J_m \dot{\hat{\omega}}_m \tag{4.46}$$

with T_m being the torque generated by the motor and $\dot{\hat{\omega}}_m$ given from Equation (4.20). The estimated motor fiction coefficients obtained from the identification experiment are used for calculating $T_{F,m}$ based on Equation (4.45). The predicted model output is given by

$$\hat{y} = \hat{K}_S \left(\theta_m - \theta_l\right) + \hat{D}_S \left(\omega_m - \omega_l\right) \ . \tag{4.47}$$

The identified parameters are shown in Table 4.7 along with the 95% confidence intervals of each parameter estimate and the correlation matrix. As it can be seen, the identified parameters do not significantly differ from the values reported in Table 4.3. Additionally, the relative estimation deviation is below 2%, which indicates

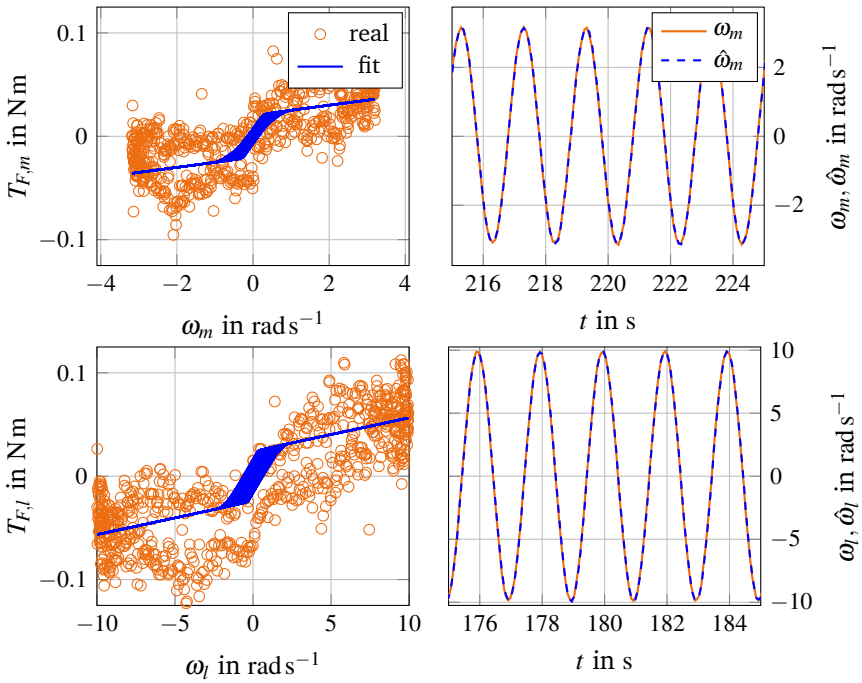

Figure 4.19: Friction parameters validation. On the left: Real and predicted velocity-friction plot for the drive motor (top) and the load (bottom). On the right: Real and estimated drive motor (top) and load (bottom) velocity from the linear observer.

sufficiently good identification. Figure 4.20 illustrates the fit of the shaft torque model with the identified parameters to the estimation and validation dataset.

Table 4.7: Identified values for the shaft parameters, with standard deviation σ, 95% confidence intervals and correlation matrix.

Estimation		**Deviation**		**95% confidence intervals**		**Correlation matrix**	
ϑ	Value	σ	%	Lower bound	Upper bound	K_S	D_S
K_S	31.55	0.1187	0.37%	31.3181	31.7832	1.00	
D_S	0.0684	0.0012	1.75%	0.0661	0.0708	-0.0056	1.00

Finally, a full parameter identification is carried out considering the parameter vector $\boldsymbol{\vartheta} = \begin{bmatrix} K_S & D_S & T_{C,m} & \beta_m & T_{C,l} & \beta_l \end{bmatrix}^T$. The real output is a vector containing the estimated motor and load accelerating torques

$$\boldsymbol{y} = \begin{bmatrix} J_m \dot{\hat{\omega}}_m \\ J_l \dot{\hat{\omega}}_l \end{bmatrix}$$

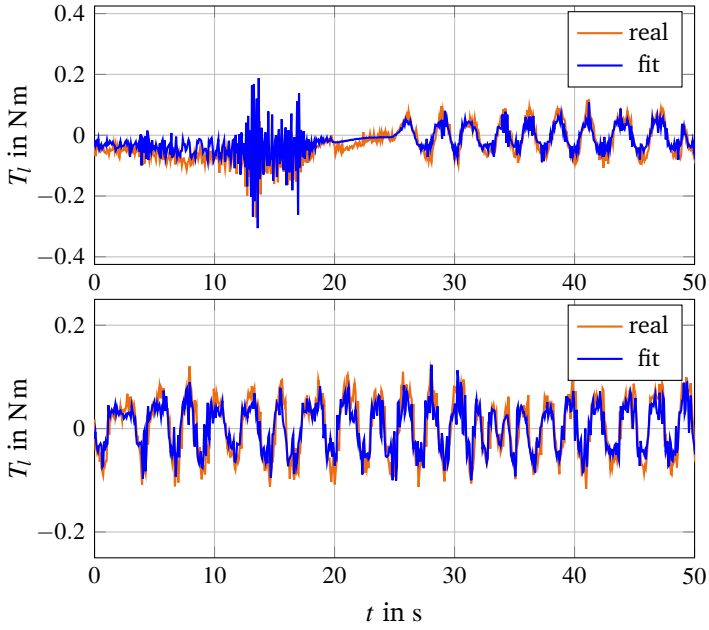

Figure 4.20: Shaft parameters estimation and validation: Time slice of 50 s showing real and predicted interconnecting torque using drive motor (top) and the load (bottom) acceleration estimates.

while the predicted output from the model is given by:

$$\hat{\boldsymbol{y}} = \begin{bmatrix} T_m - \hat{K}_S\left(\theta_m - \theta_l\right) - \hat{D}_S\left(\omega_m - \omega_l\right) - \hat{T}_{C,m}\text{sgn}(\omega_m) - \hat{\beta}_m\omega_m \\ \hat{K}_S\left(\theta_m - \theta_l\right) + \hat{D}_S\left(\omega_m - \omega_l\right) - \hat{T}_{C,l}\text{sgn}(\omega_l) - \hat{\beta}_l\omega_l \end{bmatrix}. \tag{4.48}$$

The results of the identification are presented in Table 4.8. Comparing these results to the ones in Table 4.3, reveals that the estimated values for $K_S, T_{C,m}$ and $T_{C,l}$ include the corresponding calculated values in their confidence intervals. On the contrary, the identification process predicted up to 3 times larger values for D_S, β_m and β_l. This is due to the fact that D_S has not any significant contribution to the system outputs for the used datasets, as shown in the sensitivity analysis earlier. Moreover, the correlation between the viscous and Coulomb friction coefficients, also seen in Table 4.9, indicates that the estimated values for β_m, β_l are not trustworthy and, therefore, the constant speed experiments are more suitable for their estimation. Figure 4.21 shows the fit of the identified model to the data used for the parameter estimation and to a different dataset used for validation.

Table 4.8: Identified values for the single-axis system parameters, with standard deviation σ, 95% confidence intervals and relative deviation.

Estimation		**Deviation**		**95% confidence intervals**	
$\boldsymbol{\vartheta}$	Value	σ	%	Lower bound	Upper bound
K_S	32.979	0.2454	0.75%	32.427	33.389
D_S	0.1471	0.0013	0.85%	0.1417	0.1496
$T_{C,m}$	0.0223	0.0007	3.28%	0.0209	0.0238
β_m	0.0028	0.0001	3.62%	0.0026	0.0030
$T_{C,l}$	0.0267	0.0007	2.74%	0.0253	0.0282
β_l	0.0034	0.0001	2.97%	0.0032	0.0036

Table 4.9: Correlation matrix for the entire parameter vector of the single-axis system. As also seen in the previous experiments, the Coulomb and viscous friction coefficients are highly correlated to each other.

Correlation matrix for the estimated parameters

	K_S	D_S	$T_{C,m}$	β_m	$T_{C,l}$	β_l
K_S	1					
D_S	0.0271	1				
$T_{C,m}$	-0.2833	-0.0170	1			
β_m	-0.2438	0.0020	$\mathbf{-0.7655}$	1		
$T_{C,l}$	0.2847	-0.117	-0.0805	-0.0696	1	
β_l	0.2432	0.0315	-0.0691	-0.0591	$\mathbf{-0.7649}$	1

4.5 Conclusions

This chapter presented a detailed description of the single-axis system used in this research. A generic presentation of a typical machining process was provided, followed by a discussion on the machine positioning accuracy and the phenomena that can degrade its performance. A mathematical model of the single-axis system was derived including the electrical and mechanical dynamics of the drive motor and the load. Since the closed-loop electrical dynamics of the motor correspond to a unit gain plus a small bounded perturbation, the model was reduced to a double-mass oscillator description. The unknown model parameters, namely the friction and shaft coefficients, were first calculated based on constant-speed experiments and the shaft physical characteristics. A parameter sensitivity analysis was carried out providing insight into the identifiability of each parameter. Following these observations, optimization-based system identification was performed for the drive-train parameters, both in groups and all together. The results showed that the estimated values for half of the parameters are consistent to the ones calculated

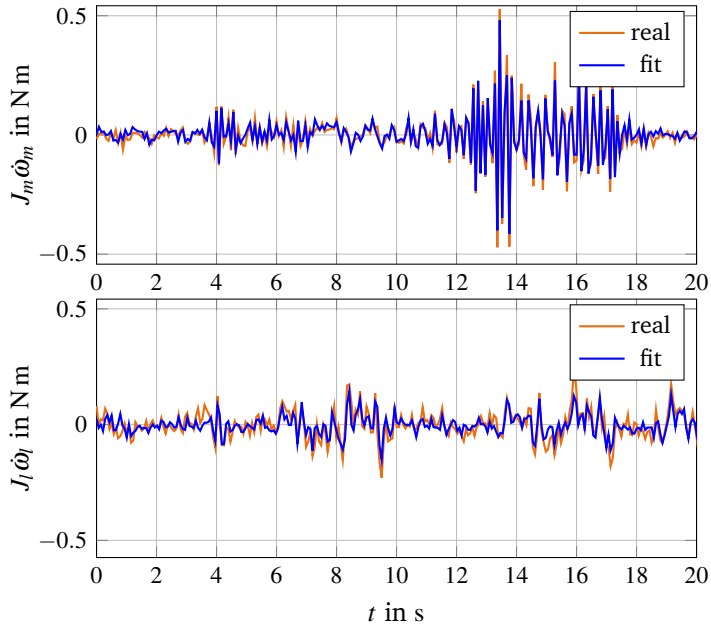

Figure 4.21: Time slice of 20 s showing real and predicted accelerating torques for the motor and load based on the estimated parameters. (Top): Fit of the model to the estimation dataset for the motor accelerating torque. (Bottom): Validation of the identified model by fitting it to the load accelerating torque in a different dataset.

based on the physical characteristics of the system. The rest of the parameters were estimated up to 3 times larger than their calculated values, which was expected due to high correlation to each other and low sensitivity of the system outputs to them.

The calibrated model of the single-axis system provides a sufficient description of the physical system for control and estimation purposes. Since the main objective of the project is the robust positioning of the machine axis with respect to varying system parameters, exact knowledge of the friction and shaft coefficients is not necessary. Yet, it allows the evaluation of the adaptation features of some of the control designs presented in the following chapter and, as such, accurate model identification is desirable. Some future extensions that may enhance the accuracy of the system description include the use of more complete models for friction, such as the LuGre model and the introduction and identification of a model for the torque input perturbations d_e.

Chapter 5

Advanced Friction-Resilient Axis Positioning Control

5.1 Introduction

This chapter discusses the design and performance of different nonlinear friction-resilient controllers for axis positioning in machine tools. Friction develops between the various contacting surfaces of the machine axes over time due to wear and tear and can significantly degrade the axis positioning accuracy. The lumped frictional phenomena can effectively be described as decelerating torques in the motor and load velocity dynamics. Based on this description, state-of-the-art position control loops used in the industry, typically consisting of P-PI cascades, provide sufficient friction compensation after commissioning of the machine. However, when the friction characteristics change due to equipment wear and general tear (e.g. accumulation of workpiece chips in the axes' guideways, linear axes lubrication film failure [116] etc.), the conventional P-PI solutions fail to maintain workpiece tolerances unless their parameters are re-tuned. This often leads to significant downtime periods and additional re-commissioning costs.

For this reason, several machine tool axis position control designs based on nonlinear control theory are investigated. These positioning algorithms exhibit powerful robustness properties with respect to unknown and varying disturbances such as friction. This motivates a comparative study of the explored nonlinear position control strategies that juxtaposes their performance with that of the standard P-PI solutions. The increasing Coulomb friction on the drive-motor side in combination with the uncertain values of the rest friction parameters will constitute the main degrading disturbance against which the evaluation of the methods' robustness will be performed. The control objective can be formulated as follows:

Problem 1 (Friction-resilient high-accuracy axis positioning for machine tools)**.** *Consider the single-axis system described in Equations* (4.16) *and* (4.18a)-(4.18d)*. Let the positioning error be denoted by* e_θ *and let* $T_{C,m}^{max}$ *be an upper bound for the Coulomb friction magnitude* $T_{C,m}$ *on the motor side. Design a closed-loop control strategy that ensures:*

$$|e_\theta(t)| \leq 10 \text{ mrad } \forall t \geq t_0 > 0 \text{ and for } T_{C,m} \leq T_{C,m}^{max}$$

where t_0 *denotes a time short after the starting up of the positioning task for the machine.*

The bound $T_{C,m}^{max}$ describes the maximum value of Coulomb friction, above which alleviation of the positioning degradation is not addressed by means of low-level axis control. The accuracy specifications were selected in accordance to the discussion in Section 4.2.1.

The rest of the chapter is organised as follows: Section 5.2 illustrates the key features of the two main control principles considered in this project, namely sliding-mode and adaptive, via two simple examples. Sections 5.3.1 and 5.3.2 elaborate on the design of the control algorithms and provide an overview of the experimental results of the comparative study. The design and applicability challenges of two additional nonlinear controllers are discussed in Section 5.5. Finally, concluding remarks on the friction-resilient tool positioning methods are provided in Section 5.6 along with some aspects of future extensions to the designs.

5.2 Sliding-Mode and Adaptive Methodologies

The advanced position control algorithms designed for the single-axis system in this project belong to two families of nonlinear controllers, i.e. the sliding-mode and the adaptive controllers. This choice was based on the fact that controllers from these categories demonstrate robustness features against unknown or varying system dynamics and disturbances. Such characteristics make sliding-mode and adaptive controllers suitable candidates for axis positioning in machine tools with unknown and increasing friction. The most essential properties and design philosophy of these controllers will be briefly discussed in the next two subsections through two simple examples.

5.2.1 Sliding-Mode Control

Control schemes using sliding modes have two very attractive features, namely disturbance estimation and finite-time convergence. The inherent robustness of sliding-mode controllers against unknown dynamics and disturbances is achieved by using discontinuous terms in the sliding-mode algorithms. To illustrate this functionality consider the uncertain scalar system

$$\dot{x} = x + u + d(t) \ , \tag{5.1}$$

where $d(t)$ is an unknown bounded function of time. When $d(t) \equiv 0$, a state-feedback control law $u_{SF} = -(k+1)x, \ k > 0$, designed with any standard linear control technique, stabilizes the origin of the system. This is not the case, however, if $d \neq 0$, unless d is completely known and included in the control law as a feed-forward term. Using a theoretically infinitely fast switching term that varies between two extreme values $\pm k_{SMC}$ ($|d| < k_{SMC}$) disturbance rejection is achieved in finite-time [61]. A first-order SMC law for system (5.1) has the form

$$u_{SMC} = -x - k_{SMC}\text{sgn}(\sigma) \ , \tag{5.2}$$

where the signum function was defined in (II.1).

The variable σ inside the signum function is called the *sliding variable* and in the general case is a function of the system states and their derivatives. When the system trajectories are on the manifold $\mathcal{S} = \{\sigma \in \mathbb{R} | \sigma = 0\}$, referred to as the *sliding manifold* (or *sliding surface*), its dynamics assumes specific forms. These forms may ensure that the dynamics reduce in order or that the system becomes stable, tracks a reference signal, etc.. The design of the sliding manifold is central in designing SMCs and depends on the control problem (tracking, regulation, estimation, etc.) and the relative degree of the system. For the system of Equation (5.2) the sliding manifold is chosen as $\mathcal{S} = \{x \in \mathbb{R} | x = 0\}$. Figure 5.1 shows a comparison between the state-feedback controller and the SMC for the system in Equation (5.1) with $k_{SF} = k_{SMC} = 10$.

The control term that ensures that the system reaches the sliding manifold and remains there is called *equivalent control* u_{eq}, i.e. $u_{eq} = \{u \in \mathbb{R} | \dot{x} = x = 0\}$. In the case of the system in Equation (5.2) $u_{eq} = -x - d(t)$. As it can be seen, u_{eq} is not computable since d is, in general, unknown. It is approximated by the implementable switching control law u_{SMC} and this constitutes an indirect way of approximating the unknown disturbance d.

One of the main disadvantages of sliding-mode techniques is the chatter in the control signals. The high frequency fluctuation propagates to the controlled system states due to the switching terms included in the algorithms. This, eventually leads to

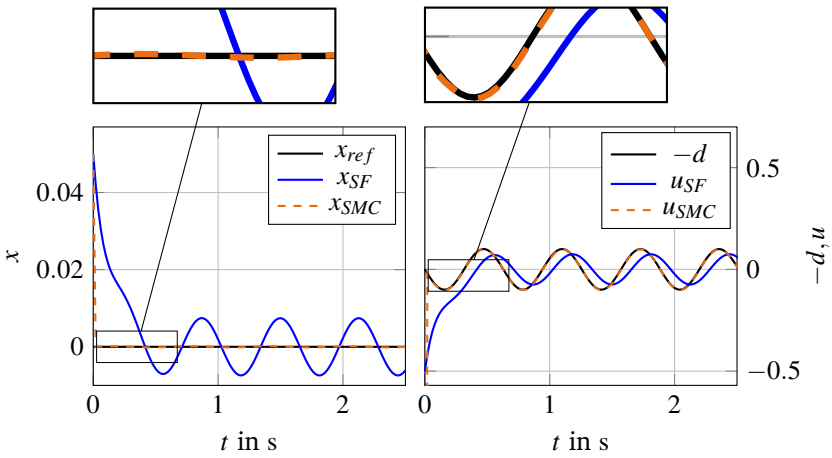

Figure 5.1: (Left) Time response of (5.1) with sinusoidal disturbance when a state-feedback and a sliding-mode controller is applied. (Right) State-feedback, sliding-mode control input and sinusoidal disturbance. The switching control signal u_{SMC} converges to the negative d, hence cancelling it.

actuator wear. Alleviation of this phenomenon can be achieved by using higher-order SMCs [61, 79], which will be discussed later in this chapter.

5.2.2 Adaptive Control

The rejection of disturbances in adaptive control algorithms is based on a different philosophy than the one in the SMC case. Instead of dominating the effect of the perturbations, the lumped disturbances are modelled by using existing structural knowledge of the perturbing phenomenon and a set of unknown parameters. Appropriate adaptive laws update the parameter values until the resulting description of the disturbance generates the same effect on the system as the real perturbation. Then, the estimated perturbation is fed back to the system through the control signal in order to cancel the real disturbance. This principle is illustrated in the following example.

Consider the system given in Equation (5.1), with the disturbance d given by

$$d \triangleq d(t, x, \boldsymbol{\vartheta}) = \boldsymbol{\phi}^T(t, x)\boldsymbol{\vartheta} \ , \tag{5.3}$$

where the Lipschitz continuous function

$$\boldsymbol{\phi}(t, x) \triangleq \begin{bmatrix} x^2 & \sin(t) \end{bmatrix}^T$$

is called the *regressor*[1] and $\boldsymbol{\vartheta} \triangleq \begin{bmatrix}\vartheta_1 & \vartheta_2\end{bmatrix}^T$ is a vector of two real unknown parameters. Consider also the task of x tracking a reference signal x_{ref}. With the tracking error defined as $e \triangleq x - x_{ref}$, the classic control approach would be applying a PI control law with additional feed-forward terms

$$u_{PI} = -x - k_P e - k_I \int_0^t e(\tau)d\tau \ , \ k_P, k_I > 0 \ , \tag{5.4}$$

whereas in the simplest adaptive control scheme, namely the MRAC, the control law is given by

$$u_{MRAC} = -x - ke - \boldsymbol{\phi}^T(t,x)\hat{\boldsymbol{\vartheta}} \ , \ k > 0. \tag{5.5}$$

The parameter estimates $\hat{\vartheta}_1, \hat{\vartheta}_2$ are provided by the adaptive laws

$$\dot{\hat{\boldsymbol{\vartheta}}} = \boldsymbol{\Gamma}\boldsymbol{\phi}e \ , \ \boldsymbol{\Gamma} \in \mathbb{R}^{2\times 2}_{>0} \ . \tag{5.6}$$

If the parameter vector is constant or varies very slowly ($\dot{\boldsymbol{\vartheta}} \approx 0$), it can be proven by arguments from Lyapunov stability theory [82] that for appropriate selection of k and $\boldsymbol{\Gamma}$, the tracking error e converges to 0, while the parameter estimation error remains bounded. If, in addition, the regressor function is *persistently exciting* (see Definition 4 in Appendix II), then the parameter estimates converge to the real parameter values [81, 82]. Figure 5.2 shows the comparison between the PI and the MRAC in tracking a sinusoid $x_{ref} = \sin(2\pi t)$.

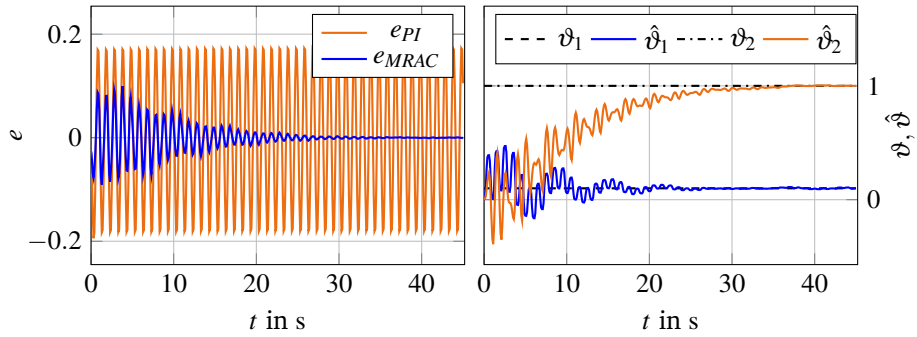

Figure 5.2: (Left) Tracking error for the system (5.1),(5.3) with PI and MRAC. (Right) Estimation of the unknown parameters. The parameter estimates converge to the real values $\vartheta_1 = 0.1$ and $\vartheta_2 = 1$.

It is interesting to notice that the PI controller in Equation (5.4) is a special case of the MRAC with one scalar parameter and $\phi(t,x) \equiv 1$. It should also be

[1] In cases of systems with nonlinear parametrization, i.e. when d cannot be written as product of a known function and an unknown parameter vector, the term regressor or *regressor function* is often used in the literature to refer to the entire perturbing term $d(t,x,\boldsymbol{\vartheta})$ with some abuse of terminology.

noted that the parametrization of $d(t)$ is not unique and that the parameters do not necessarily have any specific physical interpretation. Table 5.1 summarizes the key design assumptions and theoretical properties of sliding-mode and adaptive control methodologies.

Table 5.1: Requirements and theoretical features of sliding-mode and adaptive control methods.

Assumptions and theoretical features for rejection of disturbance d	
Sliding-mode control	**Adaptive control**
• d must be bounded for bounded state vector	• d must be bounded for bounded state vector
• A bound for d is needed	• A model (parametrization) of d is needed with $\dot{\boldsymbol{\vartheta}} \approx \mathbf{0}$
• Domination over the effect of d	• Cancellation of the effect of d
• Finite-time disturbance rejection	• Asymptotic disturbance rejection
• Chatter in the control signal	• Parameter estimation if the regressor is persistently exciting

5.3 Controller Design

State-of-the-art axis positioning solutions typically consist of three nested loops of P and PI controllers. The outer layer is the position control loop. It includes a P controller, which generates a suitable velocity setpoint based on the positioning error at each time instant. The next level is the velocity loop, which includes a PI controller that outputs the driving torque command u. The most inner loop constitutes the current control layer, regulating the electrical dynamics of the drive motor and ensuring that the commanded torque u will be generated by the motor. This architecture is illustrated in Figure 5.3.

Following Assumption 4.3.1 and the discussion on the residual input torque ripples d_e in Section 4.3, the design of all the nonlinear controllers in this project will concern only the two outer (position and velocity) loops. Additionally, the following assumption is made:

Assumption 5.3.1. ***(Compensated input disturbances)***
The input disturbance d_e is compensated via input filtering or appropriate feedforward terms and is not considered in the design, i.e. $d_e \approx 0$.

The compensation of d_e is usually addressed in the current control layer by means of fine-tuning the PI controllers in this loop. It is also possible to filter out specific frequencies from the torque ripples, since they depend on the interaction of the drive motor stator windings and the rotor magnets, hence on known fixed motor characteristics. Under this perspective and given that d_e is much smaller than the torques considered in the positioning problem (friction, shaft torques), Assumption 5.3.1 does not cause any loss of generality in the methods' design. The proposed

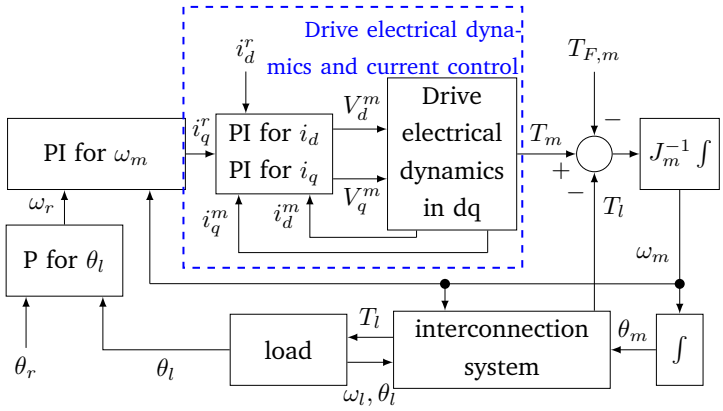

Figure 5.3: State-of-the-art machine-tool axis control.

control designs can be categorized with respect to their architectures in two groups, namely the *position-velocity cascaded controllers* and the *direct position controllers*. The notation presented in Table 5.2 is used throughout the entire design analysis. The interpolator that outputs the load position reference signal θ_r also provides

Table 5.2: Basic design notation. The gain of the position P controller is denoted by k_{pos}.

Symbol	Description	Definition
θ_r	Load position reference	–
e_θ	Load positioning error	$e_\theta \triangleq \theta_l - \theta_r$
ω_r	Motor velocity reference	$\omega_r \triangleq k_{pos} e_\theta + \dot{\theta}_r$
e_ω	Motor velocity error	$e_\omega \triangleq \omega_m - \omega_r$

the derivatives of θ_r up to any requested order. This is always possible since the interpolation is done by using polynomial functions of time. Hence, for all the designs it is assumed that $\theta_r(t)$ is a smooth function of time.

5.3.1 Position-Velocity Cascaded Control

The cascaded architecture consisting of a position controller in connection to a velocity controller is maintained in the first group of friction-resilient nonlinear controllers presented in this section. The proportional controller in the position loop is preserved, while the PI that follows is replaced by a nonlinear controller. This architecture can be seen in Figure 5.4. Three control schemes with this structure are proposed, each of them including a different velocity nonlinear controller. The design of these controllers and their performance are discussed in detail in Paper A and are summarized in the following.

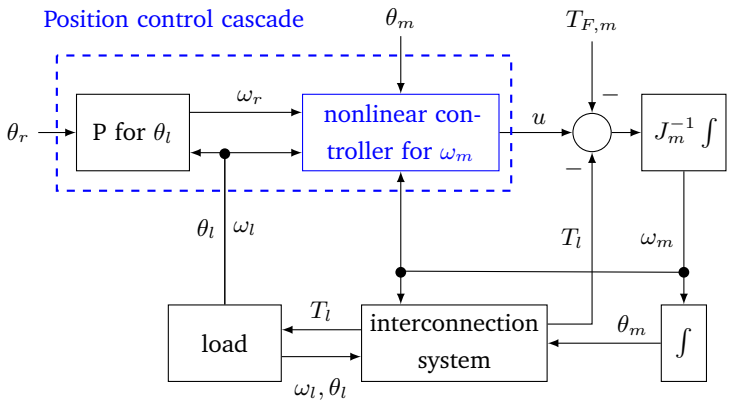

Figure 5.4: Cascaded position-velocity control architecture.

5.3.1.1 Motor Velocity Super-Twisting Sliding-Mode Controller (STSMC)

The STSMC is a second-order sliding-mode controller, which provides some chattering attenuation in the control signal, compared to the conventional SMC in (5.2). The first step in the design is the selection of the sliding variable s. Since it is desired that the drive-motor velocity tracks the output of the position P controller, the sliding variable is chosen to be the motor velocity error, i.e.

$$s \triangleq e_\omega = \omega_m - \underbrace{\left(k_{pos} e_\theta + \dot{\theta}_r\right)}_{\omega_r},$$

where θ_r is the position reference signal and k_{pos} is the P controller proportional gain. Notice that the first derivative of the θ_r is added to the velocity reference as a feedforward term. This *precontrol* practice [18] is often used in position servo systems to allow less aggressive velocity reference signals. The corresponding sliding

surface is defined as

$$\mathcal{S} = \{s(t) \in \mathbb{R} | s = \dot{s} = 0\} \ . \tag{5.7}$$

The dynamics of the sliding variable s reads:

$$\begin{aligned}
\dot{s} &= \dot{\omega}_m - \dot{\omega}_r \\
&= \frac{1}{J_m} \left[\underbrace{u - T_{F,m} - \frac{K_S}{N}\left(\frac{\theta_m}{N} - \theta_l\right) - \frac{D_S}{N}\left(\frac{\omega_m}{N} - \omega_l\right) - J_m\left(k_{pos}\omega_l - k_{pos}\dot{\theta}_r + \ddot{\theta}_r\right)}_{\psi(\boldsymbol{x})} \right] \\
&= \frac{1}{J_m}\left[u + \psi(\boldsymbol{x})\right] \ ,
\end{aligned} \tag{5.8}$$

where $\boldsymbol{x} = \begin{bmatrix} \omega_m & \theta_m & \omega_l & \theta_l \end{bmatrix}^T$ is the state vector of the single-axis system. Notice that the derivative of the motor velocity reference can be analytically calculated from

$$\dot{\omega}_r = k_{pos}\dot{e}_\theta + \ddot{\theta}_r = k_{pos}\omega_l - k_{pos}\dot{\theta}_r + \ddot{\theta}_r \ . \tag{5.9}$$

Assumption 5.3.2. ***(Lipschitz continuity)***
The matched perturbation $\psi(\boldsymbol{x})$ is Lipschitz continuous.

The STSMC algorithm is given in [70]

$$u = -k_1 |s|^{\frac{1}{2}} \text{sgn}(s) + v \tag{5.10}$$

$$\dot{v} = -k_2 \text{sgn}(s) \ . \tag{5.11}$$

For appropriate positive gains k_1, k_2 it is proven [70, 73] that if Assumption (5.3.2) holds globally, the control signal in (5.10),(5.11) brings the velocity error dynamics to the sliding manifold $\mathcal{S}$ in finite-time, where it remains for all future times. The selection of the controller gains can be formulated as an Linear Matrix Inequality (LMI) problem. However, such solutions often suggest high values for k_1, k_2, which, in turn, make the algorithm sensitive to noise measurements.

In order for Assumption 5.3.2 to hold, the signum function defined in (II.1), is approximated by

$$\text{sgn}(y) \approx \frac{2}{\pi} \arctan(py) \triangleq w(p, y) \ , \tag{5.12}$$

where p is a large positive number representing the slope of the signum function near 0. This approximation is necessary to remove the discontinuity in the perturbation $\psi(\boldsymbol{x})$ coming from the friction model in (4.16).

5.3.1.2 Motor Velocity Nonlinear (model-reference) Adaptive Controller (NAC)

The design of the NAC is based on expressing the drive-motor velocity error dynamics as the sum of known terms and the product of an also known regressor function by an unknown parameter vector. A prerequisite in the design of NAC is that the following assumption holds:

Assumption 5.3.3. ***(Lipschitz continuity)***
The regressor function $\phi(\boldsymbol{x})$ is Lipschitz continuous.

By selecting the friction and shaft coefficients as the components of the unknown parameter vector

$$\boldsymbol{\vartheta} \triangleq \begin{bmatrix} K_S & D_S & T_{C,m} & T_{S,m} & \beta_m \end{bmatrix}^T \tag{5.13}$$

the velocity error dynamics is written as:

$$\dot{e}_\omega = \frac{1}{J_m}\left[u + \phi^T(\boldsymbol{x})\boldsymbol{\vartheta} + J_m\dot{\omega}_r\right] \tag{5.14}$$

with the regressor function defined by

$$\phi(\boldsymbol{x}) \triangleq \begin{bmatrix} -\frac{1}{N}\left(\frac{1}{N}\theta_m - \theta_l\right) \\ -\frac{1}{N}\left(\frac{1}{N}\omega_m - \omega_l\right) \\ -\left[1 - e^{-\left(\frac{\omega_m}{\omega_S}\right)^2}\right]\text{sgn}(\omega_m) \\ -e^{-\left(\frac{\omega_m}{\omega_S}\right)^2}\text{sgn}(\omega_m) \\ -\omega_m \end{bmatrix}. \tag{5.15}$$

In order for $\phi(\boldsymbol{x})$ to satisfy Assumption 5.3.3, the signum function is approximated by (5.12).

The main idea behind the NAC algorithm is to inject through the control signal u a term that will cancel the effect of the uncertain perturbation $\phi^T(\boldsymbol{x})\boldsymbol{\vartheta}$ by replacing the unknown parameter vector with its estimate $\hat{\boldsymbol{\vartheta}}$. A set of adaptive laws update the values of $\hat{\boldsymbol{\vartheta}}$ online until the velocity error e_ω reduces to 0. The desired error dynamics is also injected through the control signal, along with additional feedforward terms to cancel known signals, such as $J_m\dot{\omega}_r$ in (5.14).

The design of the NAC algorithm is given in the following Theorem (see Paper A for the proof):

Theorem 5.3.1. *The control law*

$$u = -\boldsymbol{\phi}^T(\boldsymbol{x})\hat{\boldsymbol{\vartheta}} - ke_\omega + J_m\dot{\omega}_{m,r} \tag{5.16}$$

together with the adaptive laws

$$\dot{\hat{\boldsymbol{\vartheta}}} = \boldsymbol{\Gamma}\boldsymbol{\phi}(\boldsymbol{x})e_\omega \tag{5.17}$$

where k is a positive real number and $\boldsymbol{\Gamma}$ is a 5×5 positive definite real matrix, ensure that the velocity tracking error e_ω with dynamics given in Equation (5.14) converges to the origin $e_\omega^* = 0$ as $t \to \infty$, i.e.

$$\lim_{t\to\infty} e_\omega(t) = 0 \, .$$

Moreover, the parameter estimation error $\tilde{\boldsymbol{\vartheta}} \triangleq \boldsymbol{\vartheta} - \hat{\boldsymbol{\vartheta}}$ remains bounded for all future times.

It should be pointed out that the NAC adaptive laws guarantee only boundedness of the parameter estimation and not convergence of the parameter estimates to their real values. This, however may still be achieved if the single-axis closed-loop system trajectories are such that $\phi(\boldsymbol{x})$ is persistently exciting.

5.3.1.3 Motor Velocity Immersion & Invariance Adaptive Controller (I&I-AC)

The structure of the I&I-AC is similar to the that of NAC but the design methodology stems from a more geometrical approach to the tracking problem, including indirect calculation of the unknown parameter vector $\boldsymbol{\vartheta} \in \mathbb{R}^q$. The idea is to use appropriate control and parameter estimation laws that can make the velocity error dynamics emerge in an invariant manifold

$$\mathcal{M} = \{(\boldsymbol{x}, \hat{\boldsymbol{\vartheta}}) \in \mathbb{R}^n \times \mathbb{R}^q | \hat{\boldsymbol{\vartheta}} - \boldsymbol{\vartheta} + \boldsymbol{h}(\boldsymbol{x}) = \boldsymbol{0}\} \tag{5.18}$$

on which the parameter estimation error $\tilde{\boldsymbol{\vartheta}}$ is equal to a *computable* offset $\boldsymbol{h}(\boldsymbol{x})$. Once on this manifold, the parameter vector can be calculated from the known offset $\boldsymbol{h}(\boldsymbol{x})$ and the parameter estimates $\hat{\boldsymbol{\vartheta}}$ as

$$\boldsymbol{\vartheta} = \hat{\boldsymbol{\vartheta}} + \boldsymbol{h}(\boldsymbol{x}) \, .$$

The design of $\boldsymbol{h}(\boldsymbol{x})$ involves the solution to a system of Partial Differential Equations (PDEs) and can be very difficult or impossible to solve analytically [94]. The dimensionality and complexity of this problem is directly related to the parametrization of

the velocity error system. In order to avoid high complexity in the design of $\boldsymbol{h}(\boldsymbol{x})$, the unknown parameter vector in this method is chosen as

$$\boldsymbol{\vartheta} \triangleq \begin{bmatrix} T_{C,m} & T_{S,m} & \beta_m & b \end{bmatrix}^T , \tag{5.19}$$

with the regressor function $\boldsymbol{\phi}(\boldsymbol{x})$ defined as

$$\boldsymbol{\phi}(\boldsymbol{x}) \equiv \boldsymbol{\phi}(\omega_m) \triangleq \begin{bmatrix} -\left[1 - e^{-\left(\frac{\omega_m}{\omega_S}\right)^2}\right] \text{sgn}(\omega_m) \\ -e^{-\left(\frac{\omega_m}{\omega_S}\right)^2} \text{sgn}(\omega_m) \\ -\omega_m \\ -1 \end{bmatrix} \tag{5.20}$$

and T_l defined in Equation (4.12). This selection of the parameter vector is valid since the shaft parameters are considered known and the focus of the control design is on friction compensation. Moreover, the additional parameter b is included such that it captures minor variations of T_l coming from small uncertainties in K_S, D_S. With this selection of $\boldsymbol{\vartheta}, \boldsymbol{\phi}(\omega_m)$ the motor velocity error dynamics is written:

$$\dot{e}_\omega = \frac{1}{J_m}\left[u + \boldsymbol{\phi}^T(\boldsymbol{x})\boldsymbol{\vartheta} - \frac{1}{N}T_l\right] - \dot{\omega}_{m,r} \, . \tag{5.21}$$

The design of the I&I-AC also requires Lipschitz continuity of $\boldsymbol{\phi}(\omega_m)$ (hence, $\text{sgn}(\cdot)$ is again approximated by (5.12)) and is summarized in the following Theorem (see Paper A for the proof).

Theorem 5.3.2. *The control law*

$$u = \frac{1}{N}T_l - \boldsymbol{\phi}^T(\omega_m)\left(\hat{\boldsymbol{\vartheta}} + \boldsymbol{h}(\omega_m)\right) - k_{II}e_\omega + J_m\dot{\omega}_r \tag{5.22}$$

together with the adaptive laws

$$\dot{\hat{\boldsymbol{\vartheta}}} = \frac{\partial \boldsymbol{h}}{\partial \omega_m}\frac{1}{J_m}\left(k_{II}e_\omega - J_m\dot{\omega}_r\right) \tag{5.23}$$

with k_{II} being a positive real number and the real function $\boldsymbol{h} : \mathbb{R} \to \mathbb{R}^4$ being defined as

$$\boldsymbol{h}(\omega_m) = J_m\boldsymbol{\Gamma_{II}}\begin{bmatrix} -|\omega_m| + \frac{\omega_S\sqrt{\pi}}{2}\text{erf}(\frac{\omega_m}{\omega_S})\text{sgn}(\omega_m) \\ -\frac{\omega_S\sqrt{\pi}}{2}\text{erf}(\frac{\omega_m}{\omega_S})\text{sgn}(\omega_m) \\ -\frac{1}{2}\omega_m^2 \\ -\omega_m \end{bmatrix} \tag{5.24}$$

where $\boldsymbol{\Gamma_{II}}$ a 4×4 is a positive definite real matrix and $\text{erf}(\cdot)$ is the error function approximated by (II.5)*, ensure that the velocity tracking error e_ω with dynamics*

given in Equation (5.21) *converges to the origin* $e_\omega^* = 0$ *as* $t \to \infty$*, i.e.*

$$\lim_{t\to\infty} e_\omega(t) = 0 \, .$$

Additionally, the parameter estimation error $\tilde{\boldsymbol{\vartheta}}$ *remains bounded for all future times.*

5.3.2 Direct Position Control

In contrast to the previous architecture, the direct position control scheme does not maintain the cascaded structure of the nested position-velocity loops. The load position is directly controlled and, consequently, the design of each of the nonlinear controllers takes into account the dynamics of the entire single-axis system and not just of the drive motor. The generic direct-position control architecture is illustrated in Figure 5.5. An ABSC and two higher-order SMCs were designed for the single-axis

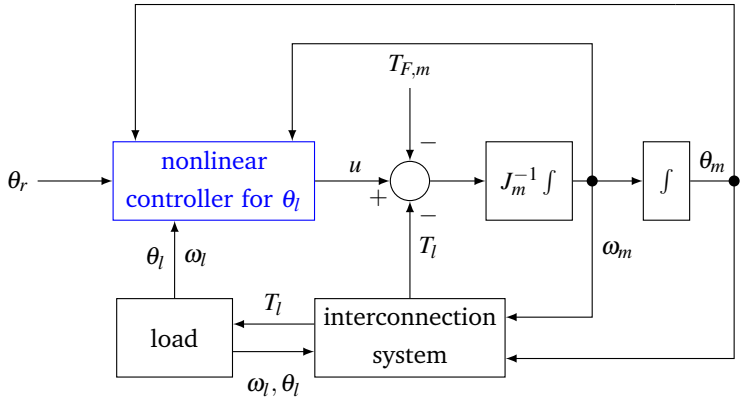

Figure 5.5: Direct-position control architecture.

system based on the direct position control architecture. The theoretical derivation and structure are analysed in Paper B and are briefly presented in the following.

5.3.2.1 Load Position Adaptive Backstepping Controller (ABSC)

Adaptive backstepping controllers, introduced in [83], utilize the idea of *virtual inputs* to directly control the outputs of nonlinear uncertain systems with relative degree higher than one. Under certain controllability conditions, such systems can be represented as a chain of integrators perturbed by an uncertain vector. Starting from the output dynamics, the latest state in the integrator chain is considered as an input and a "local" control law is designed. Then moving one step up to the

chain, the virtual input is now the state that has to be regulated to track the control input designed earlier. This procedure continues until a full backtracking to the real system input is completed. The uncertain terms are incorporated in the design together with appropriate adaptive laws, similar to those in the NAC design.

The steps needed to reach the real input correspond to the relative degree of the system. Depending on the dimension of the system, relative degree higher than two can lead to considerably complicated control and adaptive laws. The single-axis system has relative degree 3, hence three steps are needed. A change of the controlled variable from the load positioning error e_θ defined in Table 5.2 to the variable

$$z_1 \triangleq \dot{e}_\theta + c e_\theta,\ c > 0 \tag{5.25}$$

reduces the required steps to 2. If z_1 is equal to 0, then the origin $e_\theta^* = 0$ becomes an exponentially stable equilibrium point of the load position error dynamics as can be seen from (5.25).

With the shaft and friction (both motor and load) coefficients considered unknown or uncertain, the single-axis system is re-written as follows:

$$\dot{\omega}_m = \frac{1}{J_m}\left(u + \boldsymbol{\phi_1}^T(\boldsymbol{x})\boldsymbol{\vartheta}\right) \tag{5.26}$$

$$\dot{\theta}_m = \omega_m \tag{5.27}$$

$$\dot{\omega}_l = \frac{1}{J_l}\left(\boldsymbol{\phi_2}^T(\boldsymbol{x})\boldsymbol{\vartheta} + b\omega_m\right)\ ,\ b = \frac{D_S}{N} \tag{5.28}$$

$$\dot{\theta}_l = \omega_l \tag{5.29}$$

$$\boldsymbol{x} = \begin{bmatrix}\omega_m & \theta_m & \omega_l & \theta_l\end{bmatrix}^T \tag{5.30}$$

where

$$\boldsymbol{\vartheta} = \begin{bmatrix}K_S & D_S & T_{C,m} & \beta_m & T_{C,l} & \beta_l\end{bmatrix}^T \tag{5.31}$$

$$\boldsymbol{\phi_1}(\boldsymbol{x}) = \begin{bmatrix} -\frac{1}{N}\left(\frac{1}{N}\theta_m - \theta_l\right) \\ -\frac{1}{N}\left(\frac{1}{N}\omega_m - \omega_l\right) \\ -\text{sgn}(\omega_m) \\ -\omega_m \\ 0 \\ 0 \end{bmatrix},\quad \boldsymbol{\phi_2}(\boldsymbol{x}) = \begin{bmatrix} \frac{1}{N}\theta_m - \theta_l \\ -\omega_l \\ 0 \\ 0 \\ -\text{sgn}(\omega_l) \\ -\omega_l \end{bmatrix}. \tag{5.32}$$

Apart from the standard assumption of constant or slowly-varying parameters ($\dot{\boldsymbol{\vartheta}} \approx \mathbf{0}$) considered in almost all the adaptive methods, the following assumption is made:

Assumption 5.3.4. ***(Lipschitz continuity)***
The regressor functions $\boldsymbol{\phi_1}(\boldsymbol{x}), \boldsymbol{\phi_2}(\boldsymbol{x})$ are locally Lipschitz.

The design of the ABSC for the load position in the drive-train system is depicted in Figure 5.6 and is summarized in the following Theorem (see Paper B for the proof):

Theorem 5.3.3. *Consider the drive-train system described in* (5.26)-(5.32) *with unknown parameters $\boldsymbol{\vartheta}$ defined in* (5.31)*, the uncertain virtual input gain $b = \frac{D_S}{N}$ with known sign and a bounded reference signal $\theta_r(t) \in \mathcal{C}^3$ for the load position. The collective control law*

$$u = -\boldsymbol{\phi_1}^T(\boldsymbol{x})\hat{\boldsymbol{\vartheta}} + J_m\left(\psi_2 - k_2 z_2 - \frac{1}{J_l} z_1 \hat{b}\right) \tag{5.33}$$

where

$$e_\theta = \theta_l - \theta_r$$

$$z_1 = \dot{e}_\theta + c e_\theta$$

$$\alpha = \alpha(\boldsymbol{x}, \hat{\rho}, \hat{\boldsymbol{\vartheta}}, \dot{\theta}_r, \ddot{\theta}_r) = \hat{\rho}\left[J_l\left(\ddot{\theta}_r - c\omega_l + c\dot{\theta}_r - k_1 z_1\right) - \boldsymbol{\phi_2}^T(\boldsymbol{x})\hat{\boldsymbol{\vartheta}}\right] \tag{5.34}$$

$$z_2 = \omega_m - \alpha(\boldsymbol{x}, \hat{\rho}, \hat{\boldsymbol{\vartheta}}, \dot{\theta}_r, \ddot{\theta}_r)$$

$$\psi_1 = \dot{\hat{\rho}}\left[-\boldsymbol{\phi_2}^T(\boldsymbol{x})\hat{\vartheta} + J_l\left(\ddot{\theta}_r - c\omega_l + c\dot{\theta}_r - k_1 z_1\right)\right] \tag{5.35}$$

$$\psi_2 = \psi_1 + \hat{\rho}\Bigg\{ - \boldsymbol{\phi_2}^T(\boldsymbol{x})\dot{\hat{\boldsymbol{\vartheta}}} - \hat{K}_S\left(\frac{\omega_m}{N} - \omega_l\right) + J_l\left(\theta_r^{(3)} + c\ddot{\theta}_r\right) +$$

$$\left(\frac{\hat{D}_s + \hat{\beta}_l}{J_l} - c - k_1\right)\left(\boldsymbol{\phi_2}^T(\boldsymbol{x})\hat{\boldsymbol{\vartheta}} + \hat{b}\omega_m\right) - J_l k_1\left(c\omega_l - \ddot{\theta}_r - c\dot{\theta}_r\right)\Bigg\} \tag{5.36}$$

together with the adaptation laws

$$\dot{\hat{\boldsymbol{\vartheta}}} = \boldsymbol{\Gamma}\left\{\boldsymbol{\phi_2}(\boldsymbol{x})\left[\frac{z_1}{J_l} - \hat{\rho} z_2\left(\frac{\hat{D}_s + \hat{\beta}_l}{J_l} - c - k_1\right)\right] + \frac{z_2}{J_m}\boldsymbol{\phi_1}(\boldsymbol{x})\right\} \tag{5.37}$$

$$\dot{\hat{\rho}} = -\gamma_1 \cdot \operatorname{sgn}(b) z_1\left(-\frac{1}{J_l}\boldsymbol{\phi_2}^T(\boldsymbol{x})\hat{\boldsymbol{\vartheta}} + \ddot{\theta}_r - c\omega_l + c\dot{\theta}_r - k_1 z_1\right) \tag{5.38}$$

$$\dot{\hat{b}} = \gamma_2\left[\frac{1}{J_l} z_1 z_2 - \hat{\rho} z_2\left(\frac{\hat{D}_s + \hat{\beta}_l}{J_l} - c - k_1\right)\omega_m\right] \tag{5.39}$$

where $k_1, k_2, \gamma_1, \gamma_2, c > 0$ and $\boldsymbol{\Gamma}$ is a 6×6 symmetric positive definite real matrix, ensure that the position tracking error e_θ converges to the origin $e_\theta^* = 0$ as $t \to \infty$,

i.e.

$$\lim_{t\to\infty} e_\theta(t) = 0\ .$$

Moreover, the parameter estimation errors $\tilde{\boldsymbol{\vartheta}}, \tilde{\rho}, \tilde{b}$ *remain bounded for all future times.*

Similar to the cases of NAC and I&I-AC, Assumption 5.3.4 is satisfied by the approximation of the signum function in (5.12). As it can be seen from Theorem 5.3.3 the design of the ABSC is more complex compared to the cascaded adaptive solutions NAC, I&I-AC and it involves more parameters for tuning. Another challenge is the fact that one of the virtual inputs is multiplied by the uncertain term $\frac{N}{D_S}$, as shown in Equation (5.28).

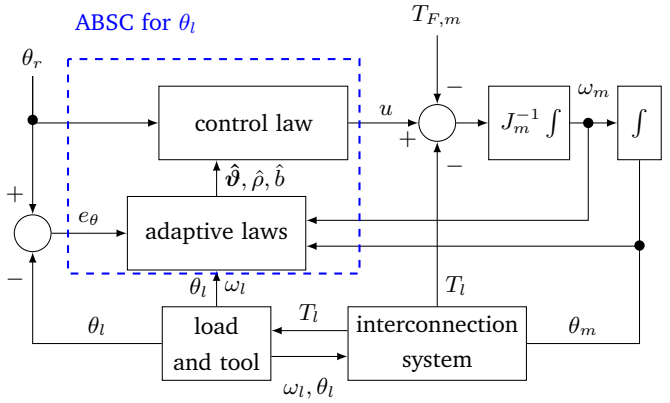

Figure 5.6: ABSC for direct load positioning.

5.3.2.2 Load Position Output Super-Twisting SMC (OSTSMC)

The STSMC algorithm given in (5.10),(5.11) is also used for the design of the Output Super-Twisting Sliding-Mode Controller (OSTSMC). Since, however the system is of relative degree higher than 2, i.e. the order of the STSMC, the sliding variable s is chosen as a linear combination of the load position error e_θ and its first time derivative. Specifically, if $e_1 \triangleq e_\theta$ and $e_2 \triangleq \dot{e}_\theta$, the sliding variable is defined as

$$s \triangleq \dot{e}_2 + (\lambda_1 + \lambda_2)\, e_2 + \lambda_1 \lambda_2 e_1\ . \tag{5.40}$$

where λ_1, λ_2 are real positive constants. Its dynamics reads:

$$\begin{aligned}\dot{s} &= \ddot{\omega}_l - \theta_r^{(3)} + (\lambda_1+\lambda_2)\left(\dot{\omega}_l - \ddot{\theta}_r\right) + \lambda_1\lambda_2\left(\omega_l - \dot{\theta}_r\right) \\ &= \frac{1}{J_l}\left[K_S\left(\frac{1}{N}\omega_m - \omega_l\right) - D_S\dot{\omega}_l - \dot{T}_{F,l} - \frac{D_S}{J_m}\left(\frac{1}{N}T_l + T_{F,m}\right)\right] \\ &- \theta_r^{(3)} + (\lambda_1+\lambda_2)\left(\dot{\omega}_l - \ddot{\theta}_r\right) + \lambda_1\lambda_2\left(\omega_l - \dot{\theta}_r\right) + \frac{D_S}{J_m J_l}u\ .\end{aligned}$$

By using the control signal

$$u = u_{SM} + \frac{J_m J_l}{D_S}\left[\theta_r^{(3)} + (\lambda_1+\lambda_2)\,\ddot{\theta}_r - \lambda_1\lambda_2\left(\omega_l - \dot{\theta}_r\right)\right] \tag{5.41}$$

to cancel known terms, the dynamics of s is simplified to:

$$\dot{s} = \psi(t, \boldsymbol{x}) + \frac{D_S}{J_m J_l}u_{SM}\ , \tag{5.42}$$

where

$$\psi(t,\boldsymbol{x}) = \frac{1}{J_l}\left[K_S\left(\frac{1}{N}\omega_m - \omega_l\right) - D_S\dot{\omega}_l - \dot{T}_{F,l} - \frac{D_S}{J_m}\left(\frac{T_l}{N} + T_{F,m}\right)\right] + (\lambda_1+\lambda_2)\,\dot{\omega}_l$$

and $\boldsymbol{x}$ denotes the drive-train state vector. The approximation of the signum function (defined in (5.12)), as well as Assumption 5.3.2 are also adopted here. Then according to the super-twisting algorithm, the term u_{SM} is given by

$$u_{SM} \triangleq \frac{J_m J_l}{D_S}\left(-c_1|s|^{\frac{1}{2}}\mathrm{sgn}(s) + v\right) \tag{5.43a}$$

$$\dot{v} = -c_2\mathrm{sgn}(s)\ . \tag{5.43b}$$

As in the case of the velocity STSMC, choosing the positive gains c_1, c_2 appropriately will bring the system (5.42) on the sliding manifold $\mathcal{S} = \{s(t) \in \mathbb{R} | s = \dot{s} = 0\}$ in finite-time. From the definition of s and e_1, e_2 it can be seen that once on the sliding manifold, the load position error and its first time-derivative have the following dynamics:

$$\begin{bmatrix}\dot{e}_1 \\ \dot{e}_2\end{bmatrix} = \begin{bmatrix}0 & 1 \\ -\lambda_1\lambda_2 & -(\lambda_1+\lambda_2)\end{bmatrix}\begin{bmatrix}e_1 \\ e_2\end{bmatrix}\ , \tag{5.44}$$

which for positive λ_1, λ_2, has an Exponentially Stable (ES) equilibrium point at the origin $\begin{bmatrix}e_1^* & e_2^*\end{bmatrix}^T = \begin{bmatrix}0 & 0\end{bmatrix}^T$. The selection of the poles λ_1, λ_2 of the system in (5.44) can be done via any method of linear control design (e.g. pole placement) and it can improve the positioning performance in the case that the tuning of the gains c_1, c_2 does not ensure convergence to the sliding manifold $\mathcal{S}$. Indeed, if $s(t) \neq 0$, the dynamics of $\boldsymbol{e} \triangleq \begin{bmatrix}e_1 & e_2\end{bmatrix}^T$ is written as

$$\begin{bmatrix}\dot{e}_1 \\ \dot{e}_2\end{bmatrix} = \underbrace{\begin{bmatrix}0 & 1 \\ -\lambda_1\lambda_2 & -(\lambda_1+\lambda_2)\end{bmatrix}}_{\boldsymbol{A_e}}\begin{bmatrix}e_1 \\ e_2\end{bmatrix} + \underbrace{\begin{bmatrix}0 \\ 1\end{bmatrix}}_{\boldsymbol{B_e}} s(t)\ . \tag{5.45}$$

The solution to (5.45) is given by

$$\boldsymbol{e}(t) = \boldsymbol{e}(t_0)e^{\boldsymbol{A_e}t} + \int_{t_0}^{t} e^{\boldsymbol{A_e}(t-\tau)}\boldsymbol{B_e}s(\tau)d\tau \ , \tag{5.46}$$

where the matrix $\boldsymbol{A_e}$ is negative definite for $\lambda_1, \lambda_2 > 0$. From (5.46) it can be seen that the larger the dominant pole is chosen, the smaller the influence of the input $s(t)$ on the error e_1 is. The generic diagram for the OSTSMC is shown in Figure 5.7.

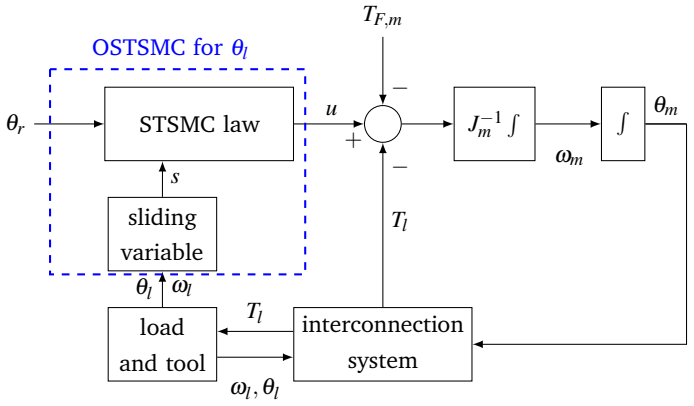

Figure 5.7: OSTSMC for direct load positioning.

5.3.2.3 Load Position Adaptive Super-Twisting SMC (ASTSMC)

The Adaptive Super-Twisting Sliding-Mode Controller (ASTSMC) [77], shown in the block diagram of Figure 5.8, extends the design of the OSTSMC by dynamically updating the value of the dominant pole λ_1 of the system in (5.44). The adaptive law for λ_1, derived in the same work, depends on the difference between the average output error and a specified accuracy limit. A modification of this adaptive law was proposed in Paper B, where the average load position error was replaced with the *maximum peak error*, defined over a time horizon of ν samples as

$$e_1^{peak} = \sup_{0 \le i \le \nu} |e_1(t - iT_s)| \ , \tag{5.47}$$

where T_s is the sampling period for the measurements. The adaptive law for λ_1 reads:

$$\dot{\lambda}_1 = -\gamma_\lambda \text{sgn}\left(e_1^{peak} - \varepsilon_\theta\right) \ , \ \gamma_\lambda > 0 \ , \tag{5.48}$$

where $\varepsilon_\theta > 0$ expresses the positioning accuracy limit. This law together with the control law (5.43a),(5.43b) ensures (see [77] for a proof) convergence of the load

position error to the compact set $\mathcal{E}_\theta = \{\zeta \in \mathbb{R} \mid |\zeta| \leq \varepsilon_\theta\}$. Once λ_1 is determined, the second (and faster) eigenvalue of the system (5.44) can be selected as a multiple of λ_1, i.e.

$$\lambda_2 = a\lambda_1, \; a > 1 \; . \tag{5.49}$$

In both the OSTSMC and the ASTSMC the estimation of $\dot{\omega}_l$ is done by using a linear observer, similar to the one in (4.20), with gain $k_{obs} > 0$.

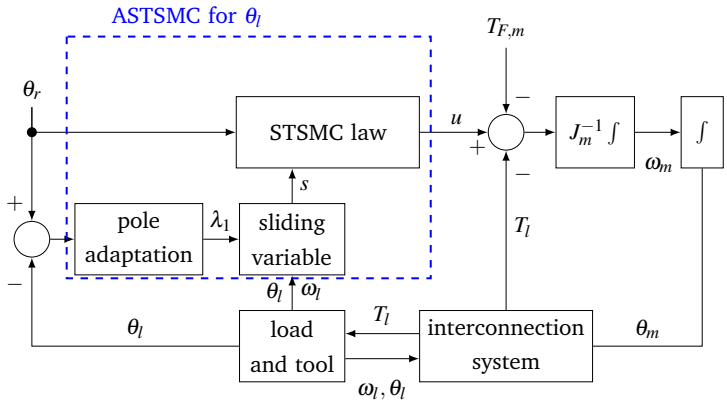

Figure 5.8: ASTSMC for direct load positioning.

By comparing the two different control architectures, it can be seen that the cascaded position-velocity control has a more modular structure, which makes the designs of the velocity controllers much simpler than the ones of direct-position control. Moreover, the resulting controllers can be easily integrated to already installed positioning solutions since only the velocity controller has to be replaced. However, their performance can be limited by the outer loop P controller due to the fact that the velocity reference signals may be varying too fast depending on the position controller tuning. Additionally, degradations on the load side are addressed only by the P controller of the outer loop. On the other hand, the direct-position controllers take into account all the dynamics in the drive train. As such, compensation for all the friction degradations, both on the motor and on the load side, is integrated in the controllers design. However, consideration of all the modelled phenomena leads to substantially more complex designs and a larger number of tunable parameters. Furthermore, their installation to a commissioned machine requires a complete replacement of the positioning system. A comparative presentation of the two different control architectures is given in Table 5.3. Table 5.4 summarizes the assumptions considered in each method, as well as the main theoretical features of the nonlinear controllers presented in this section.

Table 5.3: Comparison between cascaded and the direct position control schemes.

Advantages	Disadvantages
Position-Velocity Cascaded Control	
• Simple designs	• Velocity reference rate can be large
• Modular tuning	• Performance limited by position P controller bandwidth
• Easier integration to existing control loops	• Considers degradations only on the motor side
Direct Position Control	
• Integrated design for position and velocity control	• More complex designs
• Accounts for all the degradations in the system	• Larger number of tunable parameters
• Guaranteed smooth reference signals	• Fully replaces existing control loops

5.4 Controllers Evaluation

The designed controllers were implemented on the physical system and tested in three operation modes regarding the drive speed (slow, average and fast). Five different friction cases were considered for each operating mode. The first corresponds to the nominal friction values, while in the rest four the Coulomb friction coefficient was increased by up to 900% of its nominal value. Some of the friction levels (especially the last two cases) are unlikely to be reached in real applications, since decommissioning of the machine will occur for much lower friction degradation. However, these friction values were considered in the study for the purpose of examining the controllers' performance limits. The position reference signal in all the tests was a sinusoid

$$\theta_r(t) = \Theta_0 \sin(2\pi f_r t) \ ,$$

where Θ_0 is the position amplitude in rad and f_r is the frequency in Hz. The selection of the $\theta_r(t)$ as a trigonometric function of time was made on the basis of ensuring smooth reference signals that include reverse of the axis motion, so that the nonlinear friction phenomena (steep change in Coulomb friction) are excited. The fifteen in total different test scenarios are summarized on Table 5.5.

The evaluation of the controllers performance was done by using several quantitative and qualitative criteria. A brief explanation of the numeric performance indices is provided in Table 5.6. The first five indices constitute metrics of the absolute accuracy and efficiency of the control methods. The MAPE criterion relates

Table 5.4: Assumptions and key properties of the methods.

Assumptions	Theoretical features
STSMC	
• Matched perturbation is Lipschitz continuous	• Finite-time convergence • Robustness against any type of Lipschitz disturbances
NAC	
• Regressor function is Lipschitz continuous • Parameters are constant or slowly varying	• Velocity error converges to zero • Uniformly bounded parameter estimation error • Parameter estimation if the regressor is persistently exciting
I&I-AC	
• Regressor function is Lipschitz continuous • Parameters are constant or slowly varying	• Velocity error converges to zero • Parameters can be indirectly calculated if the regressor is persistently exciting
ABSC	
• Unknown parameters are constant or slowly varying • Regressor functions are Lipschitz continuous	• Position error converges to zero • Uniformly bounded parameter estimation error • Parameter estimation if the regressors are persistently exciting
OSTSMC	
• Perturbation is Lipschitz continuous	• Position error is exponentially stable • Robustness against Lipschitz disturbances and model uncertainties
ASTSMC	
• Perturbation is Lipschitz continuous	• Position error is exponentially stable • Robustness against Lipschitz disturbances and model uncertainties • Sliding surface poles are adjusted to the positioning error magnitude

Table 5.5: Control methods test scenarios. The colored areas correspond to the extreme friction cases.

No	Θ_0 (rad)	$T_{C,m}$ (N m)	f_r (Hz)	Increase in friction
1	1	0.035	0.1	0
2	1	0.035	0.5	0
3	1	0.035	2	0
4	1	0.11	0.1	215%
5	1	0.11	0.5	215%
6	1	0.11	2	215%
7	1	0.15	0.1	330%
8	1	0.15	0.5	330%
9	1	0.15	2	330%
10	1	0.25	0.1	615%
11	1	0.25	0.5	615%
12	1	0.25	2	615%
13	1	0.35	0.1	900%
14	1	0.35	0.5	900%
15	1	0.35	2	900%

to the tracking consistency of the controller and it is indicative of how well can one axis synchronize with the other machine axes. High MAPE implies large phase lags between reference and actual position signals, which could lead to deterioration of the synchronized axes motion and, consequently, to contour distortion errors [10, 11, 18].

The qualitative criteria include a $\theta_x - \theta_y$ circular plot, similar to the Circular Interpolation Test (CIT) plots (ballbar test plots) used in axis calibration routines [10, 18]. The trajectories θ_x, θ_y are defined as in the case of MAPE and they ideally form a circle of unit radius. The magnitude of the deviations of the real $\theta_x - \theta_y$ curve from the ideal circle visualizes the performance of the controller. The number of the tunable parameters and required signals for each controller, as well as their sum, referred to as the Complexity Index (CI), are also considered since they are indicative of each methods design and implementation complexity.

All the controllers were evaluated during the last 20 s of each experiment, which lasted 540 s. This was done, such that the estimated parameters in the adaptive schemes could reach a steady-state value and also to avoid including initial start-up errors in the analysis.

Table 5.7 shows the values of the MAE for all controllers in all the experiments. As it can be seen, almost all of the nonlinear controllers outperform at low frequencies

Table 5.6: Controllers comparison quantitative criteria. T is the period in seconds over which the evaluation was done.

Criterion	**Definition/description**	**Focus**
Maximum Absolute Error (MAE)	$\sup_{t_0 \leq t \leq t_0+T} \lvert e_\theta(t) \rvert$	Maximum peak deviation
Integral Square Error (ISE)	$\frac{1}{T}\int_{t_0}^{t_0+T} e_\theta^2(t)dt$	Speed of error decaying
Integral Timed Square Error (ITSE)	$\frac{1}{T}\int_{t_0}^{t_0+T} te_\theta^2(t)dt$	Persisting error
Control Power (CP)	$\frac{1}{T}\int_{t_0}^{t_0+T} u^2(t)dt$	Control usage
Error-Control Power product (ECP)	$\sup_{t_0 \leq t \leq t_0+T} \lvert e_\theta(t) \rvert \cdot \frac{1}{T}\int_{t_0}^{t_0+T} u^2(t)dt$	Overall efficiency
Maximum Absolute Phase Error (MAPE)	$\sup_{t_0 \leq t \leq t_0+T} \lvert e_\phi(t) \rvert$ with $e_\phi(t) = \tan^{-1}\left(\frac{\theta_y^r(t)}{\theta_x^r(t)}\right) - \tan^{-1}\left(\frac{\theta_y(t)}{\theta_x(t)}\right)$ $\theta_x(t) = \frac{1}{\Theta_0}\theta_l(t)$ $\theta_y(t) = -\frac{1}{\Theta_0}\theta_l\left(t - \frac{\pi}{2}\right)$ $\theta_x^r(t) = \frac{1}{\Theta_0}\theta_r(t) = \sin(2\pi f_r t)$ $\theta_y^r(t) = -\frac{1}{\Theta_0}\theta_r\left(t - \frac{\pi}{2}\right) = \cos(2\pi f_r t)$	Maximum phase lag

the P-PI scheme, which starts degrading already in the first non-nominal friction case with MAE up to 3 times larger than the required accuracy. The P-STSMC cascade shows the highest accuracy, which is maintained even for the extreme friction cases. Similar performance is demonstrated by the two higher-order SMCs except for the last friction case, where they exceed the prescribed accuracy limit by up tp 70%. The ABSC keeps the positioning error within the limit except for the last friction case and it has the second best performance after the P-STSMC. This is not the case, however for the cascaded adaptive controllers, which fail to maintain the positioning tolerances with MAE even larger than that of the P-PI. This degradation of the P-NAC and the P-I&I-AC can be primarily attributed to a deadzone of approximately 0.035 rad that exists by construction between the inner and outer housing cylinders of the friction adjustment clutch. The sudden change in the Coulomb friction (from nominal inside the deadzone to the increased value outside of the deadzone) violates the assumption of constant or slowly-varying parameters, i.e. the adaptive controllers cannot compensate for this phenomenon. The ABSC addresses this problem via the adjustment of other damping parameters in the load side or of the uncertain input gain b. This backlash effect is more dominant at low frequencies since the system "spends" more time in the deadzone.

Indeed, the performance of the cascaded adaptive controllers improves at 0.5 Hz with the corresponding values for the MAE being below the required accuracy limit at least for the "realistic" friction cases. The P-STSMC and the ABSC consistently provide the most accurate positioning, while the P-PI and the higher-order SMCs degrade for all the non-nominal friction values.

For fast reference signals the situation changes since the richer excitation of the system allows faster and more accurate friction compensation by the P-NAC and P-I&I-AC. The cascaded adaptive controllers maintain the positioning error below the required accuracy limit in all the friction cases and they even outperform the P-STSMC. The latter only shows a 10% error increase above the prescribed tolerances during the highest friction test. The ABSC shows performance degradation from the first tests in 2 Hz, which implies inadequate tuning for fast reference signals rather than poor adaptation properties. Moreover, the rate of positioning deterioration is smaller than that of the P-PI and the higher-order SMCs. For the "realistic" friction values, the MAE of the ABSC does not exceed the accuracy limit by more than 4 mrad. The OSTSMC and ASTSMC clearly degrade in accuracy at fast reference signals with MAE ranging from 6 to almost 50 times larger than the allowable accuracy limit.

Similar evaluation conclusions can be drawn by inspecting the histograms in Figures 5.9 and 5.10, which show the ratio of the performance indices of each controller over the corresponding PI values (dashed horizontal line).

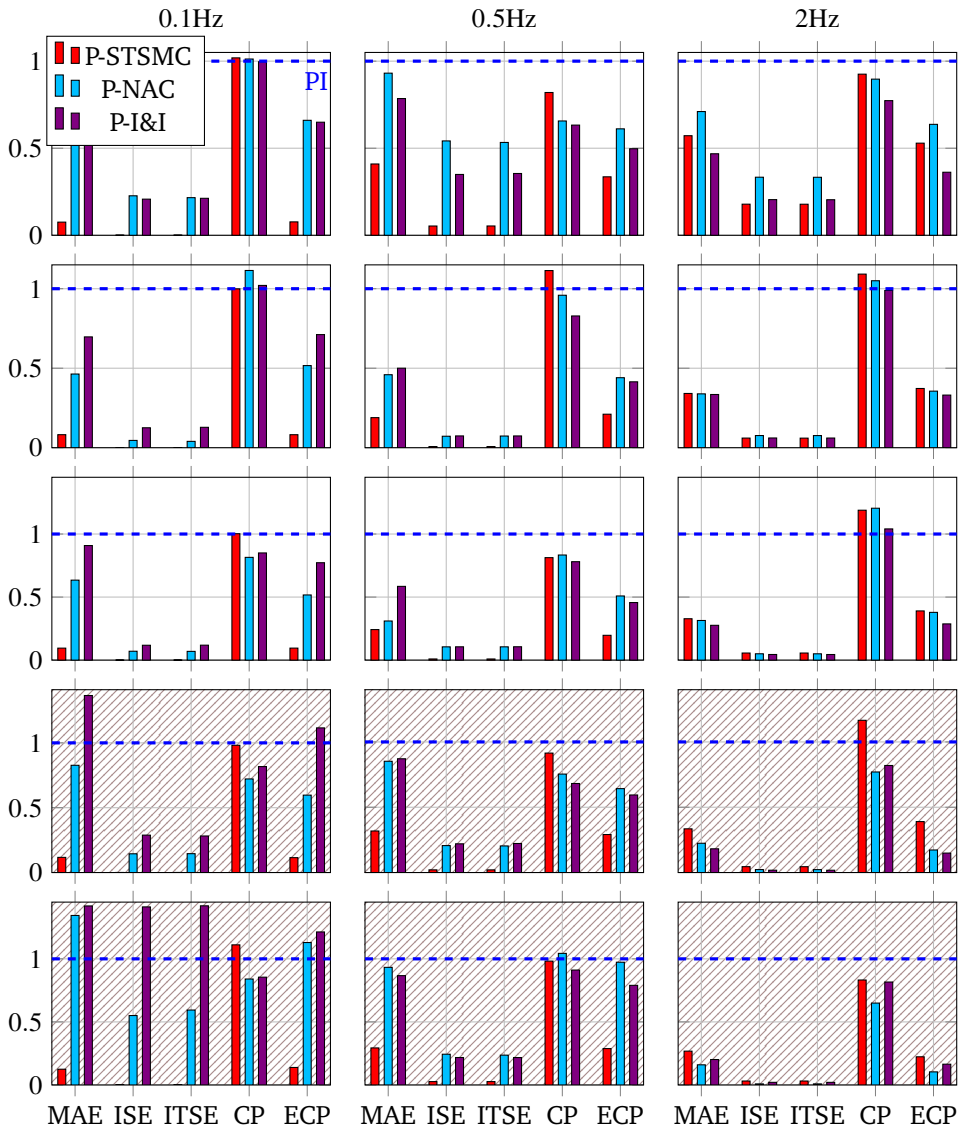

Figure 5.9: Relative performance indices of cascaded position-velocity controllers. The different cases of friction start with nominal friction and increase from top to bottom. The plots in the stripped area correspond to the extreme friction cases.

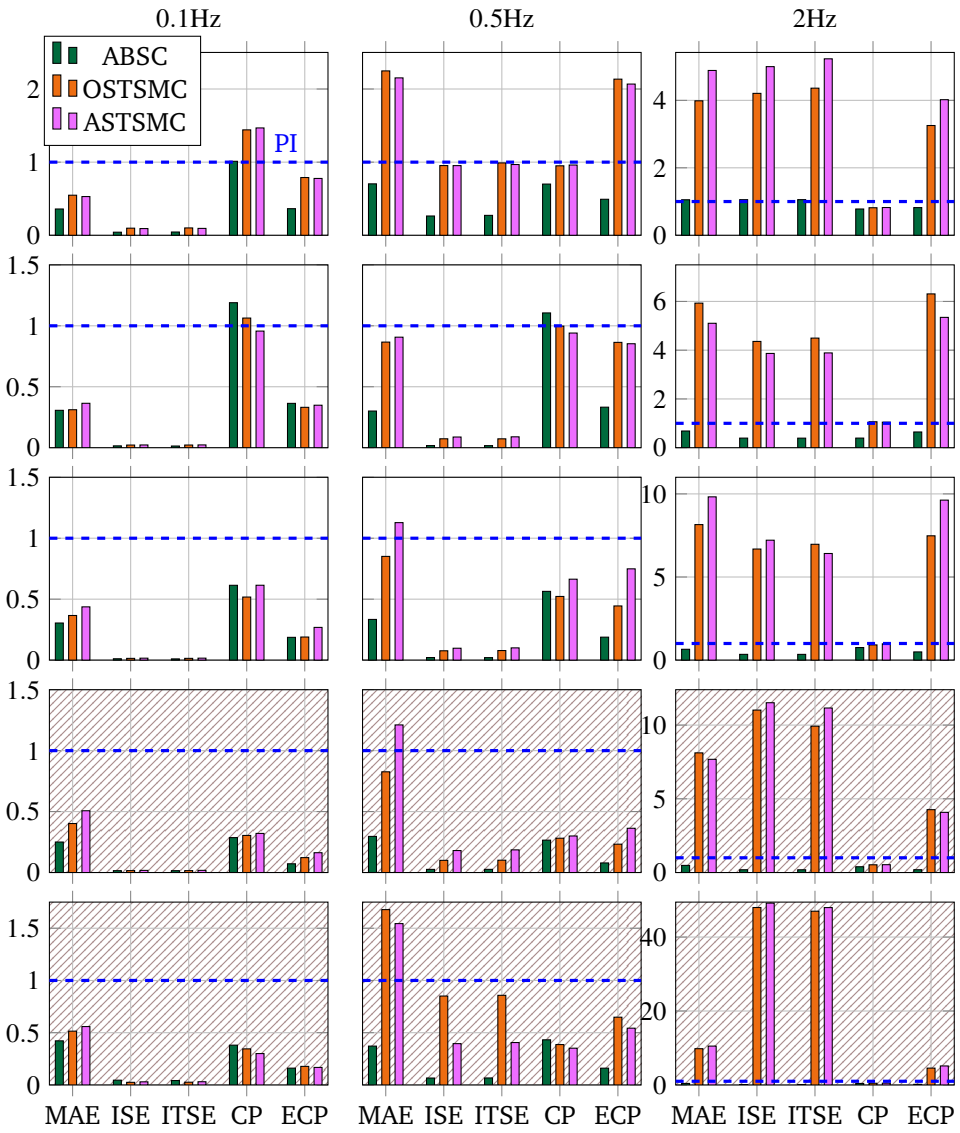

Figure 5.10: Relative performance indices of direct position controllers. The different cases of friction start with nominal friction and increase from top to bottom. The plots in the stripped area correspond to the extreme friction cases.

Table 5.7: MAE in mrad for all controllers in all scenarios. The indices 1-4 denote the four different friction cases.

Controller	nominal	1	2	3	4
MAE in mrad at 0.1 Hz					
P-PI	12	17.9	20.3	24.4	30.3
P-STSMC	0.9	1.5	1.9	2.9	3.8
P-NAC	7.8	8.3	12.9	20.2	40.7
P-I&I-AC	7.8	12.5	18.5	33.3	43
ABSC	4.3	5.5	6.2	6.2	12.8
OSTSMC	6.6	5.6	7.4	9.8	15.6
ASTSMC	6.4	6.5	8.9	12.4	16.9
MAE in mrad at 0.5 Hz					
P-PI	4.9	15.6	17	23.7	37.2
P-STSMC	2	3	4.1	7.5	10.9
P-NAC	2.2	7.5	12.2	21.1	35
P-I&I-AC	4.9	7.2	13.2	20.3	34.3
ABSC	3.4	4.7	5.7	7	13.8
OSTSMC	10.9	13.6	14.4	19.6	62.5
ASTSMC	10.5	14.2	19.1	28.7	57.5
MAE in mrad at 2 Hz					
P-PI	12.3	20.1	21.8	31.6	45.7
P-STSMC	7	6.8	7.2	10.6	12.3
P-NAC	8.7	6.8	6.9	7.1	7.3
P-I&I-AC	5.8	6.7	6	5.7	9.2
ABSC	12.9	13.7	14.2	15.3	19.2
OSTSMC	49.1	118.9	177.7	256.5	448.6
ASTSMC	60.1	102.4	214.1	242.6	480.7

It can be seen that the nonlinear controllers outperform the P-PI solution except for the case of the cascaded adaptive controllers in low frequencies and the higher-order SMCs for fast reference signals. The control effort of the advanced controllers is in most cases lower than or at the same level with that of the P-PI scheme. Comparing the controllers' overall positioning performance, as this is illustrated in Figure 5.11 by means of the average MAE over all the frequency cases, shows that the P-STSMC and the adaptive controllers offer a more robust solution to the positioning degradation problem due to friction. The average MAPE, also depicted in the same Figure, indicates that phase lagging of the actual position with respect to the reference signal equally contributes to the position error in the cases of P-PI, OSTSMC and ASTSMC.

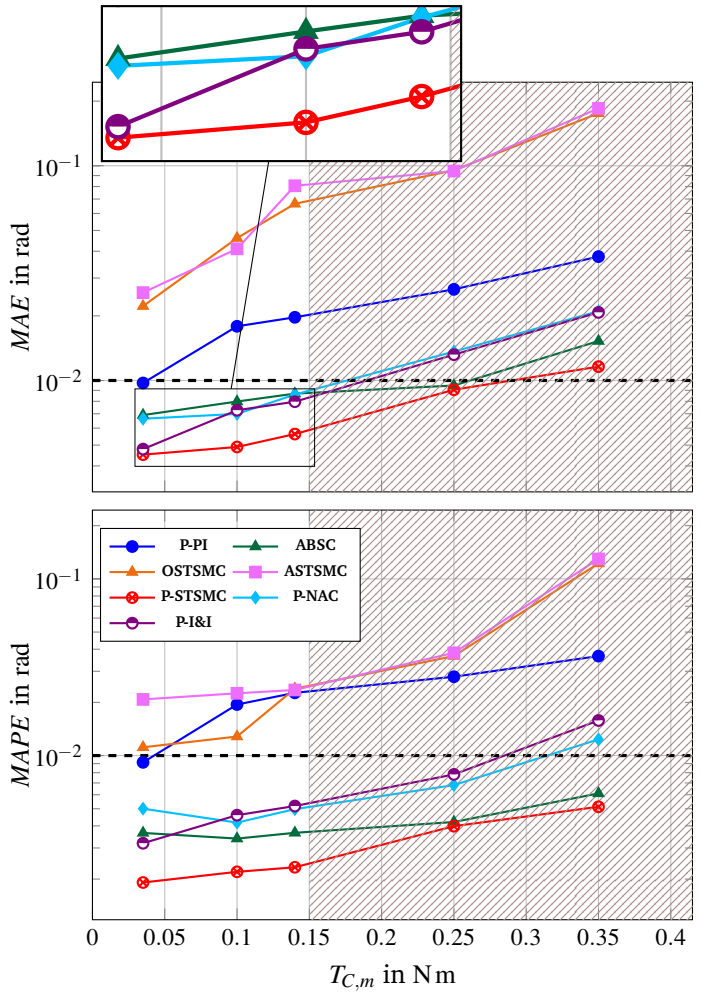

Figure 5.11: Average MAE (top) and MAPE (bottom) for all controllers and all friction cases. The dashed line corresponds to the $\pm 10^{-2}\mathrm{rad}$ accuracy bound and the stripped area denotes the extreme friction cases.

It is interesting to notice that the same STSMC algorithm but in different architecture exhibits the best and the worst positioning performance in average. In all three designs, the disturbance rejection depends on the selection of the switching gains k_1, k_2, c_1, c_2 and the bound of the perturbation derivative $\dot{\psi}(t, \boldsymbol{x})$. The larger this bound is the larger these gains have to be. In the case of the P-STSMC, $\dot{\psi}$ assumes much smaller values compared to the case of the OSTSMC and ASTSMC since it does not contain higher-order derivatives of the reference signal θ_r or the derivative of the friction torque. This allows for robust rejection of the perturbation ψ without using large values of k_1, k_2. In the case of the direct-position SMCs, increasing the switching gains c_1, c_2 leads to an increase of the chatter in the actuator to unwanted levels, without considerably improving the positioning accuracy. This can be seen in Figures 5.12 and 5.13, where the position error and torque command of each controller for the largest "realistic" friction value at 0.1 Hz and 2 Hz are shown.

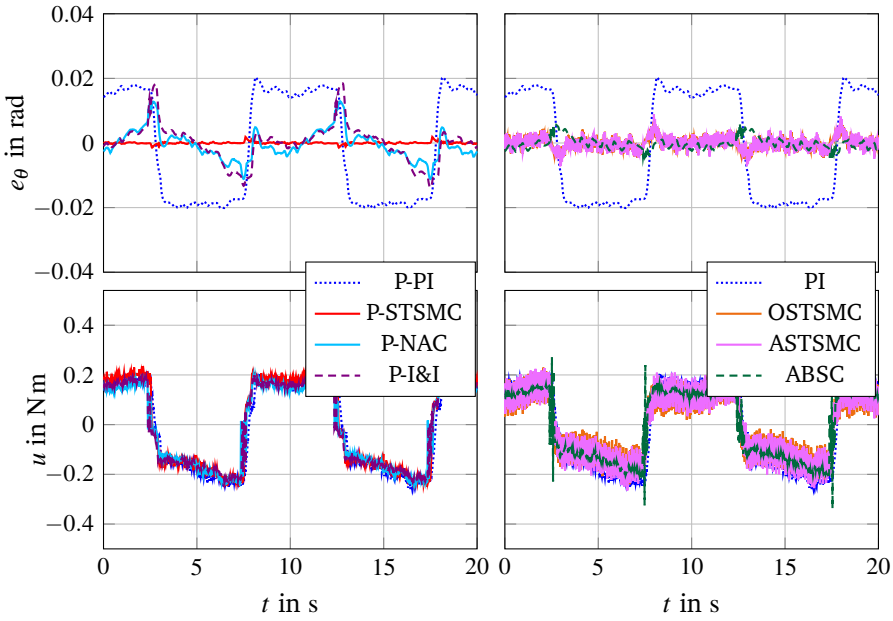

Figure 5.12: Positioning errors (top) and torque commands (bottom) for Test 7.

Comparing the adaptive schemes shows that faster reference signals that provide richer excitation to the system facilitate faster and more accuracte friction estimation and compensation. This can be seen in Figure 5.14, which shows the estimation of the motor Coulomb friction by all three adaptive controllers. Although in all cases the parameter estimation error $\tilde{T}_{C,m}$ is bounded, it approaches zero mostly during the tests at 2 Hz. Moreover, the ABSC provides less accurate estimate of $T_{C,m}$

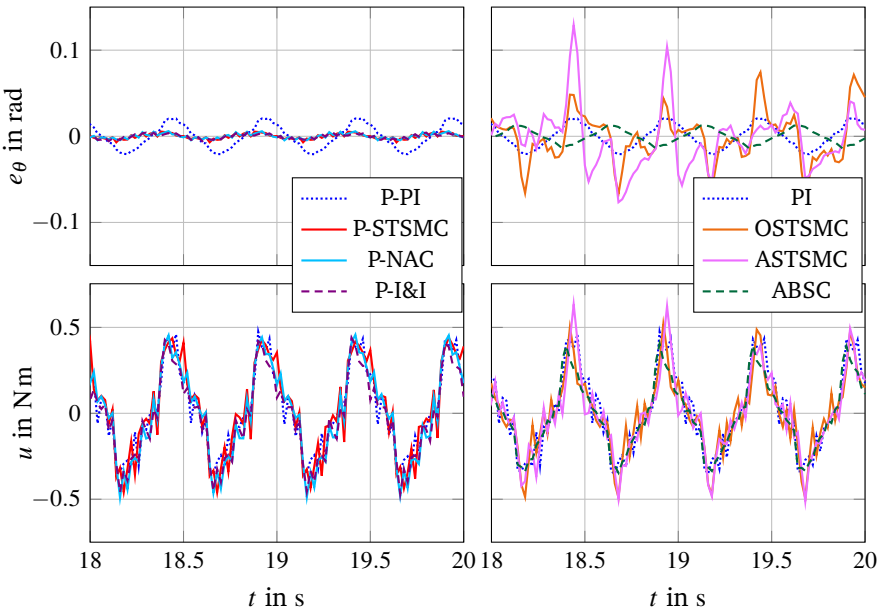

Figure 5.13: Positioning errors (top) and torque commands (bottom) for Test 9.

due to larger number of parameters (i.e. persistence of excitation conditions are more difficult to satisfy). However, the joint estimation of the uncertain gain b in ABSC and its inverse ρ results in a product $\hat{\rho}\hat{b} \approx 1$, as shown in Figure 5.15. This is important for achieving the virtual control inputs tracking but does not guarantee convergence of $\hat{\rho}, \hat{b}$ to their real values. In fact, deviations of these estimates from ρ and b affect the estimation quality of the parameter vector $\boldsymbol{\vartheta}$, as it can be seen from the adaptive laws (5.37).

A comparative visualization of the controllers performance is provided in Figures 5.16 and 5.17. The $\theta_x - \theta_y$ trajectories are plotted for the largest "realistic" friction value, for the cascaded position-velocity and the direct position controllers, respectively.

Lastly, Table 5.8 provides an overview of the controllers' design and implementation complexity by listing the tunable parameters and the signals required for each controller. As expected, since the adaptive controllers rely on exact cancellation of the degrading perturbation rather than dominating over it, they require more detailed description of the disturbance and, hence, a larger number of parameters to estimate. This results to more complicated algorithms and larger sets of tunable parameters. An overall ranking of all the controllers considered in this study, with respect to both their positioning performance and their complexity, is presented in

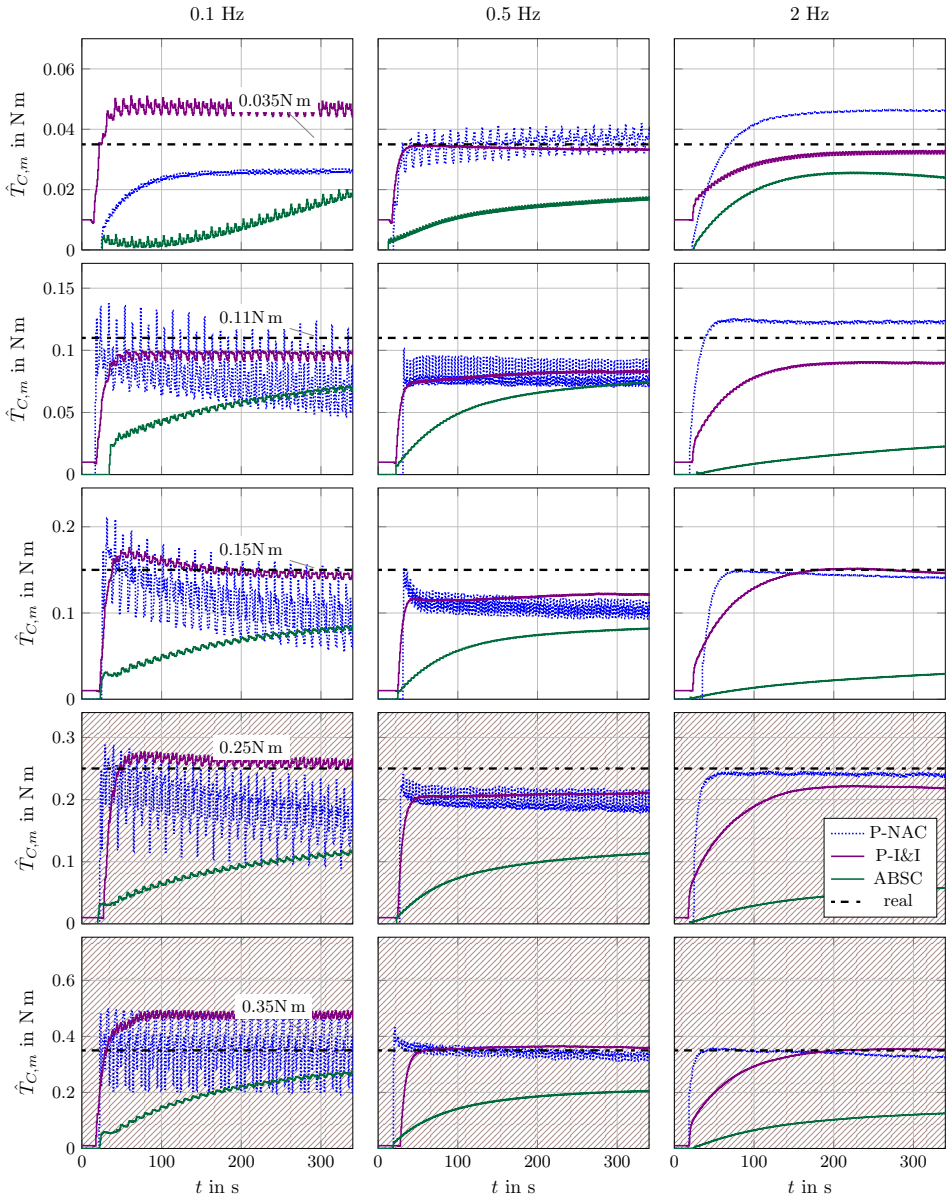

Figure 5.14: Motor Coulomb friction estimation during all NAC, I&I-AC and ABSC tests. The different cases of friction start with nominal friction and increase from top to bottom. The plots in the stripped area correspond to the extreme friction cases.

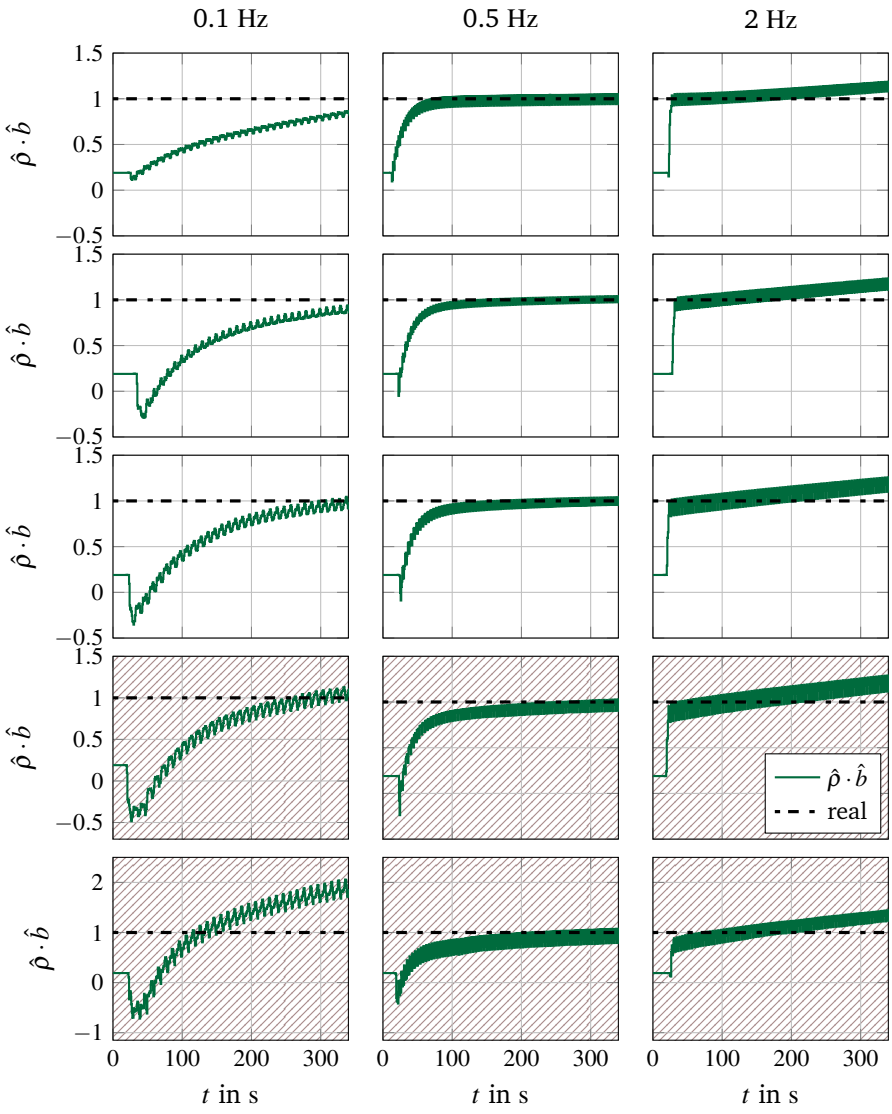

Figure 5.15: Product of the uncertain input gain estimation $\hat{b}$ and its inverse $\hat{\rho}$ in ABSC during all tests.

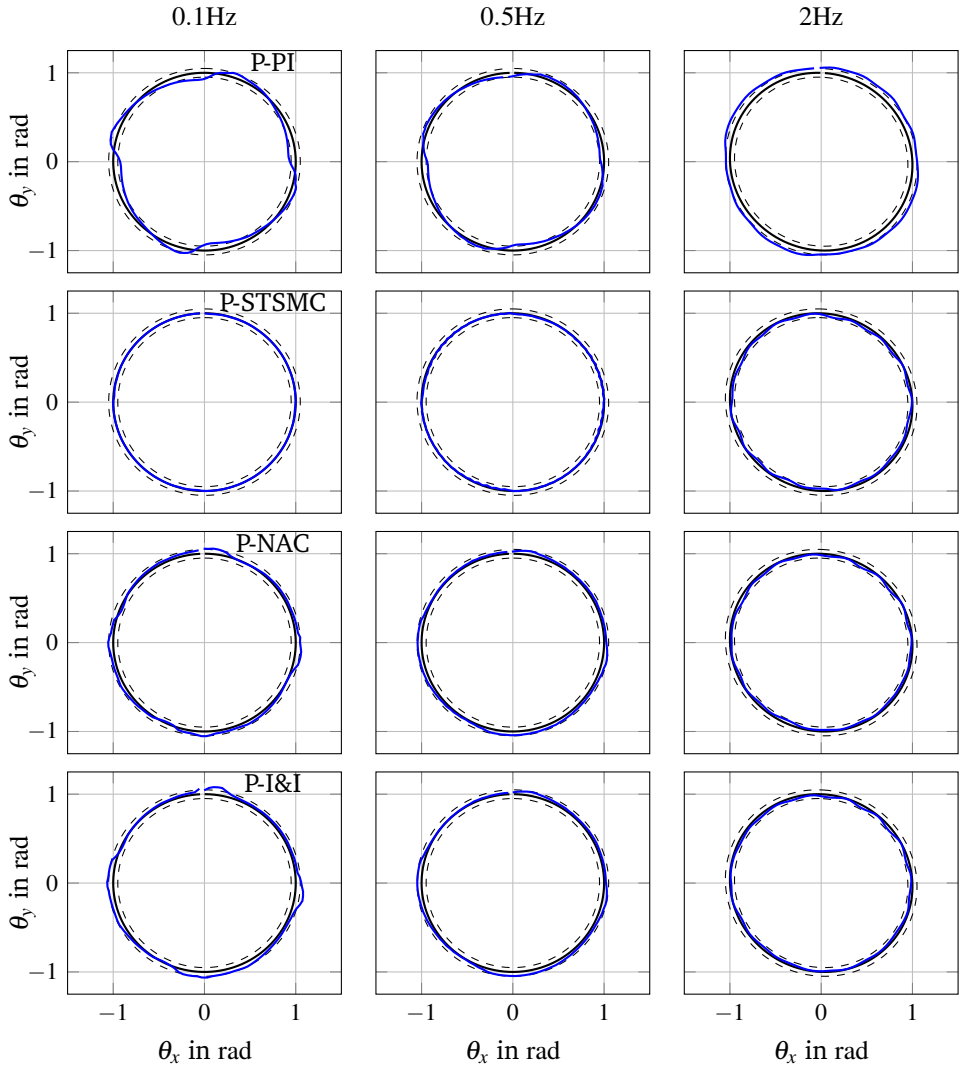

Figure 5.16: $\theta_x - \theta_y$ plot for one cycle during Tests 7 (left column), 8 (middle column) and 9 (right column) for the cascaded position-velocity controllers. The dashed circles correspond to the $\pm 10^{-2}\mathrm{rad}$ accuracy limit introduced in Problem 1. For increased clarity, both the error and the accuracy limits have been enlarged by a factor of 5.

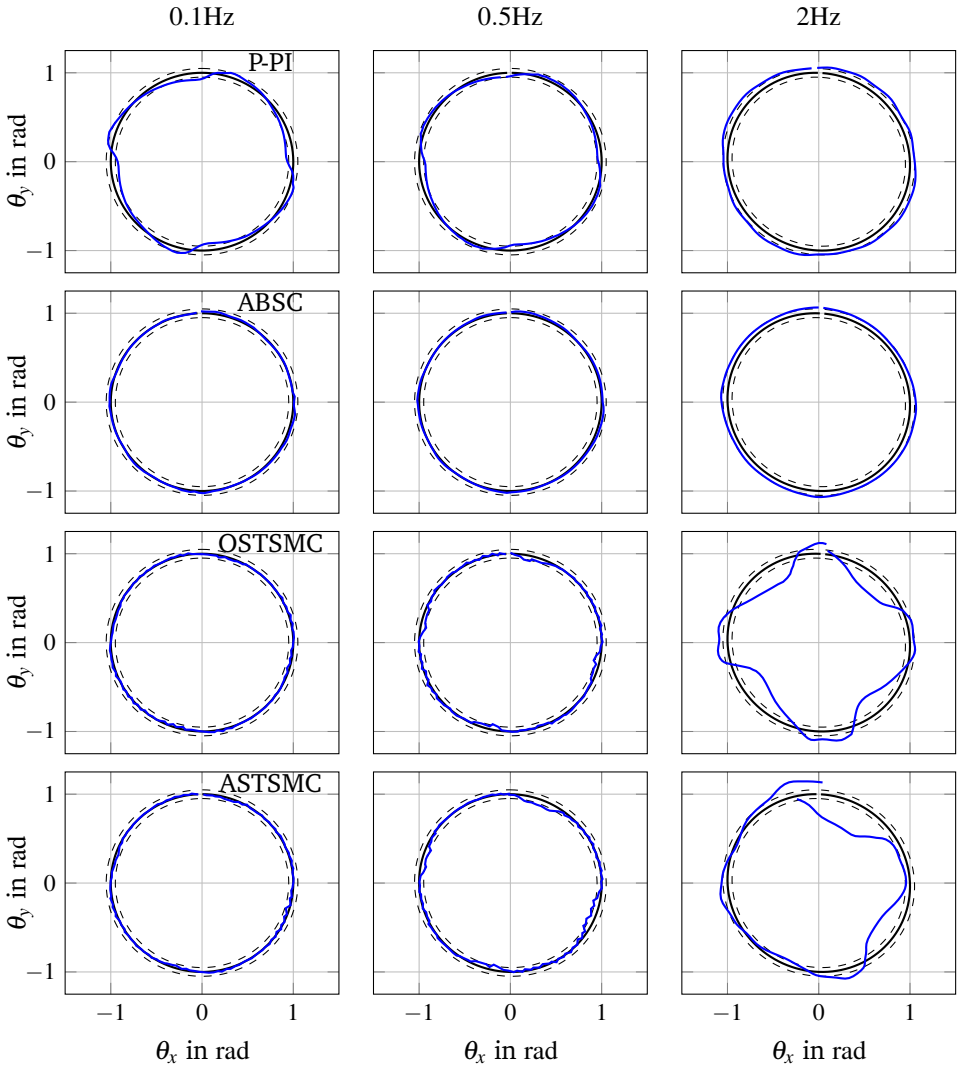

Figure 5.17: $\theta_x - \theta_y$ plot for one cycle during Tests 7 (left column), 8 (middle column) and 9 (right column) for the direct position controllers (including the P-PI scheme for comparison). The dashed circles correspond to the $\pm 10^{-2}\mathrm{rad}$ accuracy limit introduced in Problem 1. For increased clarity, both the error and the accuracy limits have been enlarged by a factor of 5.

Figure 5.18.

Table 5.8: Number of tunable parameters and signals required for each controller.

	Tunable	Total	Signals	Total	CI
P-PI	k_{pos}, k_p, T_n	3	$\theta_r, \dot{\theta}_r, \theta_l, \omega_m$	4	7
P-STSMC	k_{pos}, k_1, k_2	3	$\theta_r, \dot{\theta}_r, \ddot{\theta}_r, \theta_l, \omega_m, \omega_l$	6	9
P-NAC	$k_{pos}, k, \boldsymbol{\Gamma}, \hat{\boldsymbol{\vartheta}}_{\mathbf{0}}$	12	$\theta_r, \dot{\theta}_r, \ddot{\theta}_r, \boldsymbol{x}$	7	19
P-I&I-AC	$k_{pos}, k_{II}, \boldsymbol{\Gamma_{II}}, \hat{\boldsymbol{\vartheta}}_{\mathbf{0}}$	10	$\theta_r, \dot{\theta}_r, \ddot{\theta}_r, \theta_l, \omega_m, \omega_l$	6	16
ABSC	$c, k_1, k_2, \boldsymbol{\Gamma}, \gamma_1, \gamma_2, \hat{\boldsymbol{\vartheta}}_{\mathbf{0}}, \hat{\rho}_0, \hat{b}_0$	19	$\theta_r, \dot{\theta}_r, \ddot{\theta}_r, \theta_r^{(3)} \boldsymbol{x}$	8	27
OSTSMC	$c_1, c_2, \lambda_1, \lambda_2, k_{obs}$	5	$\theta_r, \dot{\theta}_r, \ddot{\theta}_r, \theta_r^{(3)}, \theta_l, \omega_l$	6	11
ASTSMC	$c_1, c_2, \lambda_{1,0}, \gamma_\lambda, a, \varepsilon_\theta, \nu, T_s, k_{obs}$	9	$\theta_r, \dot{\theta}_r, \ddot{\theta}_r, \theta_r^{(3)}, \theta_l, \omega_l$	6	15

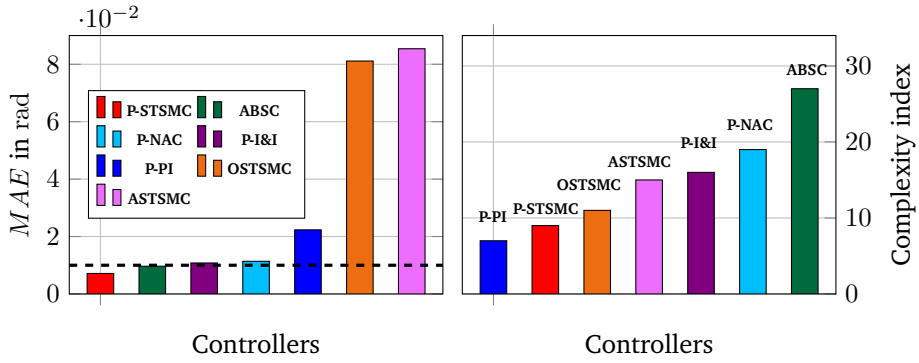

Figure 5.18: (Left): Average MAE over all tests for all controllers. The dashed line corresponds to the $\pm 10^{-2}$rad accuracy bound. (Right): Complexity index as the sum of tunable parameters and required signals for each controller.

5.5 Additional Control Designs

Two nonlinear controllers, namely the Nested Continuous Singular Terminal Sliding-Mode Controller (NCSTSMC) and the State-Feedback $\mathcal{L}_1$ adaptive controller (SFL_1), were designed, implemented and tested on the experimental setup and their performance was evaluated to be inadequate for the single-axis positioning problem. This Section presents these designs and discusses the challenges in their implementation that led to poor performance of the controllers.

5.5.1 Nested Continuous Singular Terminal Sliding-Mode Controller

The NCSTSMC [79, 80] is a fourth-order SMC for direct load positioning. Following similar analysis to the previous higher-order sliding-mode controllers, the sliding variable is selected as a vector that contains the load position error and its first and second derivatives, i.e. if $z_1 \triangleq \theta_l - \theta_r$, then

$$\boldsymbol{z} = \begin{bmatrix} z_1 & z_2 & z_3 \end{bmatrix}^T \triangleq \begin{bmatrix} z_1 & \dot{z}_1 & \ddot{z}_1 \end{bmatrix}^T$$

and the sliding manifold is defined as $\mathcal{S} \triangleq \left\{ \boldsymbol{z} \in \mathbb{R}^3 | \boldsymbol{z} = \boldsymbol{0} \right\}$. The dynamics of $\boldsymbol{z}$ is written as:

$$\dot{z}_1 = \omega_l - \dot{\theta}_r = z_2 \tag{5.50a}$$

$$\dot{z}_2 = \frac{1}{J_l}\left[K_S\left(\frac{1}{N}\theta_m - \theta_l\right) + D_S\left(\frac{1}{N}\omega_m - \omega_l\right) - T_{F,l}\right] - \ddot{\theta}_r = z_3 \tag{5.50b}$$

$$\begin{aligned}\dot{z}_3 &= \frac{1}{J_l}\frac{d}{dt}\left[K_S\left(\frac{1}{N}\theta_m - \theta_l\right) + D_S\left(\frac{1}{N}\omega_m - \omega_l\right) - \dot{T}_{F,l}\right] - \theta_r^{(3)} = \\ &= \psi(t, \boldsymbol{x}) + \frac{D_S}{J_m J_l N}u\end{aligned} \tag{5.50c}$$

where

$$\begin{aligned}\psi(t, \boldsymbol{x}) \triangleq \frac{K_S}{J_l}\left(\frac{1}{N}\omega_m - \omega_l\right) - \frac{D_S}{J_l}\left(\frac{1}{J_m N^2} + 1\right)T_l - \frac{D_S}{J_l}\left(\frac{1}{J_m N}T_{F,m} - \frac{1}{J_l}T_{F,l}\right) \\ - \frac{1}{J_l}\dot{T}_{F,l} - \theta_r^{(3)}\,.\end{aligned} \tag{5.51}$$

The NCSTSMC algorithm is given by [80]:

$$u = -\frac{J_m J_l N}{D_S}\left(k_1|\mu|^{\frac{1}{2}}\text{sgn}(\mu) + k_4 v\right) \tag{5.52a}$$

$$\dot{v} = \text{sgn}(\mu) \tag{5.52b}$$

$$\mu = z_3 + k_3\left(|z_1|^3 + |z_2|^4\right)^{\frac{1}{6}}\text{sgn}\left(z_2 + k_2|z_1|^{\frac{3}{4}}\text{sgn}(z_1)\right) \tag{5.52c}$$

For appropriate positive gains k_1, k_2, k_3, k_4 and if Assumption 5.3.2 holds, the NCSTSMC leads the system to the sliding manifold $\mathcal{S}$ in finite time, ensuring robust tool position tracking for the drive-train system.

The main challenge in this method is the lack of an algorithm for systematic tuning of the 4 controller gains. Although extensive trial-and-error tuning efforts were made, there could not be obtained a quadruplet (k_1, k_2, k_3, k_4) such that the resulting NCSTSMC law would provide performance comparable to the P-PI cascade. Another challenge in the application of the NCSTSMC is the use of $z_3 = \dot{z}_2$ on the control law. Since $\dot{z}_2$ cannot be analytically computed (it contains the unknown friction $T_{F,l}$), its estimate obtained by a differentiator has to be used

instead. This also contributes to lack of accuracy in the algorithm and introduces also the selection of the differentiator gains, making, thus, the tuning procedure even more challenging. Figure 5.19 shows the time response of the load position and

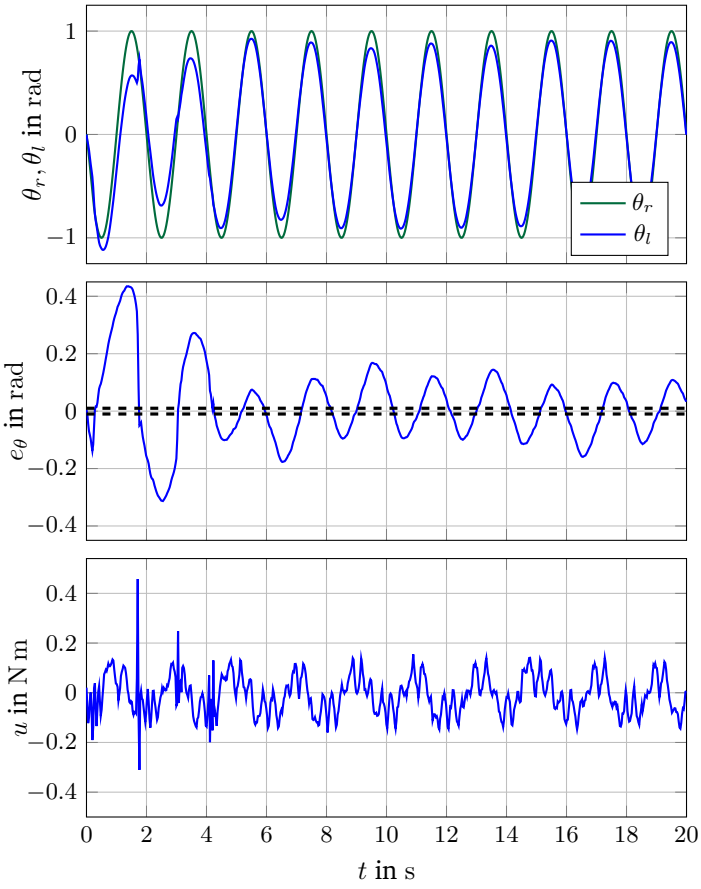

Figure 5.19: Reference and actual load position (top), positioning error (middle) and torque command (bottom) for NCSTSMC during Test 2. The dashed lines correspond to the $\pm 10^{-2}\mathrm{rad}$ accuracy bounds.

the associated positioning error and torque command for the NCSTSMC during Test 2. Even in the nominal case and at slow motion profile the controller fails to position the load with the required accuracy. The corresponding MAE is more than 20 times larger than the accuracy limit. This is better visualized in Figure 5.20, where the $\theta_x - \theta_y$ plot of the NCSTSMC is compared to that of the P-PI cascade.

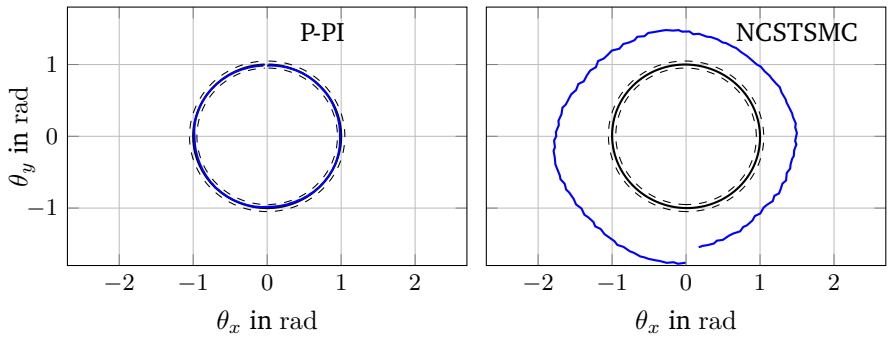

Figure 5.20: $\theta_x - \theta_y$ plot for one cycle during Test 2 (nominal friction at 0.5 Hz) for the NCSTSMC in comparison to the P-PI scheme.

5.5.2 State-Feedback $\mathcal{L}_1$ Adaptive Controller

The cascaded architecture of the SFL_1 used for the load positioning is illustrated in Figure 5.21. The reference signal for the velocity SFL_1 is provided by the outer loop P controller.

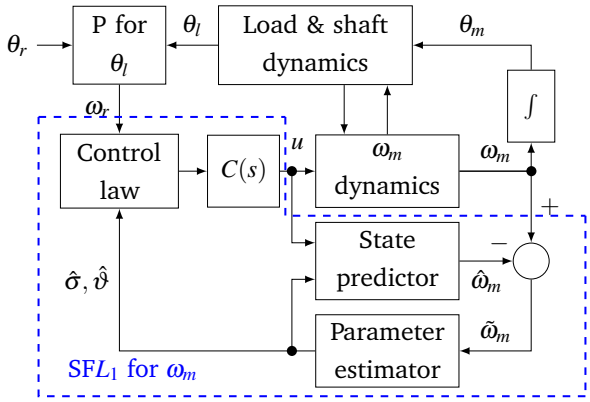

Figure 5.21: Load position control using a cascade of a P controller and a SFL_1 adaptive velocity controller.

The motor velocity model is re-parametrized in a form where all the unknown quantities in the system, i.e. model uncertainties, unmeasured disturbances etc., can be expressed based on parameters that need be estimated. Specifically, the dynamics

of the motor angular velocity can be written according to (4.18a) as

$$\dot{\omega}_m = \frac{1}{J_m}u - \frac{1}{J_m}\left(T_{F,m} + \frac{1}{N}T_l\right) = -k\omega_m + \underbrace{\frac{1}{J_m}}_{b}\left(u + \underbrace{k\omega_m - T_{F,m} - \frac{1}{N}T_l}_{n(t,\boldsymbol{\chi},\omega_m)}\right) =$$

$$= -k\omega_m + b\left[u + n(t,\boldsymbol{\chi},\omega_m)\right] \ , \tag{5.53}$$

where $k > 0$ represents the desired dynamics of the motor angular velocity and $n(t,\boldsymbol{\chi},\omega_m)$ represents the lumped disturbing torques. The vector $\boldsymbol{\chi}$ represents the state variables corresponding to the dynamics of the lumped nonlinearities n, except for ω_m. A natural choice is the position difference $\Delta\theta \triangleq \left(\frac{1}{N}\theta_m - \theta_l\right)$ and the load velocity ω_l. The following assumptions are made [99]:

Assumption 5.5.1. ***(Uniform boundedness of $n(t,\boldsymbol{\chi},0)$)***

$$\exists \Phi > 0 \text{ with } \Phi < \infty \text{ such that } |n(t,\boldsymbol{\chi},0)| \leq \Phi \ , \ \forall t \geq 0 \ .$$

Assumption 5.5.1 is valid since whenever the motor is not moving ($\omega_m \equiv 0$), the rest of the states, and by extension $T_l, T_{F,m}$, are bounded.

Assumption 5.5.2. ***(Stability of unmodelled dynamics)***
The $\boldsymbol{\chi}$-dynamics are Bounded Input-Bounded Output (BIBO) stable with respect to initial conditions $\boldsymbol{\chi_0}$ and input ω_m, i.e.

$$\exists L_1, L_2 > 0 \text{ with } L_1, L_2 < \infty \text{ such that}$$
$$\|\boldsymbol{\chi}(t)\|_{\mathcal{L}_\infty} \leq L_1 |\omega_m(t)|_{\mathcal{L}_\infty} + L_2 \ , \ \forall t \geq 0 \ .$$

Assumption 5.5.2 is valid, since the components of $\boldsymbol{\chi}$, i.e. $\Delta\theta, \omega_l$ are bounded for bounded motor angular velocity. This comes from the BIBO stability of $\boldsymbol{\chi}$ with respect to the input ω_m (see Appendix VI for the proof).

Assumption 5.5.3. ***(Semiglobal uniform boundedness of partial derivatives)***
Let $\boldsymbol{X} \triangleq \begin{bmatrix}\omega_m & \boldsymbol{\chi}^T\end{bmatrix}^T$. For arbitrary $\zeta > 0$, $\exists d_{n_{\boldsymbol{X}}}(\zeta), d_{n_t}(\zeta) > 0$ independent of time, such that $\forall \|\boldsymbol{X}\|_\infty < \zeta$ the partial derivatives of $n(t,\boldsymbol{X})$ are piecewise-

continuous and bounded,

$$\left\| \frac{\partial n}{\partial \boldsymbol{X}} \right\|_1 \leq d_{n_{\boldsymbol{x}}}(\zeta), \quad \left| \frac{\partial n}{\partial t} \right| \leq d_{n_t}(\zeta) \; .$$

Since $T_{F,m}$ has no internal dynamics, n does not depend explicitly on t. Hence, Assumption 5.5.3 corresponds to the standard Lipschitz continuity condition for the lumped disturbances introduced in the previous control designs.

If these three assumptions hold, it is shown in [99, Lemma A.1.9] that $n(\boldsymbol{\chi}, \omega_m)$ can be expressed as

$$n(\boldsymbol{\chi}, \omega_m) = \vartheta(t)|\omega_m|_{\mathcal{L}_\infty} + \sigma(t) \; , \tag{5.54}$$

where $|\omega_m|_{\mathcal{L}_\infty}$ is the $\mathcal{L}_\infty$-norm of ω_m and the functions $\vartheta(t), \sigma(t)$ have piecewise continuous derivatives. It should be noted that the unknown parameters need not have any first-principle interpretation, contrarily to the case of the adaptive techniques discussed in Sections 5.3.1 and 5.3.2. On the basis of (5.54), the dynamics of ω_m can be written as

$$\dot{\omega}_m = -k\omega_m + b(u + \vartheta|\omega_m|_{\mathcal{L}_\infty} + \sigma) \; , \tag{5.55}$$

where the time-dependency notation is dropped for brevity. If there can be found accurate estimates $\hat{\vartheta}, \hat{\sigma}$ for these two parameters, then a control law of the form

$$u = -\hat{\vartheta}|\omega_m|_{\mathcal{L}_\infty} - \hat{\sigma} + \frac{1}{b}(k\omega_r + \dot{\omega}_r) \tag{5.56}$$

will ensure asymptotic tracking of the angular velocity reference signal ω_r and, by extension, (for correct tuning of the position P controller) tracking of the load position reference. To this end, a state predictor is designed based on the re-parametrized system. Its dynamics is given by [99]:

$$\dot{\hat{\omega}}_m = -k\hat{\omega}_m + b(u + \hat{\vartheta}|\omega_m|_{\mathcal{L}_\infty} + \hat{\sigma}), \;\; \hat{\omega}_m(0) = 0 \; . \tag{5.57}$$

The following step concerns the design of the adaptive laws for $\hat{\vartheta}$ and σ based on the discrepancy between real and predicted state. The update laws are given by [99]:

$$\dot{\hat{\vartheta}} = \gamma \text{Proj}(\hat{\vartheta}, \tilde{\omega}_m P b|\omega_m|_{\mathcal{L}_\infty}), \;\; \hat{\vartheta}(0) = \hat{\vartheta}_0 \tag{5.58}$$

$$\dot{\hat{\sigma}} = \gamma \text{Proj}(\hat{\sigma}, \tilde{\omega}_m P b), \;\; \hat{\sigma}(0) = \hat{\sigma}_0 \; , \tag{5.59}$$

where γ is a positive real constant, $P > 0$ is the solution to the scalar Lyapunov equation $2kP = Q, Q > 0$ and the projection operator $\text{Proj}(\cdot, \cdot)$ (see (II.6)) is used to ensure that the parameter estimates remain within a compact set $\mathcal{D} \subset \mathbb{R}^2$. Since parameters ϑ and σ are not in general constant, γ must be chosen large enough

to ensure fast adaptation. In order to avoid high frequency content due to fast adaptation entering the closed-loop dynamics, the control signal in (5.56) is low-pass filtered by a strictly proper and stable filter $C(s)$. Once the parameters have been estimated, they can be used in a (5.56) to cancel all the unknown or unwanted signals in the system within the bandwidth of $C(s)$.

The selection of $C(s)$ should be such that, $C(s)$ is a strictly proper and stable transfer function with $C(0) = 1$. Moreover, it must satisfy the $\mathcal{L}_1$ condition [99, (2.216), p. 96]

$$|G(s)|_{\mathcal{L}_1} < \frac{\rho_r - |k_g C(s)H(s)|_{\mathcal{L}_1}|\omega_r|_{\mathcal{L}_\infty} - \rho_{in}}{L_{\rho_r}\rho_r + \Phi} \tag{5.60}$$

with:

$$H(s) \triangleq \frac{b}{s+k}\ ,\ G(s) \triangleq H(s)(1 - C(s))$$
$$k_g \triangleq \frac{k}{b}\ ,\ \rho_{in} \triangleq \frac{1}{s(s+k)}\rho_0\ ,$$

where ρ_0 is a bound for $\omega_m(0)$, $\rho_r > \rho_{in}$ is a bound for $|\omega_r|_{\mathcal{L}_\infty}$, Φ is defined in Assumption (5.5.1) and L_{ρ_r} is defined as [101]

$$L_{\rho_r} = \frac{\max\{\rho_r + \gamma_1, L_1(\rho_r + \gamma_1) + L_2\}}{\rho_r} d_{f_x}(\rho_r),\ \gamma_1 > 0\ .$$

The complete control law is given by

$$u_C(s) = C(s)u(s)\ , \tag{5.61}$$

where $u(s)$ is the Laplace transform of u defined in (5.56).

Remark 5.1. In general, it might be difficult to accurately calculate $|\omega_m|_{\mathcal{L}_\infty}$ in (5.56). For this reason a conservative bound Ω for ω_m is used instead.

Remark 5.2. The selection of k (reference dynamics) and the design of the filter can be challenging in general and may require several iterations in selecting both the order and the coefficients of $C(s)$. Many of the constants in (5.60) can not be known in advance and are, therefore, conservatively chosen. If a conservative global bound L for $\left\| \frac{\partial n}{\partial \boldsymbol{X}} \right\|$ can be estimated, then inequality (5.60) can be replaced by the standard $\mathcal{L}_1$ condition

$$|G(s)|_{\mathcal{L}_1} L < 1\ . \tag{5.62}$$

L corresponds to a global Lipschitz constant and gives an estimate of the how large $\dot{n}$ can become. From the definition of $n(\boldsymbol{\chi})$ in (5.53) it can be seen that $\dot{T}_{F,m}$ is the most dominant component of $\dot{n}$ because of the sgn$(\cdot)$ function in the friction

model. The approximation in (5.12) suggests that $L \propto p$. The choice of L can also be related to the parameter bounds used in the projection as in [99]:

$$L \approxeq \max_{\boldsymbol{\delta} \in \mathcal{D}} \|\boldsymbol{\delta}\|_1 \ , \tag{5.63}$$

where $\boldsymbol{\delta} \triangleq \begin{bmatrix} \vartheta & \sigma \end{bmatrix}^T$.

Remark 5.3. The dynamics of the reference system given by k are chosen simultaneously with the design of $C(s)$. The resulting transfer function of the reference system should be stable and proper and have dc-gain equal to 1. It should be noted that in general fast reference dynamics require an even faster control input filter. This highlights the trade-off between approaching the reference dynamics specified for each tracking problem and having a wide parameter space over which the $C(s)$ coefficients can be chosen.

Remark 5.4. Concerning the selection of the adaptation gain γ, it is noted in [99, Th. 4.1.1] that the tracking error is uniformly bounded by a constant inverse proportional to $\frac{1}{\sqrt{\gamma}}$. This implies that the larger the gain is the smaller the tracking error becomes, especially in the transient performance.

Remark 5.5. The derivative of the velocity reference ω_r needed for the implementation of the control law in (5.56) is calculated from Equation (5.9).

Figure 5.22 illustrates the design of $C(s)$ as a first-order lowpass filter

$$C(s) = \frac{\omega_C}{s + \omega_C}$$

for reference dynamics $k = 1$ and a conservative estimate for $L = 250$. For $\omega_C \geq 483.8 \ \mathrm{rad\,s^{-1}}$ condition (5.62) holds true. However, ω_C can be selected larger than this value (e.g. at $800 \ \mathrm{rad\,s^{-1}}$) to improve the performance of the closed-loop system.

Figure 5.23 shows the load positioning error and the corresponding torque command of the P-SFL_1 cascade for the cases of nominal and highest friction in all three frequency modes. As it can be seen from the top plots, the controller fails in keeping the prescribed tolerances even for the nominal operation at the lowest frequency. In the worst case (largest friction value at 2 Hz) the MAE approaches a value almost 17 times larger than the required accuracy limit. Moreover, the torque command shows increased chatter, which directly relates to the poor parameter estimation.

Similar conclusions can be drawn from the $\theta_x - \theta_y$ plot of the P-SFL_1, which is illustrated in Figure 5.24. Compared to the equivalent P-PI plot, it shows clear

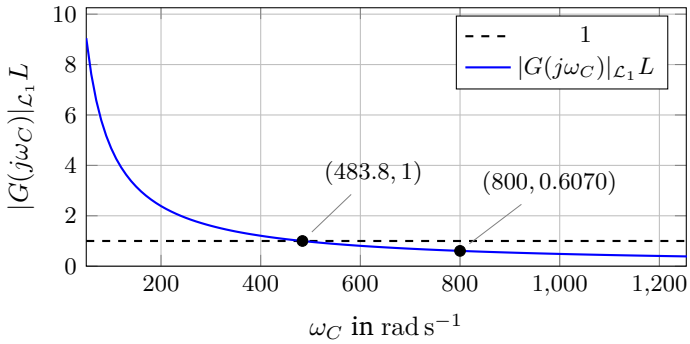

Figure 5.22: Evaluation of $|G(j\omega_C)|_{\mathcal{L}_1} L$ for $k = 1$, $L = 250$ and different values of ω_C.

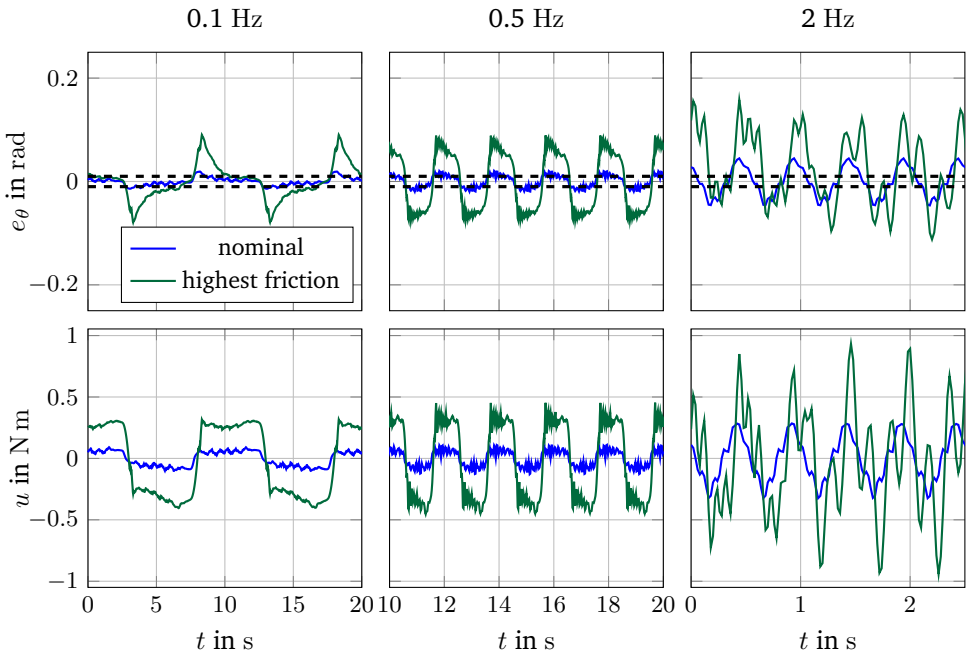

Figure 5.23: Positioning error (top) and torque command (bottom) for SFL_1 during Tests 1,2,3,13,14,15. The dashed lines correspond to the $\pm 10^{-2}$rad accuracy bounds.

degradation of the P-SFL_1 scheme, especially for fast reference signals. One of the reasons for which the SFL_1 controller performs poorly is the fact that the reference dynamics are not fast enough compared to the velocity reference signal ω_r, which is the output of the P controller. An increase of the velocity reference system pole k leads to a cut-off frequency for $C(S)$, much larger than 1500 $\mathrm{rad\,s^{-1}}$. This, in turn, compromises the decoupling between the parameter adaptation and the control of the motor velocity and, consequently, allows high-frequency content to enter the control signal, which can be damaging for the actuator.

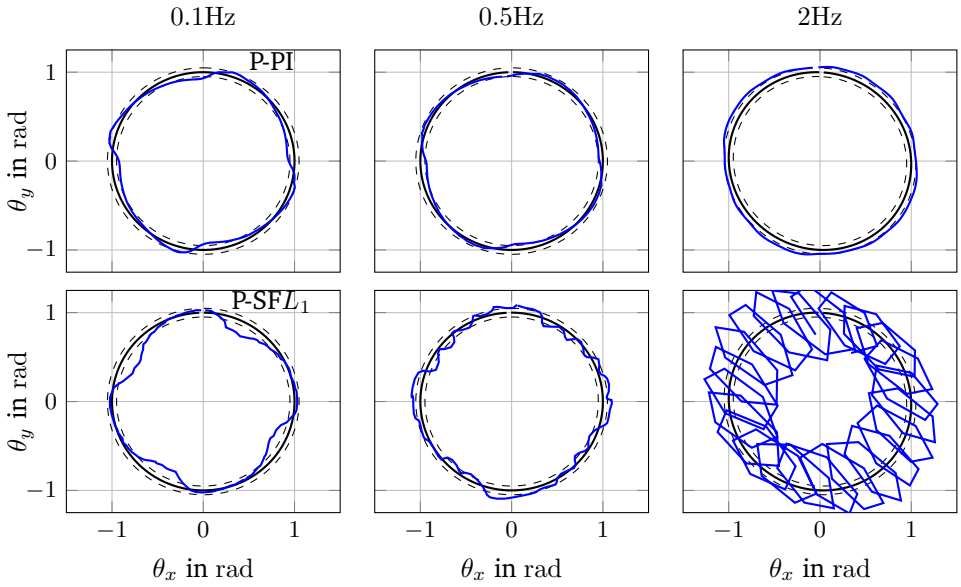

Figure 5.24: $\theta_x - \theta_y$ plot for one cycle during Tests 7 (left column), 8 (middle column) and 9 (right column) for the P-SFL_1 in comparison to the P-PI scheme.

5.6 Conclusions

The design of several nonlinear controllers for the positioning of a machine tool axis was presented in this chapter. Eight advanced control strategies employing two different architectures were analysed and compared with respect to their positioning accuracy and their robustness against unknown and increasing friction. The experimental results showed that four of the nonlinear controllers clearly performed better than the standard P-PI solution, providing better accuracy and resilience to degrading frictional torques.

The design complexity and tuning challenges of the control algorithms were also discussed in connection to the inadequate accuracy levels of some of the control methods. A possible extension of this work could include the development of systematic tuning procedures for all the controllers, related to the performance requirements, the expected level of degradation (e.g. bounds for friction) and the reference profile.

Chapter 6

Backlash Estimation

6.1 Introduction

This chapter discusses the problem of backlash estimation in machine tool systems. Developing clearances due to wear in the mechanical coupling components of machine tools have a direct degrading effect on the positioning accuracy of the machine axes. Backlash compensation algorithms can alleviate such degradations, provided that clearance sizes are accurately estimated. Knowledge of the deadzone width also provides an indication of the wear level in the coupling mechanisms and can facilitate more efficient condition-based maintenance.

The chapter starts with the formulation of the main objective as the estimation of the deadzone angle in the coupling mechanism between drive-motor and load. A variable-stiffness model is employed for the description of the backlash phenomenon and the deadzone estimator algorithm is presented. Simulation and experimental results are discussed in relation to the method efficiency and robustness. The design methodologies and the application results are detailed in a peer-review conference paper and a submitted journal article, which are included in this report as Papers D and C, respectively.

6.2 Backlash Modelling and Problem Formulation

Considering the single-axis system abstraction of a machine tool feed axis shown in Figure 4.1, backlash occurs during sudden loss and recovery of engagement between the drive motor and the load. This phenomenon can be effectively described by adding a deadband to the interconnecting torque T_l defined in Equation (4.12).

The resulting *deadzone torque* [45] is given by:

$$T_l^{DZ} = \begin{cases} K_S(\Delta\theta + \delta_1) + D_S\Delta\omega & , \ \Delta\theta < -\delta_1 \\ K_S(\Delta\theta + \delta_1 - \delta) + D_S\Delta\omega & , \ \Delta\theta > \delta - \delta_1 \\ 0 & , \ -\delta_1 \leq \Delta\theta \leq \delta - \delta_1 \ , \end{cases} \tag{6.1}$$

where δ is the width of the deadzone in rad, $0 \leq \delta_1 \leq \delta$ is the initial motor-load position offset as shown in Figure 6.1, and the position and velocity difference between motor and load are respectively defined as:

$$\Delta\theta \triangleq \frac{1}{N}\theta_m - \theta_l \tag{6.2a}$$

$$\Delta\omega \triangleq \frac{1}{N}\omega_m - \omega_l \tag{6.2b}$$

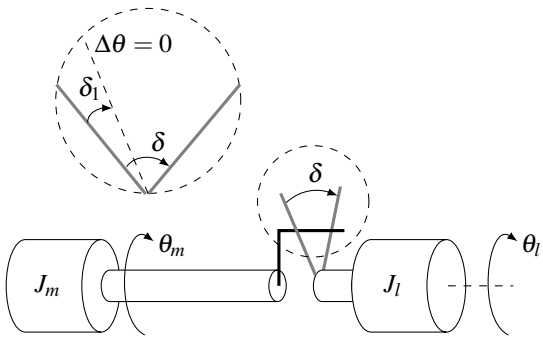

Figure 6.1: Backlash illustration: The straight dashed line in the circle denotes the relative configuration between the motor and the load rotors, which is taken as zero position difference. When the difference between the motor and the load position is larger than $-\delta_1$ or smaller than $\delta - \delta_1$, the two shafts are disengaged and no torque is applied to the motor or the load.

Although the deadzone model is simpler and more intuitive than various dynamical backlash descriptions proposed in the literature (see for example [48, 49], where backlash is described as the impact torque during engagement between two inertias), its discontinuous nature introduces many numerical difficulties that make its application to control and estimation problems challenging.

The backlash description proposed in this study constitutes a smooth version of the deadzone model by introducing a time-varying shaft stiffness approach to describe the loss and recovery of engagement between drive motor and load. Disengagement between the two inertias corresponds to zero shaft stiffness, whereas when the motor engages the load, the interconnecting shaft stiffness assumes its nominal value K_S. Thus, the stiffness changes between these two extreme values in

a fast but smooth way. The proposed model is given by

$$K_{BL} \triangleq \frac{K_S}{\pi}\left[\pi + \arctan(\alpha(\Delta\theta - \delta + \delta_1)) - \arctan(\alpha(\Delta\theta + \delta_1))\right] \tag{6.3}$$

$$T_l(\boldsymbol{x}, \delta) \triangleq \left[\Delta\theta + \delta_1 - \frac{\delta}{2}\cdot(1 + \operatorname{sgn}(\Delta\theta)) + \frac{D_S}{K_S}\Delta\omega\right]\cdot K_{BL}(\Delta\theta, \delta)\ , \tag{6.4}$$

where

$$\boldsymbol{x} \triangleq \begin{bmatrix}\omega_m & \theta_m & \omega_l & \theta_l\end{bmatrix}^T$$

is the state vector of the single-axis system containing velocities and positions. The constant α is a large positive real number that parametrizes how steep the change in the stiffness is. The larger its value, the closer the proposed model is to the deadzone description. For $\alpha \to \infty$, it is clear that $T_l \to T_l^{DZ}$. This is also illustrated in Figure 6.2, where the stiffness $K_{BL}(\Delta\theta, \delta)$ and the corresponding backlash torques are plotted for different values of the parameter α.

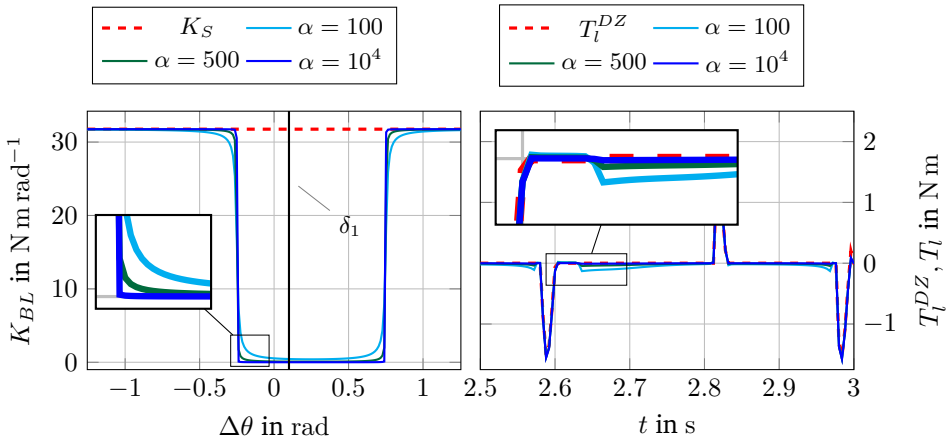

Figure 6.2: (Left) Shaft stiffness varying between two values. The larger the value of α, the steeper the change in the stiffness is. (Right) Backlash torque for a sinusoidal motion profile using the deadzone model (red dotted curve) and the varying-stiffness model (solid lines) for different values of α.

Comparing Equations (6.1) and (6.4), shows that in the proposed backlash model the stiffness is factorized from both the restoring (spring) and the damping components of the interconnecting torque. If the lubrication material in the coupling mechanism between motor and load provides damping comparable to (or larger than) the shaft damping D_S, then the term $\frac{D_S}{K_S}\Delta\omega$ in (6.4) can be replaced by the standard damping torque component $D_S\Delta\omega$ outside the brackets.

The deadzone angle estimation problem can now be formally stated as follows:

Problem 2 (Deadzone angle estimation)**.** *Given the single-axis drive-train system described in* (4.16)*,* (4.18a)-(4.18d) *and the backlash model in* (6.3)*,*(6.4)*, design an online dynamic estimator for the deadzone angle δ, such that the estimate $\hat{\delta}$ fulfils the following requirements:*

1. *Convergence to a compact set containing the real parameter value.*
2. *Maximum steady-state absolute estimation error less than* 10^{-2} rad.

The estimation accuracy requirement relates to the machining tolerances considered in the position control problem in Chapter 5.

6.3 Deadzone Angle Estimation

The problem of deadzone angle estimation belongs to the family of parameter estimation problems in nonlinearly parametrized systems. Several designs have been proposed in the literature [117, 118] to solve such problems, usually employing discontinuous adaptation laws for the estimators, such as the min-max algorithm [88] or imposing constraints on the nonlinear regressor functions with respect to their monotonicity [119] and convexity properties [120, 121].

The approach followed in this study is based on a method proposed in [122], where a generic adaptive parameter estimator was designed for systems with nonlinear smooth regressor function. The main idea in this approach was to estimate a perturbation in the system which depends on the unknown parameters and then use the adaptive estimator to invert the nonlinear mapping from the parameter vector to the perturbation. A joint perturbation-parameter estimator was proposed in [122]. Here, a modular approach is followed, i.e. the designs of the perturbation and parameter estimators are done separately, allowing for more flexibility.

By considering the single-axis system dynamics in Equations (4.18a)-(4.18d), it is easy to see that the perturbation that depends on the unknown deadzone angle is the acceleration coming from the backlash torque defined as:

$$\phi(\boldsymbol{x}, \delta) \triangleq \frac{1}{J_l} T_l(\boldsymbol{x}, \delta) \ . \tag{6.5}$$

Consequently, the method includes two steps:

1. Estimation of the perturbation ϕ.
2. Design of an adaptive estimator

$$\dot{\hat{\delta}} \triangleq \rho(\boldsymbol{x}, \hat{\phi}, \hat{\delta}) \tag{6.6}$$

that provides an estimate $\hat{\delta}$ for the deadzone angle based on the estimation $\hat{\phi}$ of ϕ.

Since ϕ affects both motor and load in the same way, i.e. as an additive perturbation in the acceleration and since all the states of the drive-train and the input torque T_m are measured, either of the velocity dynamics (motor or load) can be used for estimating ϕ.

6.3.1 Estimation of the Backlash Acceleration

The load velocity dynamics can be written in the form:

$$\dot{\omega}_l = -\frac{1}{J_l} T_{F,l} + \phi(\boldsymbol{x}, \delta) \ , \tag{6.7}$$

where ϕ was defined in Equation (6.5) and the unknown deadzone angle δ belongs to a compact set $\mathcal{D} = [0, \delta_{max}] \subset \mathbb{R}_{\geq 0}$, with δ_{max} being the largest considered deadzone angle.

A second order sliding-mode velocity observer is used for the estimation of the perturbation ϕ. In general, sliding-mode state observers are very robust with respect to disturbances and perturbing nonlinearities due to the high frequency injection signals used in their design [61, 123]. Their feature to reject disturbances in finite time is extensively exploited for indirect estimation of perturbations [79]. The observer used for the estimation of ϕ is called the *Super-Twisting Sliding-Mode Observer (STSMO)* and its design is given by:

$$\dot{\hat{\omega}}_l = -\frac{1}{J_l} T_{F,l} + v \tag{6.8}$$

with the high frequency injection signal v defined by [70]:

$$v = k_1 |\tilde{\omega}_l|^{\frac{1}{2}} \text{sgn}(\tilde{\omega}_l) + k_2 \int_0^t \text{sgn}(\tilde{\omega}_l(\tau)) d\tau \ , \tag{6.9}$$

where k_1, k_2 are positive gains and $\tilde{\omega}_l \triangleq \omega_l - \hat{\omega}_l$. If the friction is completely known and in absence of any additional disturbances, the velocity estimation error dynamics reads:

$$\dot{\tilde{\omega}}_l = \dot{\omega}_l - \dot{\hat{\omega}}_l = \phi(\boldsymbol{x}, \delta) - v \ , \tag{6.10}$$

where the arguments of T_l are omitted in favour of relaxing the notation. It is proven [73, 124] that if the positive gains k_1, k_2 are properly tuned, the velocity estimation error trajectories $\tilde{\omega}_l(t)$ reach the sliding manifold

$$\mathcal{S} \triangleq \left\{ \tilde{\omega}_l \in \mathbb{R} | \tilde{\omega}_l = \dot{\tilde{\omega}}_l = 0 \right\} \tag{6.11}$$

in some finite time t_{SM} and remain there for all future times. Substituting (6.13) in (6.10) and setting $\tilde{\omega}_l = \dot{\tilde{\omega}}_l = 0$ for $t \geq t_{SM}$ leads to

$$\phi - k_2 \int_0^{t_{SM}} \text{sgn}(\tilde{\omega}_l(\tau))d\tau = 0 \tag{6.12}$$

from where the perturbation ϕ is calculated. The estimate of ϕ at time t is, therefore, defined as:

$$\hat{\phi} = k_1 |\tilde{\omega}_l|^{\frac{1}{2}} \text{sgn}(\tilde{\omega}_l) + k_2 \int_0^t \text{sgn}(\tilde{\omega}_l(\tau))d\tau \ . \tag{6.13}$$

An additional requirement to the appropriate selection of k_1, k_2 for ensuring finite-time reaching of the sliding manifold $\mathcal{S}$ is the boundedness of T_l and $\dot{T}_l$. This is ensured by the boundedness of the state vector $\boldsymbol{x}$ and the smoothness of the backlash model. However, the bound on $\dot{T}_l$ is proportional to the stiffness slope α. This suggests that the closer the model is to the deadzone model, the larger this bound will be. Larger bounds on $\dot{T}_l$ lead to the selection of higher gains for the observer and, consequently, more chatter in the estimation signal and increased sensitivity of the perturbation estimator to measurement noise.

It is also interesting to notice that although the load velocity subsystem is scalar, a second-order SMO is used. This is due to the fact that higher order SMOs offer greater attenuation of the chatter induced by the high-frequency terms to the injection signal v [69], and by extension, to $\hat{\phi}$.

6.3.2 Adaptive Deadzone Angle Estimator Design

Based on the generic design for parameter estimators in nonlinearly parametrized systems proposed in [122], the adaptive deadzone angle estimator is given by:

$$\dot{\hat{\delta}} = \rho(\boldsymbol{x}, \hat{\phi}, \hat{\delta}) = \text{Proj}\left[\hat{\delta}, \gamma\mu(\boldsymbol{x}, \hat{\delta})\left(\hat{\phi} - \frac{1}{J_l}T_l(\boldsymbol{x}, \hat{\delta})\right)\right] \tag{6.14}$$

with $\gamma > 0$ being the adaptation gain and $\text{Proj}(\cdot,\cdot)$ the projection operator, defined in (II.6). The scalar function $\mu(\boldsymbol{x}, \hat{\delta})$ is chosen as

$$\mu(\boldsymbol{x}, \hat{\delta}) \triangleq \frac{J_l}{K_S^2}\frac{\partial T_l}{\partial \hat{\delta}}(\boldsymbol{x}, \hat{\delta}) = -\frac{J_l}{K_S \pi}\left[\chi_1(\boldsymbol{x}, \hat{\delta}) + \chi_2(\boldsymbol{x}, \hat{\delta})\right] \ , \tag{6.15}$$

where χ_1, χ_2 are defined as

$$\chi_1(\boldsymbol{x}, \hat{\delta}) \triangleq \frac{1}{2}(1 + \text{sgn}(\Delta\theta))\left[\pi + \arctan(\alpha(\Delta\theta - \delta + \delta_1)) - \arctan(\alpha(\Delta\theta + \delta_1))\right] \tag{6.16a}$$

$$\chi_2(\boldsymbol{x}, \hat{\delta}) \triangleq \left[\Delta\theta + \delta_1 - \frac{\hat{\delta}}{2} \cdot (1 + \text{sgn}(\Delta\theta)) + \frac{D_S}{K_S}\Delta\omega\right] \frac{\alpha}{1 + \left[\alpha(\Delta\theta + \delta_1 - \hat{\delta})\right]^2} \ . \tag{6.16b}$$

This particular selection of $\mu(\boldsymbol{x}, \hat{\delta})$ is made such that certain criteria [4] regarding boundedness of the perturbation rate $\left|\frac{\partial T_l}{\partial \delta}\right|$ and persistence of excitation are satisfied. It is proven in [3] that if the deadzone angle δ is constant or very slowly varying, i.e. if $\dot{\delta} \approx 0$, then the cascaded estimator consisting of the Super-Twisting Sliding-Mode Observer (STSMO) (6.8),(6.9),(6.13), connected in series to the adaptive estimator (6.14),(6.15),(6.16a),(6.16b), with the deadzone angle estimation error defined as

$$\tilde{\delta} \triangleq \delta - \hat{\delta}$$

ensures that:

1. The origin $\tilde{\delta}^* = 0$ is a Uniformly Locally Exponentially Stable (ULES) equilibrium point of the $\tilde{\delta}-$dynamics if $\hat{\phi} = \phi$.

2. The origin $\tilde{\delta}^* = 0$ is a Uniformly Globally Asymptotically Stable (UGAS) equilibrium point of the $\tilde{\delta}-$dynamics if $\hat{\phi}^* = \phi$ is a UGAS equilibrium point of the $\hat{\phi}-$dynamics.

3. The deadzone angle estimation error $\tilde{\delta}$ is Uniformly Globally Bounded (UGB) with its bound being proportional to the perturbation estimation error bound.

The last point is indicative of the deadzone angle estimator robustness with respect to model mismatches and parameter uncertainties and can give an indirect measure of the estimation quality. Specifically, it is shown in [3] that if the lumped torque perturbations $\kappa(t)$ that come from the fiction and shaft parameters uncertainty, as well as other model mismatches and the measurement noise, are bounded by a positive constant K, then

$$\lim_{t\to\infty} \left|\tilde{\delta}(t)\right| = c\frac{1}{J_l}K \ , \tag{6.17}$$

where c is a positive gain monotonically related to the Lipschitz constant of $T_l(\boldsymbol{x}, \delta)$.

The complete estimator design is illustrated in Figure 6.3 and is summarized in the following steps:

Algorithm 1 Backlash angle estimation

Measured: Sate variables $\omega_m, \theta_m, \omega_l, \theta_l$.

Output: Deadzone angle estimate $\hat{\delta}$.

1: Design a STSMO for the load velocity (Equations (6.8), (6.9)).
2: Estimate the backlash torque (Equation (6.13)).
3: Design the adaptive estimator for the deadzone angle δ (Equations (6.14)-(6.16b)).

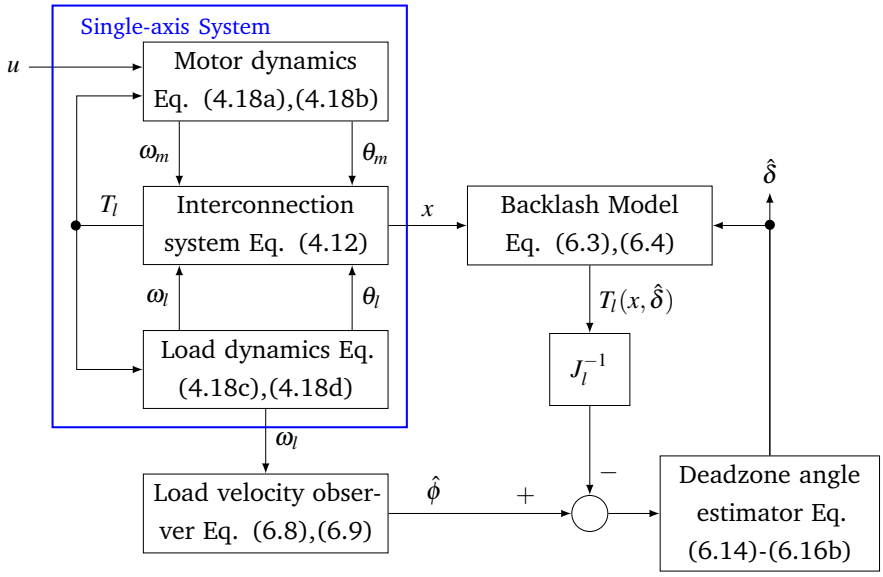

Figure 6.3: Block diagram of the single-axis system and the estimation scheme.

6.4 Simulation and Experimental Results

This section presents the results regarding the application of the proposed design for the estimation of the deadzone angle in the single-axis system. The performance of the algorithm is assessed in different scenarios first in simulation environment and then experimentally. Additional tests including large variations of the shaft and load friction parameters are carried out to evaluate the robustness of the estimator with respect to model uncertainties.

6.4.1 Simulation of the Ideal Case

The performance of the deadzone angle estimator was tested in a Simulation environment, where the drive motor was regulated by a PI controller to track a sinusoidal velocity profile. The friction and shaft coefficients were considered completely known and the deadzone model was used to emulate the backlash phenomenon in the single-axis system. The only source of uncertainty was the velocity measurement noise, which was considered zero-mean white Gaussian.

The system parameters were set according to the calibrated values obtained in Chapter 4 and the noise distribution had the same characteristics (mean and variance) as the velocity measurement noise in the real motors. The deadzone angle was considered to be $\delta = 0.2$ rad and after 3 seconds it increased by a 5% step of its

initial value. The position offset was taken $\delta_1 = \frac{\delta}{2}$.

Since the friction and shaft coefficients are completely known, the STSMO is able to provide a very accurate estimate of the perturbation ϕ, as this can be seen in Figure 6.4. The steady state absolute error for the deadzone angle estimation, shown in Figure 6.5, is less than $2.5 \cdot 10^{-4}$ rad, which is well below the accuracy requirements set in Problem 2. Moreover, the estimator captures the change in δ and provides a new estimate in less than 2 s.

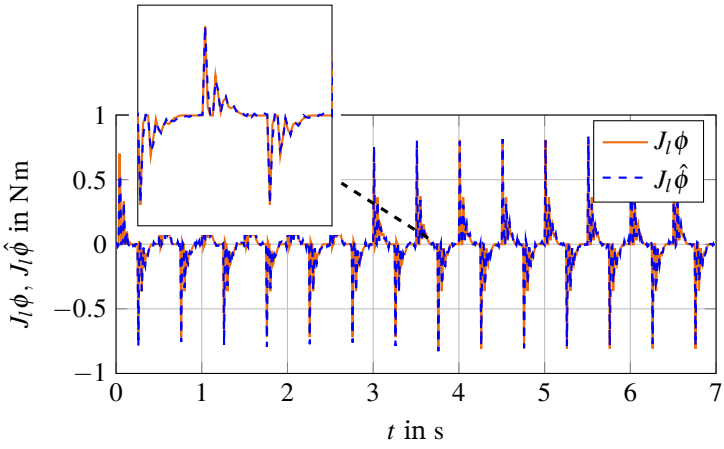

Figure 6.4: Real and estimated backlash torque scaled by the load inertia J_l.

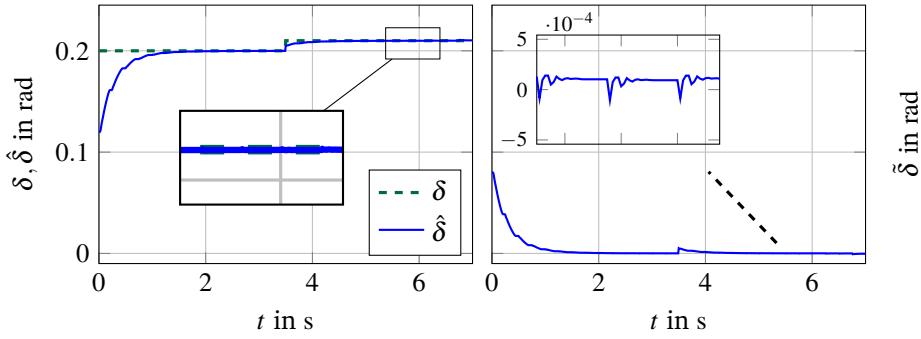

Figure 6.5: (Left): Real and estimated change of deadzone angle. (Right): Estimation error.

Finally, in order to highlight the proportionality of the steady-state absolute deadzone angle estimation error to the bound K for the backlash torque estimation error, the STSMO gains k_1, k_2 were varied and the system was simulated in the same scenario. The obtained different values for maximum peak estimation error in steady

state $\tilde{\delta}^{SS}_{peak}$ (defined in Equation (C.60)) were plotted against the corresponding bounds for $J_l|\hat{\phi}|$. As shown in Figure 6.6, the relation between the two bounds is approximately linear with proportionality factor $q \approx 0.0023$.

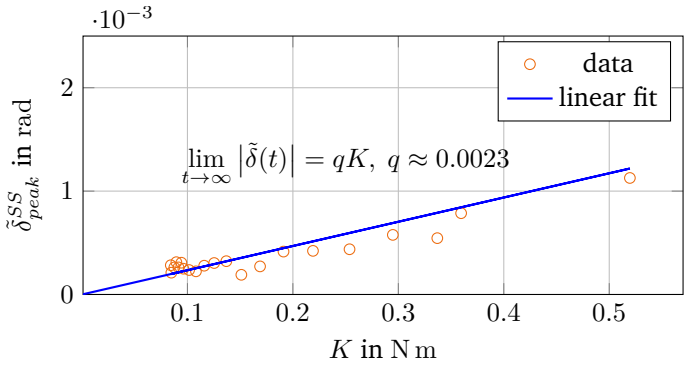

Figure 6.6: Linear relation between the bounds for the perturbation estimation error $\tilde{\phi}$ and the deadzone angle estimation error $\tilde{\delta}$.

6.4.2 Experimental Validation

The performance of the deadzone angle estimator was also experimentally assessed on the Siemens drive-train test rig. The quality of the estimation of three different deadzone angles was evaluated based on the Maximum Absolute Estimation Error (MAEE), which is defined over a time interval $T > 0$ as

$$MAEE = \sup_{t_0 \le t \le t_0+T} \left|\tilde{\delta}(t)\right|. \tag{6.18}$$

The load and shaft model parameters were considered known and their identified values from Table 4.3 were used in the experiments for the assessment of the estimation algorithm. For each deadzone angle, five more variation cases were considered for testing the robustness of the estimator with respect to parameter uncertainties. In the first four cases, one of the model parameters ($K_S, D_S, T_{C,l}, \beta_l$) was increased by 100% of their identified value. In the fifth case all four parameters were increased by the same amount, simultaneously. The drive motor was commanded to track a sinusoid reference signal for the position. The fifteen different test scenarios are shown in Table 6.1.

The estimator provides sufficiently accurate estimates for the deadzone angle, with the MAEE being smaller than $4 \cdot 10^{-3}$ rad in all tests, as shown in Table 6.2. This is also shown in Figures 6.7-6.10, where the estimation error is plotted in the nominal case and for all the parameter variations. The inherent robustness of the estimation

Table 6.1: Test scenarios.

No	δ (rad)	δ_1 (rad)	Parameter variation
$0A$	1.027	0.8924	No variation
$1A$	1.027	0.8924	100% increase in K_S
$2A$	1.027	0.8924	100% increase in D_S
$3A$	1.027	0.8924	100% increase in $T_{C,l}$
$4A$	1.027	0.8924	100% increase in β_l
$5A$	1.027	0.8924	All variations combined
$0B$	0.186	0	No variation
$1B$	0.186	0	100% increase in K_S
$2B$	0.186	0	100% increase in D_S
$3B$	0.186	0	100% increase in $T_{C,l}$
$4B$	0.186	0	100% increase in β_l
$5B$	0.186	0	All variations combined
$0C$	0.105	0.0021	No variation
$1C$	0.105	0.0021	100% increase in K_S
$2C$	0.105	0.0021	100% increase in D_S
$3C$	0.105	0.0021	100% increase in $T_{C,l}$
$4C$	0.105	0.0021	100% increase in β_l
$5C$	0.105	0.0021	All variations combined

algorithm can be better understood by considering the proportionality between perturbation and deadzone angle estimation errors given in Equation (6.17).

In the worst case, where all the parameters have been doubled, the backlash torque estimation error will be exactly the difference between the nominal backlash and friction torques:

$$J_l\tilde{\ddot{\phi}} = T_l - T_{F,l} \ . \tag{6.19}$$

This is due to the linear parametrization of the load system with respect to the shaft and load friction parameters. In order for the deadzone estimation error bound to be larger than 10^{-2} rad, the corresponding backlash estimation error has to be larger than $\frac{10^{-2}}{q} = \frac{10^{-2}}{0.0023} \approx 4.34$ N m, which is unrealistically high for the drive-train system, given that the maximum torque produced by the drive motor is 13 N m.

Figure 6.11 illustrates the estimated deadzone during Test 0A through the mapping between the backlash torque $J_l\hat{\ddot{\phi}}$ and the position difference $\Delta\theta$ between motor and load. The oscillations at the two ends of the deadzone in the estimated torque correspond to the impact between motor and load upon engagement. The estimated deadzone angle is also shown in the bottom plot of the same figure, where the stiffness K_{BL} is plotted also as a function of $\Delta\theta$.

Table 6.2: MAEE in mrad for the nominal case (Tests 0A, 0B, 0C) and all the parameter variations (Tests 1A-5A, 1B-5B, 1C-5C).

	MAEE in mrad					
δ in rad	0	1	2	3	4	5
1.027 (case "A")	1.75	0.41	1.80	3.61	2.69	1.85
0.186 (case "B")	1.90	1.04	1.87	3.31	1.96	1.80
0.105 (case "C")	0.66	1.85	0.72	1.38	0.57	0.93

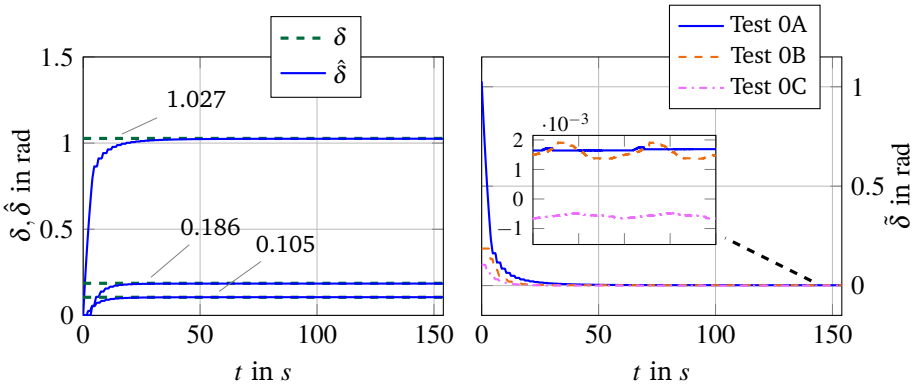

Figure 6.7: Deadzone angle estimated value (left) and the associated estimation error (right) for the nominal cases (Tests 0A, 0B, 0C).

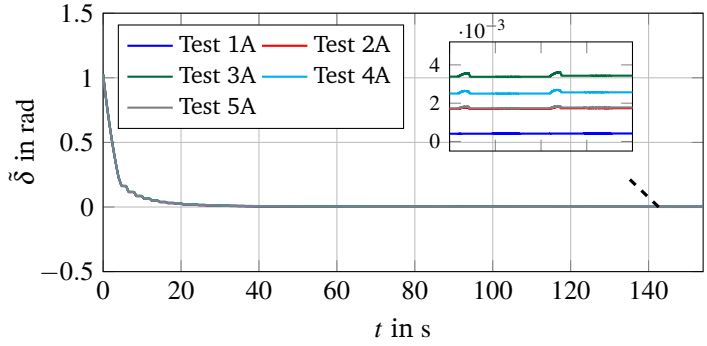

Figure 6.8: Deadzone angle estimation error during Tests 1A-5A.

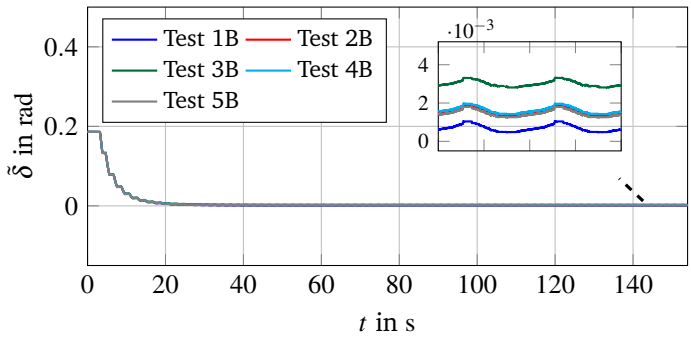

Figure 6.9: Deadzone angle estimation error during Tests 1B-5B.

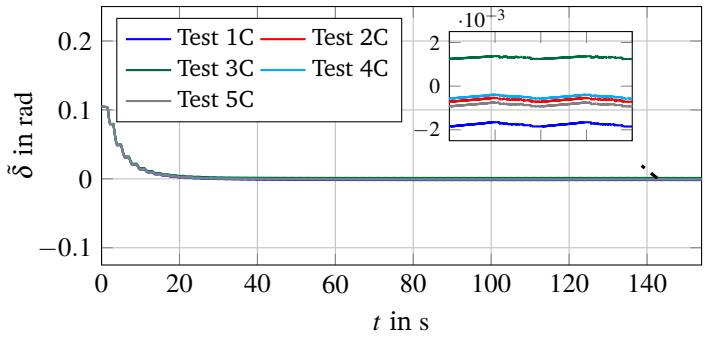

Figure 6.10: Deadzone angle estimation error during Tests 1C-5C.

Finally, the backlash hysteresis during Test 0A can be seen in the Figure 6.12, which depicts the motion transmission from the drive motor to the load. In this illustration, θ_m is considered the input position and θ_l the output position. The width of the hysteresis cycle along the horizontal axis is the estimated deadzone angle $\hat{\delta}$.

6.5 Conclusions

This chapter presented the design and application of an algorithm for the estimation of the deadzone angle in a single-axis drive train system. The estimation scheme had a cascaded structure where a STSMO was used for obtaining an estimate of the backlash torque acting on both the motor and the load. The value of this torque was then fed to an adaptive estimator that provided the deadzone angle. The method was tested both in simulation and experimentally and the results showed sufficient accuracy of the algorithm with the MAEE staying below $4.5 \cdot 10^{-3}$ rad even under

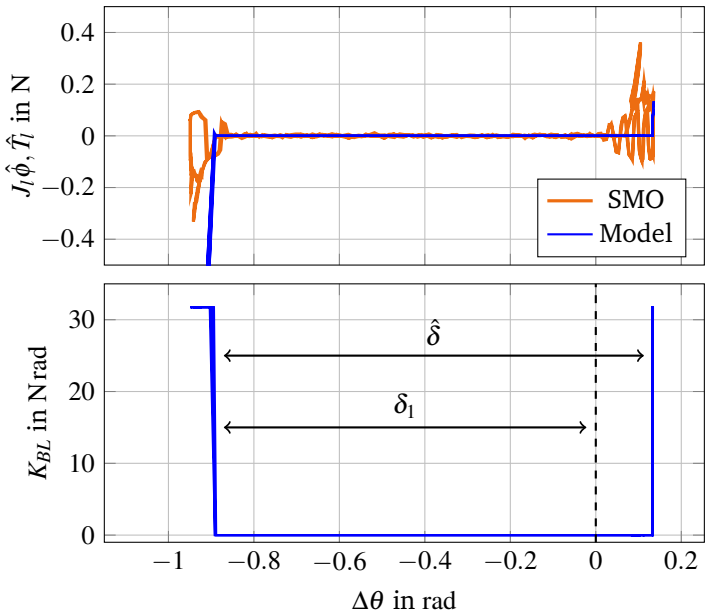

Figure 6.11: Deadzone illustration through torque-position difference (top) and torque-stiffness (bottom) plots during Test 0A.

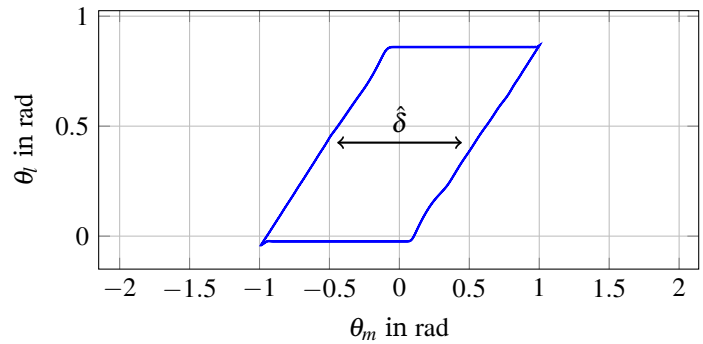

Figure 6.12: Backlash hysteresis during Test 0A.

large model parameter variations.

During some of the experiments it was observed that the sudden engagement between drive motor and load produced a periodic impact torque acting on both parts. This caused a small displacement of the load after disengagement, which resulted in an shift of the position offset δ_1. Although the quality of the estimation was practically not affected by this change, a possible future extension of the method would be the design of a joint estimator for both the deadzone angle and the position offset δ_1.

Chapter 7

Conclusions and Future Research

7.1 Summary of Conclusions

This research project addressed the general problem of maintaining and improving machine tools systems performance under conditions of developing equipment wear and degradation. The approaches made for achieving this goal and, consequently, the main contributions of the project, fall into three fields of research, namely modelling, low-level axis control and estimation.

The first contribution of this research related to efficiently describing a machine tool system to be used as a benchmark for performance assessment. Since the quality of the manufactured components is directly related to the accurate positioning of the machine axes, a detailed mathematical model of a single-axis in a machine tool was developed based on a double-mass oscillator abstraction. The unknown parameters of the system, as well as of degrading phenomena such as friction, were analysed with respect to their significance on the system outputs. The results of this sensitivity analysis showed that unique identifiability of all the parameters is difficult to achieve. Estimation of the parameters was done by using a combination of optimization-based algorithms and methods employing the physical properties of the system (e.g. natural modes of the oscillator). Additionally, a novel model for describing backlash in machine tools was developed. A smooth varying-stiffness scheme was utilised to effectively describe the sudden engagement and disengagement between the drive-motor and the load. The proposed model was parametrized by the deadzone width and facilitated accurate online backlash estimation.

The second main contribution of the project pertained to the developing of axis positioning algorithms that provide increased accuracy and robustness against unknown and increasing friction. Eight nonlinear controllers based on sliding-mode and adaptive principles were designed and implemented for the control of the load

position. The designs followed two different architectures, namely the position-velocity cascaded control and the direct position control. The first offered greater design modularity and simplicity since only the velocity PI controller was replaced by the different nonlinear controllers. These algorithms accounted for the degrading phenomena affecting the motor velocity dynamics. The second architecture provided an integrated position-velocity control solution that compensated for all the considered perturbations in the system. The resulting designs, however, were more complex and required the tuning of a larger number of parameters. The developed positioning algorithms were tested in fifteen different scenarios with combinations of three modes of motion profile (very slow, average, fast) and five different levels of unknown friction. A set of quantitative and qualitative performance indices were used to facilitate a systematic comparison of the control strategies. The results from the experimental evaluation showed that four nonlinear controllers, specifically the STSMC, ABSC, NAC and I&I-AC, provided better positioning accuracy than the standard P-PI scheme. Moreover, the prescribed tolerances were maintained in most of the cases even for the highest (unrealistic) Coulomb friction values, which indicates the superior friction-resilience properties of these controllers.

The third contribution of this research project concerned the design of an online estimator for backlash in machine tool systems. A varying-stiffness model was proposed to described backlash through the motor-load interconnecting torque and it was employed for estimating the width of the developing clearances in the single-axis system. The modular design of the algorithm included a STSMO for the load velocity, that provided an indirect estimation of the backlash torque. This estimate was then fed to an adaptive estimator that inverted the mapping from the deadzone angle to the backlash torque, thus providing an estimate of the backlash clearance width. The developed method was experimentally tested on the single-axis drive-train for three different sizes of deadzones. The evaluation results showed that the algorithm provides accurate estimates of the deadzone angle in the order of 10^{-3} rad, even in the presence of large parameter uncertainties. Comparing this accuracy level to the tolerances required in machine tools indicated that the accuracy of the estimated value was sufficient for using it in backlash compensation algorithms in axis position control, as well as for equipment wear assessment.

7.2 Future Research

The improvement of accuracy and liability of machine tool systems by means of nonlinear control and estimation is an open field for fruitful research. Some key extensions of the research presented in this thesis are summarised in the following:

System description and modelling: The developed model used in the project serves as an abstraction of a single axis in a machine tool. Additional mechanical subsystems could be integrated to the drive-train model to describe the axis dynamics in more detail, including several additional masses and more complete friction models, such as the LuGre or the generalized Maxwell-slip model. Identification of the drive-motor electrical closed-loop system could increase the model accuracy. An additional extension could include a description for the parasitic Eddy currents and the torques due to magnetic interaction between stator windings and rotor magnets.

Control design: Optimization of the controllers' parameters was not considered in this project. The development of systematic tuning methodologies for the considered controllers would be a significant future contribution to this research. A more ambitious extension could involve the development of autotuning algorithms for the controllers in order to facilitate easier commissioning for the machines. Moreover, additional degrading phenomena could be considered in relation to the robustness properties of the positioning controllers. Integration of compensating algorithms for backlash, varying load inertia and workpiece cutting forces to the existing control designs is a natural direction in continuing this research project.

Estimation: The developed positioning algorithms rely on the description of machine tools as the interconnection between drive-motors and generalized load systems. Online estimation of the load parameters such as the inertia, shaft and friction coefficients could facilitate more accurate description of the system and contribute to the correct tuning of the position controllers. Additional methods could be developed for equipment wear assessment and prognosis through parameter monitoring and change detection. Regarding the estimation of the backlash, a modification of the estimation algorithm could be made to include both the deadzone angle and the initial position motor-load offset. This, in turn, could facilitate robust backlash identification, with respect to different initial operating modes of the machine.

Paper A

Friction Resilience of Machine Tool Controls - Classic, Sliding-Mode and Nonlinear Adaptive Techniques Compared

Dimitrios Papageorgiou*[1], Mogens Blanke[2], Hans Henrik Niemann[1], Jan H. Richter[3]

[1]Department of Electrical Engineering, Automation and Control Group, Technical University of Denmark, Elektrovej Building 326, 2800, Kgs. Lyngby, Denmark.

[2]AMOS CoE, Institute of Technical Cybernetics, Norwegian University of Science and Technology, Trondheim, Norway.

[3]Siemens AG, Digital Factory Division, D-90475 Nuremberg, Germany

Abstract:
Needs for high-precision tool positioning and accurate trajectory following have renewed the focus on controller design for machine tools in the Industry 4.0 digital factory. State-of-the-art controllers are based on P and PI principles; while these achieve sufficient nominal performance and are easy to implement and understand, their performance quickly deteriorates in the presence of equipment wear, tear, and general degradation. Moreover, their good performance assumes tuning by experts when a machine is commissioned. This paper presents design and experimental validation of nonlinear controllers for a machine tool. Based on adaptive and sliding-mode principles, the nonlinear control strategies are designed to cope with unknown and increasing friction phenomena, and comparison is made with standard linear control. Experimental results from a single-axis test setup equipped with a Siemens SINAMICS S120 drive controller show the performance in nominal condition and under circumstances with increased-friction.

*Principal corresponding author. Tel.: +45 45253572; E-mail: dimpa@elektro.dtu.dk

A.1 Introduction

A vast variety of mechanical components are manufactured using automated machine tools for cutting, drilling, milling, shearing etc, on a wide range of materials. The ever-increasing sophistication in mechanical designs requires high-accuracy tool positioning in machine-tool systems, and narrow workpiece tolerances need be met. Workpiece processing is complicated by several mechanical phenomena such as variable friction and stiction, backlash, drive-train elasticity and variable load inertias. These compromise tolerances unless properly handled by the relevant closed loop controls.

In light of the emerging Industry 4.0, fully automated manufacturing systems are required that can be adapted to varying workspace conditions and must be robust to equipment degradation due to wear and tear. State-of-the-art tool-positioning solutions, which include combinations of output-feedback P and PI controllers with additional feed-forward compensation, achieve adequate performance only in nominal (fault-free) operation. This motivates the exploration of nonlinear control strategies for tool positioning. This paper compares two advanced control principles for high-accuracy positioning in machine tools with improved properties for dealing with degradation when compared to state-of -the-art PI-type controllers.

An overview of different tool-positioning strategies was provided in [14, 18] showing that in machine tools with more than one axis, the common control architectures handle the drive systems of each axis separately, and effects of dynamics of other axes are treated as disturbances. Alternatively, the control loops of all axes could be designed as a single system, as done in the control of robotic manipulators. The latter family of techniques is referred to as CCC [15]. The tool positioning task for a 2-axis machine was discussed in [16] as a contour-error regulation problem, expressing the tracking error dynamics in a task-space using suitable coordinate transformations. An experimental evaluation of these results was given in [17] and a similar problem was addressed in [22], where an adaptive controller was extended to include discontinuous parameter projection. The same problem formulation was adopted in [23], who considered a 3-axis machine and designed an adaptive CCC to account for unknown viscous friction and machine inertia. A general overview of machine tool control techniques was provided in the survey [19], who described three classes of machine-tool adaptive control techniques, each taking a different approach to update the control signal to enhance performance. Specifically, the first class, Adaptive Control with Constraints (ACC), updates the machine operating parameters, such as spindle speed and feed rate, such that constraints regarding the tool cutting forces are satisfied. The second family of methods, Adaptive Control

with Optimization (ACO), which were elaborated in [21], updates the machine parameters by solving optimization problems online. The cost function consists of performance indices pertaining to the reduction of vibration levels, tool wear etc. Lastly, the approach in Geometry Adaptive Control (GAC) involves adapting the tool geometry by adding offset distances and modifying the tool orientation, so that workpiece surface quality is maintained [20].

A common assumption made in the methods mentioned above is that the connecting shaft between the drive motors of each axis and the tool is rigid. For single-axis machines this means that the tool position can be calculated directly from the drive motor position by applying a known static coordinates transformation (rotation and translation). This considerably simplifies the analysis since the control of the tool position is reduced to controlling the position of the drive motor, an application that is widely addressed in the literature. However, in reality additional dynamics exists between the tool and the drive motor, mainly arising from the coupling components' (e.g. connecting shaft) elasticity, unbalanced masses and friction [39]. Additional hysteresis frictional phenomena are manifested when the machine is operated at low speeds and vibrations may occur at different frequencies.

Advanced nonlinear control strategies, such as SMC and nonlinear Adaptive Control, have been investigated in relation to flexible mechanical systems and friction compensation (see for example [24, 27, 40, 41]). Apart from [44] who used adaptive friction compensation in a machine tool drive, very few results have been reported on employing these techniques to high-accuracy machine tool control. One of the main challenges is the fact that in machine-tool systems, it is desirable to control the tool position indirectly, via the drive motor position. This consideration often leads to more complex control laws, the implementation of which may be difficult, especially in comparison to conventional P and PI solutions.

This paper focus on the applicability of advanced control schemes for high accuracy machine tool positioning and evaluates their robustness with respect to mechanical degradation phenomena. The paper presents a detailed design of three different nonlinear controllers for tool piece (load side) positioning in a single-axis electro-mechanical drive-train system. It is shown how these designs can be made without resting on the common academic assumption of having a totally rigid shaft between axis drive motor and tool, and thereby get closer to reality. It is further discussed how comparison of controller performance can be assessed using both quantitative and qualitative criteria, which are indicators for positioning accuracy, control power and overall complexity of each method. The paper finally shows an experimental comparison of the nonlinear methods and the standard P-PI cascade control under unknown and increasing friction.

The paper is structured as follows: Part A.2 describes the physical system considered and presents the problem being addressed. Part A.3 describes the model of the mechanical drive-train and discusses a number of assumptions pertaining to model reduction. Part A.4 presents three different control schemes used for tool positioning. The design of each architecture is provided and detailed comments are offered related to theoretical assumptions for each method and implications on applicability is discussed. Experimental results and comparison of the control schemes are presented in Part A.5. Finally, conclusions and future work are discussed in Part A.6.

A.2 System Description and Problem Formulation

A typical single-axis machine tool consists of a linear axis that linearly positions the tool. The axis is actuated by a drive motor, which is typically connected to an angular-to-linear motion conversion system (e.g. a ball-screw), which in turn positions tool itself [18].

The combined elasticity of all the mechanical components that connect to the machine spindle can be expressed as a series of torsional springs. All masses that are connected to the drive motor are lumped into a single inertia, which is accelerated by the drive motor torque. The total friction is added to the damping and constitute the decelerating torques at the shaft. This approach allows a single-axis machine tool to be described by a mechanical drive-train consisting of the drive motor, a flexible shaft with damping and a generalized load with friction. The correspondence between the single-axis machine tool and the abstraction of the mechanical drive-train can be seen in Figure A.1. This abstraction of the single-axis machine tool will be the basis for comparing the various controllers in this paper.

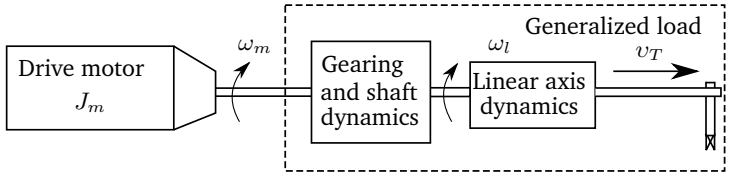

Figure A.1: Correspondence between mechanical drive-train and single-axis machine-tool systems, where v_T is the linear velocity of the tool.

A.2.1 Physical System and Accuracy

The physical system consists of two motors connected via a shaft emulating a single-axis machine tool (see Figure A.9). The drive-train comprises a 1FT7 PMSM

[106] together with a Siemens SINAMICS S120 drive converter [107]. This type of AC motor is typically used for actuating linear axes in machine tools, especially for applications demanding a high dynamic performance. This is because they can generate very high torques with relatively simple control architectures [105]. The second motor is used to emulate the load of the axis either as pure inertia or by applying various torque profiles.

The objective in machine tool axis control is to position the tool (load) at a given reference point. In applications where high precision is required, machine tools drives are equipped with high resolution absolute encoders that allow linear positioning accuracy to the order of $1 - 10\,\mu\mathrm{m}$. Typical linear axes have lead screws with pitch size ranging from $2\ \mathrm{mm}$ to $10\ \mathrm{mm}$, which leads to an angular positioning tolerance between $5 \cdot 10^{-3}$ and $2 \cdot 10^{-2}\ \mathrm{rad}$ [18]. The precision requirement considered in this study is $10^{-2}\ \mathrm{rad}$.

A.2.2 Friction as Degrading Phenomenon

The friction between the various surfaces of the machine parts may hinder the accurate positioning of the tool. Although the effects of friction are typically accounted for when commissioning the machine drive, these compensation schemes assume constant friction characteristics. However, this is not necessarily true since these characteristics can change over time due to equipment wear and varying environmental conditions. Typical examples include deformation of the bearing surfaces of the motors and linear axes, lubrication film failure or high room temperature, which can cause increased Coulomb friction and viscosity [116].

Consequently, a tool-positioning control strategy that can ensure nominal performance irrespectively of friction changes is a highly desirable feature for machine tools. This is the reason that friction with variable characteristics is chosen to be the degrading phenomenon, against which the nonlinear controllers designed for the drive-train will be compared and evaluated.

Typically, the friction acting on the drive motor is different than the one affecting the load. The first is primarily due to the contact of the bearing surfaces and possibly additional heat losses due to eddy currents. On the other hand, load friction is the combination of all the frictional torques. These extend from the gearing mechanism to the linear axis ball screw system and the various intermediate contact surfaces. Phenomena such as static friction, the Stribeck pre-sliding effect (decreasing viscous friction near the area of zero angular velocity) and hysteresis are not negligible. As such, more complete friction models, such as the *LuGre* friction model [32], are required to describe these phenomena. (For a more detailed review of the various different friction models and their evolution the reader may consider the survey done

in [29]). However, since the load in the physical system being considered is actually a motor that is identical to the drive motor, the nominal friction is considered the same on both sides. This assumption is valid on the basis of the friction sources being the same for the drive motor and the load.

A.2.3 Problem Formulation

The collective objective with respect to which the different control architectures will be compared to each other can be summarized in the following formulation of the problem:

Problem A (Friction-resilient accuracy control for single-axis machine tool)**.** *Consider a single-axis machine tool system consisting of a drive motor connected to a load with a flexible shaft. Let the tool positioning error be denoted by* e_θ *and let* $T_{C,m}^{max}$ *be an upper bound for the Coulomb friction magnitude* $T_{C,m}$ *on the motor side. Design a closed-loop control strategy that ensures:*

$$|e_\theta(t)| \leq 10 \text{ mrad } \forall t \geq t_0 > 0 \text{ and for } T_{C,m} \leq T_{C,m}^{max}$$

where t_0 *denotes a time after the starting up of the positioning task for the machine.*

A.3 Mathematical Model

Before getting into modelling details, a complete explanation of the most important variables and notation is provided in Table A.1.

A.3.1 Drive Train Modelling

The drive-train system consists of the drive motor, the flexible shaft and the load. The dynamics of a single PMSM is given in the rotating dq-frame below [109]:

$$\frac{di_d}{dt} = -\frac{r_s}{L_d} i_d + \frac{L_q}{L_d} i_q \omega_m + \frac{1}{L_d} V_d \tag{A.1}$$

$$\frac{di_q}{dt} = -\frac{r_s}{L_q} i_q - \frac{L_d}{L_q} i_d \omega_m - \frac{\lambda_m}{L_q} \omega_m + \frac{1}{L_q} V_q \tag{A.2}$$

$$\frac{d\omega_m}{dt} = \frac{1}{J_m} \left\{ \left[\frac{3P}{4} \lambda_m i_q + \frac{3P}{4} (L_q - L_d) i_d i_q \right] - T_{F,m} - T_l \right\} \tag{A.3}$$

$$\frac{d\theta_m}{dt} = \omega_m \ . \tag{A.4}$$

Table A.1: System model nomenclature.

Symbol	Description	Units
States and Outputs		
i_d	Direct axis current	A
i_q	Quadrature axis current	A
ω_m	Motor angular velocity	$\mathrm{rad\,s^{-1}}$
θ_m	Motor angular position	rad
ω_l	Load angular velocity	$\mathrm{rad\,s^{-1}}$
θ_l	Load angular position	rad
Inputs		
θ_r	Load position reference	rad
ω_r	Motor velocity reference	$\mathrm{rad\,s^{-1}}$
V_d	Direct axis voltage	V
V_q	Quadrature axis voltage	V
u	Torque command	$\mathrm{N\,m}$
Constant parameters		
r_s	Stator total windings resistance	Ω
L_d	Direct axis inductance	mH
L_q	Quadrature axis inductance	mH
λ_m	Amplitude of flux linkages	$\mathrm{V\,s\,rad^{-1}}$
P	Number of drive motor poles	$-$
N	Gearing ratio	$-$
J_m	Motor inertia	$\mathrm{kg\,m^2}$
J_l	Load inertia	$\mathrm{kg\,m^2}$
K_S	Shaft stiffness	$\mathrm{N\,m\,rad^{-1}}$
D_S	Shaft damping coefficient	$\mathrm{N\,m\,s\,rad^{-1}}$
$T_{C,m}$	Coulomb friction on the motor	$\mathrm{N\,m}$
$T_{C,l}$	Coulomb friction on the load	$\mathrm{N\,m}$
$T_{S,m}$	Static friction on the motor	$\mathrm{N\,m}$
$T_{S,l}$	Static friction on the load	$\mathrm{N\,m}$
ω_s	Stribeck velocity	$\mathrm{rad\,s^{-1}}$
β_m	Motor viscous friction coefficient	$\mathrm{N\,m\,s\,rad^{-1}}$
β_l	Load viscous friction coefficient	$\mathrm{N\,m\,s\,rad^{-1}}$
Disturbances		
d_e	Input torque ripples and harmonics	$\mathrm{N\,m}$
$T_{F,m}$	Motor friction	$\mathrm{N\,m}$
$T_{F,l}$	Load friction	$\mathrm{N\,m}$
T_l	Load torque	$\mathrm{N\,m}$

The expression in the brackets in Equation (A.3) is the torque T_m produced by the rotating magnetic field in the motor [125].

Typically, a cascade of P and PI controllers is used for controlling the different dynamics of the drive-train separately. As shown in Figure A.2, the current control is the lower level in the control design and includes two individual PI controllers for the direct and quadrature currents. All the electrical phenomena that affect the system are addressed at this level. One loop further out is the velocity PI controller and the outermost loop is closed with the position controller, typically a proportional controller.

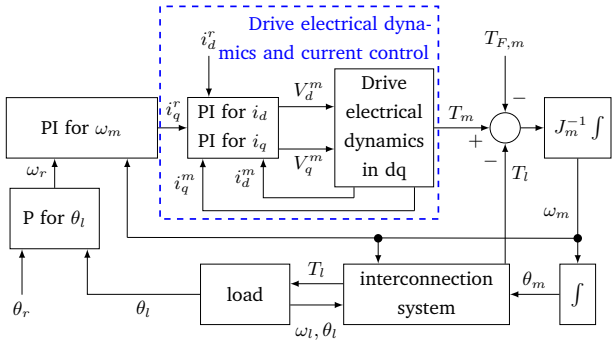

Figure A.2: State-of-the-art in industrial position control using cascaded P and PI controllers.

Since the electrical phenomena are much faster than the mechanical dynamics of the system and since the main degrading disturbance, which is the friction, appears as decelerating torque, the closed-loop electrical dynamics of the motor will not be considered in this study. The following modelling assumption is made:

Assumption A.3.1. *The closed-loop electrical dynamics can be considered as a unit gain perturbed by a finite number of torque ripples, i.e. the torque produced by the motor is the torque command plus the torque harmonics:*

$$T_m = u + d_e \ . \tag{A.5}$$

The maximum amplitude of these harmonics is approximately 0.1% of the maximum input, i.e. $|d_e| \leq 0.005 u_{max}$ and the torque ripples frequencies range from 10 Hz to 100 Hz. The validity of this assumption is illustrated in Figure A.3, where step commands and actual torque for the motor have been plotted. The power of the largest component is $1.9 \cdot 10^{-5}$ $(\mathrm{N\,m})^2$, which is lower than $(0.005 u_{max})^2$, for $u_{max} = 13$ N m [106].

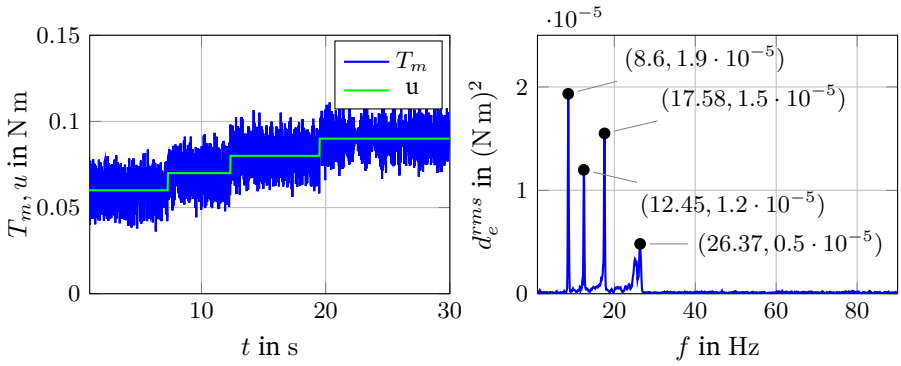

Figure A.3: (Left): Step torque commands and actual torque. (Right): Power and frequency locations of torque ripples.

The drive-train can be viewed as the dynamic interaction between the drive motor and the load inertias via a flexible shaft with friction, as shown in Figure A.4. Its model is derived by augmenting the drive motor mechanical model with that of the load including the flexible shaft (generalized load). The dynamics of the mechanical drive-train reads:

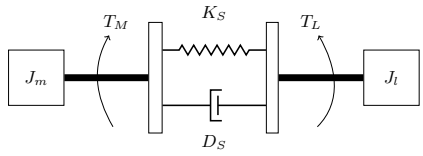

Figure A.4: Mass-spring-damper representation of the mechanical part of a drive-train system, where T_M, T_L are the accelerating torques for the inertias J_m, J_l, respectively.

$$\dot{\omega}_m = \frac{1}{J_m}(u + d_e) - \frac{1}{J_m}T_{F,m}(\omega_m) - \frac{1}{NJ_m}T_l \tag{A.6}$$

$$\dot{\theta}_m = \omega_m \tag{A.7}$$

$$\dot{\omega}_l = -\frac{1}{J_l}T_{F,l}(t, \omega_l) + \frac{1}{J_l}T_l \tag{A.8}$$

$$\dot{\theta}_l = \omega_l \tag{A.9}$$

with the interconnection torque T_l given from:

$$T_l = K_S\left(\frac{1}{N}\theta_m - \theta_l\right) + D_S\left(\frac{1}{N}\omega_m - \omega_l\right). \tag{A.10}$$

The friction torques $T_{F,m}, T_{F,l}$ acting on the motor and load, respectively, are descri-

bed in the following equations [30]:

$$T_{F,m} = \left[T_{C,m} + (T_{S,m} - T_{C,m})e^{-\left(\frac{\omega_m}{\omega_s}\right)^2}\right] \text{sgn}(\omega_m) + \beta_m \omega_m \tag{A.11}$$

$$T_{F,l} = \left[T_{C,l} + (T_{S,l} - T_{C,l})e^{-\left(\frac{\omega_l}{\omega_s}\right)^2}\right] \text{sgn}(\omega_l) + \beta_l \omega_l \tag{A.12}$$

where the Stribeck velocity ω_s is considered known from offline identification and $\text{sgn}(\cdot)$ is the signum function defined in (II.1). Figure A.5 illustrates the block diagram of the drive-train in open loop.

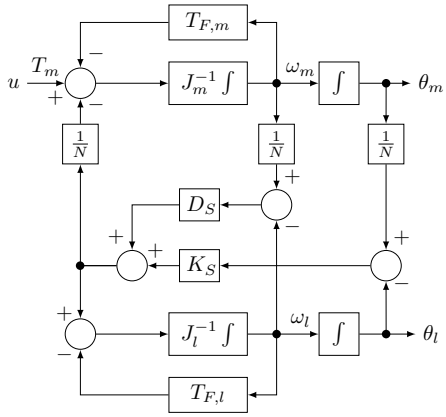

Figure A.5: Block diagram of the open-loop mechanical drive-train system.

A.4 Tool Position Control Methods

The advanced nonlinear control strategies to position the load will be discussed in this section. Three different control algorithms categorized in two main groups are presented. These two categories are the higher-order sliding-mode controllers and the nonlinear adaptive controllers.

Before the control methods are presented, the following assumption is made:

Assumption A.4.1. ***(Compensated input disturbances)***
The input disturbance d_e is compensated via input filtering or appropriate feedforward terms and is not considered in the design.

Although seemingly restrictive, Assumption A.4.1 does not cause any loss of generality in the methods' design. This is because the input uncertainties depend on the current control tuning and motor characteristics, which are both known. Hence, appropriate filtering and feed-forward compensation is the standard approach implemented in commercial products today.

A.4.1 Super-Twisting Sliding-Mode Control

Control schemes using sliding modes, first introduced in [59], have two very attractive features: disturbance estimation and finite-time convergence. The inherent robustness of sliding-mode controllers against unknown dynamics and disturbances is achieved by using discontinuous terms in the control laws.

Over the past three decades there has been more and more literature on higher-order sliding-mode algorithms for control design. The motivation for studying higher-order SMCs is the effect of chattering on the actuators of the system induced by standard SMCs. The higher the order of the controller the better chattering attenuation is achieved. A general discussion on the design of higher-order SMCs was provided in [70]. The design of second-order SMCs was addressed in [71, 72], presenting the *STSMC*, and the problem of chattering attenuation was further discussed by [69]. The application of the STSMC in motion control systems, such as electrical motors and robotic manipulators, was illustrated in [28]. Specific Lyapunov functions that are useful to prove finite time convergence and asymptotic stability of the STSMC were suggested in [73], and an adaptive scheme with dynamically changing controller gains was presented in [75]. The super-twisting sliding-mode algorithm was used in the design of a back-EMF observer for the sensorless vector control of a PMSM in [126]. The design of arbitrary-order SMCs using robust differentiators was suggested in [74].

The architecture considered for the single-axis machine tool system includes an outer loop for the control of the tool position with a P controller. Its output is given as a reference signal to a STSMC, which controls the drive motor's angular velocity. The output of the STSMC is the torque command u, which is the reference signal for the current controller. The corresponding block diagram is shown in Figure A.6.

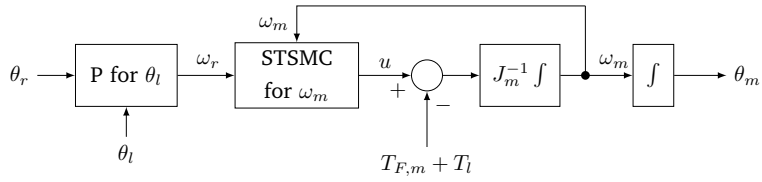

Figure A.6: Tool position control using a cascaded P controller and a STSMC.

The STSMC [28, 75, 78] is a second-order sliding-mode controller which is required for systems with relative degree 2. For systems with relative degree 1, as is the case with the subsystem of the angular velocity ω_m, the use of STSMC offers better chattering attenuation.

For the regulation of the velocity error at zero the sliding variable s is defined as

$$s \triangleq \omega_m - \omega_{m,r} \ . \tag{A.13}$$

Its dynamics reads:

$$\dot{s} = \frac{1}{J_m}\left[\underbrace{u - T_{F,m} - \frac{K_S}{N}\left(\frac{\theta_m}{N} - \theta_l\right) - \frac{D_S}{N}\left(\frac{\omega_m}{N} - \omega_l\right) - J_m\dot{\omega}_{m,r}}_{\psi(\boldsymbol{x})}\right] = \frac{1}{J_m}\left[u + \psi(\boldsymbol{x})\right] \ . \tag{A.14}$$

Assumption A.4.2. ***(Lipschitz continuity)***
The matched perturbation $\psi(\boldsymbol{x})$ is Lipschitz continuous.

The STSMC algorithm is given in [70]

$$u = -k_1|s|^{\frac{1}{2}}\text{sgn}(s) + v \tag{A.15}$$

$$\dot{v} = -k_2\text{sgn}(s) \ . \tag{A.16}$$

The STSMC algorithm ensures finite-time convergence for appropriate positive gains k_1, k_2. The selection of the STSMC gains, although it could be formulated as a LMI problem (see [73]), can be difficult, especially when specific performance requirements are imposed. In the case of high precision control, solutions coming from convergence time requirements often lead to high values of k_1, k_2, making the algorithm more sensitive to measurement noise.

Moreover, the assumption A.4.2 does not hold for the selected friction model, since the sgn$(\cdot)$ function is not Lipschitz continuous. In reality, however, this corresponds to local Lipschitz continuity with very large Lipschitz constant for velocities very close to zero. This means, when the motion changes direction, the system will leave the sliding surface and reach it again very quickly.

Since the controller is of second order and the system's relative degree (for the control of the velocity) is 1, it follows that the additional integrator in the control signal will alleviate the effect of chattering on the actuator [127].

However, Assumption A.4.2 should hold true for the method to be applicable. Since the derivative of the P controller output $\omega_{m,r}$ is used in the control law, an aggressively tuned position controller can yield signals with correspondingly high Lipschitz constants. The higher the Lipschitz constants of the functions whose derivatives are used in the control law, the larger the gains of the controller and, in effect, the more control effort needed for enforcing sliding motion on the system.

A.4.2 Nonlinear Adaptive Control

Adaptive control has been an active field of research since the early sixties. Over this time, a large corpus of literature has been developed covering topics such as regulation and tracking of linear and nonlinear systems, disturbance rejection, etc. Tutorial presentations of the general adaptive control problem were given in [81, 82]. The topics included numerous adaptive control schemes for regulation, tracking, parameter estimation and robust control. The basic scheme for this analysis was the MRAC. The approach was to parameterize the control object such that it contains a known, desired part of the dynamics (reference model dynamics) and an uncertain part dependent on unknown parameters. Theses parameters are updated dynamically until the discrepancy between the desired and obtained output is eliminated. Emphasis was given to solutions for linear systems. The problem of adaptive control for a wider class of nonlinear systems was extensively studied in [83], presenting general design principles for NAC.

A geometric approach to the adaptive control and estimation problem was made in [93] who presented the main results of the I&I-AC theory. These results were elaborated and extended to more constructive methods for I&I-AC design in [94], where several control and estimation problems were re-casted as differential geometry problems. In this approach, the control design is based on the task of finding a manifold on which the system has the required properties (stability, tracking, etc.) and rendering it invariant using an appropriate control law. An I&I-AC control was designed in [95] for robust velocity control of a PMSM and [26] employed a I&I-AC for the tracking problem of a flexible joint manipulator with time-varying mechanical stiffness.

Two control architectures are presented in the following. The first consists of a velocity NAC and a P controller for the tool position in the outer loop. The P position controller outputs the (drive motor) velocity reference signal that is fed to the NAC block. In the second scheme, the outer position P controller is retained, but the drive motor velocity is regulated by an I&I-AC. In both cases, the unknown parameters that the controllers require in their design enter the system linearly, i.e. in a product of the form

$$\boldsymbol{\phi}^T(\boldsymbol{x})\boldsymbol{\vartheta}$$

where $\boldsymbol{\vartheta}$ is the unknown parameter vector and $\boldsymbol{\phi}(\boldsymbol{x})$ is called the *regressor* function. The following assumptions are made:

Assumption A.4.3. ***(Constant unknown parameter vector)***
The unknown parameters $\boldsymbol{\vartheta}$ are assumed to be constant or at least slowly varying,

i.e. their time derivatives are considered to be zero

$$\dot{\boldsymbol{\vartheta}} = \mathbf{0} \, .$$

Assumption A.4.4. ***(Lipschitz continuity)***
The regressor $\boldsymbol{\phi}(\boldsymbol{x})$ is locally Lipschitz.

The design of the two control schemes is in the following.

A.4.2.1 Velocity Nonlinear Adaptive Controller

Figure A.7 shows the first scheme. A P controller to position the tool is used to counter-act the effects of load friction and any other torque that acts on the load. The adaptive part is applied at the level of the control of the drive motor's angular velocity. The dynamics of the latter is written according to (A.6):

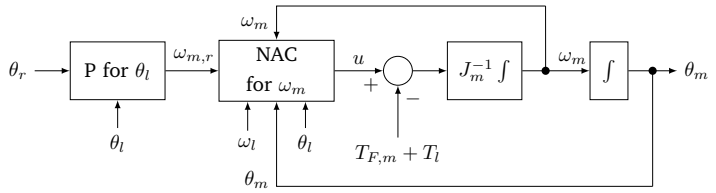

Figure A.7: Tool position control using a cascaded P controller and an NAC.

$$\dot{\omega}_m = \frac{1}{J_m}\left[u - \frac{K_S}{N}\left(\frac{1}{N}\theta_m - \theta_l\right) - \frac{D_S}{N}\left(\frac{1}{N}\omega_m - \omega_l\right) - T_{F,m}\right]$$

where the input uncertainty d_e is omitted according to Assumption A.4.1 and the friction $T_{F,m}$ is defined in (A.11). The shaft stiffness K_S, damping coefficient D_S, motor Coulomb friction $T_{C,m}$, stiction $T_{S,m}$ and the viscous friction coefficient β_m are considered unknown positive constants, where each value belongs to a known compact subset of $\mathbb{R}$. Let $\omega_{m,r} \in \mathbb{R}$ be the motor velocity reference signal coming from the position P controller. Let the velocity error be defined as

$$e_\omega \triangleq \omega_m - \omega_{m,r} \, . \tag{A.17}$$

Its dynamics is written as:

$$\begin{aligned}\dot{e}_\omega &= \frac{1}{J_m}\left[u - \frac{K_S}{N}\left(\frac{1}{N}\theta_m - \theta_l\right) - \frac{D_S}{N}\left(\frac{1}{N}\omega_m - \omega_l\right) - T_{F,m}\right] - \dot{\omega}_{m,r} \\ &= \frac{1}{J_m}\left[u + \boldsymbol{\phi}^T(\boldsymbol{x})\boldsymbol{\vartheta}\right] - \dot{\omega}_{m,r}\end{aligned} \tag{A.18}$$

where $\boldsymbol{x} = \begin{bmatrix} \omega_m & \theta_m & \omega_l & \theta_l \end{bmatrix}^T$ is the drive train state vector, $\boldsymbol{\vartheta}$ is the unknown parameter vector defined as

$$\boldsymbol{\vartheta} \triangleq \begin{bmatrix} K_S & D_S & T_{C,m} & T_{S,m} & \beta_m \end{bmatrix}^T \tag{A.19}$$

and $\boldsymbol{\phi}(\boldsymbol{x})$ is the regressor function defined as

$$\boldsymbol{\phi}(\boldsymbol{x}) \triangleq \begin{bmatrix} -\frac{1}{N}\left(\frac{1}{N}\theta_m - \theta_l\right) \\ -\frac{1}{N}\left(\frac{1}{N}\omega_m - \omega_l\right) \\ -\left[1 - e^{-\left(\frac{\omega_m}{\omega_S}\right)^2}\right] \operatorname{sgn}(\omega_m) \\ -e^{-\left(\frac{\omega_m}{\omega_S}\right)^2} \operatorname{sgn}(\omega_m) \\ -\omega_m \end{bmatrix} . \tag{A.20}$$

Theorem A.4.1. *The control law*

$$u = -\boldsymbol{\phi}^T(\boldsymbol{x})\hat{\boldsymbol{\vartheta}} - ke_\omega + J_m\dot{\omega}_{m,r} \tag{A.21}$$

together with the adaptation laws

$$\dot{\hat{\boldsymbol{\vartheta}}} = \boldsymbol{\Gamma}\boldsymbol{\phi}(\boldsymbol{x})e_\omega \tag{A.22}$$

where k is a positive real number and $\boldsymbol{\Gamma}$ a 5×5 positive definite real matrix, ensure that the velocity tracking error e_ω with dynamics given in Equation (A.18) *converges to the origin $e_\omega^* = 0$ as $t \to \infty$, i.e.*

$$\lim_{t\to\infty} e_\omega(t) = 0 .$$

Moreover, the parameter estimation error $\tilde{\boldsymbol{\vartheta}} \triangleq \boldsymbol{\vartheta} - \hat{\boldsymbol{\vartheta}}$ remains bounded for all future times.

Proof. If the parameters $\boldsymbol{\vartheta}$ were known, then a control law

$$u = -\boldsymbol{\phi}^T(\boldsymbol{x})\boldsymbol{\vartheta} + J_m\dot{\omega}_{m,r} - ke_\omega \ , \ k > 0$$

would render the origin $e_\omega^* = 0$ an asymptotically stable equilibrium point of the error system. According to [83], an equivalence-principle control law (where the estimates of the parameters are used instead)

$$u = -\boldsymbol{\phi}^T(\boldsymbol{x})\hat{\boldsymbol{\vartheta}} + J_m\dot{\omega}_{m,r} - ke_\omega \tag{A.23}$$

where $\hat{\boldsymbol{\vartheta}}$ is the estimate of the real parameter vector, will give the following tracking error dynamics

$$\dot{e}_\omega = \frac{1}{J_m}\left[\boldsymbol{\phi}^T(\boldsymbol{x})\tilde{\boldsymbol{\vartheta}} - ke_\omega\right] \tag{A.24}$$

with $\tilde{\boldsymbol{\vartheta}} = \boldsymbol{\vartheta} - \hat{\boldsymbol{\vartheta}}$. The parameter vector estimate $\hat{\boldsymbol{\vartheta}}$ is dynamically updated. In order to determine its update law, the following Lyapunov function candidate is considered:

$$V = \frac{1}{2}J_m e_\omega^2 + \frac{1}{2}\tilde{\boldsymbol{\vartheta}}^T\boldsymbol{\Gamma}^{-1}\tilde{\boldsymbol{\vartheta}}\ .$$

Noting that $\dot{\boldsymbol{\vartheta}} = \mathbf{0}$, the time derivative of V along the trajectories of (A.24) reads:

$$\dot{V} = -ke_\omega^2 + e_\omega\boldsymbol{\phi}^T(\boldsymbol{x})\tilde{\boldsymbol{\vartheta}} - \tilde{\boldsymbol{\vartheta}}^T\boldsymbol{\Gamma}^{-1}\dot{\hat{\boldsymbol{\vartheta}}}\ . \tag{A.25}$$

Taking the following update law for $\hat{\boldsymbol{\vartheta}}$

$$\dot{\hat{\boldsymbol{\vartheta}}} = \boldsymbol{\Gamma}e_\omega\boldsymbol{\phi}(\boldsymbol{x}) \tag{A.26}$$

and substituting in (A.25) yields

$$\dot{V} = -ke_\omega^2 \leq 0\ , \tag{A.27}$$

which implies that V is non-increasing. Since $V(e_\omega(t), \tilde{\boldsymbol{\vartheta}}(t)) \geq 0,\ \forall t \geq 0$, it follows that V is bounded and, by extension, $e_\omega(t), \tilde{\boldsymbol{\vartheta}}(t)$ are also bounded for all future times. Taking the second time-derivative of V leads to

$$\ddot{V} = -\frac{2k}{J_m}\left[e_\omega\boldsymbol{\phi}^T(\boldsymbol{x})\tilde{\boldsymbol{\vartheta}} - ke_\omega^2\right]\ ,$$

Boundedness of $e_\omega, \tilde{\boldsymbol{\vartheta}}$ implies that $\ddot{V}$ is also bounded and, as a result, that $\dot{V}$ is uniformly continuous. Then, since $\lim_{t\to\infty} V(t) = V(\infty) \leq V(0)$ is finite, by applying Barbalat's lemma [83, Lemma A.6] it is shown that $\lim_{t\to\infty} \dot{V}(e_\omega(t)) = 0$. From (A.27) it can be seen that

$$\lim_{t\to\infty} e_\omega(t) = 0\ ,$$

which completes the proof. ■

Remark A.1. Existence of the closed-loop system solutions requires $\boldsymbol{\phi}(\boldsymbol{x})$ to be locally Lipschitz. This does not hold since its derivative is not bounded at 0. If, however, sgn$(\cdot)$ is approximated with a sigmoid function, e.g.

$$\text{sgn}(y) \approx \frac{2}{\pi}\arctan(\alpha y) \triangleq \rho(\alpha, y)$$

where α is a positive number denoting the slope of the function near 0, then Assumption A.4.4 holds and the theorem can be applied.

This approximation is commonly used for the implementation of control algorithms with switching terms. In the case of Coulomb friction, the sensitivity of the sgn$(\cdot)$ function to noise-inflicted measurements can induce friction-compensating torques in the wrong direction and with high frequency leading to actuator damage or even instability. For large values of the scaling factor α (e.g. $\alpha \geq 100$), $\rho(\alpha, y)$ approximates sgn(y) with sufficient precision for the applications and $\lim_{\alpha\to\infty} \rho(\alpha, y) = \text{sgn}(y)$.

Remark A.2. The derivative of the velocity reference ω_r is calculated from available signals, as shown below:

$$\dot{\omega}_r = \frac{d}{dt}\left(k_{pos} e_\theta + \dot{\theta}_r\right) = k_{pos}\left(\dot{\theta}_r - \omega_l\right) + \ddot{\theta}_r \ . \tag{A.28}$$

Moreover, note that parameter convergence to the real values is not guaranteed, unless $\phi(\boldsymbol{x})$ is persistently exciting (see Definition 4 in Appendix II). However, the estimation error remains bounded for all future times.

A.4.2.2 Velocity Immersion and Invariance Adaptive Controller

The second adaptive control scheme has the same architecture as the NAC strategy shown in Figure A.7. The difference is in the type of the velocity adaptive controller. The main concept of the I&I-AC is presented in the following definition.

Definition 1. ***[94, Def. 3.1] (I&I stabilizable system)***
Consider the system

$$\dot{\boldsymbol{x}} = \boldsymbol{f}(\boldsymbol{x}) + \boldsymbol{g}(\boldsymbol{x})\boldsymbol{u}$$

where $\boldsymbol{f}, \boldsymbol{g}$ depend on an unknown parameter vector $\boldsymbol{\vartheta} \in \mathbb{R}^q$ and assume that there exists a function $\boldsymbol{\upsilon}(\boldsymbol{x}, \boldsymbol{\vartheta})$ such the control law $\boldsymbol{u} = \boldsymbol{\upsilon}(\boldsymbol{x}, \boldsymbol{\vartheta})$ renders the equilibrium $\boldsymbol{x} = \boldsymbol{x}^*$ globally asymptotically stable. Then the system is I&I stabilizable if there exist $\boldsymbol{h}(\cdot)$ and $\boldsymbol{w}(\cdot)$ such that all trajectories of the extended system

$$\dot{\boldsymbol{x}} = \boldsymbol{f}(\boldsymbol{x}) + \boldsymbol{g}(\boldsymbol{x})\boldsymbol{\upsilon}(\boldsymbol{x}, \hat{\boldsymbol{\vartheta}} + \boldsymbol{h}(\boldsymbol{x})) \tag{A.29}$$

$$\dot{\hat{\boldsymbol{\vartheta}}} = \boldsymbol{w}(\boldsymbol{x}, \hat{\boldsymbol{\vartheta}}) \tag{A.30}$$

are bounded and satisfy

$$\lim_{t\to\infty}\left[\boldsymbol{g}(\boldsymbol{x}(t))\boldsymbol{\upsilon}(\boldsymbol{x}, \hat{\boldsymbol{\vartheta}} + \boldsymbol{h}(\boldsymbol{x})) - \boldsymbol{g}(\boldsymbol{x}(t))\boldsymbol{\upsilon}(\boldsymbol{x}, \boldsymbol{\vartheta})\right] = \boldsymbol{0} \ . \tag{A.31}$$

In the I&I-AC, the standard approach is to define the manifold

$$\mathcal{M} = \{(\boldsymbol{x}, \hat{\boldsymbol{\vartheta}}) \in \mathbb{R}^n \times \mathbb{R}^q | \hat{\boldsymbol{\vartheta}} - \boldsymbol{\vartheta} + \boldsymbol{h}(\boldsymbol{x}) = \boldsymbol{0}\} \tag{A.32}$$

where $\boldsymbol{h}(\boldsymbol{x})$ is a function to be defined, and then design an update law for $\boldsymbol{\vartheta}$, which makes $\mathcal{M}$ invariant. Once the system is on this manifold, the unknown parameter

vector $\boldsymbol{\vartheta}$ can be calculated by $\boldsymbol{\vartheta} = \hat{\boldsymbol{\vartheta}} + \boldsymbol{h}(\boldsymbol{x})$. Note that the design of $\boldsymbol{h}(\boldsymbol{x})$ is also included in this process. The following steps are applied when designing the I&I-AC for the drive motor angular velocity:

The dynamics for velocity tracking error e_ω is given by

$$\dot{e}_\omega = \frac{1}{J_m}\left[u + \boldsymbol{\phi}^T(\boldsymbol{x})\boldsymbol{\vartheta} - \frac{1}{N}T_l\right] - \dot{\omega}_{m,r} \tag{A.33}$$

where now the unknown parameter vector is defined as

$$\boldsymbol{\vartheta} \triangleq \begin{bmatrix} T_{C,m} & T_{S,m} & \beta_m & b \end{bmatrix}^T \tag{A.34}$$

the regressor function $\boldsymbol{\phi}(\boldsymbol{x})$ is defined as

$$\boldsymbol{\phi}(\boldsymbol{x}) \equiv \boldsymbol{\phi}(\omega_m) \triangleq \begin{bmatrix} -\left[1 - e^{-\left(\frac{\omega_m}{\omega_S}\right)^2}\right]\text{sgn}(\omega_m) \\ -e^{-\left(\frac{\omega_m}{\omega_S}\right)^2}\text{sgn}(\omega_m) \\ -\omega_m \\ -1 \end{bmatrix} \tag{A.35}$$

and T_l is defined in Equation (A.10). Since only the varying friction is considered unknown, the shaft parameters are not included in the design. This considerably simplifies the complexity of the control algorithm. Parameter b serves as an additional integral term that can compensate for minor variations of the interconnection torque T_l due to small uncertainties in the shaft parameters.

Theorem A.4.2. *The control law*

$$u = \frac{1}{N}T_l - \boldsymbol{\phi}^T(\omega_m)\left(\hat{\boldsymbol{\vartheta}} + \boldsymbol{h}(\omega_m)\right) - k_{II}e_\omega + J_m\dot{\omega}_r \tag{A.36}$$

together with the adaptation laws

$$\dot{\hat{\boldsymbol{\vartheta}}} = \frac{\partial \boldsymbol{h}}{\partial \omega_m}\frac{1}{J_m}\left(k_{II}e_\omega - J_m\dot{\omega}_r\right) \tag{A.37}$$

with k_{II} being a positive real number and the real function $h : \mathbb{R} \to \mathbb{R}^4$ being defined as

$$\boldsymbol{h}(\omega_m) = J_m\boldsymbol{\Gamma_{II}}\begin{bmatrix} -|\omega_m| + \frac{\omega_S\sqrt{\pi}}{2}\text{erf}(\frac{\omega_m}{\omega_S})\text{sgn}(\omega_m) \\ -\frac{\omega_S\sqrt{\pi}}{2}\text{erf}(\frac{\omega_m}{\omega_S})\text{sgn}(\omega_m) \\ -\frac{1}{2}\omega_m^2 \\ -\omega_m \end{bmatrix} \tag{A.38}$$

where $\boldsymbol{\Gamma_{II}}$ a 4×4 is a positive definite real matrix and erf$(\cdot)$ *is the error function defined in* (II.5)*, ensure that the velocity tracking error e_ω with dynamics given*

in Equation (A.33) *converges to the origin* $e_\omega^* = 0$ *as* $t \to \infty$*, i.e.*

$$\lim_{t\to\infty} e_\omega(t) = 0 \, .$$

Additionally, the parameter estimation error $\tilde{\boldsymbol{\vartheta}}$ *remains bounded for all future times.*

Proof. Similarly to the case of NAC, applying the equivalence principle control law yields the following velocity error dynamics

$$\dot{e}_\omega = \frac{1}{J_m}\left[-k_{II}e_\omega - \boldsymbol{\phi}^T(\omega_m)\left(\hat{\boldsymbol{\vartheta}} + \boldsymbol{h}(\boldsymbol{x}) - \boldsymbol{\vartheta}\right)\right] \, . \tag{A.39}$$

The new feature when compared to NAC is the "parameter offset" function $\boldsymbol{h}(x)$, which quantifies the deviation of the estimated parameter vector $\hat{\boldsymbol{\vartheta}}$ from its real value. The objective is to find a function $\boldsymbol{h}(x) \equiv \boldsymbol{h}(\omega_m)$ and an update law $\dot{\hat{\boldsymbol{\vartheta}}} = \boldsymbol{w}(\boldsymbol{x}, \hat{\boldsymbol{\vartheta}})$ such that the manifold

$$\mathcal{M} = \{(\omega_m, \hat{\boldsymbol{\vartheta}}) \in \mathbb{R} \times \mathbb{R}^4 | \hat{\boldsymbol{\vartheta}} - \boldsymbol{\vartheta} + \boldsymbol{h}(\omega_m) = \boldsymbol{0}\} \tag{A.40}$$

is rendered invariant. To achieve this, the *off-the-manifold* coordinate

$$\boldsymbol{z} \triangleq \hat{\boldsymbol{\vartheta}} - \boldsymbol{\vartheta} + \boldsymbol{h}(\omega_m) \tag{A.41}$$

is defined. Its dynamics reads

$$\begin{aligned}\dot{\boldsymbol{z}} &= \dot{\hat{\boldsymbol{\vartheta}}} + \frac{\partial \boldsymbol{h}}{\partial \omega_m}\dot{\omega}_m = \boldsymbol{w}(\boldsymbol{x}, \hat{\boldsymbol{\vartheta}}) + \frac{\partial \boldsymbol{h}}{\partial \omega_m}\frac{1}{J_m}\left[u + \boldsymbol{\phi}^T(\omega_m)\boldsymbol{\vartheta} - \frac{1}{T_l}\right] \\ &= \boldsymbol{w}(\boldsymbol{x}, \hat{\boldsymbol{\vartheta}}) + \frac{\partial \boldsymbol{h}}{\partial \omega_m}\frac{1}{J_m}\left[-\boldsymbol{\phi}^T(\omega_m)\boldsymbol{z} - k_{II}e_\omega + J_m\dot{\omega}_r\right]\end{aligned} \tag{A.42}$$

where Assumption (A.4.3) and Equations (A.36), (A.41) were used. Selecting

$$\boldsymbol{w}(\boldsymbol{x}, \hat{\boldsymbol{\vartheta}}) = \frac{\partial \boldsymbol{h}}{\partial \omega_m}\frac{1}{J_m}\left(k_{II}e_\omega - J_m\dot{\omega}_r\right) \tag{A.43}$$

the dynamics of the $\boldsymbol{z}$-coordinate becomes

$$\dot{\boldsymbol{z}} = -\frac{1}{J_m}\frac{\partial \boldsymbol{h}}{\partial \omega_m}\boldsymbol{\phi}^T(\omega_m)\boldsymbol{z} \, . \tag{A.44}$$

Selecting $\boldsymbol{h}$ such that

$$\frac{\partial \boldsymbol{h}}{\partial \omega_m} = J_m\boldsymbol{\Gamma_{II}}\boldsymbol{\phi}(\omega_m) \tag{A.45}$$

suggests

$$\boldsymbol{h}(\omega_m) = J_m\boldsymbol{\Gamma_{II}}\begin{bmatrix} -|\omega_m| + \frac{\omega_S\sqrt{\pi}}{2}\text{erf}(\frac{\omega_m}{\omega_S})\text{sgn}(\omega_m) \\ -\frac{\omega_S\sqrt{\pi}}{2}\text{erf}(\frac{\omega_m}{\omega_S})\text{sgn}(\omega_m) \\ -\frac{1}{2}\omega_m^2 \\ -\omega_m \end{bmatrix} \, . \tag{A.46}$$

Substituting $\boldsymbol{h}$ in (A.44) yields

$$\dot{\boldsymbol{z}} = -\boldsymbol{\Gamma_{II}}\boldsymbol{\phi}(\omega_m)\boldsymbol{\phi}^T(\omega_m)\boldsymbol{z} \tag{A.47}$$

which verifies that the solutions $\boldsymbol{z}(t)$ of (A.47) are bounded since $\boldsymbol{\phi}(\omega_m)\boldsymbol{\phi}^T(\omega_m)$ is positive semidefinite. To prove that $\mathcal{M}$ is attractive and invariant, it is sufficient to show that

$$\lim_{t\to\infty} \boldsymbol{z}(t) = \lim_{t\to\infty} \dot{\boldsymbol{z}}(t) = 0 \, .$$

This is actually equivalent to fulfilling condition (A.31) in Definition 1. Consider the real-valued positive-definite Lyapunov function candidate $V : \mathbb{R}^4 \to \mathbb{R}$ defined as:

$$V(\boldsymbol{z}(t)) = \frac{1}{2}\boldsymbol{z}(t)^T\boldsymbol{z}(t) \geq 0 \, . \tag{A.48}$$

Its time derivative along the trajectories of (A.47) is given by

$$\dot{V}(\boldsymbol{z}(t)) = -\boldsymbol{z}^T(t)\boldsymbol{\phi}(\omega_m)\boldsymbol{\phi}^T(\omega_m)\boldsymbol{z}(t) \leq 0 \tag{A.49}$$

which implies that $V(\boldsymbol{z}(t))$ is not increasing for all $t \geq 0$. Integrating (A.49) from both sides yields

$$0 \leq \int_0^\infty \boldsymbol{z}^T(t)\boldsymbol{\phi}(\omega_m(t))\boldsymbol{\phi}^T(\omega_m(t))\boldsymbol{z}(t)dt \leq V(\boldsymbol{z}(0)) - V(\boldsymbol{z}(\infty)) \, .$$

This means that $\boldsymbol{z}(t) \in \mathcal{L}_2 \ , \ \forall t \geq 0$, while $\omega_m(t)$ remains bounded for all future times. Taking the second time derivative of V gives

$$\ddot{V}(\boldsymbol{z}(t)) = -2\boldsymbol{\phi}(\omega_m)\boldsymbol{\phi}^T(\omega_m)\boldsymbol{z}(t) - \frac{d}{dt}\left[\boldsymbol{\phi}(\omega_m)\boldsymbol{\phi}^T(\omega_m)\right]\boldsymbol{z}(t) \, . \tag{A.50}$$

The symmetric positive semidefinite matrix

$$\boldsymbol{\phi}(\omega_m)\boldsymbol{\phi}^T(\omega_m) = \begin{bmatrix} \left(1 - e^{-\left(\frac{\omega_m}{\omega_S}\right)^2}\right)^2 & \star & \star & \star \\ \left(1 - e^{-\left(\frac{\omega_m}{\omega_S}\right)^2}\right) e^{-\left(\frac{\omega_m}{\omega_S}\right)^2}\operatorname{sgn}(\omega_m) & e^{-2\left(\frac{\omega_m}{\omega_S}\right)^2} & \star & \star \\ \left(1 - e^{-\left(\frac{\omega_m}{\omega_S}\right)^2}\right)|\omega_m| & e^{-\left(\frac{\omega_m}{\omega_S}\right)^2}|\omega_m| & \omega_m^2 & \star \\ \left(1 - e^{-\left(\frac{\omega_m}{\omega_S}\right)^2}\right)\operatorname{sgn}(\omega_m) & e^{-\left(\frac{\omega_m}{\omega_S}\right)^2}\operatorname{sgn}(\omega_m) & \omega_m & 1 \end{bmatrix}^T$$

(where $\star$ denotes the symmetric elements) is not a Lipschitz continuous function because the derivative of $\operatorname{sgn}(\omega_m)$ is infinite at 0. Considering the approximation of $\operatorname{sgn}(\omega_m)$ with the function $\frac{2}{\pi}\arctan(\alpha\omega_m)$ introduced in the design of the NAC makes $\boldsymbol{\phi}(\omega_m)\boldsymbol{\phi}^T(\omega_m)$ Lipschitz continuous and, by extension, its derivative is bounded. Since the signals $\omega_m(t)$ and $\boldsymbol{z}(t)$ are also bounded, the same holds for $\ddot{V}$. This

implies that $\dot{V}$ is uniformly continuous and since $\lim_{t\to\infty} V(\boldsymbol{z}(t)) = V(\boldsymbol{z}(\infty)) \geq 0$ is finite, applying Barbalat's lemma [83, Lemma A.6] gives

$$\lim_{t\to\infty} \boldsymbol{z}(t) = \mathbf{0} \,. \tag{A.51}$$

From (A.44) it also follows that $\lim_{t\to\infty} \dot{\boldsymbol{z}}(t) = \mathbf{0}$, which proves that $\mathcal{M}$ is invariant.

The closed-loop velocity error dynamics

$$\dot{e}_\omega = -\frac{1}{J_m}\left[k_{II} e_\omega + \boldsymbol{\phi}(\omega_m)\boldsymbol{\phi}^T(\omega_m)\boldsymbol{z}\right] \tag{A.52}$$

can be seen as the cascaded interconnection of a convergent system ($\boldsymbol{z}-$dynamics) with a UGAS system (unperturbed velocity error dynamics):

$$\dot{\boldsymbol{z}} = -\frac{1}{J_m}\boldsymbol{\phi}(\omega_m)\boldsymbol{\phi}^T(\omega_m)\boldsymbol{z} \tag{A.53}$$

$$\dot{e}_\omega = -\frac{1}{J_m} k_{II} e_\omega \,. \tag{A.54}$$

Since e_ω is Input-to-State Stable (ISS) with respect to $\boldsymbol{z}$ (see IV for a proof), convergence of $\boldsymbol{z}(t)$ to zero implies that $\lim_{t\to\infty} e_\omega(t) = 0$, i.e. the velocity tracking error system is also convergent. Lastly, since $\boldsymbol{z}(t), \boldsymbol{h}(\omega_m)$ are bounded, it follows from (A.41) that the parameter estimation error $\tilde{\boldsymbol{\vartheta}}$ is also bounded, which completes the proof. ■

Finally, similar to the NAC case, $\dot{\omega}_r$ is calculated from Equation (A.28).

A comparative presentation of the assumptions considered in each method, as well as the main features of the three nonlinear control strategies is given in Table A.2.

A.5 Experiments and Evaluation

A.5.1 Experimental Setup

The experimental setup consists of two Siemens FT7042-5AF70 PMSMs connected through a stainless steel shaft. Both motors are equipped with a Siemens SINAMICS S120 drive converter with 11-bit absolute encoders for the position. A cylindrical Vari-tork 279.25.22 adjustable-friction clutch [108] is mounted on a steel base and houses the interconnecting shaft (see Figure A.8). The friction is developed between the inner cylinder, housing the shaft, and the outer bearing of the component. A ring adjusts the friction between these two surfaces, increasing it as it turns clockwise. The entire drive train with the friction component are shown in Figure A.9.

Table A.2: Assumptions and features of the methods.

Assumptions	**Theoretical features**
STSMC	
• Matched perturbation is Lipschitz continuous (A.4.2)	• Finite-time convergence • Robustness against any type of Lipschitz disturbances
NAC	
• Regressor function is Lipschitz continuous (A.4.4) • Parameters are constant or slowly varying (A.4.3)	• Velocity error converges to zero • Uniformly bounded parameter estimation error
I&I-AC	
• Regressor function is Lipschitz continuous (A.4.4) • Parameters are constant or slowly varying (A.4.3)	• Velocity error converges to zero • Parameters can be indirectly calculated if the regressor is persistently exciting

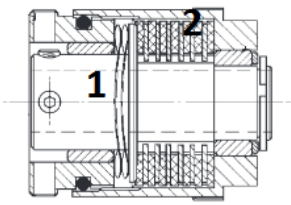

Figure A.8: Schematic of Vari-tork 273.25.22 adjustable-friction clutch: (1) inner bearing housing the interconnecting shaft, (2) outer bearing.

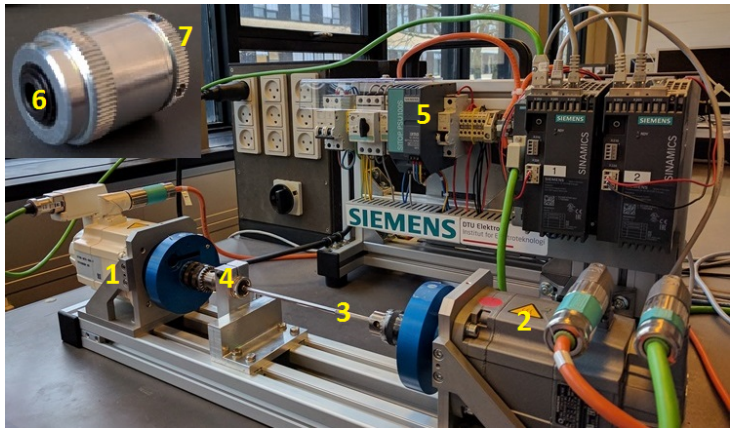

Figure A.9: Experimental setup: (1) 1FT7 drive PMSM, (2) 1FT7 load PMSM, (3) shaft, (4) friction component base, (5) Siemens SINAMICS S120 converter, (6) shaft housing, (7) friction adjustment ring.

The current control loop in the drive motor consists of two PI controllers, one for magnetizing and one for torque-generating. The design and tuning of these controllers is not included in this study.

A.5.2 Test Scenarios

Fifteen different scenarios were considered for the experimental assessment of the performance of the control algorithms. The reference for the position of the load was a sinusoid,

$$\theta_r(t) = \Theta_0 \sin(2\pi f_r t) \ ,$$

where Θ_0 is the position amplitude in rad and f_r is the frequency in Hz. Three types of nominal operation are considered, namely, a very slow one with $f_r = 0.1\mathrm{Hz}$, a slow one with $f_r = 0.5\mathrm{Hz}$ and a fast one with $f_r = 2\mathrm{Hz}$. In all three cases the amplitude is $1\ \mathrm{rad}$. For each frequency, four different cases of increased Coulomb friction and stiction are considered, ranging from 215% to 900%. Each case corresponds to a specific angular position of the friction component ring. The fifteen different scenarios are shown in Table A.3. Although friction increases of 615% and 900% (Tests 10-15) are less likely to occur in real applications, as the machine will have been decommissioned long before friction reaches such levels, the last two cases are included in the study to test the performance limits of the controllers.

Since the reference signal is a trigonometric function of time, it is easy to obtain its time derivative of any order. For the experiments, the reference generator provides up to the third time derivative of $\theta_r(t)$.

Table A.3: Test scenarios.

No	Θ_0 (rad)	$T_{C,m}$ (N m)	f_r (Hz)	Increase in friction
1	1	0.035	0.1	0
2	1	0.035	0.5	0
3	1	0.035	2	0
4	1	0.11	0.1	215%
5	1	0.11	0.5	215%
6	1	0.11	2	215%
7	1	0.15	0.1	330%
8	1	0.15	0.5	330%
9	1	0.15	2	330%
10	1	0.25	0.1	615%
11	1	0.25	0.5	615%
12	1	0.25	2	615%
13	1	0.35	0.1	900%
14	1	0.35	0.5	900%
15	1	0.35	2	900%

The controllers parameters were selected according to Table A.4. The controllers were tuned in the nominal case (with the friction clutch dismounted from the test rig), such that the maximum absolute positioning error is below $5 \cdot 10^{-3}$ rad at 0.5 Hz for all control schemes. The outer loop position P controller gain was kept the same in all schemes, and the proportional gains of all three nonlinear velocity controllers (k_1, k, k_{II}) were set after the PI proportional gain k_p.

In all control schemes, $\dot{\theta}_r$ is added as a feedforward term to the position P controller output.

A.5.3 Controllers Comparison Criteria

A combination of quantitative and qualitative criteria is employed for the comparison of the control algorithms. The first group consists of five performance indices that describe the positioning accuracy and efficiency of each method. Specifically, these indices are [129]:

- MAE. This corresponds to the maximum peak of the positioning error $e_\theta = \theta_l - \theta_r$ and it is defined over a time interval $T > 0$ as

$$MAE = \sup_{t_0 \le t \le t_0+T} |e_\theta(t)|. \tag{A.55}$$

Table A.4: Controller parameters values.

Symbol	Description	Value
Outer loop P		
k_{pos}	Proportional gain	9
PI		
k_p	Proportional gain	0.9
T_n	Integral reset time	0.06
STSMC		
k_1	Switching gain	0.9
k_2	Integral sw. gain	75
NAC		
k	Proportional gain	0.6
diag($\mathbf{\Gamma}$)	Adaptation gains	$\left[10^{-5},\ 0.5,\ 0.12,\ 0.12,\ 4.5\right]$
$\hat{\vartheta}_0$	Initial conditions	$[17,\ 0.003,\ 0,\ 0,\ 0.0008]^T$
I&I-AC		
k_{II}	Proportional gain	0.6
diag ($\mathbf{\Gamma_{II}}$)	Adaptation gains	$[0.1203,\ 0.012,\ 0.012,\ 0.012]$
$\hat{\vartheta}_0$	Initial conditions	$[0.003,\ 0,\ 0,\ 0.0008]^T$

- ISE. This is an averaged squared error index and it is defined over a time interval $T > 0$ as

$$ISE = \frac{1}{T}\int_{t_0}^{t_0+T} e_\theta^2(t)dt. \tag{A.56}$$

- ITSE. This is an averaged squared error index which focuses on the steady state error. It is defined over a time interval $T > 0$ as

$$ITSE = \frac{1}{T}\int_{t_0}^{t_0+T} te_\theta^2(t)dt. \tag{A.57}$$

- CP. This is metric of the average power of the control signal. It is defined over a time interval $T > 0$ as

$$CP = \frac{1}{T}\int_{t_0}^{t_0+T} u^2(t)dt. \tag{A.58}$$

- ECP. This describes the efficiency of the control algorithm. Lower ECP corresponds to greater efficiency. It is defined over a time interval $T > 0$ as

$$ECP = MAE \cdot CP = \sup_{t_0 \le t \le t_0+T} |e_\theta(t)| \cdot \frac{1}{T}\int_{t_0}^{t_0+T} u^2(t)dt. \tag{A.59}$$

An additional criterion that is indicative for the lag between reference and actual position of the tool is the MAPE. This error is important in machines with more than two axes, since delays in positioning, in combination with no synchronization between the axes, may result in a distorted contour. Since there is only one axis, the experiments are run twice with the reference being shifted by $\frac{\pi}{2}$ during the second time in order to emulate a circular trajectory. Specifically, the position signals are scaled appropriately so that they both have amplitude 1. The scaled x,y positions are given by

$$\theta_{x,y}(t) = \frac{1}{\Theta_0}\theta_l(t)$$

and the corresponding reference signals

$$\theta_x^r(t) = \frac{1}{\Theta_0}\theta_r(t) = \sin(2\pi f_r t)$$
$$\theta_y^r(t) = -\frac{1}{\Theta_0}\theta_r\left(t - \frac{\pi}{2}\right) = \cos(2\pi f_r t)\ .$$

Assuming that the axes have identical characteristics and control system, the MAPE is defined over a time interval $T > 0$ as

$$MAPE = \sup_{t_0 \le t \le t_0+T} |e_\phi(t)| \text{ with} \tag{A.60}$$
$$e_\phi(t) = \tan^{-1}\left(\frac{\theta_y^r(t)}{\theta_x^r(t)}\right) - \tan^{-1}\left(\frac{\theta_y(t)}{\theta_x(t)}\right)\ . \tag{A.61}$$

It should be noted that, although phase errors are primarily relevant for machines with multiple-axes, the MAPE is indicative of the positioning accuracy of just one axis. In the case of machines with more degrees of freedom, additional lag can be induced due to lack of synchronization between the different axes [18]. Added to the total lag coming from response delays at each axis, this distorts the actual machining trajectory profiles.

The qualitative criteria include a graphical depiction of the amplitude and phase errors in an $\theta_x - \theta_y$ plot, similar to the ones used in a CIT (or ballbar test) in machine tools [10]. Ideally the $\theta_x - \theta_y$ curve is a circle of radius 1. Deviations from this circular path are indicative of the controllers' accuracy with respect to radial or lag errors. Two more qualitative criteria are the number of tunable parameters and the complexity of the design of each method, which is reflected in the number of assumptions made for each method.

A.5.4 Results

The results from the experiments are presented in this section. Each controller was tested on the experimental setup for 500 s so that any slowly deteriorating

behaviour can also be captured. Controller performance was evaluated for 20 s near the end of each experiment, specifically over the time interval $[400, 420]$ s. This was done to allow the parameters in the adaptation schemes to settle, thus emulating a long-term operation of the machine and also to avoid including initial errors in the analysis due to the setpoint ramping up.

Table A.5 shows the MAE for all the different controllers during all tests. At 0.1 and 0.5 Hz, the performance of the PI already starts to degrade with the first additional friction with MAE exceeding the prescribed accuracy limit (10 mrad). For the highest friction, the error is approximately four times higher than the limit. It should be noted that improving the PI performance with respect to the MAE means that the proportional gain k_p has to be increased. This means that the system reaches its stability limits ($k_p \geq 1.8$) with MAE at best $3.8 \cdot 10^{-3}$ rad for the nominal case, as tested experimentally. The STSMC performs better than all the controllers with the lowest MAE, and also below the accuracy limit. In the case of the slowest motion profile, the STSMC achieves a MAE almost 10 times lower than the specified performance. In the last friction case the STSMC performs just over the limit without any significant chatter. This can be also seen in Figure A.10, where the positioning errors and torque commands for all controllers for test 7 are shown.

Table A.5: MAE in mrad for all controllers in all scenarios. The indices 1-4 denote the four different friction cases.

Controller	nominal	1	2	3	4
MAE in mrad at 0.1 Hz					
PI	12	17.9	20.3	24.4	30.3
STSMC	0.9	1.5	1.9	2.9	3.8
NAC	7.8	8.3	12.9	20.2	40.7
I&I-AC	7.8	12.5	18.5	33.3	43
MAE in mrad at 0.5 Hz					
PI	4.9	15.6	17	23.7	37.2
STSMC	2	3	4.1	7.5	10.9
NAC	2.2	7.5	12.2	21.1	35
I&I-AC	4.9	7.2	13.2	20.3	34.3
MAE in mrad at 2 Hz					
PI	12.3	20.1	21.8	31.6	45.7
STSMC	7	6.8	7.2	10.6	12.3
NAC	8.7	6.8	6.9	7.1	7.3
I&I-AC	5.8	6.7	6	5.7	9.2

In the same figure, as well from Table A.5, it can be seen that at low frequencies

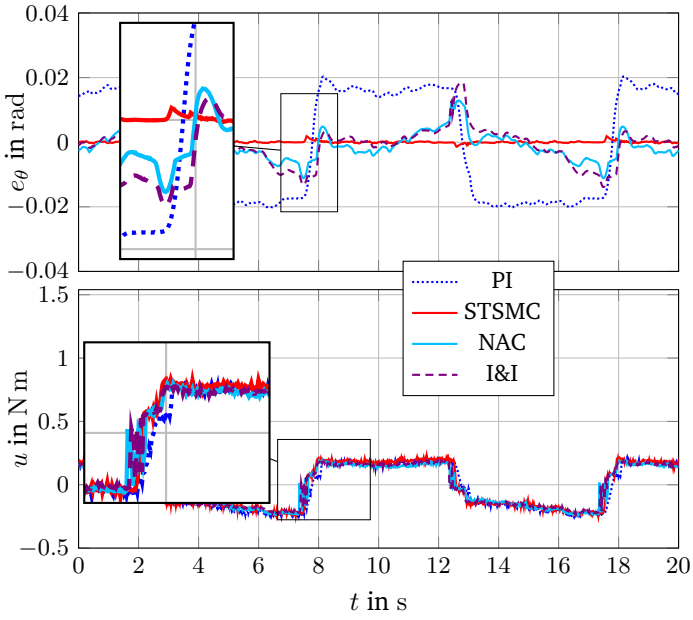

Figure A.10: Positioning errors and torque commands for Test 7. No excessive STSMC chatter is present in the command torque.

both the adaptive controllers fail to maintain the positioning error below the limit during the last three friction cases. The limit is exceeded when the sign of the velocity changes, as it can be seen in Figure A.11. This is due to the fact that the friction adjustment ring inherently has a dead zone of approximately 0.035 rad between the shaft housing and outer cylinder. The backlash that is induced causes a step change in the friction parameters (from nominal inside the dead zone to the increased value outside of the dead zone). The parameters cannot be adapted for changes as fast as these and, consequently, the adaptive controllers cannot compensate for the effects of the backlash. The hysteric behaviour of the motor friction due to the dead zone can be seen in Figure A.12, where the friction is calculated according (A.11) and the estimated parameters from I&I-AC.

The situation is different when the system operates at 2 Hz. Since the time spent within the dead zone is significantly shorter, just adapting the Coulomb friction outside the dead zone is sufficient for to keep the positioning error below the limit. The NAC and the I&I-AC have the best performance with the STSMC degrading only in the last friction case and the PI in all cases. The corresponding positioning errors and torque commands are shown in Figure A.13.

A comparative visualisation of the performance indices can be seen in Figure A.14, where the PI indices have been taken as the baseline. The figure illustrates

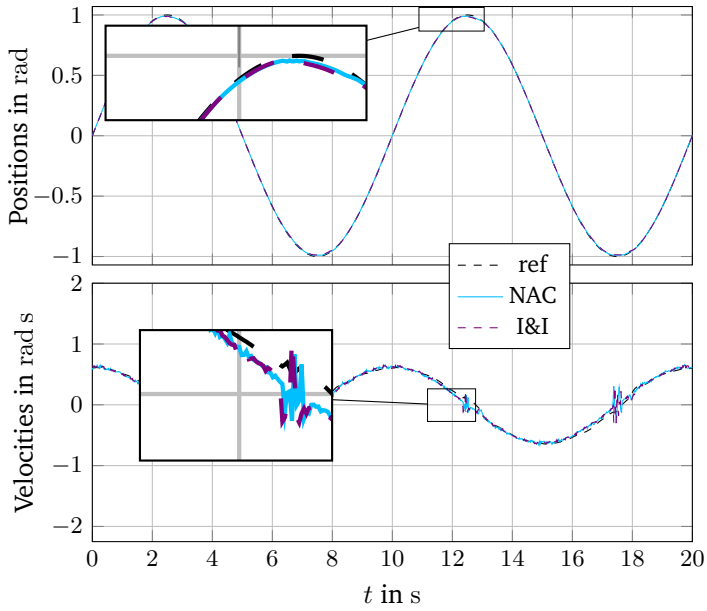

Figure A.11: Load position and motor velocity of the adaptive controllers for Test 7.

the ratio between the indices of the nonlinear controllers and the respective ones of the PI scheme. It can be observed that in 13 of the 15 experiments the nonlinear controllers outperform the PI, with the STSMC being the most efficient. At 2 Hz, the adaptive controllers have a similar performance to the STSMC with slightly better efficiency, while they significantly degrade at low frequencies as the friction increases. These results are also illustrated in Figures A.15 and A.16, where the MAE and ECP of the controllers are plotted with respect to the increasing Coulomb friction.

Figure A.17 shows the MAPE of the controllers for all friction cases at 0.1, 0.5 and 2 Hz. Comparing these plots to the ones in Figure A.15, it can be seen that the positioning error in the case of the adaptive controllers, especially during operation at low frequencies, is primarily due to deviations from the setpoint rather than the actual position lagging the reference signal. However, this is not the case for the PI, since its MAPE increases consistently as MAE increases.

A visualization of the resulting phase error, which functions as a qualitative assessment of the controllers' performance is provided in the form of $\theta_x - \theta_y$ plots shown in Figure A.18 for the third friction value (Tests 7-9). Here the positioning errors and the accuracy limits have been scaled up by a factor of 5 to improve readability. It can be seen from these graphs that the STSMC performs consistently well at all frequencies, while the adaptive controllers only perform better at 2 Hz.

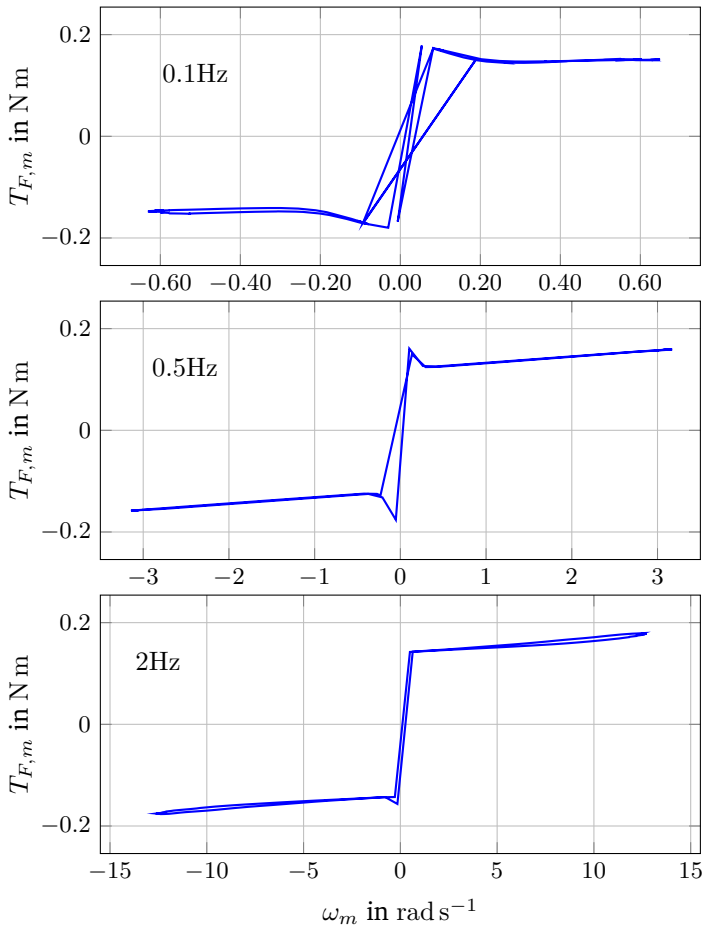

Figure A.12: Motor velocity-friction plot using the estimated values from I&I-AC in Tests 7-9 (top to bottom).

Finally, the estimation of the Coulomb friction in all tests for both the NAC and the I&I-AC is shown in Figure A.19. It can be seen that, although in all of the tests the estimated parameter approaches the real value, it does not necessarily settle close to it. This correlates with the fact that the adaptive laws (A.22) guarantee only boundedness of the parameter estimation error and not convergence to 0. For I&I-AC, the adaptation of parameter b, which captures small perturbations due to shaft uncertainties, also contributes to any deviations of the estimated friction from the real value. It is worth noticing that the estimated nominal Coulomb friction during operation at 2Hz is much closer to the real value of the parameter. This is due to the fact that in fast operation the sign of the angular velocity changes more frequently, i.e. the term of the regressor function $\phi(x)$ that corresponds to $T_{C,m}$ is

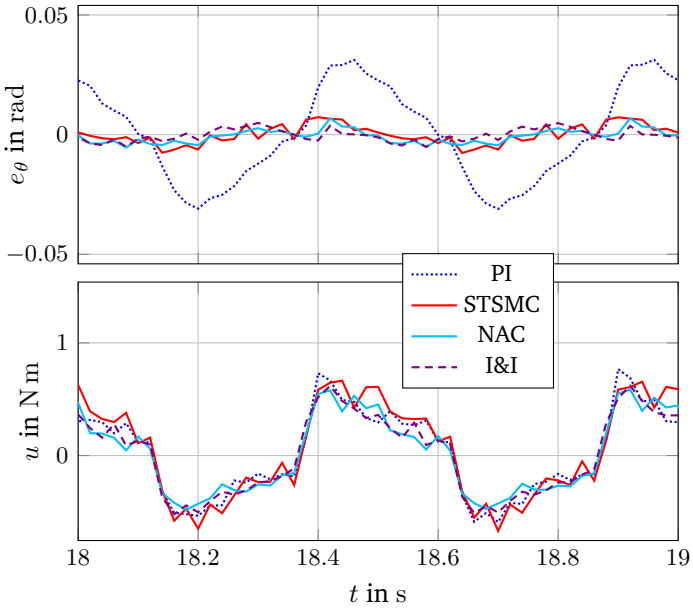

Figure A.13: Positioning errors and torque commands for Test 9.

exciting the system more than at 0.1 and 0.5 Hz.

A criterion that is indicative of the design and implementation complexity of the control methods is the number of tunable parameters and signals required. Table A.6 gives an overview of this information. The NAC has the largest number of tunable parameters and signals required in the algorithm. This is expected, since it incorporates more modelling information in its design when compared to the other three. Both the NAC and the I&I-AC require the second derivative of the position reference signal $\ddot{\theta}_r$ since this is needed to calculate of $\dot{\omega}_r$.

Table A.6: Number of tunable parameters and signals required for each controller.

	Tunable	Total	Signals	Total
PI	k_{pos}, k_p, T_n	3	$\theta_r, \dot{\theta}_r, \theta_l, \omega_m$	4
STSMC	k_{pos}, k_1, k_2	3	$\theta_r, \dot{\theta}_r, \ddot{\theta}_r, \theta_l, \omega_m, \omega_l$	6
NAC	$k_{pos}, k, \boldsymbol{\Gamma}, \hat{\boldsymbol{\vartheta}}_{\mathbf{0}}$	12	$\theta_r, \dot{\theta}_r, \ddot{\theta}_r, \boldsymbol{x}$	7
I&I-AC	$k_{pos}, k_{II}, \boldsymbol{\Gamma}_{\boldsymbol{II}}, \hat{\boldsymbol{\vartheta}}_{\mathbf{0}}$	10	$\theta_r, \dot{\theta}_r, \ddot{\theta}_r, \theta_l, \omega_m, \omega_l$	6

It should be noted that if shaft parameters K_S, D_S were considered in the case of I&I-AC, its design would be far more complicated. This is due to the fact that the regressor function $\boldsymbol{\phi}$ in (A.35) - and by extension - function $\boldsymbol{h}$, would depend on the entire state vector $\boldsymbol{x}$ instead of just the motor angular velocity ω_m. This means that

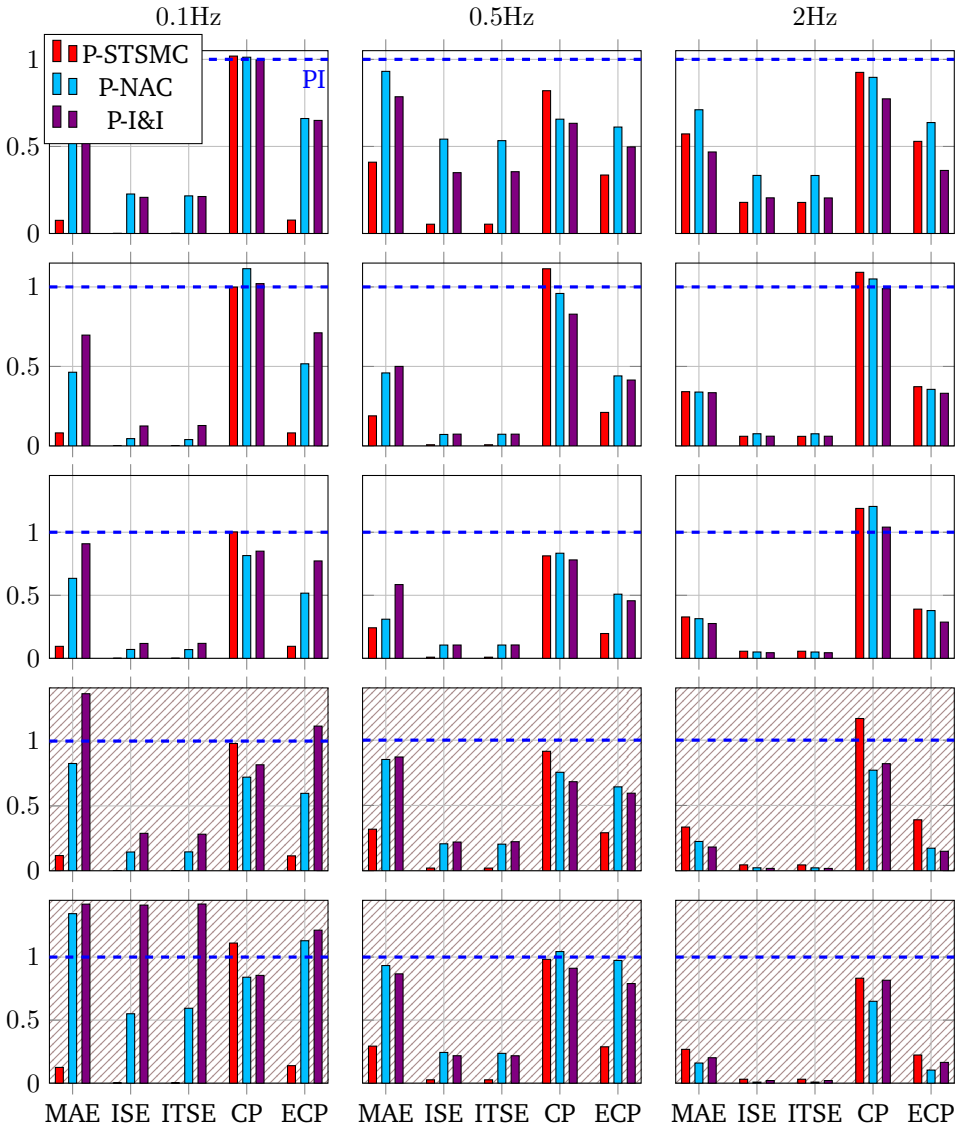

Figure A.14: Relative performance indices. The different cases of friction start with nominal friction and increase from top to bottom. The plots in the stripped area correspond to the extreme friction cases.

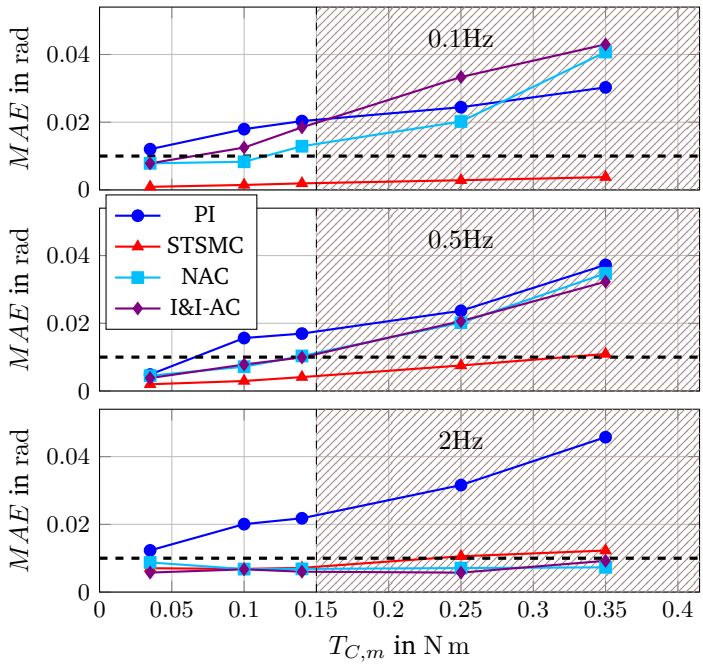

Figure A.15: MAE for all friction cases at 0.1Hz (top), 0.5Hz (middle) and 2Hz (bottom). The dashed line correspond to the $\pm 10^{-2}\text{rad}$ accuracy bound introduced in Problem A and the stripped area denotes the extreme friction cases.

instead of the Partial Differential Equation (PDE) in (A.45), the solution of a 5×5 system of PDEs would have been required, which is not a trivial task and it may not be possible to obtain a closed-form analytical solution.

Another point regarding the NAC and the I&I-AC is the selection of the initial parameter estimates $\hat{\boldsymbol{\vartheta}}_{\mathbf{0}}$. As can be seen from both (A.24) and (A.39), a higher initial parameter error gives a substantially large initial velocity error, which results in faster adaptation rates. This could cause the parameter estimates to overshoot and reach values outside their specified limits, possibly causing unwanted system behaviour. This can be alleviated to some extent by using parameter projection algorithms (see [83, 99] for more details), however, at the cost of risking that already converged parameters move away from their correct value and settle to another one.

In order to visualise the overall performance of the four controllers, a plot of the average MAE and ECP is shown in Figure A.20 for the different friction cases.

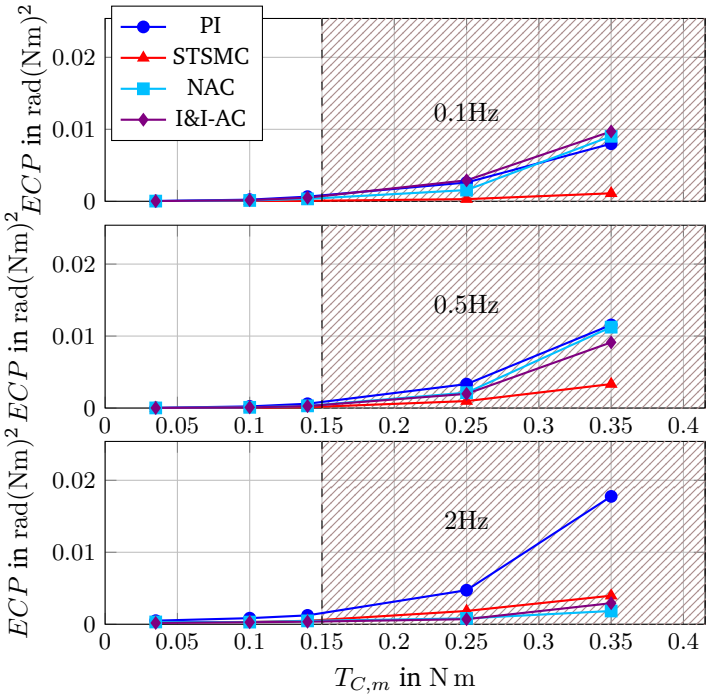

Figure A.16: ECP for all friction cases at 0.1Hz (top), 0.5Hz (middle) and 2Hz (bottom). The stripped area denotes the extreme friction cases.

A.6 Conclusions and Future Work

The problem of robust high precision position control in machine tool systems with increasing unknown friction was addressed in this paper. Three nonlinear position control schemes were designed, implemented and tested on a real single-axis drive-train consisting of state-of-the-art Siemens equipment in both nominal and increased-friction operation at three different frequencies. The nonlinear controllers were evaluated and compared to a standard P-PI cascade, typically used in industry. The comparison was based on numerical performance indices as well as qualitative criteria, such as the number of tunable parameters and design complexity.

The results demonstrated that all three nonlinear controllers perform better than the P-PI scheme, both in nominal operation and with increased friction (except for the last extreme friction case). Specifically, the STSMC has the best average performance with respect to the MAE over all of the frequency and friction cases that were investigated. At the lowest frequency it achieves a MAE 10 times smaller than that of the other three controllers. For average and fast speed motion profiles, it consistently keeps the error within the specified requirements bound in all cases

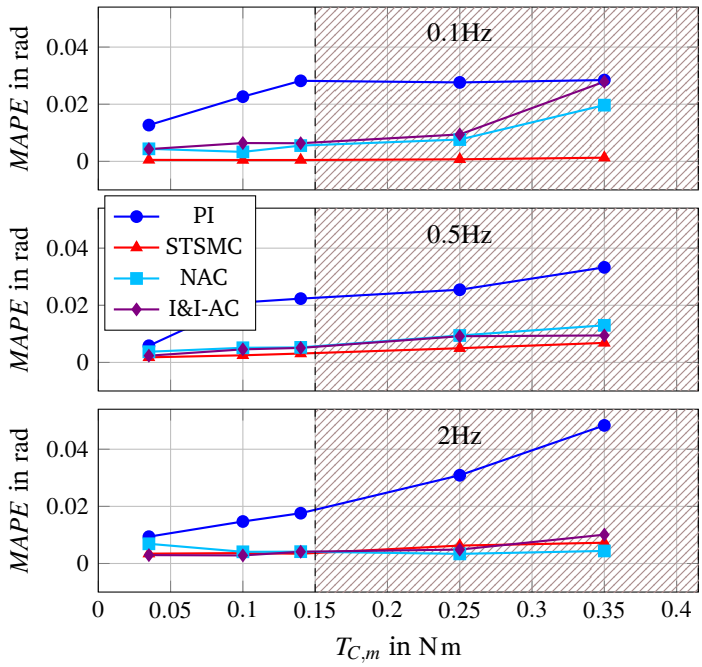

Figure A.17: MAPE for all friction cases at 0.1Hz (top), 0.5Hz (middle) and 2Hz (bottom). The stripped area denotes the extreme friction cases.

of realistic friction. The exception is the case of fast motion with the highest, and hardly realistic value of friction.

The adaptive controllers NAC and I&I-AC only provide positioning within the performance limits at 2 Hz. Although they outperform the STSMC in the extreme friction cases, they fail to keep the positioning error below the required bound at low frequencies (0.1 and 0.5 Hz) for increasing friction. The degradation of the adaptive schemes is mainly due to the effect of backlash, which is not included in the adaptive design and to slower adaptation conditions, since the friction parameter estimation rate depends on the velocity of the motor. In terms of design complexity, the STSMC appears to be simpler to implement since the number of tunable parameters is three times smaller than for the adaptive controllers.

Future work in this area will include comparison of direct position nonlinear control architectures, such as the adaptive backstepping, the nested continuous singular terminal SMC and the $\mathcal{L}_1$ adaptive control, with the ones presented in this paper. Robustness against additional degrading phenomena, such as varying load inertia and backlash should also be investigated.

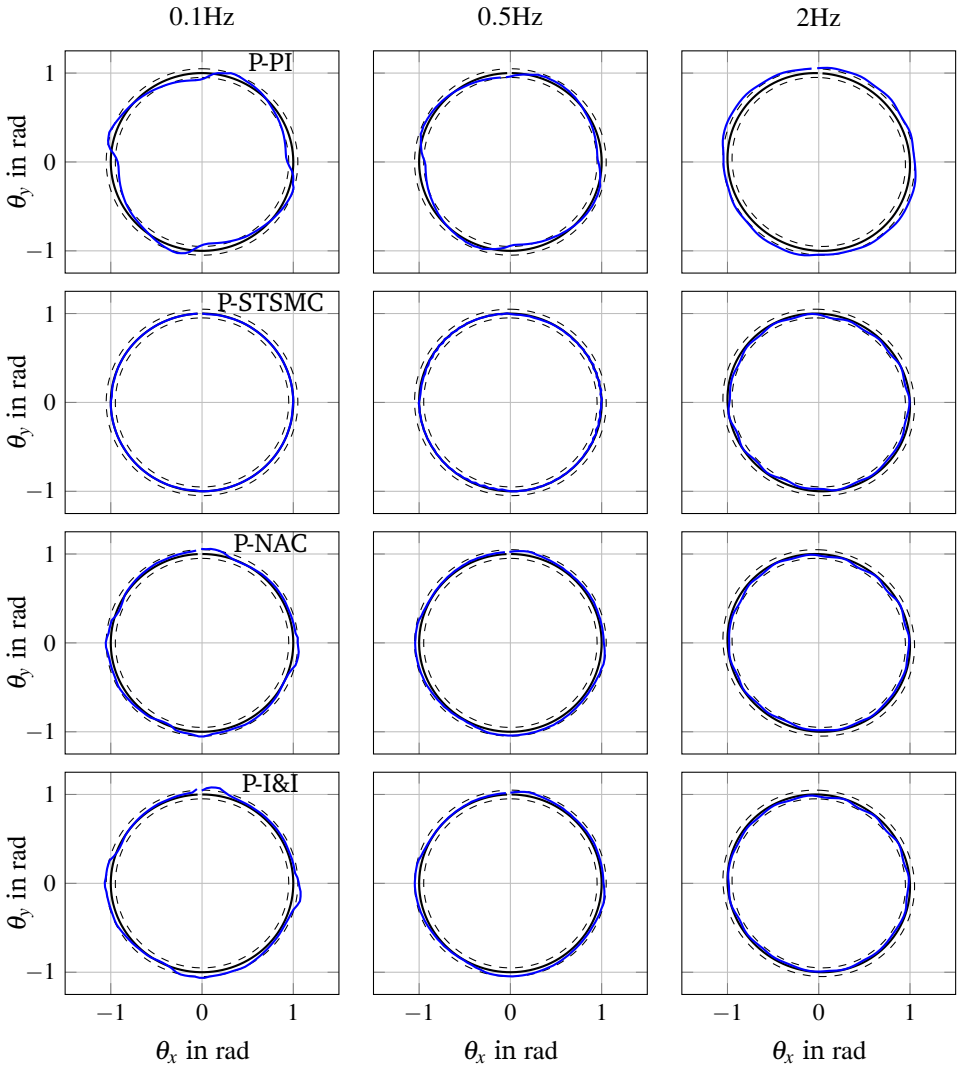

Figure A.18: $\theta_x - \theta_y$ plot for one cycle during Tests 7 (left column), 8 (middle column) and 9 (right column). From top to bottom: PI, STSMC, NAC, I&I-AC. The dashed circles correspond to the $\pm 10^{-2}\mathrm{rad}$ accuracy limit introduced in Problem A. For increased clarity, both the error and the accuracy limits have been enlarged by a factor of 5.

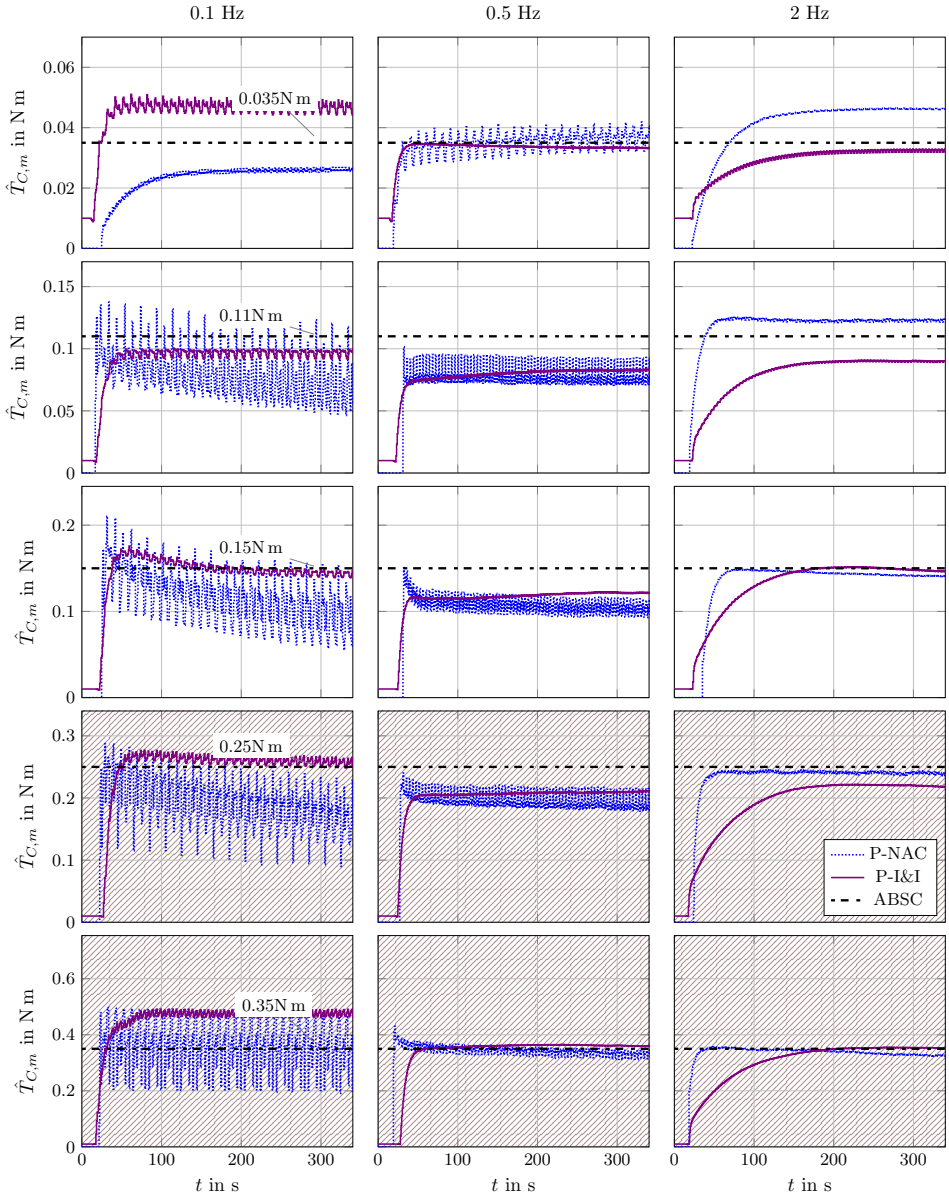

Figure A.19: Coulomb friction estimation during all NAC and I&I-AC tests. The different cases of friction start with nominal friction and increase from top to bottom. The plots in the stripped area correspond to the extreme friction cases.

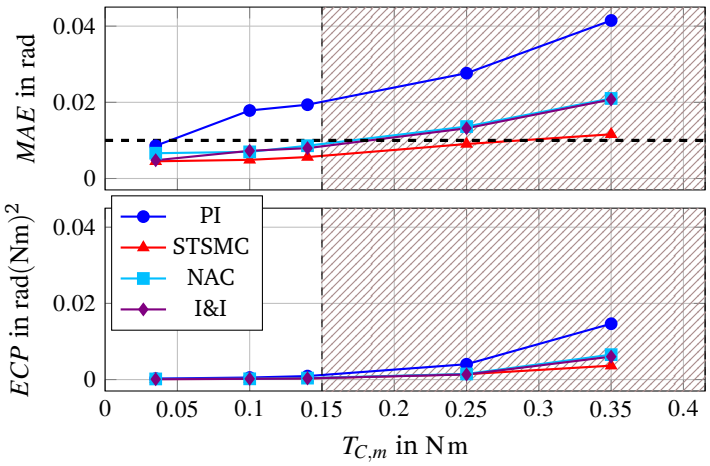

Figure A.20: Average MAE (top) and ECP (bottom) for all friction cases. The dashed line correspond to the $\pm 10^{-2}\mathrm{rad}$ accuracy bound introduced in Problem A and the stripped area denotes the extreme friction cases.

Acknowledgements

The authors would like to thank Dr. Carsten Hamm and Dr. Hans-Georg Koepken from Siemens AG, Digital Factory Division, Motion Control for their support with integrating the controllers into the existing Siemens software. Their invaluable input with respect to the real-life machine tool applications and equipment is greatly appreciated.

The project is sponsored by Siemens AG.

Paper B

Friction-Resilient Position Control for Machine Tools - Adaptive and Sliding-Mode Methods Compared

Dimitrios Papageorgiou[*1], Mogens Blanke[2], Hans Henrik Niemann[1], Jan H. Richter[3]

[1]Department of Electrical Engineering, Automation and Control Group, Technical University of Denmark, Elektrovej Building 326, 2800, Kgs. Lyngby, Denmark.

[2]AMOS CoE, Institute of Technical Cybernetics, Norwegian University of Science and Technology, Trondheim, Norway.

[3]Siemens AG, Digital Factory Division, D-90475 Nuremberg, Germany

Abstract:
Robust trajectory tracking and increasing demand for high-accuracy tool positioning have motivated research in advanced control design for machine tools. State-of-the-art solutions employ cascades of P and PI controllers for closed loop servo control of position and velocity of the tool. Although these schemes provide the required positioning accuracy in nominal conditions, performance is shown to deteriorate in the presence of degrading phenomena such as increased friction and wear. With conventional control, re-tuning would be necessarily during the lifetime of a computer controlled machine if specified accuracy should be maintained. This paper analyses the design and performance of selected direct-position controllers. Conventional solutions are compared to model-based adaptive and sliding-mode control principles, with focus on resilience to unknown and increasing friction. A single-axis test setup is used to assess the performance of different controllers.

[*]Principal corresponding author. Tel.: +45 45253572; E-mail: dimpa@elektro.dtu.dk

B.1 Introduction

Mechanical components are manufactured using automated machine tools for cutting, drilling, milling, shearing etc, on a wide range of materials. Sophisticated mechanical designs lead to narrow workpiece tolerances, which necessitate high-accuracy tool positioning. Several mechanical phenomena could compromise workpiece tolerances if not properly handled by closed-loop control. This paper will focus on friction phenomena.

To meet modern manufacturing requirements, fully automated machining systems are required that can be adapted to varying workspace conditions and must be robust to equipment degradation due to wear and tear. State-of-the-art tool-positioning solutions achieve adequate performance only under nominal conditions. In presence of equipment wear, controllers need to be frequently re-tuned. The need for achieving nominal performance even in the presence of incipient wear motivates the investigation of nonlinear control strategies for tool positioning.

Previous research that has dealt with nonlinear control techniques, such as SMC and nonlinear adaptive control (see [24, 25, 27, 40, 41]) had focus on stability of the closed-loop error dynamics, without emphasizing high-accuracy tool positioning. Friction compensation for machine tools by using nonlinear controllers has been sparsely addressed [44], while to the best of the authors' knowledge, there has not been any comprehensive real-time implementation and comparison of nonlinear solutions, especially by testing with realistic machine-tool working cycles. Friction resilience was studied in [1], who presented design and a comparative evaluation of three nonlinear controllers. The architecture of these controllers constituted a cascade of position-velocity control, which is the same architecture used by conventional state-of-the-art solutions.

This paper continues prior work [1] by considering another architecture and three new nonlinear controllers for machine tool position control. The nonlinear controls in this paper are again based on sliding-mode and adaptive methodologies. These control schemes, namely the ABSC, the OSTSMC and the ASTSMC, utilize a direct-position control architecture, i.e. they do not consist of position-velocity cascades. In this way, frictional phenomena and model uncertainties are addressed both for the drive motor and the load, in contrast to the cascaded controllers in [1], which compensated only for the drive motor friction. A machine tool specific design is made using each of the suggested methods and details on the design and analysis are provided. The proposed controllers are compared to a standard P-PI cascade control on an industrial test-rig. The comparison includes both nominal case, unknown friction and incipient friction.

The paper is organised as follows: Part B.2 gives a description of the physical system of the problem being addressed. Part B.3 provides the modelling details and assumptions for the single-axis mechanical drive-train. Part B.4 presents the different control schemes used for tool positioning. The design of each architecture is provided and comments are offered with respect to theoretical assumptions made for each method. Experimental results on the evaluation of the controllers' performance are presented in Part B.5. Section B.6 provides an overall comparison of the control schemes presented in this paper and in [1]. Finally, conclusions and future work are discussed in Part B.7.

B.2 System Description and Problem Formulation

Typical single-axis machine tools consist of a drive motor connected to an angular-to-linear motion conversion system (e.g. a ball-screw), which linearly positions the tool [18]. All the mechanical components connected to the machine spindle can be viewed as the serial interconnection of torsional springs. The lumped masses and damping of these springs motivate the description of the single-axis machine tool as mechanical drive-train comprising the drive motor, a flexible shaft with damping and a generalized load with friction as shown in Figure B.1. This drive-train abstraction of the single-axis machine tool will be the basis for comparing the different control algorithms presented in this paper.

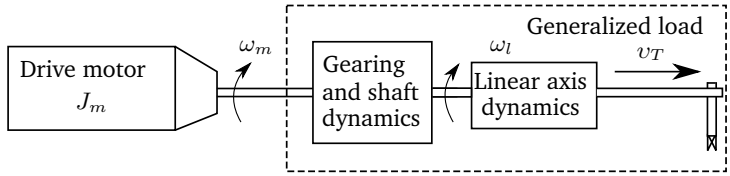

Figure B.1: Correspondence between mechanical drive-train and single-axis machine-tool systems, where ω_m, ω_l are the motor and load angular velocities, respectively, and v_T is the linear velocity of the tool.

B.2.1 Physical System and Positioning Accuracy

The physical system used in [1] (see Figure B.11) is also used in this paper. Two identical Siemens 1FT7 permanent magnet synchronous motors (PMSMs) [106] equipped with a Siemens SINAMICS S120 drive converter [107] are connected via a steel shaft. The first motor acts as the driving actuator, while the second motor emulates the load of the axis either as pure inertia or by applying various torque profiles.

The objective is to regulate the load position into tracking a given reference profile. The required precision in linear positioning in machine-tool applications typically is $1 - 10\ \mu m.$ corresponds to an angular positioning tolerance between $5 \cdot 10^{-3}$ and $2 \cdot 10^{-2}$ rad [18]. The specification for the maximum angular positioning error in this study is considered 10^{-2} rad.

B.2.2 Friction and Positioning Degradation

The friction that develops between the surfaces of the mechanical parts of the machine acts as a decelerating torque both on the drive motor and the load. Its positioning-degrading effect is usually addressed by adding appropriate feed-forward terms in the low-level control algorithms. Although calculation of the friction characteristics is typically done during the commissioning of the machine drive, these compensation schemes assume constant friction characteristics. As a result, they fail to preserve positioning accuracy when friction parameters change due to equipment wear [39] (for example deformation of the bearing surfaces of the motors and linear axes, lubrication film failure etc.) or environmental changes,s such increased workspace temperature, which can cause increased Coulomb friction and viscosity [116].

Consequently, a tool-positioning control strategy that can ensure nominal performance irrespectively of friction changes is a highly desirable feature for machine tools. This is the reason that friction with variable characteristics is chosen to be the degrading phenomenon, against which the nonlinear controllers designed for the drive-train will be compared and evaluated.

The friction acting on the drive motor can be different than the one affecting the load. Depending the motion profile of the machine different friction models can be used. When the motor moves fast (above 30 rpm) Coulomb and viscous friction dominate. In the case of very low motor speed (below 5 rpm) more complex phenomena, such as hysteresis and Stribeck pre-sliding take place. In such cases more complicated models are used [29, 32]. Since the load in the physical system is identical to the drive motor, the nominal friction is considered the same on both sides. This assumption is valid on the basis of the friction sources being the same for the drive motor and the load.

B.2.3 Problem Formulation

The problem addressed in this paper is the same from [1] and is repeated in the following for completeness:

Problem B (Friction-resilient accuracy control for single-axis machine tool)**.** *Consider a single-axis machine tool system consisting of a drive motor connected to a load with a flexible shaft. Let the tool positioning error be denoted by* e_θ *and let* $T_{C,m}^{max}$ *be an upper bound for the Coulomb friction magnitude* $T_{C,m}$ *on the motor side. Design a closed-loop control strategy that ensures:*

$$|e_\theta(t)| \leq 10 \text{ mrad } \forall t \geq t_0 > 0 \text{ and for } T_{C,m} \leq T_{C,m}^{max}$$

where t_0 *denotes a time after the starting up of the positioning task for the machine.*

In the above problem formulation the bound $T_{C,m}^{max}$ describes the maximum value of Coulomb friction, above which alleviation of the positioning degradation is not addressed by means of low-level axis control.

B.3 Mathematical Model

B.3.1 Drive Train Mechanical Dynamics

The drive train system comprises a drive motor connected to a load via a flexible shaft. Based on Figure B.1 the mechanical dynamics can be described as the interaction between the motor and the load inertias, as seen in Figure B.2.

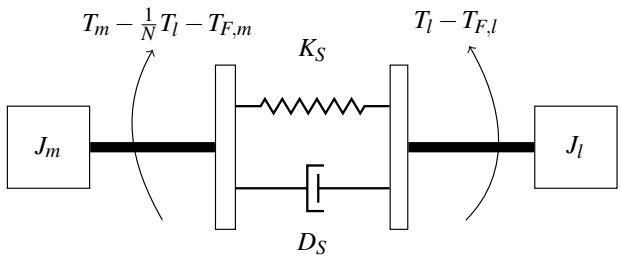

Figure B.2: Drive-train mechanical dynamics. The torque generated by the drive motor is denoted with T_m, the interconnecting torque is T_l, N is the gearing ratio between motor and load and $T_{F,m}, T_{F,l}$ is the friction on the motor and the load side, respectively.

This description corresponds to a two-mass-spring-damper system, with dynamics

given by:

$$\dot{\omega}_m = \frac{1}{J_m} T_m - \frac{1}{J_m} T_{F,m}(\omega_m) - \frac{1}{N J_m} T_l \tag{B.1}$$

$$\dot{\theta}_m = \omega_m \tag{B.2}$$

$$\dot{\omega}_l = -\frac{1}{J_l} T_{F,l}(t, \omega_l) + \frac{1}{J_l} T_l - \frac{1}{J_l} T_{ext}(t) \tag{B.3}$$

$$\dot{\theta}_l = \omega_l \tag{B.4}$$

where ω_m, θ_m and ω_l, θ_l are the velocities and positions of the motor and the load, respectively, T_m is the torque generated by the drive motor and the interconnection torque T_l is given from:

$$T_l = K_S \left(\frac{1}{N} \theta_m - \theta_l \right) + D_S \left(\frac{1}{N} \omega_m - \omega_l \right) . \tag{B.5}$$

The friction torques $T_{F,m}, T_{F,l}$ acting on the motor and load, respectively, are described by the Coulomb-viscous model [30]:

$$T_{F,i} = T_{C,i} \text{sgn}(\omega_i) + \beta_i \omega_i \; i \in \{m, l\} \tag{B.6}$$

where $\text{sgn}(\cdot)$ is the signum function defined in (II.1).

B.3.2 Closed-Loop Electrical Dynamics

The input torque T_m to the mechanical drive train is the output of the drive motor's electrical subsystem, which includes the dynamics of the direct and quadrature axis currents i_d and i_q, respectively [109]. The control of i_d, i_q such that a given torque command u is generated by the drive motor is done separately from the rest of the system dynamics and it is not considered in this study. As in [1], the following modelling assumption is made:

Assumption B.3.1. *The closed-loop electrical dynamics can be considered as a unit gain perturbed by a finite number of torque ripples, i.e. the produced torque by the motor is the torque command plus a bounded disturbance:*

$$T_m = u + d_e \; . \tag{B.7}$$

The torque disturbance d_e contains harmonics with maximum amplitude approximately 0.5% of the maximum torque at frequencies below 100 Hz. This can be validated from Figure B.3, which shows the response of the actual drive motor torque to different step commands. For the motor of the physical system $u_{max} = 13 \text{ N m}$ [106].

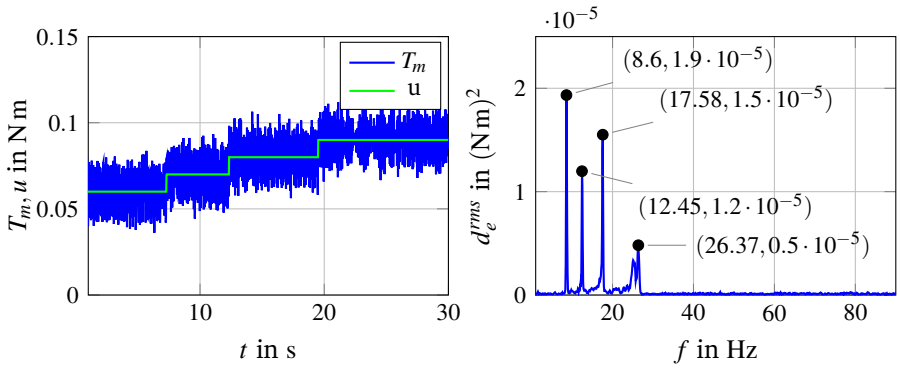

Figure B.3: (Left): Step torque commands and actual torque. (Right): Power and frequency locations of torque ripples.

Table B.1 provides a complete explanation of the notation used in the equations above.

B.4 Tool Position Control Methods

State-of-the-art industrial solutions for load positioning include a cascade of P and PI controllers, that command the necessary accelerating torque for the drive motor. Two individual PI controllers (for the direct and quadrature currents) ensure that this torque is actually generated by the motor. The control scheme is shown in Figure B.4. As mentioned in Section B.3, the generated motor torque is assumd to

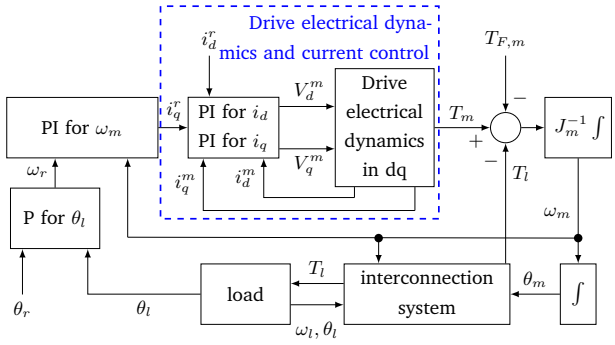

Figure B.4: State of the art in industrial position control using cascaded P and PI controllers.

be equal to the torque command plus a bounded input disturbance d_e. Moreover, the following design assumption is made:

Table B.1: System model nomenclature

Symbol	Description	Units
States and Outputs		
ω_m	Motor angular velocity	$\mathrm{rad\,s^{-1}}$
θ_m	Motor angular position	rad
ω_l	Load angular velocity	$\mathrm{rad\,s^{-1}}$
θ_l	Load angular position	rad
Inputs		
θ_r	Load position reference	rad
ω_r	Motor velocity reference	$\mathrm{rad\,s^{-1}}$
u	Torque command	$\mathrm{N\,m}$
Constant parameters		
N	Gearing ratio	$-$
J_m	Motor inertia	$\mathrm{kg\,m^2}$
J_l	Load inertia	$\mathrm{kg\,m^2}$
K_S	Shaft stiffness	$\mathrm{N\,m\,rad^{-1}}$
D_S	Shaft damping coefficient	$\mathrm{N\,m\,s\,rad^{-1}}$
$T_{C,m}$	Coulomb friction on the motor	$\mathrm{N\,m}$
$T_{C,l}$	Coulomb friction on the load	$\mathrm{N\,m}$
β_m	Motor viscous friction coefficient	$\mathrm{N\,m\,s\,rad^{-1}}$
β_l	Load viscous friction coefficient	$\mathrm{N\,m\,s\,rad^{-1}}$
Disturbances		
d_e	Input torque ripples and harmonics	$\mathrm{N\,m}$
$T_{F,m}$	Motor friction	$\mathrm{N\,m}$
$T_{F,l}$	Load friction	$\mathrm{N\,m}$
T_l	Load torque	$\mathrm{N\,m}$

Assumption B.4.1. ***(Compensated input disturbances)***
The input disturbance d_e is compensated via input filtering or appropriate feedforward terms and is not considered in the design, i.e.

$$d_e \approxeq 0 \ .$$

Considering that the input uncertainties depend on the current control tuning and motor characteristics, which are both known, rejection of d_e is possible via appropriate filtering and feed-forward compensation. On this basis, Assumption B.4.1 is not very restrictive in practice.

In the methods presented in [1], the cascaded architecture of shown in Figure

B.4 was preserved, i.e. a P controller was used in the outer loop outputting the reference to the velocity nonlinear controllers. The generic control structure used in [1] can be seen in Figure B.5.

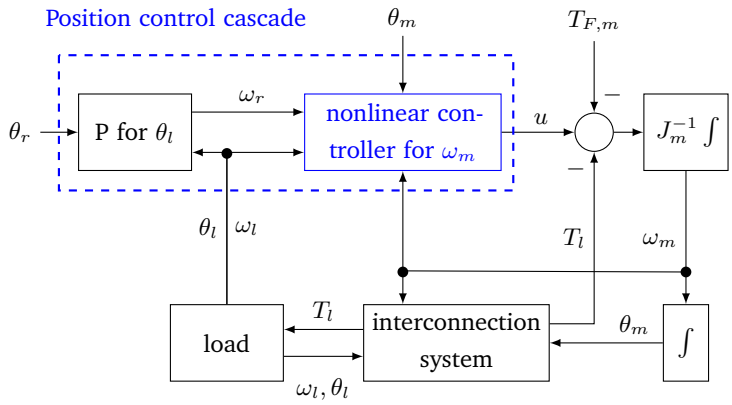

Figure B.5: Cascaded position-velocity control architecture.

This section presents the design of three direct-position nonlinear controllers based on adaptive and sliding-mode methods. The control of the load position θ_l is achieved directly by each nonlinear controller without the use of any cascaded structure. Consequently, the design of all these three controllers take into account the dynamics of the entire drive-train system and not just of the drive motor, as was the case in [1]. This generic control scheme is illustrated in Figure B.6.

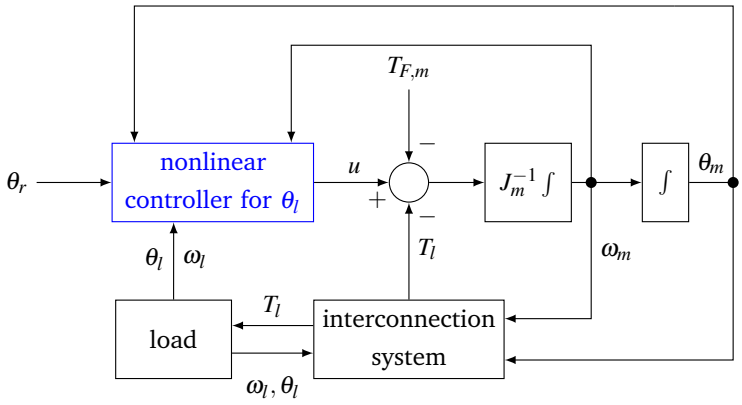

Figure B.6: Direct-position control architecture.

Notation: In the following we will denote an estimate of a parameter or state ξ by $\hat{\xi}$

and the associated estimation error by $\tilde{\xi}$, such that it holds:

$$\tilde{\xi} = \xi - \hat{\xi}. \tag{B.8}$$

B.4.1 Nonlinear Adaptive Backstepping Control

The ABSC scheme for nonlinear systems is presented in [83]. The control algorithms developed in this work apply to a general class of nonlinear systems with linear parametrization. In [130] and [42] adaptive backstepping controllers are designed for a PMSM and a double-motor driving servo system, respectively. LuGre friction compensation is achieved in [41] via a ABSC. The unknown friction dynamics are estimated by a double adaptive observer system and the estimate is fed to the control law.

Backstepping controllers for systems with relative degree larger than 1 are based on the concept of *virtual input*. At each level of the control design a state variable is regulated so that it serves as control input for the next step. In the adaptive version of backstepping controllers the unknown quantities can be expressed as uncertain or unknown parameters. The control design follows similar steps but now update laws for the unknown parameters are designed as well.

The adaptive backstepping control scheme for the drive-train system is shown in Figure B.7. The system has relative degree 3, since it is desired to control the load position via applying torques at the drive motor inertia. This implies that three steps of backtracking will be needed. Instead of doing that, we define the manifold

$$\mathcal{M} = \{y \in \mathbb{R} \mid \dot{y} + cy = 0,\ c > 0\} \tag{B.9}$$

and design the control law such that $\mathcal{M}$ is rendered invariant with respect to the trajectories of the position tracking error. Once the positioning error reaches $\mathcal{M}$, it converges exponentially (see (B.9)) to zero with a rate of convergence c. The friction parameters and the shaft characteristics are considered to be unknown or uncertain. The drive-train dynamics is written in parametric form as

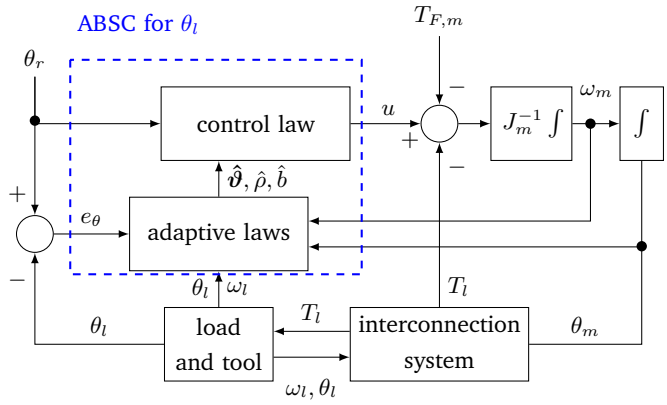

Figure B.7: ABSC direct position controller.

$$\dot{\omega}_m = \frac{1}{J_m}\left(u + \boldsymbol{\phi_1}^T(\boldsymbol{x})\boldsymbol{\vartheta}\right) \tag{B.10}$$

$$\dot{\theta}_m = \omega_m \tag{B.11}$$

$$\dot{\omega}_l = \frac{1}{J_l}\left(\boldsymbol{\phi_2}^T(\boldsymbol{x})\boldsymbol{\vartheta} + b\omega_m\right) \ , \ b = \frac{D_S}{N} \tag{B.12}$$

$$\dot{\theta}_l = \omega_l \tag{B.13}$$

$$\boldsymbol{x} = \begin{bmatrix}\omega_m & \theta_m & \omega_l & \theta_l\end{bmatrix}^T \tag{B.14}$$

$$\boldsymbol{\vartheta} = \begin{bmatrix}K_S & D_S & T_{C,m} & \beta_m & T_{C,l} & \beta_l\end{bmatrix}^T \tag{B.15}$$

$$\boldsymbol{\phi_1}(\boldsymbol{x}) = \begin{bmatrix} -\frac{1}{N}\left(\frac{1}{N}\theta_m - \theta_l\right) \\ -\frac{1}{N}\left(\frac{1}{N}\omega_m - \omega_l\right) \\ -\text{sgn}(\omega_m) \\ -\omega_m \\ 0 \\ 0 \end{bmatrix}, \quad \boldsymbol{\phi_2}(\boldsymbol{x}) = \begin{bmatrix} \frac{1}{N}\theta_m - \theta_l \\ -\omega_l \\ 0 \\ 0 \\ -\text{sgn}(\omega_l) \\ -\omega_l \end{bmatrix} \tag{B.16}$$

The following assumptions are made:

Assumption B.4.2. ***(Constant unknown parameter vector)***
The unknown parameters $\boldsymbol{\vartheta}$ are assumed to be constant or at least slowly varying, i.e. their time derivatives are considered to be zero

$$\dot{\boldsymbol{\vartheta}} = \mathbf{0} \ .$$

Assumption B.4.3. ***(Lipschitz continuity)***
The regressor functions $\boldsymbol{\phi_1}(\boldsymbol{x}), \boldsymbol{\phi_2}(\boldsymbol{x})$ are locally Lipschitz.

The design of the controller follows in the next theorem.

Theorem B.4.1. *Consider the drive-train system described in* (B.10)-(B.16) *with unknown parameters $\boldsymbol{\vartheta}$ defined in* (B.15)*, the uncertain virtual input gain $b = \frac{D_S}{N}$ with known sign and a bounded reference signal $\theta_r(t) \in \mathcal{C}^3$ for the load position. The collective control law*

$$u = -\boldsymbol{\phi_1}^T(\boldsymbol{x})\hat{\boldsymbol{\vartheta}} + J_m\left(\psi_2 - k_2 z_2 - \frac{1}{J_l} z_1 \hat{b}\right) \tag{B.17}$$

where

$$e_\theta = \theta_l - \theta_r$$
$$z_1 = \dot{e}_\theta + c e_\theta$$
$$\alpha = \alpha(\boldsymbol{x}, \hat{\rho}, \hat{\boldsymbol{\vartheta}}, \dot{\theta}_r, \ddot{\theta}_r) = \hat{\rho}\left[J_l\left(\ddot{\theta}_r - c\omega_l + c\dot{\theta}_r - k_1 z_1\right) - \boldsymbol{\phi_2}^T(\boldsymbol{x})\hat{\boldsymbol{\vartheta}}\right] \tag{B.18}$$
$$z_2 = \omega_m - \alpha(\boldsymbol{x}, \hat{\rho}, \hat{\boldsymbol{\vartheta}}, \dot{\theta}_r, \ddot{\theta}_r)$$
$$\psi_1 = \dot{\hat{\rho}}\left[-\boldsymbol{\phi_2}^T(\boldsymbol{x})\hat{\vartheta} + J_l\left(\ddot{\theta}_r - c\omega_l + c\dot{\theta}_r - k_1 z_1\right)\right] \tag{B.19}$$
$$\psi_2 = \psi_1 + \hat{\rho}\Bigg\{ - \boldsymbol{\phi_2}^T(\boldsymbol{x})\dot{\hat{\boldsymbol{\vartheta}}} - \hat{K}_S\left(\frac{\omega_m}{N} - \omega_l\right) + J_l\left(\theta_r^{(3)} + c\ddot{\theta}_r\right) +$$
$$\left(\frac{\hat{D}_s + \hat{\beta}_l}{J_l} - c - k_1\right)\left(\boldsymbol{\phi_2}^T(\boldsymbol{x})\hat{\boldsymbol{\vartheta}} + \hat{b}\omega_m\right) - J_l k_1\left(c\omega_l - \ddot{\theta}_r - c\dot{\theta}_r\right)\Bigg\} \tag{B.20}$$

together with the adaptation laws

$$\dot{\hat{\boldsymbol{\vartheta}}} = \boldsymbol{\Gamma}\left\{\boldsymbol{\phi_2}(\boldsymbol{x})\left[\frac{z_1}{J_l} - \hat{\rho} z_2\left(\frac{\hat{D}_s + \hat{\beta}_l}{J_l} - c - k_1\right)\right] + \frac{z_2}{J_m}\boldsymbol{\phi_1}(\boldsymbol{x})\right\} \tag{B.21}$$
$$\dot{\hat{\rho}} = -\gamma_1 \cdot \operatorname{sgn}(b) z_1\left(-\frac{1}{J_l}\boldsymbol{\phi_2}^T(\boldsymbol{x})\hat{\boldsymbol{\vartheta}} + \ddot{\theta}_r - c\omega_l + c\dot{\theta}_r - k_1 z_1\right) \tag{B.22}$$
$$\dot{\hat{b}} = \gamma_2\left[\frac{1}{J_l} z_1 z_2 - \hat{\rho} z_2\left(\frac{\hat{D}_s + \hat{\beta}_l}{J_l} - c - k_1\right)\omega_m\right] \tag{B.23}$$

where $k_1, k_2, \gamma_1, \gamma_2, c > 0$ and $\boldsymbol{\Gamma}$ is a 6×6 symmetric positive definite real matrix, ensure that the position tracking error e_θ converges to the origin $e_\theta^* = 0$ as $t \to \infty$,

i.e.

$$\lim_{t\to\infty} e_\theta(t) = 0\ .$$

Moreover, the parameter estimation errors $\tilde{\boldsymbol{\vartheta}}, \tilde{\rho}, \tilde{b}$ remain bounded for all future times.

Proof. The control design is done in two steps, starting from the position error dynamics and moving towards the angular velocity of the drive-motor, which is directly affected by the actuator.

Step 1

Define the off-the-manifold $\mathcal{M}$ variable $z_1 \triangleq \dot{e}_\theta + ce_\theta$ and a corresponding Lyapunov function candidate

$$V_1(z_1) = \frac{1}{2}z_1^2$$

The time derivative of V_1 along the dynamics of z_1 is written

$$\dot{V}_1 = z_1\left[\frac{1}{J_l}\left(\boldsymbol{\phi_2}^T(\boldsymbol{x})\boldsymbol{\vartheta} + b\omega_m\right) - \ddot{\theta}_r + c\omega_l - \dot{\theta}_r\right] \tag{B.24}$$

From the equation above it can be seen that if ω_m is seen as a virtual input to the subsystem, then a stabilizing function

$$\alpha(\boldsymbol{x}, \rho, \boldsymbol{\vartheta}, \dot{\theta}_r, \ddot{\theta}_r) = \rho\left[-\boldsymbol{\phi_2}^T(\boldsymbol{x})\boldsymbol{\vartheta} + J_l\left(\ddot{\theta}_r - c\omega_l + c\dot{\theta}_r - k_1 z_1\right)\right]$$
$$\rho \triangleq \frac{1}{b}$$

where $k_1 > 0$, will make $\dot{V}_1$ negative definite. However, since both $\boldsymbol{\vartheta}$ and ρ are unknown, this control law is not implementable. A certainty equivalence law, where $\boldsymbol{\vartheta}$ and ρ are substituted with their estimates $\hat{\boldsymbol{\vartheta}}$ and $\hat{\rho}$, respectively, is used instead. The goal then is to regulate ω_m such that it tracks $\alpha(\boldsymbol{x}, \hat{\rho}, \hat{\boldsymbol{\vartheta}}, \dot{\theta}_r, \ddot{\theta}_r)$ at all times. Subsequently, V_1 is augmented with the quadratic parameter estimation errors as

$$V_\alpha(z_1, \tilde{\boldsymbol{\vartheta}}, \tilde{\rho}) = V_1 + \frac{1}{2}\tilde{\boldsymbol{\vartheta}}^T\boldsymbol{\Gamma}^{-1}\tilde{\boldsymbol{\vartheta}} + \frac{1}{2\gamma_1}|b|\tilde{\rho}^2 \tag{B.25}$$

Taking the time derivative of V_α and substituting ω_m with $\alpha(\boldsymbol{x}, \hat{\rho}, \hat{\boldsymbol{\vartheta}}, \dot{\theta}_r, \ddot{\theta}_r)$ while noting that $\rho b = 1$ leads to

$$\dot{V}_\alpha = -k_1 z_1^2 + \frac{1}{J_l}z_1\boldsymbol{\phi_2}^T(\boldsymbol{x})\tilde{\boldsymbol{\vartheta}} - \tilde{\boldsymbol{\vartheta}}^T\boldsymbol{\Gamma}^{-1}\dot{\hat{\boldsymbol{\vartheta}}} - \frac{1}{\gamma_1}|b|\tilde{\rho}\dot{\hat{\rho}}$$
$$- \frac{1}{J_l}z_1\tilde{\rho}b\left[-\boldsymbol{\phi_2}^T(\boldsymbol{x})\hat{\boldsymbol{\vartheta}} + J_l\left(\ddot{\theta}_r - c\omega_l + c\dot{\theta}_r - k_1 z_1\right)\right] \tag{B.26}$$

where assumption B.4.2 was used. From (B.26) it can be seen that selecting appropriate adaptation laws for $\hat{\boldsymbol{\vartheta}}$ and $\hat{\rho}$ eliminates the parameter estimation errors,

rendering V_α negative definite. However, to avoid over-parametrization, these terms will be treated in the next step.

Step 2

Define the error variable $z_2 \triangleq \omega_m - \alpha$. The dynamics of z_1 can now be written as

$$\dot{z}_1 = \frac{1}{J_l}\left(\boldsymbol{\phi_2}^T(\boldsymbol{x})\boldsymbol{\vartheta} + bz_2 + b\alpha\right) - \ddot{\theta}_r + c\omega_l - \dot{\theta}_r \tag{B.27}$$

and therefore

$$\begin{aligned}\dot{V}_\alpha = &-k_1 z_1^2 + \frac{1}{J_l} z_1 \left(\boldsymbol{\phi_2}^T(\boldsymbol{x})\tilde{\boldsymbol{\vartheta}} + bz_2\right) - \tilde{\boldsymbol{\vartheta}}^T \boldsymbol{\Gamma}^{-1}\dot{\hat{\boldsymbol{\vartheta}}} - \frac{1}{\gamma_1}|b|\tilde{\rho}\dot{\hat{\rho}} \\ &- \frac{1}{J_l} z_1 \tilde{\rho} b \left[-\boldsymbol{\phi_2}^T(\boldsymbol{x})\hat{\boldsymbol{\vartheta}} + J_l\left(\ddot{\theta}_r - c\omega_l + c\dot{\theta}_r - k_1 z_1\right)\right]\end{aligned} \tag{B.28}$$

The dynamics of z_2 reads

$$\begin{aligned}\dot{z}_2 &= \frac{1}{J_m}\left(u + \boldsymbol{\phi_1}^T(\boldsymbol{x})\boldsymbol{\vartheta}\right) - \dot{\alpha} \\ &= \frac{1}{J_m}\left(u + \boldsymbol{\phi_1}^T(\boldsymbol{x})\boldsymbol{\vartheta}\right) - \frac{d}{dt}\left\{\hat{\rho}\left[J_l\left(\ddot{\theta}_r - c\omega_l + c\dot{\theta}_r - k_1 z_1\right) - \boldsymbol{\phi_2}^T(\boldsymbol{x})\hat{\boldsymbol{\vartheta}}\right]\right\} \\ &= \frac{1}{J_m}\left(u + \boldsymbol{\phi_1}^T(\boldsymbol{x})\hat{\boldsymbol{\vartheta}}\right) - \psi_2 - \hat{\rho}\left(\frac{\hat{D}_S + \hat{\beta}_l}{J_l} - c - k_1\right)\boldsymbol{\phi_2}^T(\boldsymbol{x})\tilde{\boldsymbol{\vartheta}} \\ &- \hat{\rho}\left(\frac{\hat{D}_S + \hat{\beta}_l}{J_l} - c - k_1\right)\tilde{b}\omega_m\end{aligned} \tag{B.29}$$

where ψ_2 is defined in (B.19)-(B.20). Detailed calculation of $\dot{\alpha}$ is presented in VII.

Extending V_α to the new Lyapunov function candidate

$$V_2(z_1, z_2, \tilde{\boldsymbol{\vartheta}}, \tilde{\rho}, \tilde{b}) = V_\alpha + \frac{1}{2}z_2^2 + \frac{1}{2\gamma_2}\tilde{b}^2 \tag{B.30}$$

and taking its derivative along the trajectories of $z_1, z_2, \tilde{\boldsymbol{\vartheta}}, \tilde{\rho}, \tilde{b}$ while considering also (B.17), (B.27), (B.28) and (B.29) yields after straightforward calculations:

$$\begin{aligned}&\dot{V}_2 = -k_1 z_1^2 - k_2 z_2^2 + \\ &\tilde{\boldsymbol{\vartheta}}^T\left\{\boldsymbol{\phi_2}(\boldsymbol{x})\left[\frac{z_1}{J_l} - \hat{\rho} z_2\left(\frac{\hat{D}_s + \hat{\beta}_l}{J_l} - c - k_1\right)\right] + \frac{z_2}{J_m}\boldsymbol{\phi_1}(\boldsymbol{x}) - \boldsymbol{\Gamma}^{-1}\dot{\hat{\boldsymbol{\vartheta}}}\right\} \\ &- \tilde{\rho}|b|\left[\operatorname{sgn}(b) z_1\left(-\frac{1}{J_l}\boldsymbol{\phi_2}^T(\boldsymbol{x})\hat{\boldsymbol{\vartheta}} + \ddot{\theta}_r - c\omega_l + c\dot{\theta}_r - k_1 z_1\right) + \frac{1}{\gamma_1}\dot{\hat{\rho}}\right] \\ &+ \tilde{b}\left[\frac{1}{J_l} z_1 z_2 - \hat{\rho} z_2\left(\frac{\hat{D}_s + \hat{\beta}_l}{J_l} - c - k_1\right)\omega_m - \frac{1}{\gamma_2}\dot{\hat{b}}\right].\end{aligned} \tag{B.31}$$

Substituting the adaptation laws (B.21), (B.22), (B.23) into (B.31) yields

$$\dot{V}_2 = -k_1 z_1^2 - k_2 z_2^2 \leq 0 \tag{B.32}$$

with $k_1, k_2 > 0$. From this it can be seen that V_2 is non-increasing and since $V_2(z_1(0), z_2(0), \tilde{\boldsymbol{\vartheta}}(0), \tilde{\rho}(0), \tilde{b}(0)) < \infty$, this implies that $z_1, z_2, \tilde{\boldsymbol{\vartheta}}, \tilde{\rho}, \tilde{b}$ are bounded for all future times, i.e. $z_1, z_2, \tilde{\boldsymbol{\vartheta}}, \tilde{\rho}, \tilde{b} \in \mathcal{L}_\infty$. From Equation (B.27), since all the signals on the right side are bounded, it follows that $\dot{z}_1 \in \mathcal{L}_\infty$. Moreover, integrating (B.32) with respect to time gives

$$0 \leq \int_0^\infty \begin{bmatrix} z_1 & z_2 \end{bmatrix} \begin{bmatrix} k_1 & 0 \\ 0 & k_2 \end{bmatrix} \begin{bmatrix} z_1 \\ z_2 \end{bmatrix} \leq V_2(z_1(0), z_2(0), \tilde{\boldsymbol{\vartheta}}(0), \tilde{\rho}(0), \tilde{b}(0)) \ ,$$

which implies that $z_1, z_2 \in \mathcal{L}_2$. Then, by Corollary A.7 in [83, p. 491], it is shown that $\lim_{t\to\infty} \begin{bmatrix} z_1(t) & z_2(t) \end{bmatrix}^T = \begin{bmatrix} 0 & 0 \end{bmatrix}^T$, which means that the off-the-manifold $\mathcal{M}$ variable z_1 decays to 0.

The dynamics of the load positioning error e_θ can be written according to (B.9) as

$$\dot{e}_\theta = -ce_\theta + z_1 \tag{B.33}$$

which can be viewed as the cascaded interconnection of a UGAS and a convergent system (the dynamics of the unperturbed e_θ and those of z_1, respectively). Moreover, the system in (B.33) is ISS with respect to the input variable z_1 (see V for a proof). Then $\lim_{t\to\infty} z_1(t) = 0$ implies that $\lim_{t\to\infty} e_\theta(t) = 0$, i.e. the positioning error system is also convergent, which completes the proof. ■

Remark B.1. Existence of the closed-loop solutions requires $\boldsymbol{\phi_1}(\boldsymbol{x}), \boldsymbol{\phi_2}(\boldsymbol{x})$ to be locally Lipschitz. This does not hold since both regressor functions include the sign function, whose derivative is not bounded at 0. The approximation

$$\text{sgn}(y) \approx \frac{2}{\pi} \arctan(py) \triangleq \nu(p, y) \tag{B.34}$$

removes the problem of non-smoothness of the regressor functions and allows the application of the theorem. This approximation is commonly used in the implementation of control algorithms with switching terms, since in reality discontinuities corresponds to impractically fast jumps in the actuation signals. The parameter p is a positive number denoting the slope of the function near 0.

B.4.2 Second-Order Sliding-Mode Control

High-order SMCs discussed in detail in [70] combine the finite-time convergence and robustness features of conventional SMC schemes with chattering attenuation, and more importantly, they can be applied to systems with relative degree higher than 1. The *STSMC* presented in [69, 71, 72] is a second-order SMC, which for systems with relative degree 1 ensures finite-time convergence and reduced chattering. Given

a dynamical system

$$\dot{s}(\boldsymbol{x}(t)) = \psi(t, \boldsymbol{x}(t)) + bu \ , \ b \neq 0 \ , \tag{B.35}$$

where $\boldsymbol{x}(t)$ are bounded internal states, the STSMC

$$u \triangleq u_{SM} = \frac{1}{b}\left(-c_1|s|^{\frac{1}{2}}\text{sgn}(s) + v\right) \tag{B.36}$$

$$\dot{v} = -c_2\text{sgn}(s) \tag{B.37}$$

with c_1, c_2 appropriate positive gains ensures that the system reaches the manifold

$$\mathcal{S} = \{s(t) \in \mathbb{R} | s = \dot{s} = 0\} \ , \tag{B.38}$$

referred to as the *sliding manifold*, in finite time. In [73] it is proven by using Strict Lyapunov functions that if $|\psi(t, \boldsymbol{x})| \leq \delta|s|^{\frac{1}{2}}$, where $\delta > 0$, finite-time convergence is always possible for appropriate selection of the positive gains c_1, c_2. The variable s is often called the *sliding variable*, it is a function of the states of the system and their derivatives and it can explicitly depend on time.

Two variations of the STSMC for direct load position control will be presented in the following, namely the OSTSMC and the ASTSMC. In the analysis that follows, the next assumption is made:

Assumption B.4.4. ***(Lipschitz continuity)***
The perturbation $\psi(t, \boldsymbol{x})$ is Lipschitz continuous.

B.4.2.1 Output Super-Twisting SMC

The architecture of the OSTSMC is shown in Figure B.8. For the regulation of the load position error at zero the following auxiliary variables are defined:

$$\begin{aligned} e_1 &\triangleq \theta_l - \theta_r \\ e_2 &\triangleq \dot{e}_1 = \omega_l - \dot{\theta}_r \ . \end{aligned}$$

Selecting the sliding variable s as a linear combination of $e_1, e_2, \dot{e}_2$ allows establishing a desired dynamical behavior for the positioning error (and its derivative) once the system reaches the sliding manifold S defined in (B.38). With this approach the STSMC algorithm can be applied circumventing the problem that the drive-train system has relative degree 3.

The sliding variable is defined as

$$s \triangleq \dot{e}_2 + (\lambda_1 + \lambda_2)\, e_2 + \lambda_1\lambda_2 e_1 \ . \tag{B.39}$$

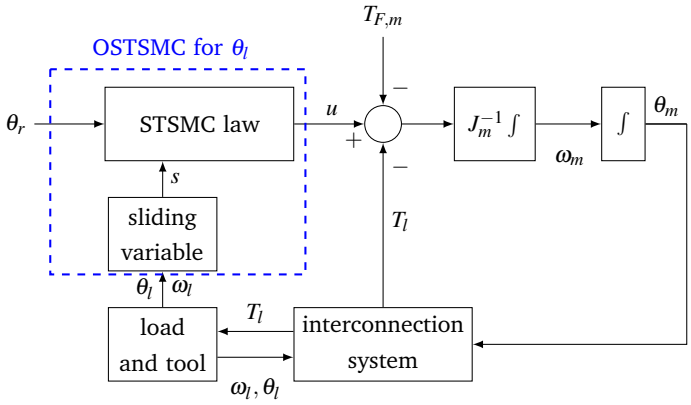

Figure B.8: OSTSMC direct position controller.

where λ_1, λ_2 are real positive constants. Its dynamics reads:

$$\begin{aligned}\dot{s} &= \dddot{\omega}_l - \theta_r^{(3)} + (\lambda_1+\lambda_2)\left(\ddot{\omega}_l - \ddot{\theta}_r\right) + \lambda_1\lambda_2\left(\dot{\omega}_l - \dot{\theta}_r\right) \\ &= \frac{1}{J_l}\left[K_S\left(\frac{1}{N}\dot{\omega}_m - \dot{\omega}_l\right) - D_S\ddot{\omega}_l - \dot{T}_{F,l} - \frac{D_S}{J_m}\left(\frac{1}{N}T_l + T_{F,m}\right)\right] \\ &- \theta_r^{(3)} + (\lambda_1+\lambda_2)\left(\ddot{\omega}_l - \ddot{\theta}_r\right) + \lambda_1\lambda_2\left(\dot{\omega}_l - \dot{\theta}_r\right) + \frac{D_S}{J_m J_l}u\,.\end{aligned}$$

Defining the control signal

$$u = u_{SM} + \frac{J_m J_l}{D_S}\left[\theta_r^{(3)} + (\lambda_1+\lambda_2)\,\ddot{\theta}_r - \lambda_1\lambda_2\left(\omega_l - \dot{\theta}_r\right)\right] \tag{B.40}$$

to cancel known terms the sliding surface dynamics finally reads:

$$\dot{s} = \psi(t, \boldsymbol{x}) + b u_{SM} \tag{B.41}$$

where

$$\begin{aligned}\psi(t,\boldsymbol{x}) &= \frac{1}{J_l}\left[K_S\left(\frac{1}{N}\dot{\omega}_m - \dot{\omega}_l\right) - D_S\ddot{\omega}_l - \dot{T}_{F,l} - \frac{D_S}{J_m}\left(\frac{T_l}{N} + T_{F,m}\right)\right] + (\lambda_1+\lambda_2)\,\ddot{\omega}_l \\ b &= \frac{D_S}{J_m J_l}\,.\end{aligned}$$

Application of the control law (B.36),(B.37) will bring the system (B.41) on the sliding manifold $\mathcal{S}$ in finite-time, i.e. $\dot{s} = s = 0$. From the definition of s and e_1, e_2, this leads to the following dynamical system

$$\begin{bmatrix}\dot{e}_1 \\ \dot{e}_2\end{bmatrix} = \begin{bmatrix}0 & 1 \\ -\lambda_1\lambda_2 & -(\lambda_1+\lambda_2)\end{bmatrix}\begin{bmatrix}e_1 \\ e_2\end{bmatrix} \tag{B.42}$$

which is a Linear Time-Invariant (LTI) system with its eigenvalues $-\lambda_1, -\lambda_2$ being design parameters. Choosing λ_1 and λ_2 positive ensures that the position error and its first time-derivative decay to 0 exponentially, i.e. $e_1^* = 0$ is ES.

Remark B.2. The design of the sliding surface s requires knowledge of $\dot{e}_2$, i.e. of $\dot{\omega}_l$, which is not measured. For the estimation of this signal any dynamic differentiator or observer can be used (e.g. sliding-mode exact differentiators [131]). A Luenberger linear observer is used in this design.

Remark B.3. Assumption B.4.4 is violated at zero velocity. This is due to the fact that $\psi(t, \boldsymbol{x})$ contains the derivative of sgn$(\cdot)$ function, which is not Lipschitz continuous. In reality, however, this corresponds to a locally Lipschitz continuous function with very large Lipschitz constant when the velocities are close to zero. This implies, that when the motion changes direction the system will leave the sliding manifold and it will reach it again very fast.

Remark B.4. As it can be seen from the design of the algorithm, there are two possible strategies for tuning the controller. One is increasing the gains c_1, c_2. By doing so, the system reaches the sliding manifold $\mathcal{S}$ in finite time and remains thereafter for all future times. Then, according to (B.42), the positioning error will decay exponentially to zero. Increasing the controller gains too much, however, is usually not desirable since it often leads into exerting large torques at high frequency switching, which is damaging for the actuator. The second tuning strategy pertains to increasing the magnitude of the dominant pole λ_1 (and consequently of λ_2), while keeping c_1, c_2 low. In this case, the system does not reach the sliding manifold in finite-time and if it does, it may move away from it temporarily (e.g. during change of motion direction). Then $s \neq 0$. Let $s = \Delta(t)$, where $\Delta(t)$ is a bounded scalar function. Then one can obtain from Equation (B.39):

$$\begin{bmatrix} \dot{e}_1 \\ \dot{e}_2 \end{bmatrix} = \begin{bmatrix} 0 & 1 \\ -\lambda_1\lambda_2 & -(\lambda_1 + \lambda_2) \end{bmatrix} \begin{bmatrix} e_1 \\ e_2 \end{bmatrix} + \begin{bmatrix} 0 \\ 1 \end{bmatrix} \Delta(t) \tag{B.43}$$

From (B.43) and the general solution of LTI systems it is clear that faster poles λ_1, λ_2 will decrease the effect of the input $\Delta(t)$ on the states, i.e. the positioning error and its first derivative.

B.4.2.2 Adaptive Super-Twisting SMC

The design of ASTSMC presented in [77] extends the OSTSMC by an adaptive law for the dominant pole λ_1 of the system (B.42). The core control algorithm is also given by (B.36), (B.37), (B.40). The architecture of the ASTSMC can be seen in Figure B.9.

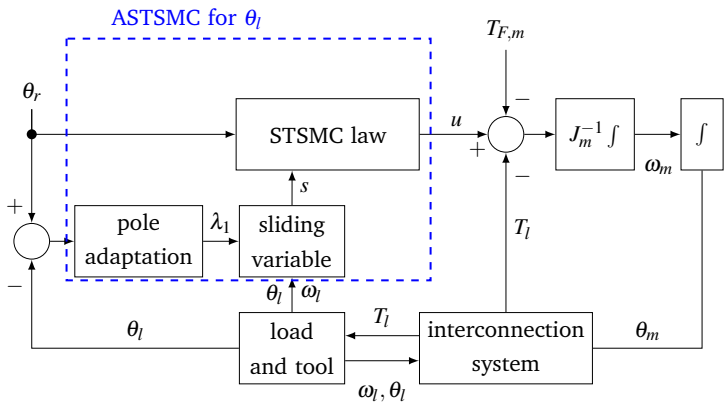

Figure B.9: ASTSMC direct position controller.

The adaptive law for λ_1 is based on the average absolute positioning error. Indeed, by using Lyapunov stability theory and the analysis of the STSMC done in [73], the authors in [77] proved that the adaptive law

$$\dot{\lambda}_1 = -\gamma_\lambda \text{sgn}\left(e_1^{av} - \varepsilon_\theta\right), \ \gamma_\lambda > 0 \tag{B.44}$$

in combination with the OSTSMC described in (B.36),(B.37),(B.39) ensures finite time convergence of the load position error e_1 to the compact set $\mathcal{E}_\theta = \{\zeta \in \mathbb{R} \mid |\zeta| \leq \varepsilon_\theta\}$, where $\varepsilon_\theta > 0$ expresses the positioning accuracy limit. Considering λ_1 as the dominant (slower) eigenvalue of system (B.42), λ_2 can be selected proportionally to λ_1, i.e.

$$\lambda_2 = a\lambda_1, \ a > 1 \ . \tag{B.45}$$

The average absolute positioning error e_1^{av} used in (B.44) is given over a horizon of ν samples by [77]

$$e_1^{av} = \frac{1}{\nu}\sum_{i=0}^{\nu-1} |e_1(t - iT_s)|$$

where T_s is the sampling period. Since it is the maximum error peaks that define he accuracy in the positioning, the threshold ε_θ in (B.44) can be compared to the maximum peak e_1^{peak} of the error signal within the same time horizon of ν samples, instead of the error average e_1^{av}. Specifically, by defining

$$e_1^{peak} = \sup_{0 \leq i \leq \nu} |e_1(t - iT_s)| \tag{B.46}$$

the sliding surface poles change depending on how "tight" the $\pm e_1^{peak}$ envelope that contains the position error is. This, in principle, improves the overall efficiency of

the controller since the poles, and by extension the control effort, increase only to the level where the positioning error is no larger than the pre-specified bound. Increasing the magnitude of λ_1 beyond a certain value may lead to instability of the closed-loop system. For this reason, a saturation functionality is used for λ_1.

The assumptions considered for each control method, as well as the main features of the four nonlinear controllers are summarised in Table B.2.

Table B.2: Methods' assumptions and key properties.

Assumptions	**Theoretical properties**
ABSC	
• Unknown parameters are constant (B.4.2). • Regressor functions are Lipschitz continuous (B.4.3)	• Position error converges to zero • Uniformly bounded parameter estimation error • Parameter estimation if the regressors are persistently exciting
OSTSMC	
• Perturbation is Lipschitz continuous (B.4.4)	• Position error is exponentially stable • Robustness against any type of Lipschitz disturbances and model uncertainties
ASTSMC	
• Perturbation is Lipschitz continuous (B.4.4)	• Position error is exponentially stable • Robustness against any type of Lipschitz disturbances and model uncertainties • Sliding surface poles are adjusted to the positioning error magnitude

B.5 Experiments and Evaluation

B.5.1 Experimental Setup

The experimental setup described in [1] is also used for the evaluation of the controllers presented in this paper. The test rig consists of two Siemens 1FT7042-5AF70 PMSMs connected through a stainless steel shaft. A Siemens SINAMICS S120

drive converter with 11-bit absolute position encoders is used. A Vari-tork 279.25.22 adjustable-friction clutch [108], mounted on the steel shaft (see Figure B.10) is used to vary the friction on the motor side. The experimental setup is shown in Figure B.11.

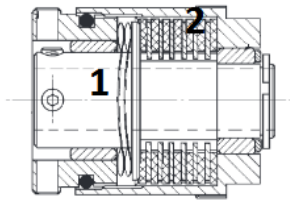

Figure B.10: Schematic of Vari-tork 273.25.22 adjustable-friction clutch: (1) inner bearing housing the interconnecting shaft, (2) outer bearing.

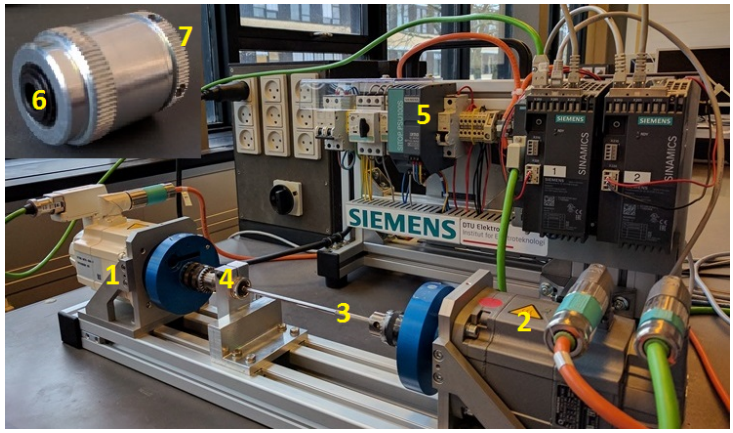

Figure B.11: Experimental setup: (1) 1FT7 drive PMSM, (2) 1FT7 load PMSM, (3) shaft, (4) friction component base, (5) Siemens SINAMICS S120 converter, (6) shaft housing, (7) friction adjustment ring.

B.5.2 Test Scenarios

Fifteen different scenarios were considered for the experimental assessment of the performance of the control algorithms. A sinusoidal reference signal

$$\theta_r(t) = \Theta_0 \sin(2\pi f_r t) \ ,$$

where Θ_0 is the position amplitude in rad and f_r is the frequency in Hz was used as a basis for the test scenarios. Such reference signal could describe the motion

profile of one axis of a machine tool that follows a circular contour. The choice of this reference signal was also motivated by the fact that the largest tool-positioning errors in machine tools occur during the change of motion direction of the axes [18]. Five cases of friction (including the nominal case) were considered, with the last two of them corresponding to extreme friction values. These values were used to assess the performance limits of the designed controllers. Similarly to [1], three speed profiles were considered (very slow, slow, fast) by varying the sinusoidal signal frequency. The fifteen different scenarios are shown in Table B.3.

Table B.3: Test scenarios. In connection to Problem B, the motor Coulomb friction bound is taken equal to $T_{C,m}^{max} = 0.15$ N m.

No	Θ_0 (rad)	$T_{C,m}$ (N m)	f_r (Hz)	Increase in friction
1	1	0.035	0.1	0
2	1	0.035	0.5	0
3	1	0.035	2	0
4	1	0.11	0.1	215%
5	1	0.11	0.5	215%
6	1	0.11	2	215%
7	1	0.15	0.1	330%
8	1	0.15	0.5	330%
9	1	0.15	2	330%
10	1	0.25	0.1	615%
11	1	0.25	0.5	615%
12	1	0.25	2	615%
13	1	0.35	0.1	900%
14	1	0.35	0.5	900%
15	1	0.35	2	900%

The controllers were tuned in the nominal friction case at 0.5 Hz, such that the maximum absolute positioning error is no larger than $5 \cdot 10^{-3}$ rad for all control schemes (whenever this was possible). In the PI scheme $\dot{\theta}_r$ is added as a feedforward term to the position P controller output. The values of the controllers tuning parameters are presented in Table B.4.

B.5.3 Controllers Comparison Criteria

The quantitative criteria for the comparison of the controllers that were introduced in [1] are also used in this paper. They are briefly summarised in Table B.5 for completeness:

Table B.4: Controller parameters values.

Symbol	Description	Value
Outer loop P and $\dot{\omega}_l$ estimation		
k_{pos}	Proportional gain	9
k_{obs}	$\dot{\omega}_l$ observer gain	75.4
PI		
k_p	Proportional gain	0.9
T_n	Integral reset time	0.06
ABSC		
k_1	z_1 gain	200
k_2	z_2 gain	200
c	Proportional gain	54
diag($\mathbf{\Gamma}$)	Adaptation gains	$\left[10^{-5},\ 0.012 \cdot (1, 10, 1, 1, 1)\right]$
γ_1	Adaptation gain	0.2
γ_2	Adaptation gain	0.01
$\hat{\boldsymbol{\vartheta}}_{\mathbf{0}}$	Initial conditions	$[17,\ 0.03,\ 0,\ 0.001\ 0,\ 0.001]^T$
$\hat{\rho}_0$	Initial conditions	19
$\hat{b}_0$	Initial conditions	0.01
OSTSMC		
c_1	Switching gain	0.001
c_2	Integral sw. gain	5.4
λ_1	Sliding mode pole	17
λ_2	Sliding mode pole	35
ASTSMC		
c_1	Switching gain	0.001
c_2	Integral sw. gain	5.4
$\lambda_{1,0}$	Initial conditions	10
γ_λ	Adaptation gain	0.5
a	Pole scaling	2
ε_θ	Precision limit	10 (mrad)
ν	Number of samples	500
T_s	e_1 sampling period	4 (ms)

Table B.5: Controller comparison criteria.

Criterion	Definition/description	Focus
MAE	$\sup_{t_0 \le t \le t_0+T} \lvert e_\theta(t) \rvert$	Maximum peak deviation
ISE	$\frac{1}{T}\int_{t_0}^{t_0+T} e_\theta^2(t)dt$	Speed of error decaying
ITSE	$\frac{1}{T}\int_{t_0}^{t_0+T} te_\theta^2(t)dt$	Persisting error
CP	$\frac{1}{T}\int_{t_0}^{t_0+T} u^2(t)dt$	Control usage
ECP	$\sup_{t_0 \le t \le t_0+T} \lvert e_\theta(t) \rvert \cdot \frac{1}{T}\int_{t_0}^{t_0+T} u^2(t)dt$	Overall efficiency
MAPE	$\sup_{t_0 \le t \le t_0+T} \lvert e_\phi(t) \rvert$ with $e_\phi(t) = \tan^{-1}\left(\frac{\theta_y^r(t)}{\theta_x^r(t)}\right) - \tan^{-1}\left(\frac{\theta_y(t)}{\theta_x(t)}\right)$, $\theta_x(t) = \frac{1}{\Theta_0}\theta_l(t)$, $\theta_y(t) = -\frac{1}{\Theta_0}\theta_l\left(t-\frac{\pi}{2}\right)$, $\theta_x^r(t) = \frac{1}{\Theta_0}\theta_r(t) = \sin(2\pi f_r t)$, $\theta_y^r(t) = -\frac{1}{\Theta_0}\theta_r\left(t-\frac{\pi}{2}\right) = \cos(2\pi f_r t)$	Maximum phase lag

Along with these metrics, two qualitative criteria are used for the evaluation of the controllers. The first is a graphical representation of the MAPE in an $\theta_x - \theta_y$ plot, similar to the ones used in a CIT in machine tools [10]. Larger deviations from the unit-radius circular path imply increased radial or lag errors. Additionally, the total number of tunable parameters and available signals needed for each method are considered, which reflect the design complexity of each control strategy.

B.5.4 Results

The section presents the results obtained by the experimental evaluation of the control methods. As in [1], the controllers were evaluated over the last 20s of each experiment, which had duration of 540s. This ensured that starting-up errors did not influence the performance assessment and that there was sufficient time for the adaptation of any parameters.

Table B.6: MAE in mrad for all controllers in all scenarios. The indices 1-4 denote the four different friction cases.

Controller	nominal	1	2	3	4
MAE in mrad at 0.1 Hz					
P-PI	12	17.9	20.3	24.4	30.3
ABSC	4.3	5.5	6.2	6.2	12.8
OSTSMC	6.6	5.6	7.4	9.8	15.6
ASTSMC	6.4	6.5	8.9	12.4	16.9
MAE in mrad at 0.5 Hz					
P-PI	4.9	15.6	17	23.7	37.2
ABSC	3.4	4.7	5.7	7	13.8
OSTSMC	10.9	13.6	14.4	19.6	62.5
ASTSMC	10.5	14.2	19.1	28.7	57.5
MAE in mrad at 2 Hz					
P-PI	12.3	20.1	21.8	31.6	45.7
ABSC	12.9	13.7	14.2	15.3	19.2
OSTSMC	49.1	118.9	177.7	256.5	448.6
ASTSMC	60.1	102.4	214.1	242.6	480.7

The MAE for each control in all friction cases and reference profiles is presented in Table B.6. It can be seen that the ABSC has consistently the best performance in all tests. Specifically, the MAE of the ABSC is kept well below the precision limit in the first four friction cases at 0.1 and 0.5 Hz. During operation at 2 Hz the controller marginally performs above he precision limit. The performance gradually deteriorates as friction increases but the MAE is 30-60% smaller than that of the PI. In the worst "realistic" scenario (Test 13) the ABSC MAE is $4.2\ \mathrm{mrad}$ above the precision limit and it is 35% smaller that in the PI case. The precision of ABSC can be improved by increasing the gains k_1, k_2 at the cost, however, of making the method more sensitive to measurement noise. Figure B.12 illustrates the estimation of the motor Coulomb friction and the product $\hat{\rho}\hat{b}$ during Test 5. It can be seen that the friction estimate approaches a value close to the real Coulomb friction. Moreover, the product $\hat{\rho}\hat{b}$ converges to 1, its real value since by definition $\rho = \frac{1}{b}$.

Both of the sliding-mode designs outperform the PI only in the first three tests (0.1 Hz with no extreme friction values) while they are consistently worse than the ABSC. At 0.5 Hz they have similar accuracy to the PI (except for the last friction case) and at 2 Hz their performance rapidly deteriorates, with MAE up to 10 times larger than the one in the PI case. Figures B.13 and B.14 show the positioning errors and corresponding torque commands for all the controllers during Tests 7 and 9,

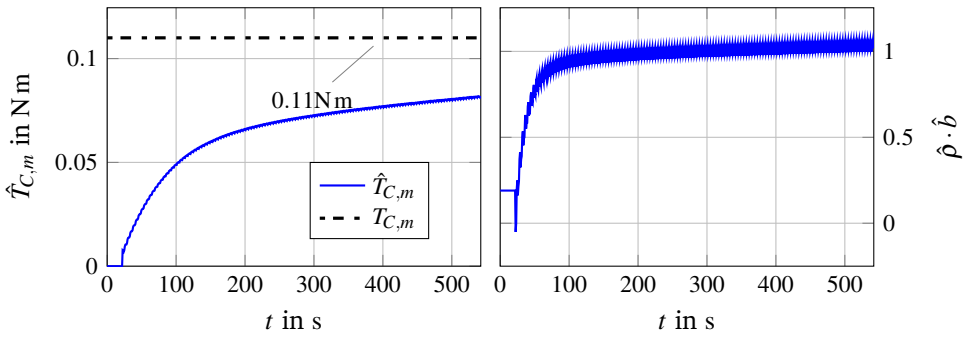

Figure B.12: (Left): Estimation of motor Coulomb friction $T_{C,m}$ from the ABSC algorithm during Test 5. (Right): Product of the uncertain input gain b and its inverse ρ during Test 5.

respectively.

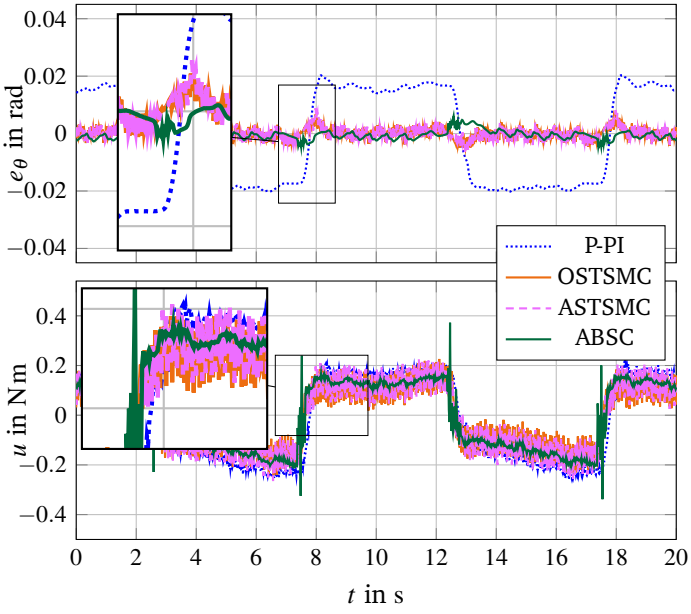

Figure B.13: Positioning errors and torque commands for Test 7.

From and Table B.6 it can be seen that the OSTSMC and ASTSMC have similar performance in terms of both accuracy and control input profile. This is expected since the only difference in their design is that in the case of ASTSMC the poles shaping the sliding surface are adapted to the positioning error magnitude rather than being fixed. The saturation and scaling of the poles is tuned such that whenever

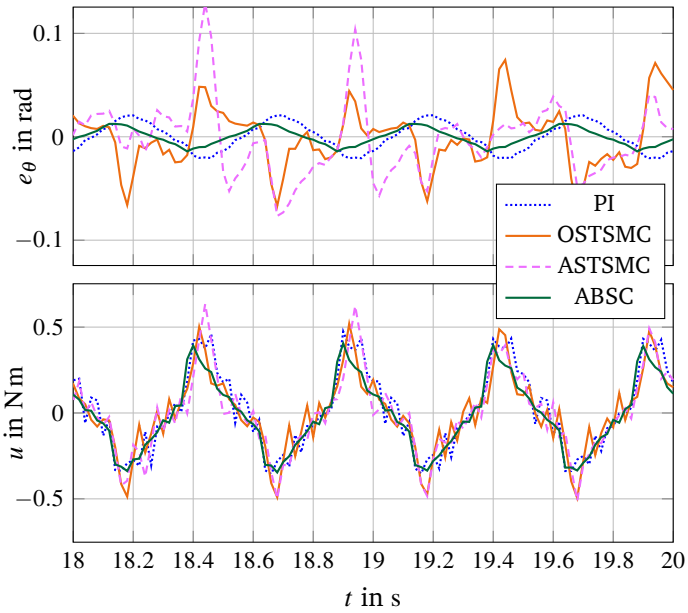

Figure B.14: Positioning errors and torque commands for Test 9.

the precision requirement is not met, the ASTSMC design converges to the one of OSTSMC, i.e. the selected values for λ_1, λ_2 in OSTSMC are the pole saturation limits in ASTSMC. This can also be seen in Figure B.15, where the adaptation of the sliding surface poles and the position error envelope are depicted.

Another reason for which the OSTSMC and ASTSMC show worse performance for fast reference profiles is the fact that the design of the sliding manifold requires knowledge of $\dot{\omega}_l$, which is not measured. Since the load acceleration is estimated by a linear observer, the quality of the estimation depends on how large the observer proportional gain is in comparison to how fast the velocity changes. The effect of noise on the measured signals do not allow arbitrary increase of the observer gain and, as such, faster reference profiles lead to less accurate estimation of $\dot{\omega}_l$. Improvement of the performance of these two sliding-mode methods requires considerably increasing the gains c_1, c_2. This however also induces more chattering in the control signal (see bottom plot in Figure B.14) that can be damaging for the actuator.

The same observations on the each method's performance can be made by looking at Figures B.16 and B.17, where the MAE and ECP of each controller is plotted with respect to the friction and frequency cases.

Figure B.18 shows the MAPE of all the controllers for the three different reference

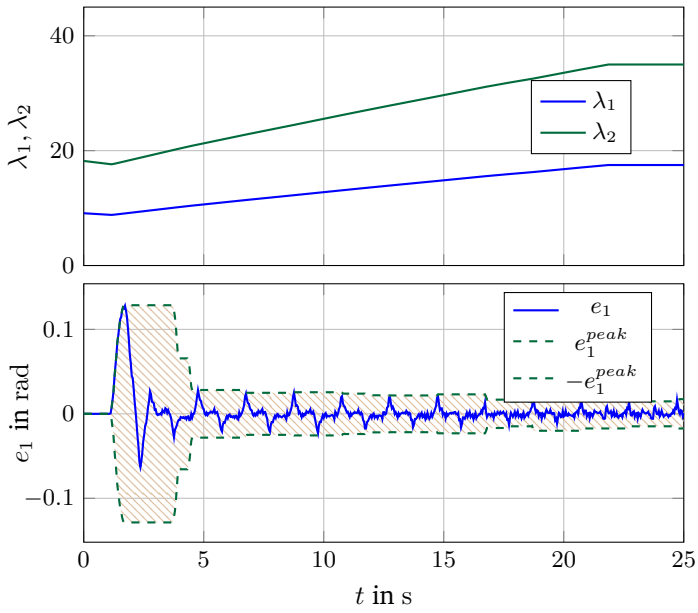

Figure B.15: (Top): Evolution of the ASTSMC sliding surface poles λ_1, λ_2 during Test 8. (Bottom): Position error e_1 and its amplitude envelope $\pm e_1^{peak}$ during Test 8.

profiles and increasing friction. It can be seen that phase lag between reference signal and actual position response significantly contributes to the positioning error in the sliding-mode designs at 2 Hz. On the contrary, the MAPE in the ABSC case is the smallest compared to all the other methods, which indicates that the ABSC positioning error is mainly due to amplitude deviations from the position setpoint at each time instant.

The relative performance indices of the three nonlinear controllers are illustrated in the histograms of Figure B.19. Each column represents the ratio of a performance index over the corresponding value for the PI case. It can also be seen from this illustration that ABSC shows the best performance, while both OSTSMC and ASTSMC significantly degrade, especially at 2 Hz.

A comparative visualisation of the controllers' performance is given in Figure B.20, where the $\theta_x - \theta_y$ plots for the largest "realistic" friction value (Tests 7-9) are shown for each controller. It can clearly be seen from the distortion of the circular paths that the ABSC outperfroms the PI and maintains the positioning tolerances, with the MAE being marginally above the performance limit only at 2 Hz. ON the contrary, both the OSTSMC and the ASTSMC performs sufficiently well only at 0.1 Hz, where their degradation at 2 Hz is clearly worse than that of the PI.

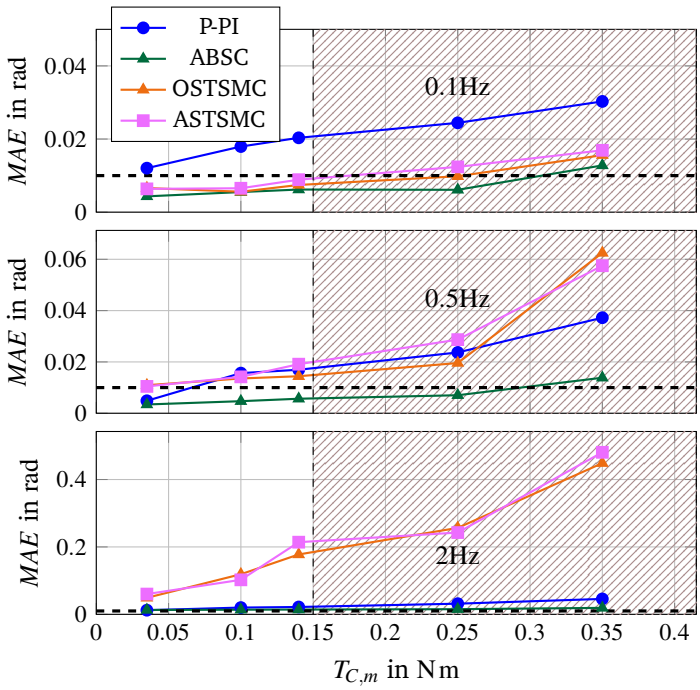

Figure B.16: MAE for all friction and frequency cases. The dashed line corresponds to the $\pm 10^{-2}$rad accuracy bound and the stripped area denotes the extreme friction cases.

Lastly, the design and implementation complexity of each control strategy can be deducted from the number of tunable parameters and required signals, shown in Table B.7. As it can be seen, the ABSC is the most demanding algorithm with respect to tuning effort, since it has 19 tunable parameters and its design requires 8 signals to be available. The ASTSMC and the OSTSMC follow in complexity with 9 and 5 tunable parameters, respectively and the same number of required signals, namely 6. The PI has the simplest design with only 3 tunable parameters and 4 required signals.

Table B.7: Number of tunable parameters and signals required for each controller.

	Tunable	Total	Signals	Total
P-PI	k_{pos}, k_p, T_n	3	$\theta_r, \dot{\theta}_r, \theta_l, \omega_m$	4
ABSC	$c, k_1, k_2, \mathbf{\Gamma}, \gamma_1, \gamma_2, \hat{\boldsymbol{\vartheta}}_{\mathbf{0}}, \hat{\rho}_0, \hat{b}_0$	19	$\theta_r, \dot{\theta}_r, \ddot{\theta}_r, \theta_r^{(3)} \boldsymbol{x}$	8
OSTSMC	$c_1, c_2, \lambda_1, \lambda_2, k_{obs}$	5	$\theta_r, \dot{\theta}_r, \ddot{\theta}_r, \theta_r^{(3)}, \theta_l, \omega_l$	6
ASTSMC	$c_1, c_2, \lambda_{1,0}, \gamma_\lambda, a, \varepsilon_\theta, \nu, T_s, k_{obs}$	9	$\theta_r, \dot{\theta}_r, \ddot{\theta}_r, \theta_r^{(3)}, \theta_l, \omega_l$	6

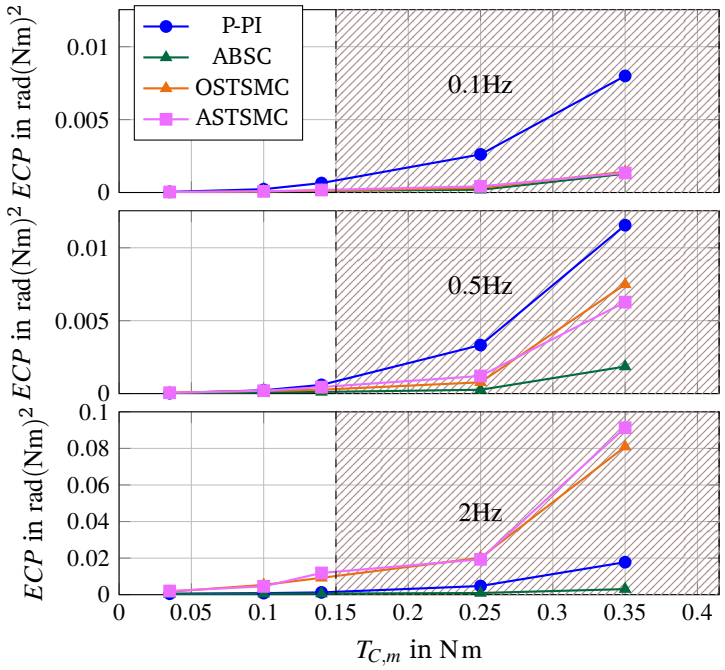

Figure B.17: ECP for all friction and frequency cases. The stripped area denotes the extreme friction cases.

B.6 Discussion

The experimental results showed that the ABSC outperformed all the other methods in all the tests. Specifically, the positioning tolerances were kept for all the cases of "realistic" friction degradation. The two sliding-mode schemes, namely the OSTSMC and ASTSMC have no substantial advantages compared to the state-of-the-art PI solution, in terms of either positioning precision or resilience to unknown and increasing friction. The design of the sliding surface on the basis of the "direct-position control" architecture requires the use of high gains, so that the finite-time convergence features of the sliding-mode algorithms are achieved. This, however, is impractical due to the significant actuator chattering. Consequently, the performance degradation of the OSTSMC and the ASTSMC was more severe than in the case of the PI.

Juxtaposing the results presented in this paper with the findings documented in [1], leads to the conclusion that the most effective tool positioning method under unknown and increasing friction is the cascaded P-STSMC scheme. This can also be seen in Figure B.22, where the average MAE for each of the 7 considered control

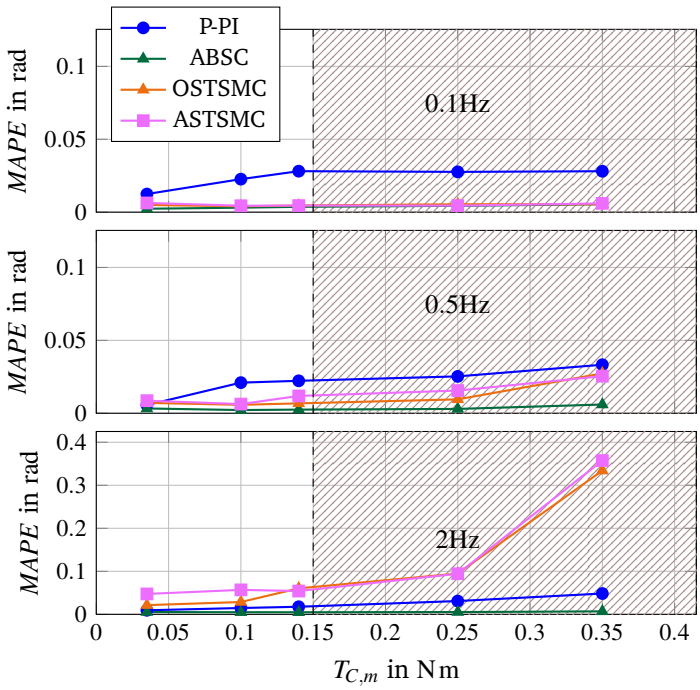

Figure B.18: MAPE for all friction and frequency cases. The stripped area denotes the extreme friction cases.

methods over the three different reference profiles are plotted against the increasing motor Coulomb friction. The results are presented in logarithmic scale for increased readability.

From this plot it can be seen that the STSMC consistently has the best performance in terms of positioning accuracy, followed by the three adaptive controllers ABSC, NAC and I&I-AC, then the PI and, lastly, the OSTSMC and ASTSMC. It should be noted that the difference in the architecture considered in [1] and the one in this paper plays a key role to the discrepancy of the performance between controller of the same family. Specifically, although the STSMC and the OSTSMC,ASTSMC utilize the same sliding-mode algorithm, their different architectures require the design of different sliding surfaces. In the case of the OSTSMC and ASTSMC the definition of the sliding manifold contains the dynamics of the load position error, all the uncertainties and disturbances at both the motor and the load side, as well as, the not measurable term $\dot{\omega}_l$. On the other hand, the sliding variable in the case of STSMC is defined as the motor velocity error [1].

It is also interesting to note that all three adaptive techniques show a similar

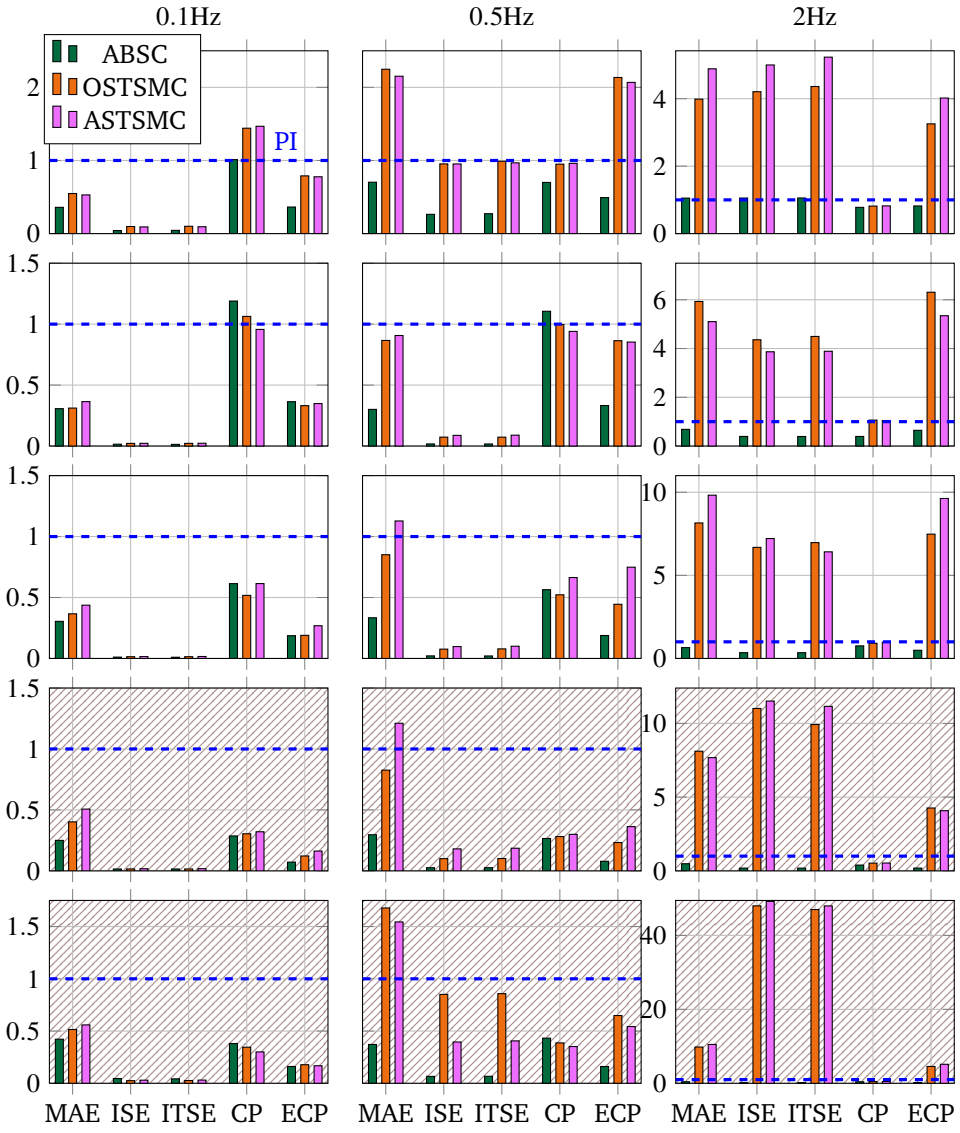

Figure B.19: Relative performance indices. The different cases of friction start with nominal friction and increase from top to bottom. The plots in the shaded area correspond to the extreme friction cases.

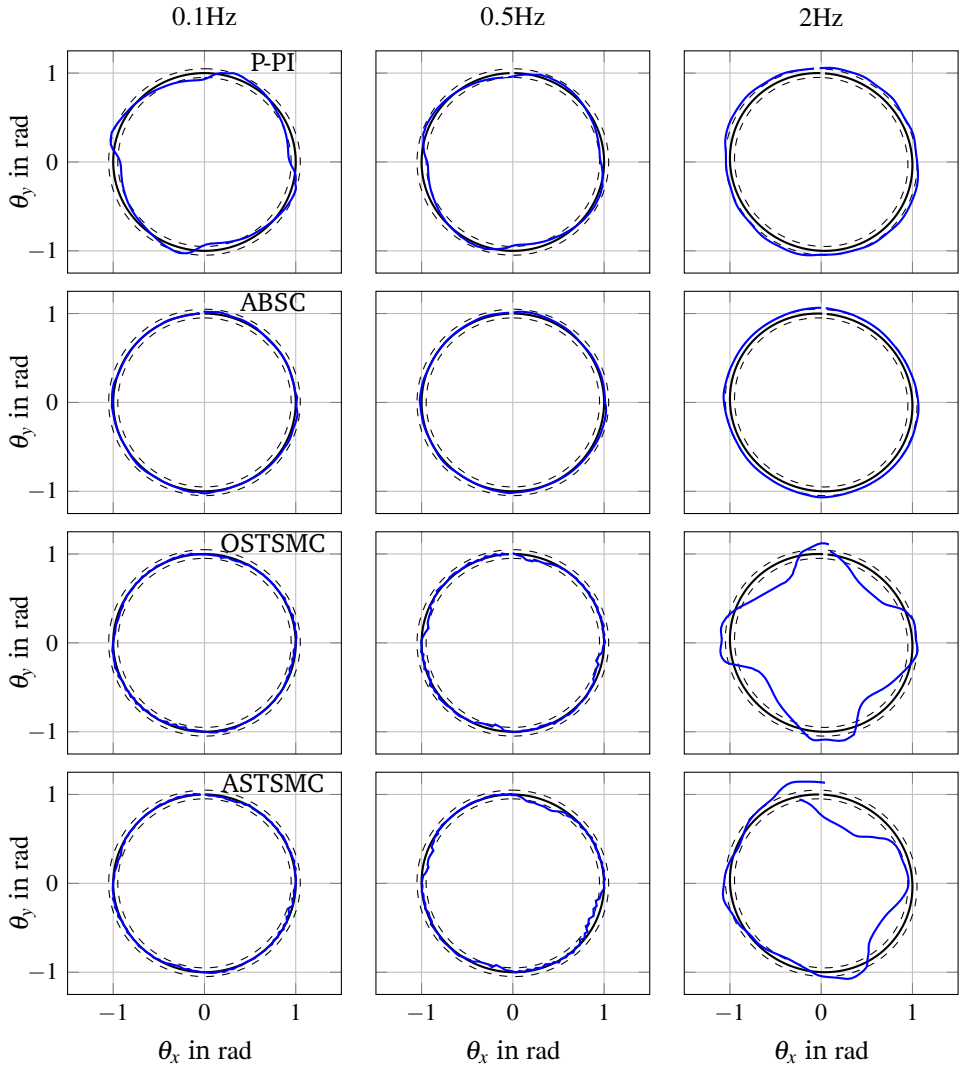

Figure B.20: $\theta_x - \theta_y$ plot for one cycle during Tests 7 (left column), 8 (middle column) and 9 (right column). From top to bottom: P-PI, ABSC, OSTSMC, ASTSMC. The dashed circles correspond to the $\pm 10^{-2}\mathrm{rad}$ accuracy limit. For increased clarity, both the error and the accuracy limits have been enlarged by a factor of 5.

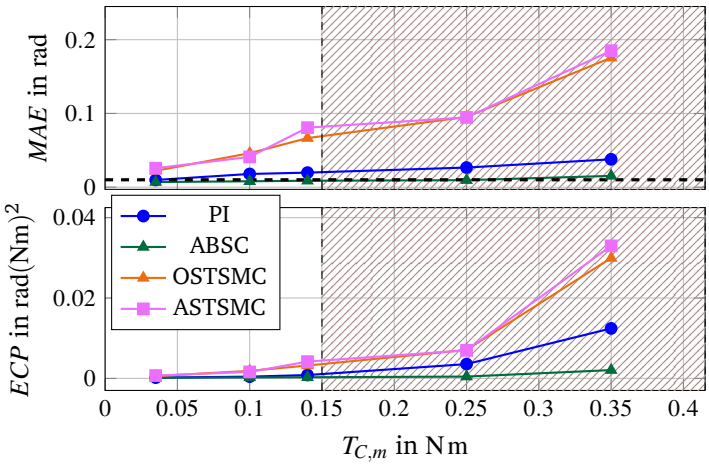

Figure B.21: Average MAE (top) and ECP (bottom) for all friction cases. The dashed line corresponds to the $\pm 10^{-2}\mathrm{rad}$ accuracy bound and the stripped area denotes the extreme friction cases.

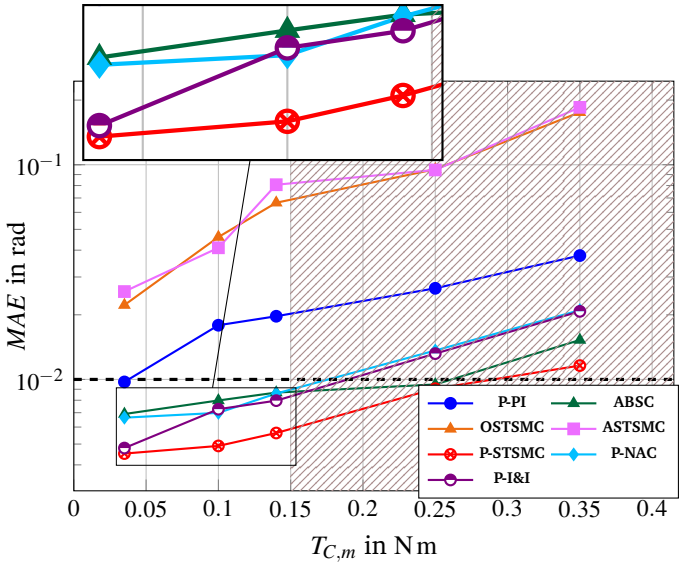

Figure B.22: Average MAE for all controllers including the ones presented in [1]. The dashed line corresponds to the $\pm 10^{-2}\mathrm{rad}$ accuracy bound and the stripped area denotes the extreme friction cases.

performance with the ABSC being slightly better. As it was discussed in [1], the degradation of the NAC and I&I-AC was primarily to the unmodelled backlash in the friction adjustment component. The ABSC was able to partially account for this phenomenon through the adaptation of the input gains ρ, b, as well as, the load friction parameters, which are not considered in the design of the NAC and I&I-AC. However, the former control scheme is more complex since its implementation involves the tuning of almost twice as many parameters compared to the cascaded adaptive solutions.

Finally, an overall ranking of the methods based on the average MAE over all the experiments and the *complexity index*, which is the sum of tunable parameters and required signals, is illustrated in Figure B.23. It can be concluded that the STSMC provides the best combination of accuracy, friction resilience and low design and application complexity.

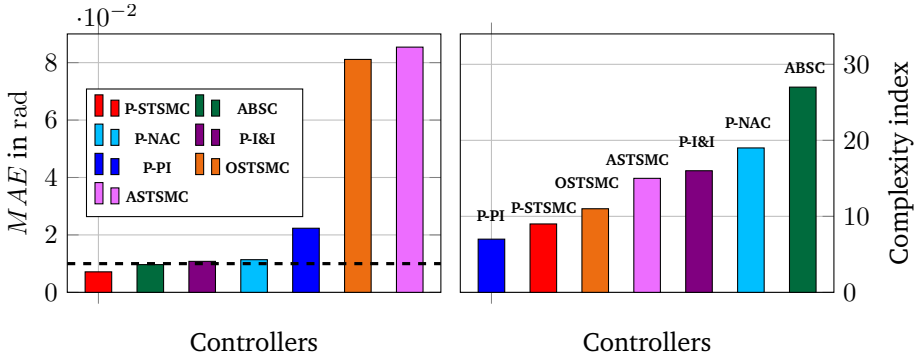

Figure B.23: (Left): Average MAE over all tests for all controllers including the ones presented in [1]. The dashed line corresponds to the $\pm 10^{-2}\mathrm{rad}$ accuracy bound. (Right): Complexity index as the sum of tunable parameters and required signals for each controller.

B.7 Conclusions and Future Work

This paper discussed the design and application of three friction-resilient nonlinear control methods, namely the adaptive backstepping controller, the output super-twisting sliding-mode controller and the adaptive super-twisting sliding-mode controller, for high-accuracy positioning in machine tools. All three strategies shared a direct-position control architecture, i.e. no cascaded structure was employed. In this way, friction and model uncertainties on both the drive-motor and the load were addressed. The controllers were implemented and tested on a real single-axis drive train with state-of-the-art Siemens equipment. The performance of each technique

was assessed in terms of both maximum deviation from the reference trajectory and overall efficiency at nominal and increased-friction operation. The design and implementation complexity of each method was also considered. A systematic comparison with conventional P-PI solutions, as well as cascaded nonlinear controllers, showed that the adaptive backstepping controller outperformed the P-PI scheme in all tests, maintaining the positioning tolerances even under incipient friction.

Acknowledgements

The authors would like to thank Dr. Carsten Hamm and Dr. Hans-Georg Koepken from Siemens AG, Digital Factory Division, Motion Control for their support with integrating the controllers into the existing Siemens software. Their invaluable input with respect to the real-life machine tool applications and equipment is greatly appreciated. The project is sponsored by Siemens AG.

Paper C

Robust Backlash Estimation for Industrial Drive-Train Systems - Theory and Validation

Dimitrios Papageorgiou[*1], Mogens Blanke[2], Hans Henrik Niemann[1], Jan H. Richter[3]

[1]Department of Electrical Engineering, Automation and Control Group, Technical University of Denmark, Elektrovej Building 326, 2800, Kgs. Lyngby, Denmark.

[2]AMOS CoE, Institute of Technical Cybernetics, Norwegian University of Science and Technology, Trondheim, Norway.

[3]Siemens AG, Digital Factory Division, D-90475 Nuremberg, Germany

Abstract:
Backlash compensation is used in modern machine tool controls to ensure high-accuracy positioning. When wear of a machine causes deadzone width to increase, high-accuracy control may be maintained if the deadzone is accurately estimated. Deadzone estimation is also an important parameter to indicate the level of wear in a machine transmission, and tracking its development is essential for condition-based maintenance. This paper addresses the backlash estimation problem using sliding-mode and adaptive estimation principles and shows that prognosis of the development of wear is possible in both theory and practice. The paper provides proof of asymptotic convergence of the suggested estimator and it shows how position offset between motor and load is efficiently utilized in the design of a very efficient estimator. The algorithm is experimentally tested on a drive-train system with state-of-the-art Siemens equipment. The experiments validate the theory and shows that expected performance and robustness to parameter uncertainties are both achieved.

[*]Principal corresponding author. Tel.: +45 45253572; E-mail: dimpa@elektro.dtu.dk

C.1 Introduction

Developing backlash in coupling equipment due to wear is one of the main reasons for performance degradation in machine tool systems. Since high-accuracy tool positioning is fundamental for maintaining the workpiece tolerances, backlash compensation solutions are used in nearly all modern CNC algorithms. As such, knowledge of the deadzone angles in advance is essential for integrating backlash compensation in the position servo loops of the machine drive motors. In this context, online estimation methods may facilitate an automatic compensation solution for developing backlash and also provide valuable information for prognosis and equipment lifetime.

The backlash phenomenon in various mechanical systems has been extensively studied over the past three decades. Indirect backlash estimation methods pertain to identifying torques and accelerations of the system parts that are affected by the backlash and from these signals drawing conclusions on the width of the deadzones. A characteristic example is the work in [51], where backlash estimation in a gearing system was done via calculation of the speed change of the driving part of the gear. An EKF was employed by [52, 53], for estimating the backlash torque in a two-mass motor arm and in an automotive powertrain. The backlash function parameters were identified offline based on this estimated torque. The author in [54] used describing functions to model the effects of backlash in a closed loop motion system. He presented an online calculation making use of a static relation between backlash model parameters and controller gains. Optimization techniques for offline identification of backlash torque were employed by [55] for cascaded linear systems and by [56], for a vehicle drive-line system, where position, velocity and torque measurements were used. The backlash torque was modelled with a "contact"/"non-contact" approach in [47]. The "non-contact" torque was modelled by a differentiable function of deadzone width and assessed the backlash amplitude indirectly through "non-contact" torque estimation in a nonlinear observer. Experimental validation was presented in [57], using a sliding-mode observer.

In most of the previous studies, backlash was described as the resulting torque when contact of the two moving parts of the coupling takes place. Direct estimation of the deadzone angle has mainly been addressed as an offline identification problem with methods that are valid for perturbations around a linearisation point of the system [52, 53, 55, 56]. In our prior work [4] we proposed a smooth backlash model based on variable shaft stiffness and outlined the basic ideas of a cascaded architecture for backlash estimation, based on sliding-mode and adaptive principles, along with simulations.

This paper extends our previous work by presenting a complete theoretical framework for the desing of the deadzone angle estimator. Specifically, the varying-stiffness model is modified to a more generic scheme that includes the initial motor-to-load position offset. The cascaded design of the estimation algorithm, outlined in [4], is presented in more detail and proofs of its convergence and stability properties in connection to the estimator's modular structure are provided. Moreover, a robustness analysis of the algorithm with respect to modelling uncertainties is carried out and bounds are given for the deadzone estimation error. Finally, the theoretical findings are validated both with simulations and through a number of experiments performed on a real single-axis drive train with state-of-the-art Siemens equipment.

The paper is organized as follows: Section C.2 states the estimation problem discussed in this study, describes the drive-train system and presents the modified backlash model based on varying shaft stiffness. Section C.3 analytically describes the design of the deadzone estimation scheme and provides the convergence and stability proof for the adaptive estimator. The effect of model uncertainties on the performance of the algorithm is discussed in Section C.4, where a proof for the boundedness of the estimation error is presented. Section C.5 illustrates the estimator performance in a simulation environment. Experimental validation of the theoretical findings is provided in Section C.6 and finally, conclusions are drawn and future work is discussed in Section C.7.

C.2 System Description and Problem Formulation

C.2.1 Drive Train Modelling

As discussed in [4], a typical single-axis machine tool can be described as a drive train, which consists of the drive motor, a flexible shaft with damping and backlash and a generalised load with friction. The correspondence between the single-axis machine tool and the abstraction of the drive-train can be seen in Figure C.1.

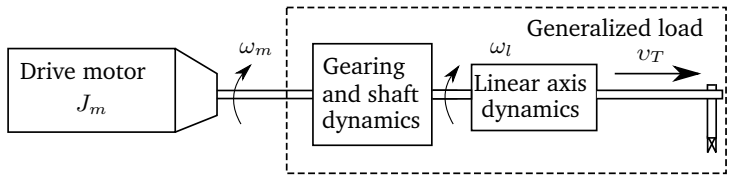

Figure C.1: Correspondence between mechanical drive-train and single-axis machine-tool systems. The angular velocities of the motor and the load are denoted by ω_m, ω_l, respectively, while v_T is the tool linear velocity.

The drive component is a PMSM, typically used for actuating linear axes in machine tools, especially for highly dynamic tasks. The motor is position-controlled with a cascade of a P and a PI controller, used for the position and the velocity loops, respectively.

In general, the electrical closed-loop dynamics is much faster than this of the mechanical system. Moreover, since the focus of this work is on the identification of backlash, i.e. on the level of the accelerations, and since the torque produced by the motor is measured, the closed-loop electrical dynamics of the motor will not be considered in this study. This does not affect the design of the estimation algorithms as it will become clearer later in the analysis.

The dynamics of the mechanical drive-train system reads:

$$\dot{\omega}_m = \frac{1}{J_m}\left(u - T_{F,m} - \frac{1}{N}T_l\right) \tag{C.1}$$

$$\dot{\theta}_m = \omega_m \tag{C.2}$$

$$\dot{\omega}_l = \frac{1}{J_l}\left(T_l - T_{F,l}\right) \tag{C.3}$$

$$\dot{\theta}_l = \omega_l \ , \tag{C.4}$$

where $\omega_m, \theta_m, \omega_l, \theta_l$ are the angular velocity and position of the motor and the load, respectively, J_m, J_l are the corresponding inertias and N is the gearing ratio. In the backlash-free case the interconnecting torque T_l is given from:

$$T_l = K_S\left(\frac{1}{N}\theta_m - \theta_l\right) + D_S\left(\frac{1}{N}\omega_m - \omega_l\right) \tag{C.5}$$

where K_S is the shaft stiffness and D_S the damping coefficient. The friction torques acting on the drive motor and the load express different frictional phenomena. $T_{F,m}$ comes mostly from the contacting surfaces of the motor bearings while $T_{F,l}$ describes the total Coulomb and viscous friction in the load. The two friction torques are modelled as described in the following equations [30]:

$$T_{F,m} = T_{C,m}\text{sgn}(\omega_m) + \beta_m\omega_m \tag{C.6}$$

$$T_{F,l} = T_{C,l}\text{sgn}(\omega_l) + \beta_l\omega_l \tag{C.7}$$

where $\text{sgn}(\cdot)$ is the signum function defined in (II.1). The parameters $\beta_m, \beta_l, T_{C,m}, T_{C,l}$ are considered constant. Figure C.2 illustrates the block diagram of the drive-train system in open loop.

C.2.2 Backlash Modelling

Backlash shows up as a loss of engagement between two moving parts (e.g. motor and load) due to a developing gap (deadzone) in the coupling mechanisms

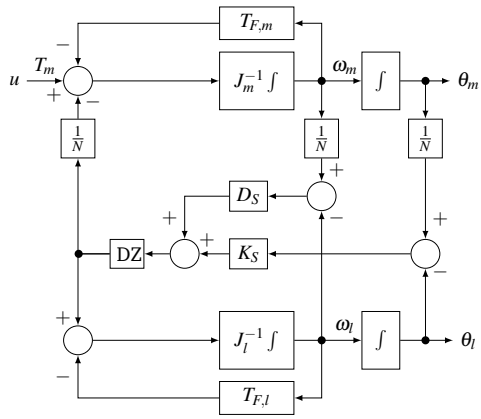

Figure C.2: Block diagram of the open-loop mechanical drive-train system. The block labelled "DZ" represents the backlash deadzone.

as shown in Figure C.3. The backlash phenomenon can be interpreted as a sudden change either in the load inertia or in the shaft stiffness. In general, the backlash torque is modelled after the restoring and damping torques in a mass-spring-damper system. While in the deadzone, these two torques are either vanishing or becoming very small, nearly zero. A number of studies have been carried out regarding the description of the torques due to backlash. The most intuitive and common one is the deazone model [30, 45], where the interconnecting torque T_l becomes zero inside the deadzone. Outside the deadzone the angle difference is offset by the width of the deadzone angle. A similar approach is found in [46], where the ratio of the angle differences over the deadzone width is considered. Dynamical models described in [48] and [50] pertain to expressing the backlash torque as a sudden impact. The torque is again given by a mass-spring-damper system, where the elastic linear relative deformation of the two colliding coupling parts has its own stiff dynamics. A different dynamical model is described in [45] and [49], where a backlash angle is defined and its dynamics is used for calculating the impact torque.

In [4] we introduced a smooth backlash model based on changing shaft stiffness, to overcome the numerical difficulties present in state-of-the-art discontinuous models. This model is modified in this paper to include an initial position offset between motor and load, as seen in Figure C.3.

Defining the angular position and velocity differences between drive motor and

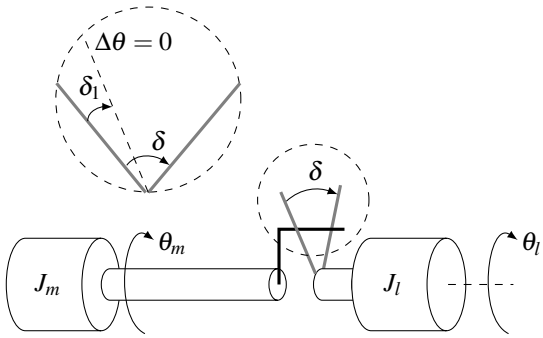

Figure C.3: Backlash illustration: The straight dashed line denotes the relative configuration between the motor and the load rotors that is taken as zero position difference. When the difference between the motor and the load position is larger than $-\delta_1$ or smaller than $\delta - \delta_1$, then the two shafts are disengaged and no torque is applied to the motor or the load.

load as

$$\Delta\theta \triangleq \frac{1}{N}\theta_m - \theta_l \tag{C.8}$$

$$\Delta\omega \triangleq \frac{1}{N}\omega_m - \omega_l \tag{C.9}$$

the interconnecting torque T_l in the deadzone model is given by

$$T_l^{DZ} = \begin{cases} K_S(\Delta\theta + \delta_1) + D_S\Delta\omega & , \Delta\theta < -\delta_1 \\ K_S(\Delta\theta + \delta_1 - \delta) + D_S\Delta\omega & , \Delta\theta > \delta - \delta_1 \\ 0 & , \ 0 \leq \Delta\theta + \delta_1 \leq \delta \ , \end{cases} \tag{C.10}$$

where δ is the width of the deadzone in rad. In the modified smooth model the shaft stiffness and the backlash torque is described by:

$$K_{BL} = \frac{K_S}{\pi}\left[\pi + \arctan(\alpha(\Delta\theta - \delta + \delta_1))\right] - \frac{K_S}{\pi}\arctan(\alpha(\Delta\theta + \delta_1)) \tag{C.11}$$

$$T_l(\boldsymbol{x}, \delta) = \left[\Delta\theta + \delta_1 - \frac{\delta}{2}\cdot(1 + \mathrm{sgn}(\Delta\theta)) + \frac{D_S}{K_S}\Delta\omega\right]\cdot K_{BL}(\Delta\theta, \delta) \ , \tag{C.12}$$

where

$$\boldsymbol{x} \triangleq \begin{bmatrix} \omega_m & \theta_m & \omega_l & \theta_l \end{bmatrix}^T$$

is the state vector, $0 \leq \delta_1 \leq \delta$ is the initial motor-load position offset and α is a large positive real number that parametrizes how steep the change in the stiffness is. For $\alpha \to \infty$, it is clear that $T_l \to T_l^{DZ}$. This can also be seen in Figure C.4, where the stiffness $K_{BL}(\Delta\theta, \delta)$ and the corresponding backlash torques are plotted for different values of the parameter α. A complete explanation of the most important variables and notation used in the modelling of the system is provided in Table C.1.

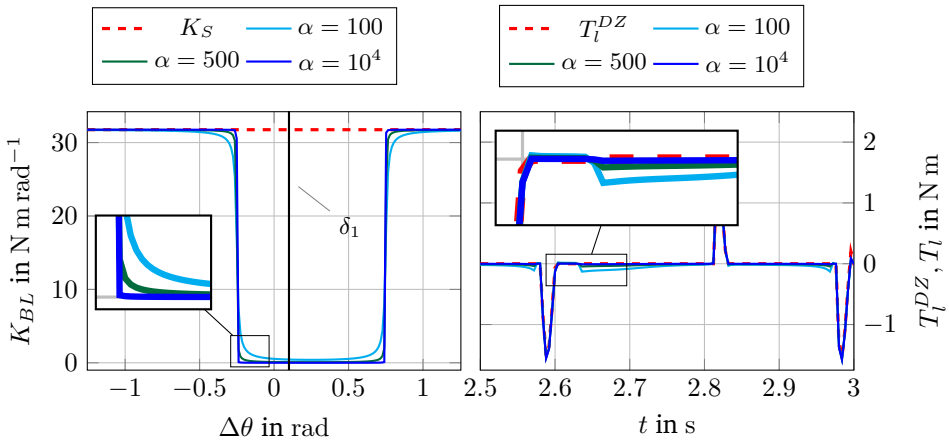

Figure C.4: (Left) Shaft stiffness varying between two values. The larger the value of α, the steeper the change in the stiffness is. (Right) Backlash torque for a sinusoidal motion profile using the deadzone model (red dotted curve) and the varying-stiffness model (solid lines) for different values of α.

Table C.1: System model nomenclature

Symbol	Description	Units
States and Outputs		
ω_m, ω_l	Motor/load angular velocity	rad s^{-1}
θ_m, θ_l	Motor/load angular position	rad
Inputs and disturbances		
u	Torque command	N m
$T_{F,m}, T_{F,l}$	Motor/load friction	N m
T_l	Interconnecting/backlash torque	N m
Constant parameters		
J_m, J_l	Motor/load inertia	kg m^2
K_S	Shaft stiffness	N m rad^{-1}
D_S	Shaft damping coefficient	N m s rad^{-1}
N	Gearing ratio	–
$T_{C,m}, T_{C,l}$	Coulomb friction on the motor/load	N m
β_m, β_l	Viscous friction coefficients	N m s rad^{-1}
δ, δ_1	Deadzone angle/position offset	rad

C.2.3 Problem Formulation

The collective objective can be summarised in the following problem formulation:

Problem 3 (Deadzone angle estimation)**.** *Given the single-axis drive-train system described in* (C.1)-(C.7) *and the backlash model in* (C.11),(C.12)*, design an online dynamic estimator for the deadzone angle δ, such that the estimate $\hat{\delta}$ fulfills the following requirements:*

- *Convergence to a compact set containing the real parameter value.*
- *Maximum steady-state absolute estimation error less than 10^{-2} rad.*

C.3 Backlash Deadzone Angle Estimation

The estimation of the deazone angle belongs to the family of problems of online parameter estimation in systems with nonlinear parametrization, treated in numerous works in the literature. The reader is indicatively referred to [88, 117, 118, 119, 120, 121].

The approach presented in [4] is partially based on a method for parameter estimation in nonlinearly parametrized systems presented in [122]. The basic idea relates to estimating a perturbation of the system dynamics that depends on the unknown parameter and then finding an adaptation law for estimating the parameter itself. In [122] both the perturbation and the unknown parameter are estimated simultaneously using the two estimation blocks (perturbation and parameter) in feedback interconnection. In [4] these two estimation tasks are separated to allow for an independent design for each of them. In this section the estimation scheme presented in [4] is elaborated and a proof of its convergence and stability properties is provided.

C.3.1 Method Overview

As in [4], the dynamics of the load shown in Equation (C.3) is used to apply the method for the deadzone angle estimation. This is because all the states are measured and the unknown parameter δ affects the dynamics of both the motor and the load in the same way, i.e. through the torque T_l. The load velocity subsystem can be re-written in the form:

$$\dot{\omega}_l = -\frac{1}{J_l} T_{F,l} + \phi(\boldsymbol{x}, \delta) \tag{C.13}$$

with

$$\phi(\boldsymbol{x}, \delta) \triangleq \frac{1}{J_l} T_l(\boldsymbol{x}, \delta) \tag{C.14}$$

and δ being the unknown parameter, which belongs to a compact set $\mathcal{D} \subset \mathbb{R}_{\geq 0}$. The method is divided in two parts:

1. Obtain an estimation $\hat{\phi}$ of the perturbation ϕ.
2. Derive an adaptation law for the deadzone angle

$$\dot{\hat{\delta}} \triangleq \rho(\boldsymbol{x}, \hat{\phi}, \hat{\delta}) \tag{C.15}$$

based on $\hat{\phi}$.

C.3.2 Sliding-mode Perturbation Observer

A second-order SMO is used for finding an estimate of ϕ. Its structure is given by [61, 123]:

$$\dot{\hat{\omega}}_l = -\frac{1}{J_l} T_{F,l} + v \tag{C.16}$$

where $\tilde{\omega}_l = \omega_l - \hat{\omega}_l$ is the velocity estimation error and v is an appropriate high frequency term, called the *injection signal*, that depends on the innovation signal $\tilde{\omega}_l$.

From (C.3) and (C.16) the dynamics of the velocity estimation error in absence of any model or parameters uncertainties reads:

$$\dot{\tilde{\omega}}_l = \dot{\omega}_l - \dot{\hat{\omega}}_l = \frac{1}{J_l} T_l - v \tag{C.17}$$

where the arguments of T_l are omitted for brevity. With he sliding manifold is defined as

$$\mathcal{S} \triangleq \left\{ \tilde{\omega}_l \in \mathbb{R} : \tilde{\omega}_l = \dot{\tilde{\omega}}_l = 0 \right\} \tag{C.18}$$

the design of v is given in [70]:

$$v = k_1 |\tilde{\omega}_l|^{\frac{1}{2}} \text{sgn}(\tilde{\omega}_l) + k_2 \int_0^t \text{sgn}(\tilde{\omega}_l(\tau)) d\tau \tag{C.19}$$

where k_1, k_2 are positive gains. The resulting observer is called the STSMO and it is proven in [73, 124] that for appropriate positive gains k_1, k_2 the injection signal v brings the observer error dynamics on the sliding manifold $\mathcal{S}$ in *finite time*, where it remains thereafter.

If the error dynamics reaches the sliding manifold, then $\dot{\tilde{\omega}}_l = \tilde{\omega}_l = 0$ for all future times, which from Equation (C.16) leads to

$$v = \frac{1}{J_l} T_l \ . \tag{C.20}$$

In other words, if the injection signal v is designed such that the estimation error dynamics reaches the sliding manifold S and remains thereafter, then the unknown perturbation $\phi = \frac{1}{J_l} T_l$ is indirectly calculated from (C.20) [79]. Hence, the unknown perturbation can be estimated at each time instant t by

$$\hat{\phi} = k_1 |\tilde{\omega}_l|^{\frac{1}{2}} \text{sgn}(\tilde{\omega}_l) + k_2 \int_0^t \text{sgn}(\tilde{\omega}_l(\tau)) d\tau \tag{C.21}$$

Remark C.1. The choice of a second order SMO for a system of relative degree 1 (the subsystem is scalar) was made due to the property of higher order SMOs of alleviating the chattering in the injection and estimation signals [61, 69].

Remark C.2. Apart from the appropriate selection of k_1, k_2, finite-time estimation additionally requires that $T_l, \dot{T}_l$ be bounded. This is ensured by the boundedness of the state vector and the smoothness of the backlash model. However, the bound on $\dot{T}_l$ is proportional to α. This means that the closer the model is to the deadzone model, the larger this bound will be, which in turn leads to higher gains for the observer and, consequently, more chattering in the estimation signal.

C.3.3 Adaptive Backlash Angle Estimator

The adaptive deadzone angle estimator is based on the design proposed in [122] for the estimation of unknown parameters in nonlinearly parametrized systems. For the rest of the analysis we consider that the unknown parameter δ lies in a compact set $\mathcal{D} = [0, \delta_{max}] \subset \mathbb{R}_{\geq 0}$, with δ_{max} being the largest considered deadzone angle and we define the backlash angle estimation error as

$$\tilde{\delta} = \delta - \hat{\delta} \, .$$

The following assumptions are made:

Assumption C.3.1. *The deadzone angle is constant, i.e.*

$$\dot{\delta} = 0 \, .$$

Assumption C.3.2. *There exists a piecewise continuous function $\sigma : \mathbb{R}^4 \to \mathbb{R}_{\geq 0}$ and a function $\mu : \mathbb{R}^4 \times \mathcal{D} \to \mathbb{R}$, both of them bounded for bounded state vector*

$\boldsymbol{x}$, such that $\forall \boldsymbol{x} \in \mathbb{R}$ and all pairs $\delta_1, \delta_2 \in \mathcal{D}$,

$$\mu(\boldsymbol{x}, \delta_1)\frac{1}{J_l}\frac{\partial T_l}{\partial \delta}(\boldsymbol{x}, \delta_2) \geq \sigma(\boldsymbol{x}) \; . \tag{C.22}$$

Assumption C.3.3. *There exists a positive real constant number $L > 0$ such that $\forall \delta_1, \delta_2 \in \mathcal{D}$,*

$$\frac{1}{J_l}|T_l(\boldsymbol{x}, \delta_2) - T_l(\boldsymbol{x}, \delta_1)| \leq L\sqrt{\sigma(\boldsymbol{x})}|\delta_2 - \delta_1| \; . \tag{C.23}$$

Assumption C.3.4. *There exist positive real numbers T, ε such that $\forall t \in \mathbb{R}_{\geq 0}$,*

$$\int_t^{t+T} \sigma(\boldsymbol{x}(\tau))d\tau \geq \varepsilon \; . \tag{C.24}$$

The following Theorem constitutes the core of the adaptive estimator design:

Theorem C.3.1. *Consider the dynamics of the load velocity given by Equations* (C.11)*,* (C.12)*,* (C.13) *and* (C.14)*. Consider also an estimate $\hat{\phi}$ of the interconnecting perturbation ϕ with the associated estimation error defined as*

$$\tilde{\phi} \triangleq \phi - \hat{\phi} \; . \tag{C.25}$$

The adaptive estimator

$$\dot{\hat{\delta}} = \rho(\boldsymbol{x}, \hat{\phi}, \hat{\delta}) = \text{Proj}\left[\hat{\delta}, \gamma\mu(\boldsymbol{x}, \hat{\delta})\left(\hat{\phi} - \frac{1}{J_l}T_l(\boldsymbol{x}, \hat{\delta})\right)\right] \tag{C.26}$$

with $\gamma > 0$ being the adaptation gain and Proj$(\cdot, \cdot)$ *the projection operator defined in* (II.6)*, ensures that the estimation error $\tilde{\delta}$ asymptotically converges to 0, uniformly in $\boldsymbol{x}$ if assumptions C.3.2-C.3.4 are satisfied and $\tilde{\phi}^* = 0$ is an UGAS equilibrium of the perturbation estimation error dynamics $\tilde{\phi}$.*

Proof. The proof is inspired by the proof of Proposition 4 in [122] and the stability theory of interconnected systems in [132]. Under Assumption C.3.1, the dynamics of the parameter estimation error is written as

$$\dot{\tilde{\delta}} = \dot{\delta} - \dot{\hat{\delta}} = -\text{Proj}\left[\hat{\delta}, \gamma\mu(\boldsymbol{x}, \hat{\delta})\left(\hat{\phi} - \frac{1}{J_l}T_l(\boldsymbol{x}, \hat{\delta})\right)\right] \; . \tag{C.27}$$

Defining the perturbation estimation error as in (C.25) allows expressing the dynamics of $\tilde{\delta}$ as:

$$\dot{\tilde{\delta}} = -\text{Proj}\left[\hat{\delta}, \gamma\mu(\boldsymbol{x},\hat{\delta})\left(\phi - \tilde{\phi} - \frac{1}{J_l}T_l(\boldsymbol{x},\hat{\delta})\right)\right] . \tag{C.28}$$

From (C.28) it can be easily seen that the total error dynamics can be described as the cascaded interconnection of the unperturbed error system given by (C.28) for $\tilde{\phi} \equiv 0$ and the output $\tilde{\phi}$ of the (interconnecting torque) perturbation estimation error system as shown in Figure C.5.

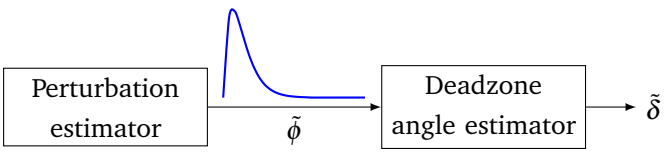

Figure C.5: Cascaded interconnection of the perturbation and angle estimation error systems.

The proof is now split in two parts: First it is shown that the unperturbed system of the deadzone angle estimation error is ULES and then it will be shown that a UGAS estimate of ϕ renders the total cascaded system UGAS.

Substituting $\tilde{\phi} = 0$ in (C.28) leads to

$$\dot{\tilde{\delta}} = -\text{Proj}\left[\hat{\delta}, \gamma\mu(\boldsymbol{x},\hat{\delta})\frac{1}{J_l}\left(T_l(\boldsymbol{x},\delta) - T_l(\boldsymbol{x},\hat{\delta})\right)\right] . \tag{C.29}$$

The shortened notation

$$\mu \triangleq \mu(\boldsymbol{x},\hat{\delta})$$
$$\hat{T}_l \triangleq T_l(\boldsymbol{x},\hat{\delta}) .$$

will be used in the following for brevity. Define the Lyapunov function candidate

$$V(t,\tilde{\delta}) = \frac{1}{2}\left(\frac{1}{\gamma} - \kappa\int_t^\infty e^{(t-\tau)}\sigma(\boldsymbol{x}(\tau))d\tau\right)\tilde{\delta}^2 \tag{C.30}$$

where κ is a real positive number to be defined. The function is positive definite since

$$\alpha_1(|\tilde{\delta}|) \leq V(t,\tilde{\delta}) \leq \alpha_2(|\tilde{\delta}|)$$

with a_1, a_2 being class-$\mathcal{K}_\infty$ functions (see Definition 7 in Appendix III) defined as:

$$\alpha_1(|\tilde{\delta}|) = \left(\frac{1}{\gamma} - \kappa \sup_{\boldsymbol{x}\in\mathcal{B}_r}\sigma(\boldsymbol{x})\right)|\tilde{\delta}|^2 \tag{C.31}$$

$$\alpha_2(|\tilde{\delta}|) = \frac{1}{\gamma}|\tilde{\delta}|^2 \tag{C.32}$$

for $\kappa < \frac{1}{\gamma \sup\limits_{\boldsymbol{x}\in\mathcal{B}_r} \sigma(\boldsymbol{x})}$, where $\mathcal{B}_r = \left\{\boldsymbol{x} \in \mathbb{R}^4 \middle| \|\boldsymbol{x}\| \leq r, r < \infty\right\}$. The time derivative of V along the trajectories of the estimation error reads:

$$\begin{aligned}
\dot{V}(t,\tilde{\delta}) &= \frac{\partial V}{\partial t}(t,\tilde{\delta}) + \frac{\partial V}{\partial \tilde{\delta}}(t,\tilde{\delta})\dot{\tilde{\delta}} = \\
&= \frac{1}{2}\tilde{\delta}^2 \frac{\partial}{\partial t}\left[-\kappa \int_t^\infty e^{(t-\tau)}\sigma(\boldsymbol{x}(\tau))d\tau\right] - \tilde{\delta}\left(\frac{1}{\gamma} - \kappa\int_t^\infty e^{(t-\tau)}\sigma(\boldsymbol{x}(\tau))d\tau\right)\dot{\hat{\delta}} = \\
&= \frac{\kappa}{2}\tilde{\delta}^2\left[\frac{\partial}{\partial t}\int_0^t e^{(t-\tau)}\sigma(\boldsymbol{x}(\tau))d\tau - \int_0^\infty \frac{\partial}{\partial t}e^{(t-\tau)}\sigma(\boldsymbol{x}(\tau))d\tau\right] \\
&- \tilde{\delta}\frac{1}{\gamma}\text{Proj}\left[\hat{\delta}, \gamma\mu\cdot\frac{1}{J_l}\left(T_l - \hat{T}_l\right)\right] \qquad \text{(C.33)} \\
&- \tilde{\delta}\kappa\int_t^\infty e^{(t-\tau)}\sigma(\boldsymbol{x}(\tau))d\tau \cdot \text{Proj}\left[\hat{\delta}, \gamma\mu\cdot\frac{1}{J_l}\left(T_l - \hat{T}_l\right)\right]. \qquad \text{(C.34)}
\end{aligned}$$

Using the property

$$-\tilde{\delta}\frac{1}{\gamma}\text{Proj}\left[\hat{\delta}, \gamma\mu\cdot\frac{1}{J_l}\left(T_l - \hat{T}_l\right)\right] \leq -\tilde{\delta}\mu\cdot\frac{1}{J_l}\left(T_l - \hat{T}_l\right)$$

presented in Lemma E.1 in [83] and Theorem 11.1 from [133] (see Appendix VIII), as well as, the property

$$\int_0^\infty e^{(t-\tau)}\sigma(\boldsymbol{x}(\tau))d\tau \geq e^{-T}\int_t^{t+T}\sigma(\boldsymbol{x}(\tau))d\tau,\ T>0 \qquad \text{(C.35)}$$

(see Appendix IX for a proof) Equation (C.34) gives

$$\begin{aligned}
\dot{V}(t,\tilde{\delta}) &\leq \frac{\kappa}{2}\tilde{\delta}^2\left(\sigma(\boldsymbol{x}) - e^{-T}\int_t^{t+T}\sigma(\boldsymbol{x}(\tau))d\tau\right) - \tilde{\delta}\int_0^1 \mu\cdot\frac{1}{J_l}\frac{\partial T_l}{\partial\delta}(\hat{\delta}+p\tilde{\delta})\tilde{\delta}dp \\
&+ \left|\tilde{\delta}\right|\kappa\gamma\left|\int_t^\infty e^{(t-\tau)}\sigma(\boldsymbol{x}(\tau))d\tau\right| |\mu|\frac{1}{J_l}\left|T_l - \hat{T}_l\right|. \qquad \text{(C.36)}
\end{aligned}$$

Using Assumptions (C.3.2)-(C.3.4) in the inequality above and introducing M, Σ as upper bounds for $|\mu(\boldsymbol{x},\delta)|, |\sigma(\boldsymbol{x})|$, respectively leads to

$$\dot{V} \leq -\left(1-\frac{\kappa}{2}\right)\sigma(\boldsymbol{x})\tilde{\delta}^2 - \frac{\kappa}{2}\varepsilon e^{-T}\tilde{\delta}^2 + \kappa\gamma\cdot M\cdot\Sigma\cdot L\sqrt{\sigma(\boldsymbol{x})}\left|\tilde{\delta}\right|^2 = -\boldsymbol{\psi}^T\boldsymbol{Q}\boldsymbol{\psi} \qquad \text{(C.37)}$$

where

$$\begin{aligned}
\boldsymbol{\psi}^T &= \begin{bmatrix}\left|\tilde{\delta}\right| & \sqrt{\sigma(\boldsymbol{x})}\left|\tilde{\delta}\right|\end{bmatrix} \\
\boldsymbol{Q} &= \begin{bmatrix}\frac{\kappa}{2}\varepsilon e^{-T} & -\frac{\kappa}{2}\gamma\cdot M\cdot\Sigma\cdot L \\ -\frac{\kappa}{2}\gamma\cdot M\cdot\Sigma\cdot L & 1-\frac{\kappa}{2}\end{bmatrix}
\end{aligned}$$

and the property

$$\int_t^\infty e^{(t-\tau)}d\tau = 1 \qquad \text{(C.38)}$$

was used. From Inequality (C.37) it can be seen that $\dot{V}$ is negative definite if κ is chosen as

$$\kappa < \frac{2}{1 + \frac{e^T}{\varepsilon} M^2 \Sigma^2 \gamma^2 L^2} \ . \tag{C.39}$$

For such κ and by defining

$$\lambda_{min}(\boldsymbol{Q}) = \min_{i \in \{1,2\}} \{\lambda_i \in \mathbb{R}_{\geq 0} | P_{\boldsymbol{Q}}(\lambda_i) = 0\}$$

where $P_{\boldsymbol{Q}}$ is the characteristic polynomial of $\boldsymbol{Q}$, Equation (C.37) is written:

$$\dot{V}(t, \tilde{\delta}) \leq -\underbrace{\lambda_{min}(Q)}_{\alpha_3} \left\| \frac{1}{\sqrt{\sigma(\boldsymbol{x})}} \right\|_2^2 \left|\tilde{\delta}\right|^2 \leq -\alpha_3 \left|\tilde{\delta}\right|^2 \ . \tag{C.40}$$

Moreover,

$$\begin{aligned} \left|\frac{\partial V}{\partial \tilde{\delta}}\right| &= \left|\tilde{\delta}\left(\frac{1}{\gamma} - \kappa \int_t^\infty e^{(t-\tau)} \sigma(\boldsymbol{x}(\tau)) d\tau\right)\right| \leq \left|\frac{1}{\gamma} - \kappa e^{-T} \int_t^{t+T} \sigma(\boldsymbol{x}(\tau)) d\tau\right| \left|\tilde{\delta}\right| \\ &\leq \left|\frac{1}{\gamma} - \kappa e^{-T} \Sigma \int_t^{t+T} d\tau\right| \left|\tilde{\delta}\right| \leq \underbrace{\left|\frac{1}{\gamma} - \kappa e^{-T} \Sigma T\right|}_{\alpha_4} \left|\tilde{\delta}\right| = \alpha_4 \left|\tilde{\delta}\right| \end{aligned} \tag{C.41}$$

which implies that $\frac{\partial V}{\partial \tilde{\delta}}$ is Uniformly Bounded (UB). Then the equilibrium point $\tilde{\delta}^* = 0$ is ULES [128, Th. 4.10, p. 154].

Next it will be shown that the system in (C.28) is ISS (see Definition 10 in Appendix II) with respect to $\tilde{\phi}$.

Taking the time derivative of V along the trajectories of the perturbed system (C.28) now and following the same steps as in the case of the unperturbed system leads to the following:

$$\begin{aligned} \dot{V}(t, \tilde{\delta}) &\leq -\alpha_3 \left|\tilde{\delta}\right|^2 - \tilde{\delta}\left(\frac{1}{\gamma} - \kappa \int_t^\infty e^{t-\tau} \sigma(\boldsymbol{x}(\tau)) d\tau\right) \gamma \mu \tilde{\phi} \\ &\leq -\alpha_3 \left|\tilde{\delta}\right|^2 + \left|\tilde{\delta}\right| \left(1 - \kappa\gamma e^{-T} \int_t^{t+T} \sigma(\boldsymbol{x}(\tau)) d\tau\right) \mu \left|\tilde{\phi}\right| \\ &\leq -\alpha_3 \left|\tilde{\delta}\right|^2 + \left|\tilde{\delta}\right| \left(1 - \kappa\gamma e^{-T} \varsigma \cdot T\right) M \left|\tilde{\phi}\right| \\ &\leq \left|\tilde{\delta}\right| \left[\left(1 - \kappa\gamma e^{-T} \varsigma \cdot T\right) M \left|\tilde{\phi}\right| - \vartheta \alpha_3 \left|\tilde{\delta}\right|\right] - (1 - \vartheta) \alpha_3 \left|\tilde{\delta}\right|^2 \\ &\leq -(1 - \vartheta) \alpha_3 \left|\tilde{\delta}\right|^2 \end{aligned} \tag{C.42}$$

for all $\tilde{\delta} \in \mathbb{R}$ that satisfy

$$\left|\tilde{\delta}\right| \geq \frac{\left(1 - \kappa\gamma e^{-T} \varsigma \cdot T\right) M}{\alpha_3 \vartheta} \left|\tilde{\phi}\right| = \underbrace{R \left|\tilde{\phi}\right|}_{r(|\tilde{\phi}|)} \tag{C.43}$$

with $0 < \vartheta < 1$,

$$R \triangleq \frac{\left(1 - \kappa\gamma e^{-T\varsigma \cdot T}\right) M}{\alpha_3 \vartheta} \,. \tag{C.44}$$

and $\varsigma \geq 0$ being a lower bound for $|\sigma(\boldsymbol{x})|$. Then, according to [128, Th. 419], the perturbed system (C.28) is ISS with respect to $\tilde{\phi}$.

Lastly, since the unperturbed system is ULES and the perturbed system (C.28) is ISS with respect to $\tilde{\phi}$ (which implies uniform global boundedness of the solutions of (C.28)), then if $\tilde{\phi}^* = 0$ is UGAS, then the deadzone angle estimation error $\tilde{\delta}$ asymptotically converges to the real value δ [132, Lemma 1], which completes the proof. ■

The uniform global asymptotic stability of the equilibrium $\tilde{\phi}^* = 0$ is theoretically guaranteed by the STSMO, which ensures finite-time convergence of the perturbation estimate to its real value (which is a stronger stability property).

The final steps of the design concern satisfying Assumptions C.3.2-C.3.4. Selecting $\mu(\boldsymbol{x}, \hat{\delta})$ as

$$\mu(\boldsymbol{x}, \hat{\delta}) = \frac{J_l}{K_S^2} \frac{\partial T_l}{\partial \hat{\delta}}(\boldsymbol{x}, \hat{\delta}) \tag{C.45}$$

condition (C.22) is satisfied with

$$\sigma(\boldsymbol{x}) = \frac{1}{K_S^2} \left(\frac{\partial T_l}{\partial \hat{\delta}}\right)^2 = \frac{1}{\pi^2} \left[\chi_1(\boldsymbol{x}, \hat{\delta}) + \chi_2(\boldsymbol{x}, \hat{\delta})\right]^2 \tag{C.46}$$

where χ_1, χ_2 are defined as

$$\chi_1(\boldsymbol{x}, \hat{\delta}) = \frac{1}{2}(1 + \text{sgn}(\Delta\theta)) \cdot \left[\pi + \arctan(\alpha(\Delta\theta - \hat{\delta} + \delta_1)) - \arctan(\alpha(\Delta\theta + \delta_1))\right] \tag{C.47}$$

$$\chi_2(\boldsymbol{x}, \hat{\delta}) = \left[\Delta\theta + \delta_1 - \frac{\hat{\delta}}{2} \cdot (1 + \text{sgn}(\Delta\theta)) + \frac{D_S}{K_S}\Delta\omega\right] \cdot \frac{\alpha}{1 + \left[\alpha(\Delta\theta + \delta_1 - \hat{\delta})\right]^2} \tag{C.48}$$

The adaptive law for the parameter estimate $\hat{\delta}$ is finally given by:

$$\dot{\hat{\delta}} = \text{Proj}\left\{\hat{\delta}, \gamma \frac{J_l}{K_S^2} \frac{\partial T_l}{\partial \hat{\delta}}(\boldsymbol{x}, \hat{\delta}) \left[\hat{\phi} - \frac{1}{J_l} T_l(\boldsymbol{x}, \hat{\delta})\right]\right\}, \ \gamma > 0 \tag{C.49}$$

where

$$\frac{\partial T_l}{\partial \hat{\delta}}(\boldsymbol{x}, \hat{\delta}) = -\frac{K_S}{\pi} \left[\chi_1(\boldsymbol{x}, \hat{\delta}) + \chi_2(\boldsymbol{x}, \hat{\delta})\right] \tag{C.50}$$

Since $\boldsymbol{x}$ and $\sigma(\boldsymbol{x})$ are bounded and $\mathcal{D}$ is compact, it is easy to show that there exits $L > 0$, such that condition (C.23) holds. Indeed:

$$\left|\frac{\partial T_l}{\partial \delta}\right|_{\delta = \hat{\delta}} = \left|\frac{K_S}{\pi} \left[\chi_1(\boldsymbol{x}, \hat{\delta}) + \chi_2(\boldsymbol{x}, \hat{\delta})\right]\right| \tag{C.51}$$

which is bounded since both $\boldsymbol{x}$ is bounded and $\hat{\delta}$ belongs to a compact set. Assume that $\sigma(\boldsymbol{x}) \neq 0$ and let $\varsigma > 0$ be a lower bound for $\sigma(\boldsymbol{x})$. Equation (C.51) implies that there exists positive constant real number L_0 such that for each pair $(\delta, \hat{\delta})$ the following inequality holds:

$$\frac{1}{J_l}\left|T_l(\boldsymbol{x},\delta) - T_l(\boldsymbol{x},\hat{\delta})\right| \leq L_0\left|\tilde{\delta}\right| \leq \underbrace{\frac{L_0}{\sqrt{\varsigma}}}_{L}\sqrt{\sigma(\boldsymbol{x})}\left|\tilde{\delta}\right| = L\sqrt{\sigma(\boldsymbol{x})}\left|\tilde{\delta}\right| \ .$$

If $\sigma(\boldsymbol{x}) = 0$, then $\left[\chi_1(\boldsymbol{x},\hat{\delta}) + \chi_2(\boldsymbol{x},\hat{\delta})\right] = 0$, which implies $\frac{\partial T_l}{\partial \delta} = 0$. In this case the backlash torque T_l is insensitive to changes in δ, i.e. $T_l(\boldsymbol{x},\delta) = T_l(\boldsymbol{x},\hat{\delta})$, which satisfies again condition (C.23).

The inequality $\int_t^{t+T}\sigma(\boldsymbol{x}(\tau))d\tau \geq \varepsilon$ expresses a type of Persistence of Excitation (PE) condition. From (C.46)-(C.48) it can be seen that this condition does not hold if during the time interval $[t, t+T]$ the system is always within the deadzone. This, however, is expected, since in that case there is no engagement between motor and load, hence no information about the stiffness of the shaft connecting them.

Remark C.3. The specific $\mu(\boldsymbol{x},\hat{\delta})$ function results into a gradient-type adaptive law, which is very common in the literature of adaptive techniques. This choice, although it is sufficient in the specific estimation problem, cannot be generalized for nonlinearly parametrized systems since it does not always guarantee parameter convergence.

The complete estimator design is illustrated in Figure C.6 and is summarized in the following steps:

Algorithm 1 Backlash angle estimation

Measured: Sate variables $\omega_m, \theta_m, \omega_l, \theta_l$.

Output: Deadzone angle estimate $\hat{\delta}$.

1: Design a STSMO for the load velocity (Equations (C.16), (C.19)).
2: Estimate the backlash torque (Equation (C.21)).
3: Design the adaptive estimator for the deadzone angle δ (Equations (C.47)-(C.50)).

C.4 Robustness Analysis

The previous section discussed the problem of estimating the deadzone angle in the case where an asymptotic estimate or an exact measurement of the interconnecting torque $T_l = J_l\phi$ is available. Specifically, it was shown that the adaptive estimator ensures that the equilibrium point $\tilde{\delta}^* = 0$ of the estimation error system is:

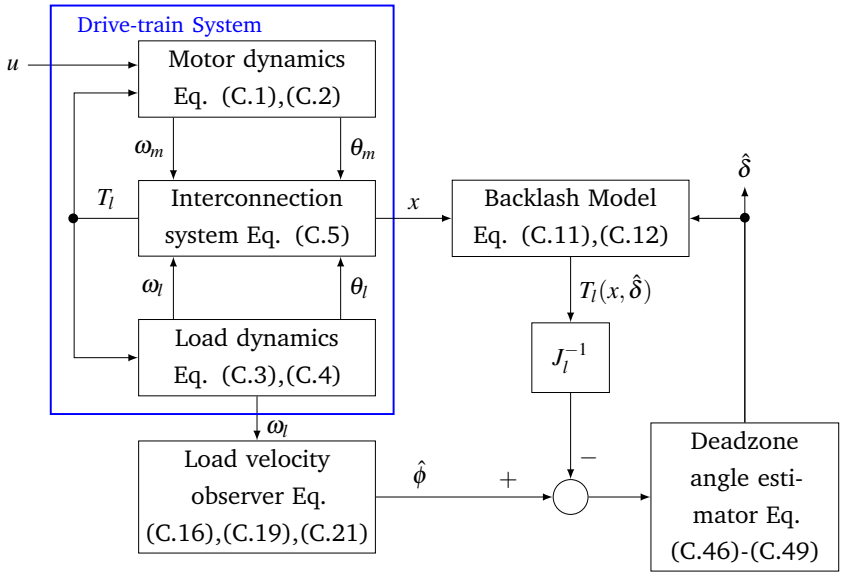

Figure C.6: Block diagram of the single-axis mechanical drive-train system and the estimation scheme.

- ULES if an exact measurement of ϕ is available or
- UGAS if an asymptotic estimate $\hat{\phi}$ of the real perturbation ϕ is used instead.

In real applications, however, such assumptions on the availability of a measurement or even an asymptotic estimate of ϕ may not necessarily hold. The effect of measurement noise, parameters uncertainty and modelling mismatches allow, under the assumption of boundedness of the uncertainties, at best for convergence of the interconnecting perturbation estimation error to a compact set.

In order to illustrate this better, consider the real interconnecting torque T_l' defined as

$$T_l' = \left[\Delta\theta + \delta_1 - \frac{\delta}{2}\cdot(1+\mathrm{sgn}(\Delta\theta)) + \frac{D_S+\Delta D_S}{K_S+\Delta K_S}\Delta\omega\right]\cdot K_{BL}'(\Delta\theta,\delta) + \Delta_m(t) \tag{C.52}$$

$$K_{BL}' = \frac{K_S+\Delta K_S}{\pi}\cdot[\pi + \arctan(\alpha(\Delta\theta+\delta_1-\delta)) - \arctan(\alpha(\Delta\theta+\delta_1))] \tag{C.53}$$

and the real friction torque

$$T_{F,l}' = T_{F,l} + \Delta T_{F,l}(t,\omega_l) \tag{C.54}$$

where all the perturbations due to parameter uncertainty (ΔK_S and ΔD_S) and model mismatches ($\Delta_m(t)$ and $\Delta T_{F,l}(t,\omega_l)$) are bounded for bounded states for all

$t \geq t_0$. From (C.52)-(C.54) it can be easily seen that the real interconnecting torque can be written as the torque defined in (C.11),(C.12) perturbed by a bounded signal:

$$T_l' = T_l + \varkappa(t) \tag{C.55}$$

where $|\varkappa(t)| \leq K$, with K being a positive real number, represents the effect of noise and all the uncertainties on the model (including this of friction).

It is clear from the description above that using the STSMO (C.16), (C.19) (or any other asymptotic estimator for the interconnecting torque) will lead to an estimate of $T_l + \varkappa(t)$ instead of just T_l. This implies that the perturbation estimation error $\tilde{\phi}$ will not decay to zero but it will converge to a compact set, specifically:

$$\left|\tilde{\phi}\right| \leq \Phi = \frac{1}{J_l} K \, . \tag{C.56}$$

The assumption of uniform boundedness of the perturbation estimation error $\tilde{\phi}$ is not conservative considering that the states (positions and velocities) of the closed-loop system, as well as the friction torque are bounded signals and there exists no feedback of the estimation $\hat{\phi}$ to the closed-loop dynamics. It will be shown in the following that in this case, the adaptive estimator (C.47)-(C.50) ensures global uniform boundedness of the deadzone angle estimation error.

Proposition A. *The adaptive deadzone angle estimator defined in Equations* (C.47)-(C.50)*, where the perturbation estimation error* $\tilde{\phi} = \frac{1}{J_l} T_l' - \hat{\phi}$ *is uniformly bounded by a positive constant real number* Φ*, ensures that the trajectories of the deadzone angle estimation error* $\tilde{\delta}(t)$ *are UGB. Moreover, as* $t \to \infty$*, the bound is proportional to the perturbation estimation error bound* Φ*.*

Proof. The ISS property of the system (C.27) with respect to the perturbing input $\tilde{\phi}$ implies:

$$\left|\tilde{\delta}(t)\right| \leq \beta_1\left(\left|\tilde{\delta}(t_0)\right|, t - t_0\right) + \beta_2\left(\sup_{0 \leq \tau \leq t} \tilde{\phi}(\tau)\right) \, , \forall \left|\tilde{\delta}\right| \geq r(\left|\tilde{\phi}\right|)$$

where $r(\left|\tilde{\phi}\right|) = R\left|\tilde{\phi}\right|$, $\beta_1 : \mathbb{R}_{\geq 0} \times \mathbb{R}_{\geq 0} \to \mathbb{R}_{\geq 0}$ is a class-$\mathcal{KL}$ function and $\beta_2 : \mathbb{R}_{\geq 0} \to \mathbb{R}_{\geq 0}$ is a class-$\mathcal{K}$ function (see Definitions 7 and 8 in Appendix II), with β_2 calculated as in the following [128, Th. 4.19]:

$$\beta_2\left(\sup_{0 \leq \tau \leq t} \tilde{\phi}(\tau)\right) = \alpha_1^{-1} \circ a_2 \circ r(\Phi) = \underbrace{\frac{R}{\sqrt{1 - \kappa \sup_{x \in \mathbb{R}} \sigma(x) \cdot \gamma}}}_{c > 0} \Phi \tag{C.57}$$

where R was defined in (C.44).

This implies that there exists an arbitrarily large positive real number ζ, such that

$$\forall \eta \in (0, \zeta) \;\; \exists \upsilon = \upsilon(\eta)$$

for which it holds:

$$\left|\tilde{\delta}(t_0)\right| \leq \eta \Rightarrow \left|\tilde{\delta}(t)\right| \leq \upsilon \;,\; \forall t \geq t_0 \;. \tag{C.58}$$

Then, according to Definition 4.6 in [128], the solutions of (C.27) are UGB. Moreover, since $\beta \in \mathcal{KL}$, it holds that:

$$\lim_{t\to\infty} \left|\tilde{\delta}(t)\right| \leq \lim_{t\to\infty} \left(\beta\left(\left|\tilde{\delta}(t_0)\right|, t - t_0\right) + c\Phi\right) = c\Phi \tag{C.59}$$

which completes the proof. ■

C.5 Simulation Results

Simulations were carried out in order to demonstrate the convergence and accuracy properties of the estimation scheme. The drive motor velocity was regulated to track a sinusoidal reference signal $\omega_r = 4\pi \sin(4\pi t)$. The system parameters (motor and load friction, shaft coefficients, motor and load inertias) were considered completely known and the velocity measurements were inflicted with zero-mean white Gaussian noise with $\sigma_{meas} = 0.0316 \ \mathrm{rad\,s^{-1}}$. Emulation of the backlash phenomenon was done by using the deadzone model. The deadzone angle was initially set to $\delta = 0.2 \ \mathrm{rad}$. An increase by a 5% step of its initial value occurred after the first 3 seconds of the simulation. Finally, the position offset was taken $\delta_1 = \frac{\delta}{2}$.

In absence of model parameters uncertainties, the STSMO estimated the perturbation ϕ with substantial accuracy, as it can be seen in C.7. Figure C.8 shows the estimation of the deadzone angle and the detection of the change in its value. In both cases, convergence was achieved in less than $2 \ \mathrm{s}$, while the absolute steady state estimation error was less than $2.5 \cdot 10^{-4} \ \mathrm{rad}$. This accuracy sufficiently meets the requirements set in Problem 3.

The $\Delta\theta, J_l\hat{\phi}$ and θ_m, θ_l plots in Figure C.9 illustrate the estimated deadzone width and the corresponding backlash hysteresis relation between the drive motor and load positions.

The relation between the bound K for the backlash torque estimation error and the steady-state deadzone estimation absolute error was investigated with additional simulation scenarios, where only the STSMO gains k_1, k_2 were varied. In each scenario, the peak steady state deadzone estimation error was calculated as the maximum absolute estimation error over the last T_p seconds of the simulation

$$\tilde{\delta}^{SS}_{peak} = \max_{t_f - T_p \leq t \leq t_f} \left|\tilde{\delta}(t)\right| \tag{C.60}$$

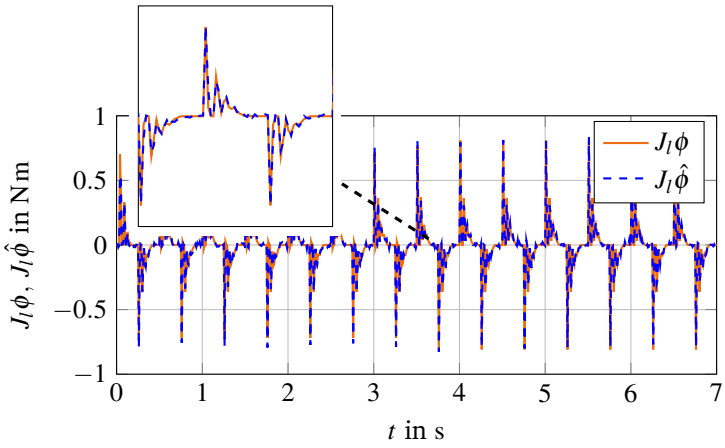

Figure C.7: Real and estimated backlash torque scaled by the load inertia J_l.

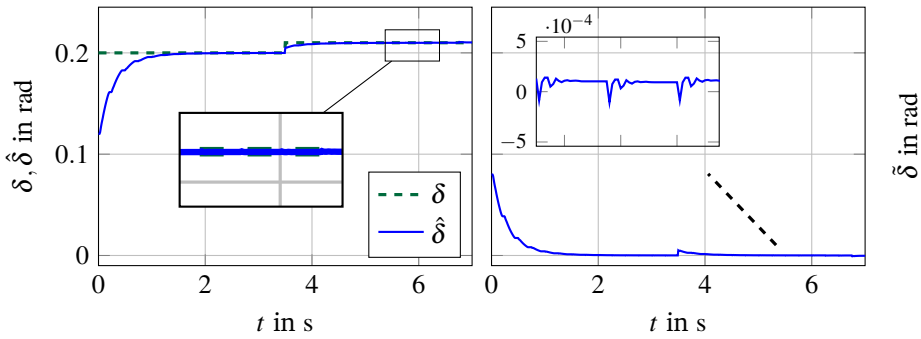

Figure C.8: (Left): Real and estimated change of deadzone angle. (Right): Estimation error.

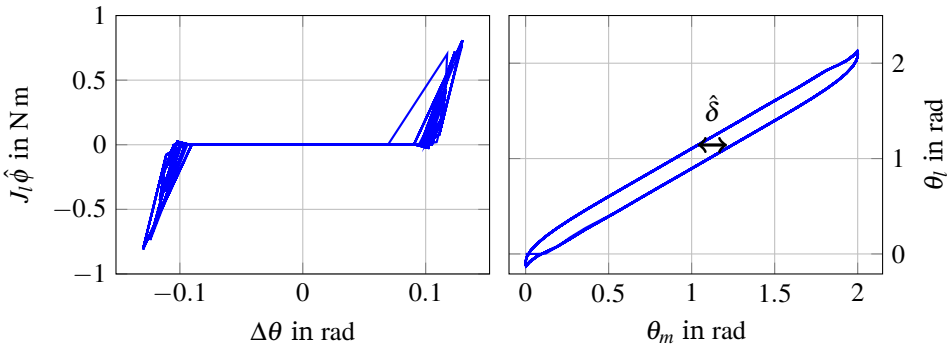

Figure C.9: (Left): Deadzone illustration through torque-position difference. (Right): Backlash hysteresis.

where t_f denotes the end time of each simulation. The different obtained values for $\tilde{\delta}^{SS}_{peak}$ were plotted against the corresponding bounds for $J_l|\hat{\phi}|$. Figure C.10 shows the approximately linear relation between the two bounds, with a slope $q \approx 0.0023$.

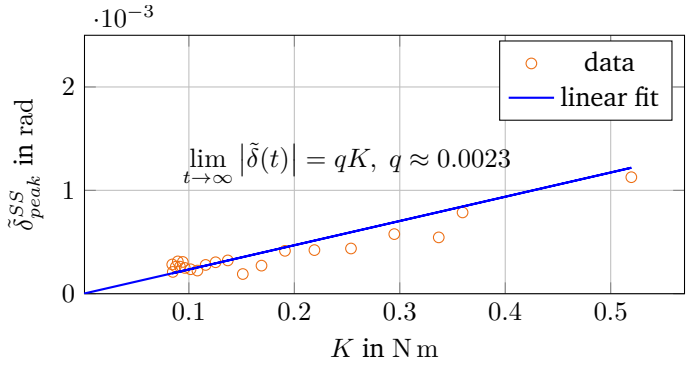

Figure C.10: Linear relation between the bounds for the perturbation estimation error $\tilde{\phi}$ and the deadzone angle estimation error $\tilde{\delta}$.

C.6 Experimental Results

C.6.1 Experimental Setup

The experimental setup consists of two Siemens FT7042-5AF70 PMSMs connected through a stainless steel shaft. Both motors are equipped with a Siemens SINAMICS S120 drive converter with 11-bit absolute encoders for the position. Three custom-made jaw couplings are mounted (one at a time) on a steel base and house the two parts of the interconnecting shaft (see Figure C.12). The total deadzone angle for each of the couplings is 1.027 rad, 0.186 rad and 0.105 rad ($58.8445°$, $10.6685°$ and $6.0161°$, respectively). The entire drive train with the friction component are shown in Figure C.11.

The load motor (see Figue C.11) serves as a pure inertia in the experiments. The design and tuning of the position, velocity and current control loops in the drive motor were not included in this study.

C.6.2 Test Scenarios

The identified parameters of the physical system were used in the experiments for the assessment of the estimation algorithm. Five more variation cases were considered for testing the robustness and performance of the deadzone estimator

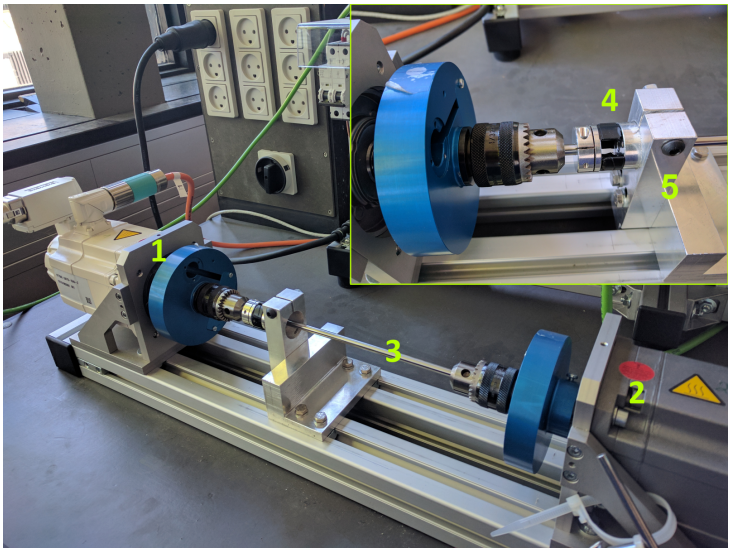

Figure C.11: Experimental setup: (1) 1FT7 drive PMSM, (2) 1FT7 load PMSM, (3) shaft, (4) backlash mechanism, (5) mounting base.

Figure C.12: Jaw coupling detail.

against parameter uncertainties. In each of these additional tests one of the four uncertain parameters (shaft and friction coefficients) was increased by 100% of their identified value. In the fifth test all four parameters ($K_S, D_S, T_{C,l}, \beta_l$) were increased simultaneously. The reference for the position of the drive motor was a sinusoid,

$$\theta_r(t) = \Theta_0 \sin(2\pi f_r t) \ ,$$

where in all the tests $\Theta_0 = 1$ rad and $f_r = 0.5$ Hz. The fifteen different scenarios are shown in Table C.2. The parameters of the identified physical system, as well as, those of the SMO and adaptive estimator are collectively given in Table C.3.

Table C.2: Test scenarios.

No	δ (rad)	δ_1 (rad)	Parameter variation
$0A$	1.027	0.8924	No variation
$1A$	1.027	0.8924	100% increase in K_S
$2A$	1.027	0.8924	100% increase in D_S
$3A$	1.027	0.8924	100% increase in $T_{C,l}$
$4A$	1.027	0.8924	100% increase in β_l
$5A$	1.027	0.8924	All variations combined
$0B$	0.186	0	No variation
$1B$	0.186	0	100% increase in K_S
$2B$	0.186	0	100% increase in D_S
$3B$	0.186	0	100% increase in $T_{C,l}$
$4B$	0.186	0	100% increase in β_l
$5B$	0.186	0	All variations combined
$0C$	0.105	0.0021	No variation
$1C$	0.105	0.0021	100% increase in K_S
$2C$	0.105	0.0021	100% increase in D_S
$3C$	0.105	0.0021	100% increase in $T_{C,l}$
$4C$	0.105	0.0021	100% increase in β_l
$5C$	0.105	0.0021	All variations combined

Table C.3: System and estimator parameters values.

Symbol	Description	Value
STSMO parameters		
k_1	Switching gain	0.5
k_2	Integral switching gain	70
Estimator parameters		
α	Stiffness model slope	10^4
γ	Adaptation gain	$5 \cdot 10^{-4}$
$\hat{\delta}_0$	Initial conditions	0 rad
δ_{max}	Maximum deadzone	2π rad
Load system parameters		
J_l	Inertia	$0.000831\ \mathrm{kg\,m^2}$
K_S	Shaft stiffness	$31.75\ \mathrm{N\,m\,rad^{-1}}$
D_S	Shaft damping coefficient	$0.054\ \mathrm{N\,m\,s\,rad^{-1}}$
N	Gearing ratio	1
$T_{C,l}$	Coulomb friction	$0.0792\ \mathrm{N\,m}$
β_l	Viscous friction coefficient	$0.031\ \mathrm{N\,m\,s\,rad^{-1}}$

C.6.3 Results

This section presents the results obtained from the experiments on the estimation of the deadzone angle. The performance of the estimator was evaluated based on the MAEE, which is defined over a time interval $T > 0$ as

$$MAEE = \sup_{t_0 \le t \le t_0 + T} \left| \tilde{\delta}(t) \right|. \tag{C.61}$$

Figure C.13 shows the estimation of the deadzone angle for the cases where the identified parameters of the system were used (Tests 0A, 0B, 0C). As it can be seen, the estimation error $\tilde{\delta}$ converges to a compact set including the origin, while the corresponding MAEE is less than 10^{-2} rad in all the tests, specifically $1.75 \cdot 10^{-3}$ rad, $1.90 \cdot 10^{-3}$ rad and $0.66 \cdot 10^{-3}$ rad for Test 0A, 0B and 0C, respectively.

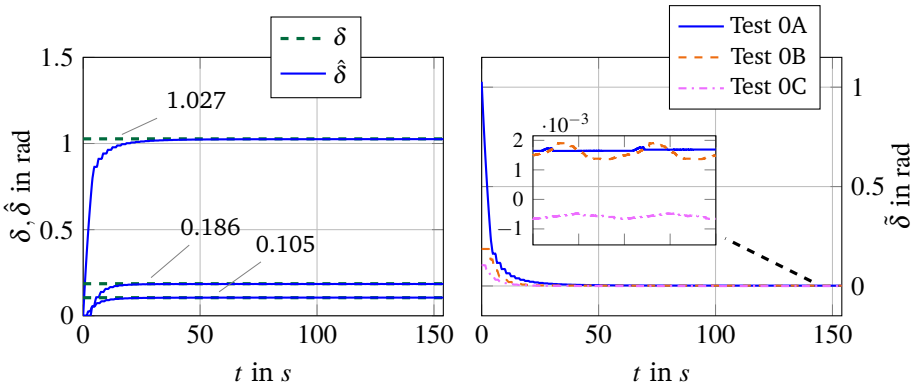

Figure C.13: Deadzone angle estimated value (left) and the associated estimation error (right) for the nominal cases (Tests 0A, 0B, 0C).

The position of the motor and the load can be seen in figure C.14 (top). While in the deadzone, the load does not move although the drive motor shaft does. This loss of engagement is also shown in the bottom plot of the same figure, where the connecting shaft stiffnes is depicted. Whenever the system is in the deadzone, the shaft stiffness is 0. During the initial part of the motion in the positive direction the stiffness it is zero even though the load is moving. This is due to the fact that impact torque exerted by the drive motor on the load temporarily accelerates the load, making it move even though there is no actual engagement.

An illustration of the estimated deadzone is given in Figure C.15, where the backlash torque $J_l \hat{\phi}$ estimate and the equivalent calculation based on the stiffness model (top plot) are depicted as functions of the position difference between motor and load. The oscillations at the two ends of the deadzone in the estimated torque

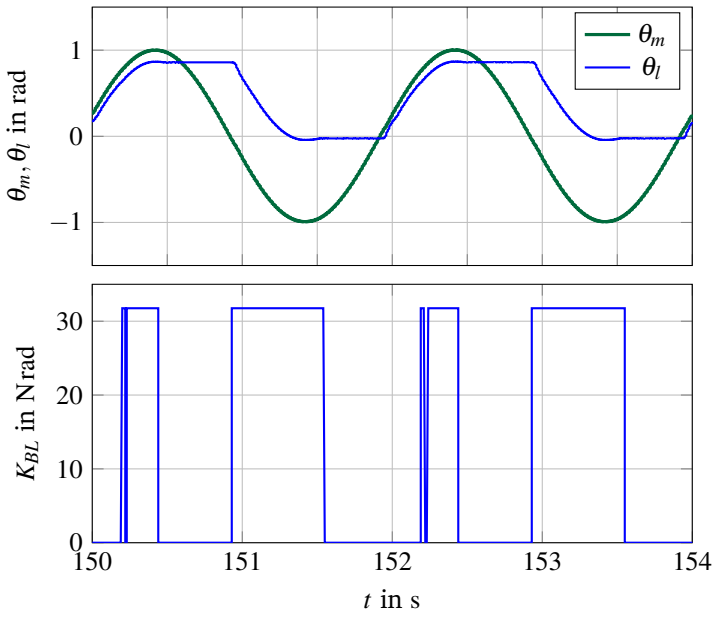

Figure C.14: Motor and load position (top) and the calculated shaft stiffness (bottom) for the nominal case with $\delta = 1.027$ rad (Test 0A).

correspond to the impact between motor and load upon engagement. The bottom plot in the same figure shows the stiffness K_{BL} also as a function of $\Delta\theta$.

The backlash hysteresis can be seen in the top plot of Figure C.16, which shows 4 s of the time response of the load position with respect to this of the motor. The bottom plot shows the drive motor and load phase portraits, i.e. the plots of their angular velocities with respect to their positions.

Figure C.17 illustrates the actual and estimated by the SMO load angular velocity during Test 0A. As it can be seen in the bottom plot, the velocity estimation error is smaller than $0.4\ \mathrm{rad\,s^{-1}}$ in magnitude. Such an error is sufficiently small, so that the estimated backlash torque, shown in Figure C.18, can be considered accurate enough to be used in the deadzone estimation algorithm.

The deadzone angle estimation error for all the parameter variations is show in Figures C.19, C.20, C.21 (for Tests 1A-5A, 1B-5B and 1C-5C, respectively). As it can be seen, in all the considered cases, the estimates converge to a constant value sufficiently close to the real one. Specifically, all the estimation errors do not exceed $4 \cdot 10^{-3}$rad in magnitude, which implies more than 40% better performance from that required in Problem 3. The MAEE during all Tests are presented in Table C.4.

Remark C.4. The sudden engagement between drive motor and load produced a

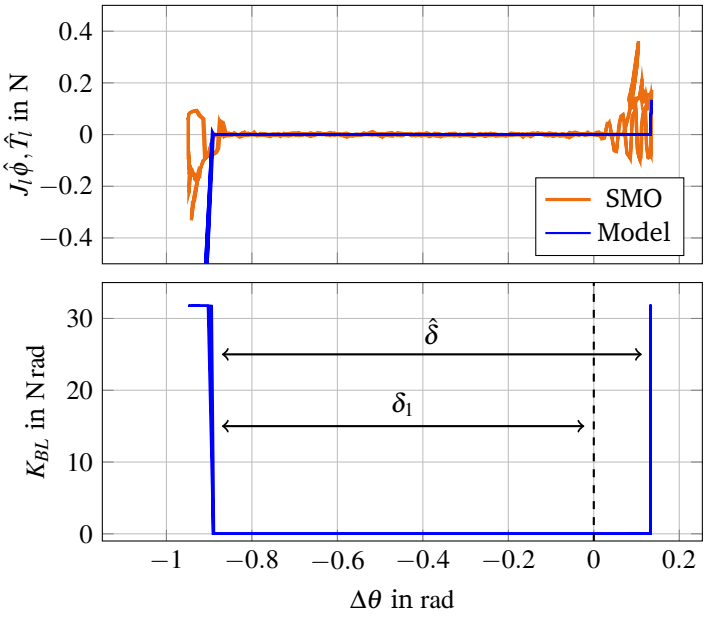

Figure C.15: Deadzone illustration through torque-position difference (top) and torque-stiffness (bottom) plots during Test 0A.

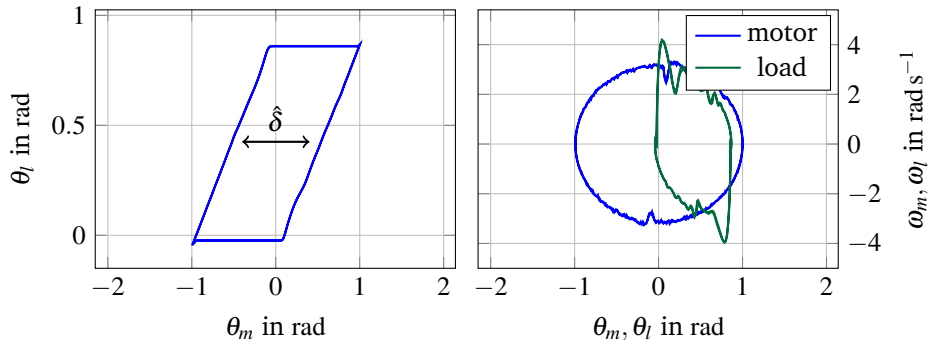

Figure C.16: Backlash hysteresis (left) and phase portraits for the motor and load (right) during Test 0A.

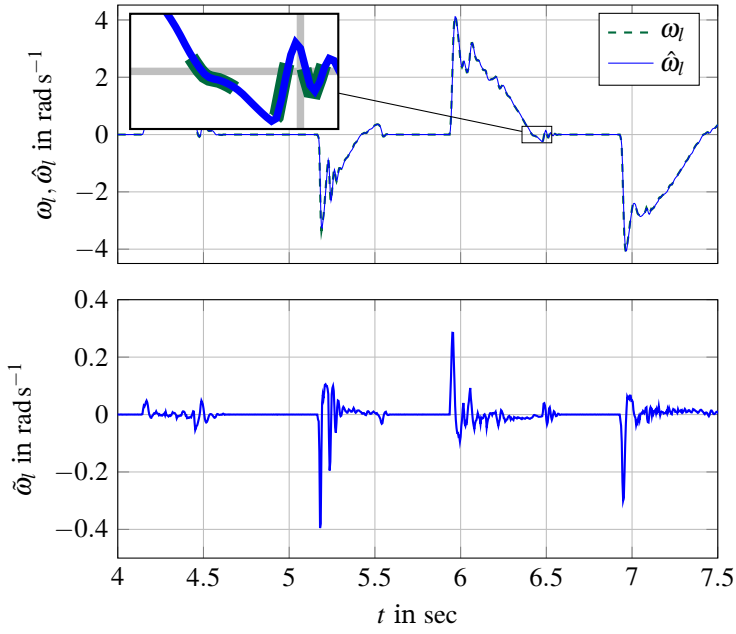

Figure C.17: Real and estimated load velocity (top) and the associated estimation error (bottom) during Test 0A.

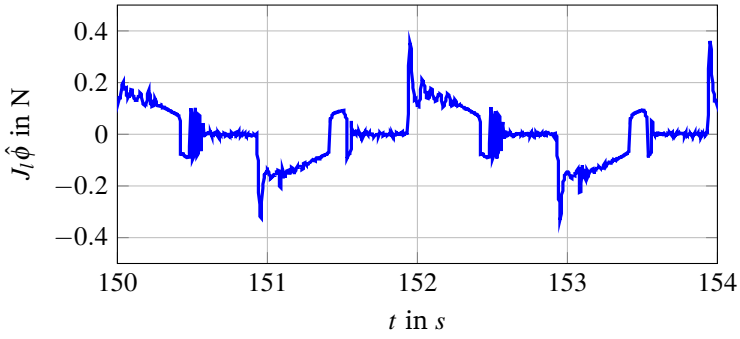

Figure C.18: Estimated backlash torque for the nominal case with $\delta = 1.027$ rad (Test 0A).

Table C.4: MAEE in mrad for the nominal case (Tests 0A, 0B, 0C) and all the parameter variations (Tests 1A-5A, 1B-5B, 1C-5C).

	MAEE in mrad					
δ in rad	0	1	2	3	4	5
1.027 (case "A")	1.75	0.41	1.80	3.61	2.69	1.85
0.186 (case "B")	1.90	1.04	1.87	3.31	1.96	1.80
0.105 (case "C")	0.66	1.85	0.72	1.38	0.57	0.93

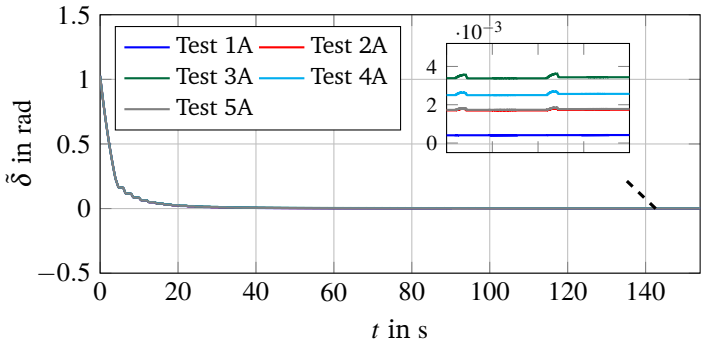

Figure C.19: Deadzone angle estimation error during Tests 1A-5A.

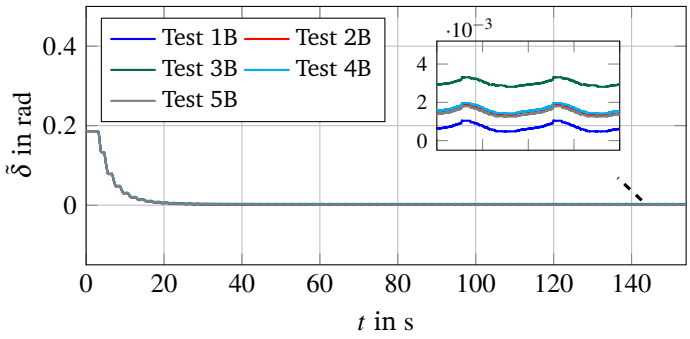

Figure C.20: Deadzone angle estimation error during Tests 1B-5B.

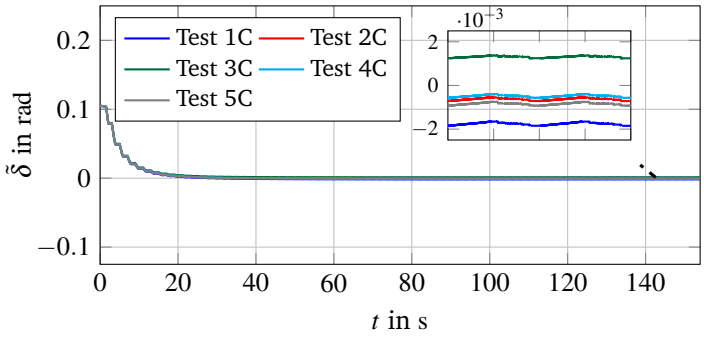

Figure C.21: Deadzone angle estimation error during Tests 1C-5C 4.

periodic impact torque acting on both parts. This caused a small displacement of the load, which resulted in an shift of the position offset δ_1. However, the effect of this change in the offset on the quality of the estimation was practically negligible.

C.7 Conclusions

A deadzone angle estimation method for a single-axis drive-train with backlash was presented in this paper. The design is a modified version of the cascaded SMO-adaptive estimator scheme presented in [4], which now includes an initial position offset between drive motor and load. The stability and robustness properties of the algorithm were discussed in the context of model and parameter uncertainties. Specifically, it was proven that the estimation error is UGAS in absence of model and parameter mismatches and UGB otherwise, with the bound being proportional to the total perturbation estimation error bound.

The theoretical findings were experimentally validated on a real single-axis drive train with state-of-the-art Siemens equipment for the cases where the deadzone was equal to $1.027\ \mathrm{rad}$, $0.186\ \mathrm{rad}$ and $0.105\ \mathrm{rad}$. The method was tested both for the identified system parameters and for the case of 100% offset in each of these parameters. In all the tests convergence was achieved in approximately $40\ \mathrm{s}$ and with precision in the order of $10^{-3}\ \mathrm{rad}$.

Future work will include the assessment of the algorithm performance in estimating even smaller angles and also the design of an joint estimation scheme for both the deadzone angle and the initial position offset.

Acknowledgements

The sponsorship of this project by Siemens AG is gratefully acknowledged.

Paper D

Backlash Estimation for Industrial Drive-Train Systems

Dimitrios Papageorgiou[*1], Mogens Blanke[2], Hans Henrik Niemann[1], Jan H. Richter[3]

[1]Department of Electrical Engineering, Automation and Control Group, Technical University of Denmark, Elektrovej Building 326, 2800, Kgs. Lyngby, Denmark.

[2]AMOS CoE, Institute of Technical Cybernetics, Norwegian University of Science and Technology, Trondheim, Norway.

[3]Siemens AG, Digital Factory Division, D-90475 Nuremberg, Germany

Abstract:
Backlash in gearing and other transmission components is a common positioning-degrading phenomenon that develops over time in industrial machines. High-performance machine tool controls use backlash compensation algorithms to maintain accurate positioning of the tool to cope with such deadzone phenomena. As such, estimation of the magnitude of deadzones is essential. This paper addresses the generic problem of accurately estimating the width of the deadzone in a single-axis mechanical drive train. The paper suggests a scheme to estimate backlash between motor and load, employing a sliding-mode observer and a nonlinear adaptive estimator. The efficacy of the approach is illustrated via simulations.

[*]Principal corresponding author. Tel.: +45 45253572; E-mail: dimpa@elektro.dtu.dk

D.1 Introduction

Developing backlash due to wear in spindles, gears, clutches and guides is one of the main reasons for performance degradation in machine tool systems. Since high precision tool positioning is fundamental for obtaining the required quality of the machined end-products, backlash compensation is used in nearly all modern CNC algorithms. Compensation necessitates knowledge of the backlash offset angle so that it can be used in the position servo loops that control motors on the machine's axes. In such context, online estimation methods may facilitate automatic compensation for developing backlash.

A substantial amount of research has been conducted on estimation of the backlash phenomenon for various systems over the past three decades. In [51] the backlash in a gearing system was indirectly estimated by calculating the bounce, i.e. the change of the speed of the driving part of the gear due to the backlash impact when exiting the deadzone. EKF was employed in [52] for estimating a backlash torque in a two-mass motor arm, based on torque and position measurements. Modelling of backlash torque was presented in [47], who used a differentiable function to represent backlash and suggested a nonlinear observer for estimation of backlash amplitude. This method was validated experimentally in [57], in which a sliding-mode observer was used for estimation of backlash torque. Based on this estimation, backlash function parameters were identified offline. The effect of the deadband due to backlash in a closed loop motion system was studied in [54] using describing functions. The function parameters were calculated online using a static relation for controller gains. Backlash in automotive powertrains was described in [53] based on position difference between drive motor and load. A Kalman filter was shown to estimate backlash within 10% error. A four-parameter model was used in [55] to describe backlash effects in generic linear cascaded systems. The backlash identification was treated as a quasi-linear problem such that iterative algorithms could be used. Minimization of a quadratic prediction error was employed in [56], where position, velocity and torque measurements were used for offline identification of backlash torques in a vehicle drive-line system.

In the previous approaches, the backlash phenomenon was described through the resulting torque upon contact of two parts of a coupling. In the cases where the deadzone angle was identified directly, this was done offline or around a linearization point of the system. The previous results showed the need for new ideas for high accuracy estimation of backlash if compensation shall be useful in machinery systems where very high precision is required.

This paper considers the problem of designing a dynamic estimator for the

deadzone angle of a developing backlash in a single-axis drive-train system. The proposed method employs modelling of backlash in terms of variable shaft stiffness, depending on the deadzone size, and it addresses the requirement for fast and accurate estimation of the deadzone angle. Similarly to [57], a second order STSMO is used to estimate the backlash torque. This value is utilized by an adaptive estimator designed with the purpose to determine the deadzone angle.

The paper is organized as follows: Section D.2 states the problem in concise terms, describing the drive-train system as an abstraction of a single-axis machine tool, and presents a model for backlash based on varying shaft stiffness. The design of the parameter estimator is presented in Section D.3 and Section D.4 presents results obtained from high fidelity simulations. Finally, conclusions are drawn and results are discussed in Section D.5.

D.2 System Description and Problem Formulation

A typical single-axis machine tool consists of a linear axis, which positions the tool. The axis is actuated by a drive motor that is typically connected to an angular-to-linear motion conversion device (e.g. a ball-screw).

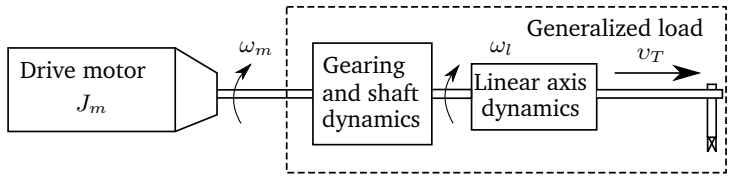

Figure D.1: Correspondence between mechanical drive-train and single-axis machine-tool systems. The angular velocities of the motor and the load are denoted by ω_m, ω_l, respectively, while v_T is the tool linear velocity.

The combined elasticity, friction, damping and total mass of all the mechanical components that connect to the drive shaft can be lumped into a generalised load. The single-axis machine tool can then be viewed as a mechanical drive train comprising the drive motor, a flexible shaft with damping and backlash, and a load with friction as show in Figure D.1.

D.2.1 Drive Train Modelling

With identification of backlash being in focus of this work, angular accelerations, velocities and difference of angles between mechanical components are essential. Torque produced by the drive motor is measured, hence the closed-loop electrical

dynamics of the motor need not be considered. An overview of the most important variables and notation used in the modelling of the system is provided in Table D.1.

Table D.1: System model nomenclature

Symbol	Description	Units
States and Outputs		
ω_m, ω_l	Motor/load angular velocity	$\mathrm{rad\,s^{-1}}$
θ_m, θ_l	Motor/load angular position	rad
Inputs and disturbances		
u	Torque command	$\mathrm{N\,m}$
$T_{F,m}, T_{F,l}$	Motor/load friction	$\mathrm{N\,m}$
T_l	Interconnection/backlash torque	$\mathrm{N\,m}$
Constant parameters		
J_m, J_l	Motor/load inertia	$\mathrm{kg\,m^2}$
K_S	Shaft stiffness	$\mathrm{N\,m\,rad^{-1}}$
D_S	Shaft damping coefficient	$\mathrm{N\,m\,s\,rad^{-1}}$
N	Gearing ratio	$-$
$T_{C,m}, T_{C,l}$	Coulomb friction on the motor/load	$\mathrm{N\,m}$
β_m, β_l	Motor/load viscous friction coefficient	$\mathrm{N\,m\,s\,rad^{-1}}$
δ	Deadzone angle	rad

The dynamics of the mechanical drive-train system reads:

$$\dot{\omega}_m = \frac{1}{J_m}u - \frac{1}{J_m}T_{F,m} - \frac{1}{NJ_m}T_l \tag{D.1}$$

$$\dot{\theta}_m = \omega_m \tag{D.2}$$

$$\dot{\omega}_l = -\frac{1}{J_l}T_{F,l} + \frac{1}{J_l}T_l \tag{D.3}$$

$$\dot{\theta}_l = \omega_l\ . \tag{D.4}$$

In the backlash-free case the interconnecting torque T_l is given from:

$$T_l = K_S\left(\frac{1}{N}\theta_m - \theta_l\right) + D_S\left(\frac{1}{N}\omega_m - \omega_l\right) \tag{D.5}$$

where K_S, D_S and N are defined in Table D.1 and are assumed to be known. The friction torques acting on the drive motor and the load are modelled as described in the following equation ([30]):

$$T_{F,i} = T_{C,i}\mathrm{sgn}(\omega_i) + \beta_i\omega_i,\ i \in \{m, l\} \tag{D.6}$$

where sgn : $\mathbb{R} \to \{-1, 0, 1\}$ is the signum function defined as:

$$\text{sgn}(\xi) = \begin{cases} 1 & \text{if } \xi > 0 \\ \upsilon \in [-1, 1] & \text{if } \xi = 0 \\ -1 & \text{if } \xi < 0 \, . \end{cases} \tag{D.7}$$

and the parameters $\beta_m, \beta_l, T_{C,m}, T_{C,l}$ are considered known and constant.

D.2.2 Backlash Modelling

Backlash is the effect of sudden disengagement between drive motor and load as shown in Figure D.2. A number of static and dynamic models have been developed, based on the interconnecting (restoring and damping) torque in a mass-spring-damper system (see for example [45, 48, 50] and [49]). The most intuitive and common one is the deadzone model presented by [45], in which the interconnecting torque T_l becomes zero inside the deadzone, while outside of it the angle difference (between motor and load) is offset by the width of the deadzone angle.

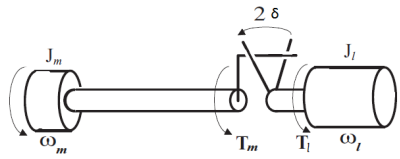

Figure D.2: Backlash: When the difference between the motor and the load position is smaller than δ, then the two shafts are disengaged and no torque is applied to the motor or the load. The picture is taken from [49].

Although the existing backlash models can accurately describe the phenomenon, the discontinuities that they contain make these models difficult to use in control and estimation design. A model for backlash, which is based on changing shaft stiffness, will be presented in this section and compared to the deadzone model. This model will subsequently be used for deadzone estimation and monitoring.

Defining the angular position and velocity differences between drive motor and load as

$$\Delta\theta \triangleq \frac{1}{N}\theta_m - \theta_l \tag{D.8a}$$

$$\Delta\omega \triangleq \frac{1}{N}\omega_m - \omega_l \tag{D.8b}$$

the interconnection torque T_l in the deadzone model is given by

$$T_l^{DZ} = \begin{cases} K_S(\Delta\theta - \delta \cdot \text{sgn}(\Delta\theta)) + D_S\Delta\omega & , \ |\Delta\theta| > \delta \\ 0 & , \ |\Delta\theta| \leq \delta \ . \end{cases} \tag{D.9}$$

The proposed model is based on factorization of the backlash torque as a function of shaft stiffness. The latter is very small, virtually zero, when inside the deadzone, and assumes its nominal value outside of it. The transition between the two extreme values of the stiffness is fast but smooth. The corresponding torque reads:

$$T_l = \left[\Delta\theta - \delta \cdot \text{sgn}(\Delta\theta) + \frac{D_S}{K_S}\Delta\omega\right] \cdot K_{BL}(\Delta\theta, \delta) \tag{D.10}$$

$$K_{BL} = \frac{K_S}{\pi}\left[\pi + \arctan(\alpha(\Delta\theta - \delta)) - \arctan(\alpha(\Delta\theta + \delta))\right] \tag{D.11}$$

The positive constant α expresses the rate of change in the stiffness as it can be seen in Figure D.3. For $\alpha \to \infty$, it is clear that $T_l \to T_l^{DZ}$.

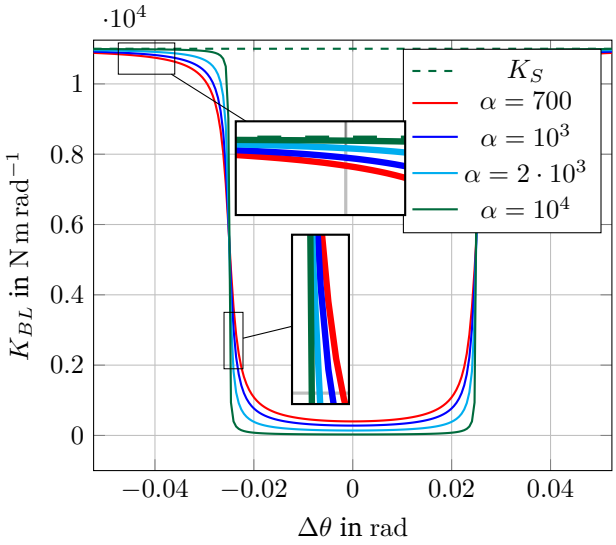

Figure D.3: Shaft stiffness varying between two values. The larger the value of α, the steeper the change in the stiffness is.

D.2.3 Problem Formulation

The collective objective can be summarised in the following problem formulation:

Problem C (Deadzone angle estimation)**.** *Given the single-axis drive-train system described in* (D.1)-(D.6) *and the backlash model in* (D.10),(D.11)*, design an online dynamic estimator for the deadzone angle* δ *with the following requirements:*

- *Maximum steady-state estimation error less than* 10^{-3} rad.
- *Asymptotic convergence to the real parameter value.*

D.3 Backlash Deadzone Angle Estimation

Estimation of the deazone angle belongs to a family of problems of online parameter estimation in systems with nonlinear parametrization that has been treated in numerous works in the literature. The approach followed in this paper is based on a method for parameter estimation in nonlinearly parametrized systems presented in [122]. The basic idea relates to estimating a perturbation of the system dynamics that depends on the unknown parameter and then finding an adaptive law for estimating the parameter itself.

D.3.1 Method Overview

Consider that the system dynamics is described by

$$\dot{\boldsymbol{x}} = \boldsymbol{f}(\boldsymbol{x}) + \boldsymbol{g}(\boldsymbol{x})\left[\boldsymbol{u}(\boldsymbol{x}) + \boldsymbol{d}(\boldsymbol{x}, \delta)\right] \tag{D.12}$$

where $\boldsymbol{x} \in \mathbb{R}^n$ is measured, $\boldsymbol{f} : \mathbb{R}_{\geq 0} \times \mathbb{R}^n \to \mathbb{R}^n$ and $\boldsymbol{g} : \mathbb{R}_{\geq 0} \times \mathbb{R}^n \to \mathbb{R}^{n \times m}$ are the unforced system dynamics and gain, respectively, which can be evaluated from the measurements, $\delta \in \mathcal{D} \subset \mathbb{R}$ is the unknown parameter, $\boldsymbol{u} \in \mathbb{R}^m$ is the control input and $\boldsymbol{d} : \mathbb{R}_{\geq 0} \times \mathbb{R}^n \times \mathcal{D} \to \mathbb{R}^m$ is a matched disturbance vector, which can be evaluated if δ is known. The method pertains to finding an estimation $\hat{\boldsymbol{\phi}}$ of the perturbation

$$\boldsymbol{\phi} \triangleq \boldsymbol{g}(\boldsymbol{x})\boldsymbol{d}(\boldsymbol{x}, \delta) \tag{D.13}$$

and then derive an adaptive law

$$\dot{\hat{\delta}} = \rho(\boldsymbol{x}, \hat{\boldsymbol{\phi}}, \hat{\delta}) \tag{D.14}$$

for estimating the unknown parameter.

Regarding the drive-train system, all states are measured and the unknown parameter δ affects the dynamics of both the motor and the load in the same way,

i.e. through the torque T_l. We can then choose either of the subsystems in (D.1), (D.3) on which to apply the method. For simplicity, the load velocity dynamics is chosen. The system can be written in the form of (D.12) with

$$\begin{aligned}\boldsymbol{f}(\boldsymbol{x}) &\equiv f(\omega_l) = \frac{1}{J_l} T_{F,l} \\ \boldsymbol{g}(\boldsymbol{x}) &\equiv g = \frac{1}{J_l} \\ \boldsymbol{d}(\boldsymbol{x}, \delta) &= T_l \ ,\end{aligned}$$

where T_l has been defined in (D.10), (D.11) and

$$\boldsymbol{x} \triangleq \begin{bmatrix} \omega_m & \theta_m & \omega_l & \theta_l \end{bmatrix}^T$$

is the state vector of the drive-train system. The method is divided in two parts: estimation of the perturbation ϕ and derivation of the adaptive law $\rho(\boldsymbol{x}, \hat{\phi}, \hat{\delta})$.

D.3.2 Sliding-Mode Perturbation Observer

A second-order SMO was used for finding an estimate of ϕ. In general SMOs can offer finite-time estimation of unmeasured states by using high-frequency injection signals in their design, which depend on the observer innovation term (i.e. the error between real and predicted output) as shown in [61]. By doing so, the estimation error dynamics reaches the *sliding manifold*, i.e. a manifold on which the error and its first time derivative are zero, and remain so thereafter. This provides at the same time an estimation of any unknown perturbations that affects the system dynamics ([79]). This idea can be clarified as follows.

Consider the load velocity dynamics presented in (D.3) and a SMO given by

$$\dot{\hat{\omega}}_l = -\frac{1}{J_l} T_{F,l} + v(\tilde{\omega}_l) \tag{D.15}$$

where $\tilde{\omega}_l = \omega_l - \hat{\omega}_l$ is the state estimation error and v is an appropriate high frequency term depending on the error signal $\tilde{\omega}_l$. Define the sliding manifold $\mathcal{S} = \left\{\tilde{\omega}_l \in \mathbb{R} : \tilde{\omega}_l = \dot{\tilde{\omega}}_l = 0\right\}$. The dynamics of the state estimation error reads:

$$\dot{\tilde{\omega}}_l = \dot{\omega}_l - \dot{\hat{\omega}}_l = \frac{1}{J_l} T_l - v \ . \tag{D.16}$$

If the error dynamics reaches the sliding manifold, then $\dot{\tilde{\omega}}_l = \tilde{\omega}_l = 0$ for all future times, which means that $v = \frac{1}{J_l} T_l$. In other words, if the injection signal v is designed such that the estimation error dynamics reaches the sliding manifold $\mathcal{S}$ and remains on the manifold thereafter, then the unknown perturbation $\phi = \frac{1}{J_l} T_l$ is estimated indirectly by v. The design of v can be obtained as in [70]:

$$v = k_1 |\tilde{\omega}_l|^{\frac{1}{2}} \text{sgn}(\tilde{\omega}_l) + k_2 \int_0^t \text{sgn}(\tilde{\omega}_l(\tau)) d\tau \tag{D.17}$$

where k_1, k_2 are positive gains. The resulting observer is referred to as the STSMO and it is proven in [124] that for appropriate gains k_1, k_2, the term v brings the observer error dynamics onto the sliding manifold $\mathcal{S}$. Hence, the unknown perturbation can be estimated by (D.17), where

$$\hat{\phi} = k_1 |\tilde{\omega}_l|^{\frac{1}{2}} \text{sgn}(\tilde{\omega}_l) + k_2 \int_0^t \text{sgn}(\tilde{\omega}_l(\tau)) d\tau \ . \tag{D.18}$$

The choice of a second order SMO for a system of relative degree 1 (the subsystem is scalar) was made due to the property of higher order SMOs to alleviate the chattering in the injection and estimation signals ([61]).

Remark D.1. Finite-time estimation of ϕ is ensured by selecting v as in (D.17) with k_1, k_2 being appropriately chosen positive gains. One additional requirement is that $T_l, \dot{T}_l$ need be bounded, which is ensured by the boundedness of the state vector and the smoothness of the backlash model. However, the bound on $\dot{T}_l$ is proportional to α. This means that the closer the model is to the deadzone model, the larger this bound will be, which in turn leads to higher gains for the observer.

D.3.3 Adaptive Backlash Angle Estimator

The estimator design is inspired by the method proposed in [122] for the estimation of unknown parameters. For the rest of the analysis we consider that the unknown parameter δ lies in a compact set $\mathcal{D} \subset \mathbb{R}$, with $\dot{\delta} = 0$ and we define the backlash angle estimation error as $\tilde{\delta} = \delta - \hat{\delta}$.

Considering the dynamics of the load velocity expressed in the form of (D.12) with $g = \frac{1}{J_l}$ and $d(\boldsymbol{x}, \delta) = T_l(\boldsymbol{x}, \delta)$ defined in (D.9),(D.11), the adaptive estimator for the deadzone angle is given by ([122]):

$$\dot{\hat{\delta}} = \rho(\boldsymbol{x}, \hat{\phi}, \hat{\delta}) = \text{Proj}\left[\hat{\delta}, \gamma \mu(\boldsymbol{x}, \hat{\delta}) \left(\hat{\phi} - \frac{1}{J_l} T_l(\boldsymbol{x}, \hat{\delta})\right)\right] \tag{D.19}$$

with $\gamma > 0$ being the adaptive gain, $\hat{\phi}$ an asymptotic estimate of $\frac{1}{J_l} T_l$ and Proj$(\cdot, \cdot)$ the projection operator defined in (II.6). In the adaptive law (D.19) $\mu(\boldsymbol{x}, \hat{\delta})$ is a real-valued function defined on $\mathbb{R}^4 \times \mathcal{D}$, bounded for bounded $\boldsymbol{x}$, with the following property:

Property D.1. *For all pairs $\delta_1, \delta_2 \in \mathcal{D}$ and $\forall \boldsymbol{x} \in \mathbb{R}$,*

$$\mu(\boldsymbol{x}, \delta_1) \frac{1}{J_l} \frac{\partial T_l}{\partial \delta}(\boldsymbol{x}, \delta_2) \geq \sigma(\boldsymbol{x}) \tag{D.20}$$

where $\sigma(\boldsymbol{x})$ is a non-negative real-valued function defined on $\mathbb{R}^4$ with the following two properties:

Property D.2. *There exists a positive real constant number $L > 0$ such that $\forall \delta_1, \delta_2 \in \mathcal{D}$,*

$$\frac{1}{J_l}|T_l(\boldsymbol{x}, \delta) - T_l(\boldsymbol{x}, \hat{\delta})| \leq L\sqrt{\sigma(x)}|\tilde{\delta}| \ . \tag{D.21}$$

Property D.3. *There exist positive real numbers T, ε such that $\forall t \in \mathbb{R}_{\geq 0}$,*

$$\int_t^{t+T} \sigma(\boldsymbol{x}(\tau))d\tau \geq \varepsilon \ . \tag{D.22}$$

Following a similar reasoning as the one in the proof of Proposition 4 in [122], it can be shown that the estimation error $\tilde{\delta}$ converges asymptotically to 0, and uniformly in $\boldsymbol{x}$ if an asymptotic estimate of ϕ is available.

The design of the adaptive deadzone angle estimator includes steps to find suitable functions μ and σ with the properties (D.1)-(D.3). Selecting $\mu(\boldsymbol{x}, \hat{\delta})$ as

$$\mu(\boldsymbol{x}, \hat{\delta}) = \frac{1}{K_S^2}\frac{\partial T_l}{\partial \delta}(\boldsymbol{x}, \hat{\delta}) \tag{D.23}$$

condition (D.20) is satisfied with

$$\sigma(\boldsymbol{x}) = \frac{1}{K_S^2}\left(\frac{\partial T_l}{\partial \delta}\right)^2 = \frac{1}{\pi^2}\left[\chi_1(\boldsymbol{x}, \hat{\delta}) + \chi_2(\boldsymbol{x}, \hat{\delta})\right]^2 \tag{D.24}$$

where χ_1, χ_2 are defined as

$$\chi_1(\boldsymbol{x}, \hat{\delta}) = \text{sgn}(\Delta\theta)\left[\pi + \arctan(\alpha(\Delta\theta - \hat{\delta})) - \arctan(\alpha(\Delta\theta + \hat{\delta}))\right] \tag{D.25}$$

$$\chi_2(\boldsymbol{x}, \hat{\delta}) = \left[\Delta\theta - \hat{\delta}\cdot\text{sgn}(\Delta\theta) + \frac{D_S}{K_S}\Delta\omega\right]\left\{\frac{\alpha}{1 + \left[\alpha(\Delta\theta - \hat{\delta})\right]^2} + \frac{\alpha}{1 + \left[\alpha(\Delta\theta + \hat{\delta})\right]^2}\right\} . \tag{D.26}$$

Since $\boldsymbol{x}$ and $\sigma(\boldsymbol{x})$ are bounded and $\mathcal{D}$ is compact, it is easy to show that there exits $L > 0$, such that condition (D.21) holds. The inequality $\int_t^{t+T} \sigma(\boldsymbol{x}(\tau))d\tau \geq \varepsilon$ expresses a type of PE condition. From (D.24)-(D.26) it can be seen that this condition does not hold if, during the time interval $[t, t+T]$, the system is always within the deadzone. This, however, is expected, since in that case, there is no engagement between motor and load, hence no information about the stiffness of the shaft that connects them.

The adaptive law for the parameter estimate $\hat{\delta}$ is finally given by:

$$\dot{\hat{\delta}} = \text{Proj}\left\{\hat{\delta}, \gamma\frac{1}{K_S^2}\frac{\partial T_l}{\partial \delta}(\boldsymbol{x}, \hat{\delta})\left[\hat{\phi} - \frac{1}{J_l}T_l(\boldsymbol{x}, \hat{\delta})\right]\right\}, \ \gamma > 0 \tag{D.27}$$

where

$$\frac{\partial T_l}{\partial \delta}(\boldsymbol{x}, \hat{\delta}) = -\frac{K_S}{\pi}\left[\chi_1(\boldsymbol{x}, \hat{\delta}) + \chi_2(\boldsymbol{x}, \hat{\delta})\right] \ . \tag{D.28}$$

Remark D.2. By using the STSMO in (D.15), (D.17), we ensure that $\hat{\phi}$ will converge to the real perturbation ϕ in finite-time, which is a stronger convergence property than the one required by the adaptive estimator. However, the effect of measurement noise and parameter or model uncertainties (e.g. in friction) may compromise the exact estimation of ϕ. In this case, by using arguments from the stability of interconnected systems, one can show that the deadzone angle estimation error will not converge asymptotically to zero but it will reach a compact set $[\delta - e_\delta, \delta + e_\delta]$, where $0 < e_\delta \leq c|\phi - \hat{\phi}|,\ c > 0$.

Remark D.3. It is interesting to note that the selection of the specific $\mu(\boldsymbol{x}, \hat{\delta})$ function results into a gradient-type adaptive law, which is very common in the literature of adaptive techniques. Although for nonlinearly parametrized systems it does not always guarantee parameter convergence as it does for linear-in-the-parameters systems, it is a natural first choice for the adaptive law.

The complete estimator design is summarized in the following algorithm:

Algorithm 1 Backlash angle estimation

Measured: State variables $\omega_m, \theta_m, \omega_l, \theta_l$.

Output: Deadzone angle estimate $\hat{\delta}$.

1: Design a STSMO for the load velocity (Equations (D.15), (D.17)).
2: Estimate the backlash torque (Equation (D.18)).
3: Design the adaptive estimator for the deadzone angle δ (Equations (D.25)-(D.28)).

D.4 Simulation Results

The drive-train system described in Equations (D.1)-(D.5) was simulated in Matlab to assess the performance of the estimation algorithm. The deadzone model in (D.9) was used to emulate the backlash phenomenon. A PI controller was used to regulate the drive motor velocity into following a sinusoidal profile $\omega_m^{ref} = \Omega \sin(\nu t)$. A 5% change in the deadzone angle was considered for the evaluation of the algorithm. The velocity measurements were afflicted with white Gaussian noise $w \sim \mathcal{N}(0, \sigma^2_{meas})$. High precision absolute position encoders were used and the error due to quantization was ignored. Table D.2 shows the values of the constants used for the simulations. The compact set $\mathcal{D}$ is the real axis interval $[0, 1]$, the estimator was initialized at $\hat{\delta}(0) = \hat{\delta}_0$, γ was chosen to be 0.1 and the sampling time was 2 ms.

Figure D.5 shows the real torque applied in the system according to the deadzone model and its estimation by the STSMO. A small lag can be observed in the estimation

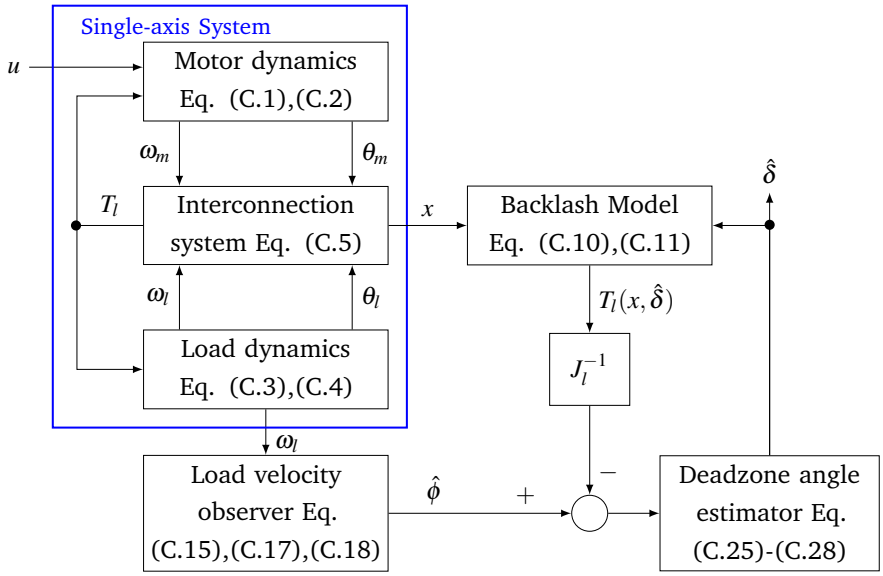

Figure D.4: Block diagram of the closed-loop mechanical drive-train system and the estimation scheme.

Table D.2: Values used in the simulations

Symbol	Value	Units
J_m, J_l	$8.31 \cdot 10^{-4}$	$\mathrm{kg\,m^2}$
K_S	31.7557	$\mathrm{N\,m\,rad^{-1}}$
D_S	0.0038	$\mathrm{N\,m\,s\,rad^{-1}}$
α	10^5	–
N	1	–
$T_{C,m}, T_{C,l}$	0.0492	$\mathrm{N\,m}$
β_m, β_l	0.0008	$\mathrm{N\,m\,s\,rad^{-1}}$
k_1	32.712	–
k_2	12.0154	–
$\hat{\delta}_0$	0.02	rad
γ	0.1	–
δ_1	0.1	rad
δ_2	0.105	rad
Ω	10	$\mathrm{rad\,s^{-1}}$
ν	$24/(2\pi)$	$\mathrm{rad\,s^{-1}}$
σ_{meas}	0.0316	$\mathrm{rad\,s^{-1}}$

of $\hat{\phi}$, which, however, does not affect the performance of the algorithm. Increasing the gains k_1, k_2 of the observer reduces the delay in estimation but makes the method more sensitive to measurement noise.

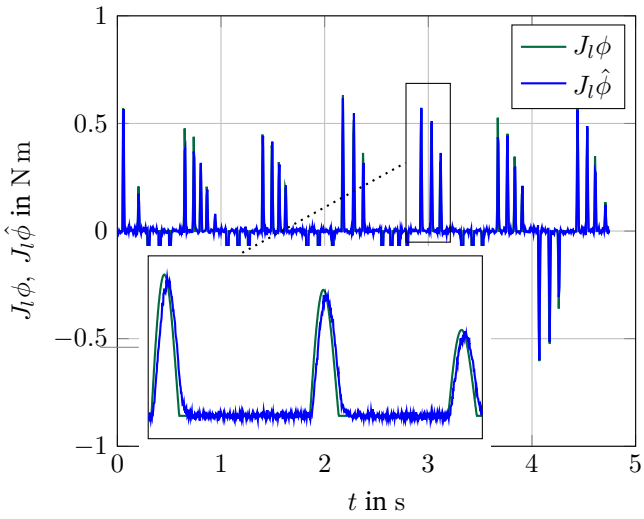

Figure D.5: Real and estimated backlash torque scaled by the load inertia J_l.

The real and estimated deadzone angle, as well as the estimation error, are shown in Figure D.6. The plots show that the deadzone angle is estimated with sufficient accuracy in less that 2 s. Specifically, the average steady state estimation error is less than 10^{-3} rad, which the order of magnitude for positioning precision in machine tool applications [18]. Larger sensor noise has a direct impact on the speed of convergence and the steady-state deviation.

D.5 Conclusions

A method for deadzone angle estimation in a single-axis drive-train with backlash has been presented in this paper. The interconnecting torque acting on motor and load was first estimated using a STSMO, followed by an adaptive algorithm that was designed to estimate deadzone angle. The method was tested in a simulation framework, where the adaptive estimator was able to track the real value of the deadzone angle, as well as a 5% increase in the backlash. The parameter convergence was achieved in less than 2 s with precision in the order of 10^{-3} rad. Such precision will allow for use of the estimated parameter in backlash compensation algorithms, that are used in many machine-tool controls. Moreover, detection of changes in the

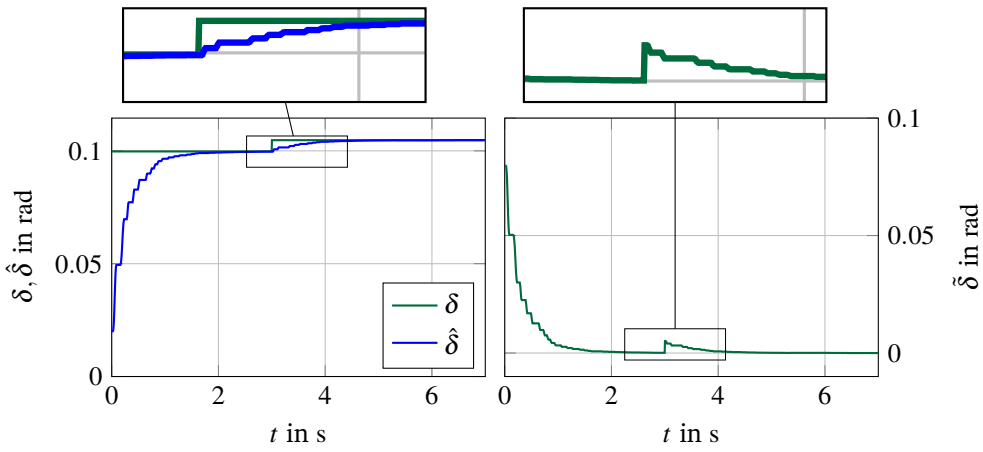

Figure D.6: (Left): Real and estimated change of deadzone angle. (Right): Estimation error.

deadzone angle can infer a measure of wear in the mechanical components (i.e. gearing, ball screw, couplings or guides) of the system.

Experimental validation of the method is ongoing.

Acknowledgements

The project is sponsored by Siemens AG.

Supplementary Material

I The dq0 Transformation

In applications where high accuracy and acceleration are required and, thus, torque-current control of PMSMs is essential, it is convenient to utilize a different description of the 3-phase quantities of the motor (currents and voltages). This alternative description, referred to as the dq0 transformation, is given by [125]

$$\begin{bmatrix} f_d \\ f_q \\ f_0 \end{bmatrix} = \frac{2}{3} \begin{bmatrix} \cos(\theta) & \cos\left(\theta - \frac{2\pi}{3}\right) & \cos\left(\theta + \frac{2\pi}{3}\right) \\ -\sin(\theta) & -\sin\left(\theta - \frac{2\pi}{3}\right) & -\sin\left(\theta + \frac{2\pi}{3}\right) \\ \frac{1}{2} & \frac{1}{2} & \frac{1}{2} \end{bmatrix} \begin{bmatrix} f_a \\ f_b \\ f_c \end{bmatrix} \tag{I.1}$$

where f can be voltage, current or magnetic flux. For balanced 3-phase PMSMs, such as the Siemens 1FT7, the f_0 component is always zero.

With this transformation the effect of all electrical currents (and voltages) of the motor is analysed in two components, namely the *magnetizing current*, also referred to as the direct axis current, i_d (direct axis voltage V_d) and the *torque current* or quadrature axis current, i_q (similarly, quadrature axis voltage V_q) as shown in Figure D.7. The magnetizing current is responsible for the generation of the magnetic field of the stator, whereas the quadrature axis current is responsible for the generation of the torque due to the interaction of the two magnetic fields (of the stator and the rotor).

The reason for choosing the dq-frame description is because the sinusoidal nonlinearities induced by the alternating input voltages to the model are removed and the inputs can be considered as if they were DC (i.e. only their amplitudes are considered). This allows for independent control of the motor torque from the flux of the magnetic field of the stator, which is the basic principle of *vector control* [125], typically employed in highly-dynamic industrial application, such as machine tools.

II Basic Definitions

Definition 2 (**signum function**). *The signum function* $\operatorname{sgn}(\cdot)$ *is defined as:*

$$\operatorname{sgn}(y) = \begin{cases} 1 & \text{if } y > 0 \\ \upsilon \in [-1, 1] & \text{if } y = 0 \\ -1 & \text{if } y < 0 \end{cases}. \tag{II.1}$$

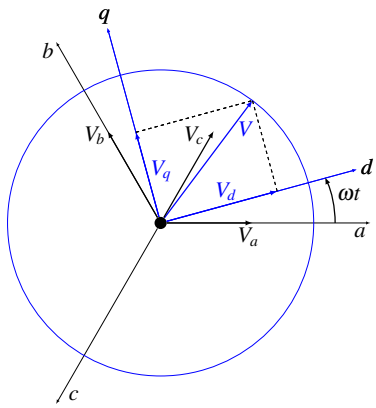

Figure D.7: Analysis of three-phase voltages in the $dq-$frame. The three phases V_a, V_b, V_c are combined in one vector V which rotates at the frequency of the phases. V is then analysed in two normal components V_d, V_q on a frame that rotates with the same angular velocity ω.

Definition 3 (**Pseudoinverse of a real matrix**). *The left pseudoinverse of a real matrix* $\boldsymbol{A}$ *are respectively defined as [134]:*

$$\boldsymbol{A}^{+} = \left(\boldsymbol{A}^{T}\boldsymbol{A}\right)\boldsymbol{A}^{T} . \tag{II.2}$$

Similarly, the right pseudoinverse of A is given by:

$$\boldsymbol{A}^{+} = \boldsymbol{A}\left(\boldsymbol{A}^{T}\boldsymbol{A}\right) . \tag{II.3}$$

Definition 4 (**PE [82]**). *A piecewise continuous signal vector* $\boldsymbol{\phi} : \mathbb{R}^{+} \rightarrow \mathbb{R}^{n}$ *is Persistently Exciting with a level of excitation* $\alpha_0 > 0$ *if there exist constants* $\alpha_1, T_0 > 0$ *such that*

$$\alpha_0 \boldsymbol{I} \leq \frac{1}{T_0}\int_{t}^{t+T_0} \boldsymbol{\phi}(\tau)\boldsymbol{\phi}^{T}(\tau)d\tau \leq \alpha_1 \boldsymbol{I} . \tag{II.4}$$

Definition 5 (**The error function**). *The error function* $\mathrm{erf}(\cdot)$ *is defined as:*

$$\mathrm{erf}(y) = \frac{2}{\sqrt{\pi}}\int_{0}^{y} e^{-\tau^2} d\tau. \tag{II.5}$$

For implementation purposes, the error function can be approximated by the hyperbolic tangent function, i.e.

$$\mathrm{erf}(y) \approx \tanh(y) = \frac{e^{y} - e^{-y}}{e^{y} + e^{-y}} .$$

Definition 6 (**The Projection operator [99]**). *Let* Ω_l *be a convex subset of the parameter space* $\mathcal{D}$ *defined as*

$$\Omega_c \triangleq \{\boldsymbol{\delta} \in \mathcal{D} | h(\boldsymbol{\delta}) \leq l\} ,$$

where $\boldsymbol{\delta}$ is the unknown parameter vector, l is a positive real constant and $h : \mathcal{D} \to \mathbb{R}$ is a smooth convex function. The projection operator is defined as follows:

$$Proj(\hat{\boldsymbol{\delta}}, \tau) = \begin{cases} \tau & , h(\hat{\boldsymbol{\delta}}) < 0 \\ \tau & , h(\hat{\boldsymbol{\delta}}) \geq 0 \;\&\; \nabla h^T \tau \leq 0 \\ \tau - \frac{\nabla h}{|\nabla h|} \left\langle \frac{\nabla h}{|\nabla h|}, \tau \right\rangle h(\hat{\boldsymbol{\delta}}) & , h(\hat{\boldsymbol{\delta}}) \geq 0 \;\&\; \nabla h^T \tau > 0 \end{cases} , \tag{II.6}$$

where the convex function h has been chosen according to [99]:

$$h(\hat{\boldsymbol{\delta}}) \triangleq \frac{(\epsilon_\delta + 1)\hat{\boldsymbol{\delta}}^T \hat{\boldsymbol{\delta}} - \delta_{max}^2}{\epsilon_\delta \delta_{max}^2} . \tag{II.7}$$

In the above definition of h, δ_{max} is a conservative upper bound for $\|\boldsymbol{\delta}\|_\infty$ and ϵ_δ is a small positive number. The operator $\langle \cdot, \cdot \rangle$ denotes the inner product.

Definition 7 ($\mathcal{K}$, $\mathcal{K}_\infty$ functions [128, Def. 4.2]). *A continuous function $\alpha : [0, a) \to (0, \infty]$ is said to belong to class-$\mathcal{K}$ if it is strictly increasing and $\alpha(0) = 0$. It is said to belong to class-$\mathcal{K}_\infty$ if $a = \infty$ and $\alpha(r) \to \infty$ as $r \to \infty$.*

Definition 8 ($\mathcal{KL}$, $\mathcal{KL}_\infty$ functions [128, Def. 4.3]). *A continuous function $\beta : [0, a) \times (0, \infty] \to (0, \infty]$ is said to belong to class-$\mathcal{KL}$ (respectively $\mathcal{KL}_\infty$) if, for each fixed s, the mapping $\beta(s, r)$ belongs to class-$\mathcal{K}$ (respectively $\mathcal{K}_\infty$) with respect to r and, for each fixed r, the mapping $\beta(r, s)$ is decreasing with respect to s and $\beta(r, s) \to 0$ as $s \to \infty$.*

III Elements of Lyapunov Stability Theory

Definition 9 ([83, Def. A.4, p. 490]). *Consider the system*

$$\dot{\boldsymbol{x}} = \boldsymbol{f}(t, \boldsymbol{x}) \tag{III.1}$$

where the function $\boldsymbol{f} : [0, \infty) \times \mathcal{D} \to \mathbb{R}^n$ with $\mathcal{D} \subset \mathbb{R}^n$ is locally Lipschitz in $\boldsymbol{x}$ and piecewise continuous in t. The equilibrium point $\boldsymbol{x}^* = \mathbf{0}$ of the system (III.1) *is:*

- *uniformly stable, if there exists a class-$\mathcal{K}$ function $\gamma(\cdot)$ and a positive constant c, independent of t_0, such that*

$$\|\boldsymbol{x}(t)\| \leq \gamma(\|\boldsymbol{x}(t_0)\|), \; \forall t \geq t_0 \geq 0, \; \forall \boldsymbol{x}(t_0) \text{ with } \|\boldsymbol{x}(t_0)\| < c \; ; \tag{III.2}$$

- *uniformly asymptotically stable, if there exists a class-$\mathcal{KL}$ function $\beta(\cdot, \cdot)$ and a positive constant c, independent of t_0, such that*

$$\|\boldsymbol{x}(t)\| \leq \beta(\|\boldsymbol{x}(t_0, t - t_0)\|), \; \forall t \geq t_0 \geq 0, \; \forall \boldsymbol{x}(t_0) \text{ with } \|\boldsymbol{x}(t_0)\| < c \; ; \tag{III.3}$$

- *exponentially stable, if* (III.3) *is satisfied with* $\beta(r,s) = kre^{-as}$ $k, a > 0$;
- *globally uniformly stable, if* (III.2) *is satisfied with* $\gamma \in \mathcal{K}_\infty$ *for any initial state* $\boldsymbol{x}(t_0)$;
- *globally uniformly asymptotically stable, if* (III.3) *is satisfied with* $\beta \in \mathcal{KL}_\infty$ *for any initial state* $\boldsymbol{x}(t_0)$;
- *globally exponentially stable, if* (III.3) *is satisfied for any initial state* $\boldsymbol{x}(t_0)$ *and with* $\beta(r,s) = kre^{-as}$ $k, a > 0$.

Lemma (Barbalat's lemma [83, Lem. A.6, p. 491]). *Consider the function* $\phi : [0,\infty) \to \mathbb{R}$. *If* ϕ *is uniformly continuous and* $\lim_{t\to\infty} \int_0^\infty \phi(\tau)d\tau$ *exists and is finite, then*

$$\lim_{t\to\infty} \phi(t) = 0 \ .$$

Corollary ([83, Col. A.7, p. 491]). *Consider the function* $\phi : [0,\infty) \to \mathbb{R}$. *If* $\phi, \dot{\phi} \in \mathcal{L}_\infty$ *and* $\phi \in \mathcal{L}_p$ *for some* $p \in [1,\infty)$, *then*

$$\lim_{t\to\infty} \phi(t) = 0 \ .$$

Theorem (LaSalle-Yoshizawa [83, Th. A.8, p. 492]). *Let* $\boldsymbol{x}^* = \mathbf{0}$ *be an equilibrium point of the system* (III.1), *where* $\mathcal{D} = \mathbb{R}$ *and is* $\boldsymbol{f}$ *locally Lipschitz in* $\boldsymbol{x}$ *uniformly in* t. *Let also* $V : [0,\infty) \times \mathbb{R}^n \to [0,\infty)$ *be a continuously differentiable function such that*

$$\gamma_1(\boldsymbol{x}) \leq V(t,\boldsymbol{x}) \leq \gamma_2(\boldsymbol{x})$$
$$\dot{V} = \frac{\partial V}{\partial t} + \frac{\partial V}{\partial \boldsymbol{x}}\boldsymbol{f}(t,\boldsymbol{x}) \leq -W(\boldsymbol{x}) \leq 0$$

$\forall t \geq 0$, $\forall \boldsymbol{x} \in \mathbb{R}^n$, *where* γ_1, γ_2 *are class-*$\mathcal{K}_\infty$ *functions and* W *is a continuous function. Then, all solutions of* (III.1) *are globally uniformly bounded and satisfy*

$$\lim_{t\to\infty} W(\boldsymbol{x}(t)) = 0 \ .$$

In addition, if $W(\boldsymbol{x})$ *is positive definite, then the equilibrium* $\boldsymbol{x}^* = \mathbf{0}$ *is globally uniformly asymptotically stable.*

Theorem ([128, Th. 4.10, p. 154]). *Let* $\boldsymbol{x}^* = \mathbf{0}$ *be an equilibrium point for* (III.1) *and* $\mathcal{D} \subset \mathbb{R}^n$ *be a domain containing* $\boldsymbol{x}^* = \mathbf{0}$. *Let also* $V : [0,\infty) \times \mathcal{D} \to \mathbb{R}$ *be a continuously differentiable function such that*

$$k_1\|\boldsymbol{x}\|^a \leq V(t,\boldsymbol{x}) \leq k_2\|\boldsymbol{x}\|^a$$
$$\frac{\partial V}{\partial t} + \frac{\partial V}{\partial \boldsymbol{x}}\boldsymbol{f}(t,\boldsymbol{x}) \leq -k_3\|\boldsymbol{x}\|^a$$

$\forall t \geq 0$ *and* $\forall \boldsymbol{x} \in \mathcal{D}$, *where* k_1, k_2, k_3 *and* a *are positive constants. Then,* $\boldsymbol{x}^* = \mathbf{0}$ *is exponentially stable. If the assumptions hold globally, then* $\boldsymbol{x}^* = \mathbf{0}$ *is globally exponentially stable.*

Definition 10 (Input-to-State Stability [128, Def. 4.7, p. 175]). *Consider the system*

$$\dot{\boldsymbol{x}} = \boldsymbol{f}(t, \boldsymbol{x}, \boldsymbol{u}) \tag{III.4}$$

where $\boldsymbol{f} : [0, \infty) \times \mathbb{R}^n \times \mathbb{R}^m \to \mathbb{R}^n$ is piecewise continuous in t and locally Lipschitz in $\boldsymbol{x}$ and $\boldsymbol{u}$. The input $\boldsymbol{u}$ is a piecewise continuous, bounded function of t for all $t \geq 0$. The system (III.4) *is said to be ISS with respect to the input $\boldsymbol{u}$ if there exist a class-$\mathcal{KL}$ function β and a class-$\mathcal{K}$ function γ such that for any initial state $\boldsymbol{x}(t_0)$ and any bounded input $\boldsymbol{u}(t)$, the solution $\boldsymbol{x}(t)$ exists for all $t \geq t_0$ and satisfies*

$$\|\boldsymbol{x}(t)\| \leq \beta(\|\boldsymbol{x}(t_0)\|, t - t_0) + \gamma\left(\sup \lim_{t_0 \leq \tau \leq t} \|\boldsymbol{u}(\tau)\|\right) . \tag{III.5}$$

Theorem ([128, Th. 4.19, p. 176]). *Consider the system* (III.4). *Let also $V : [0, \infty) \times \mathbb{R}^n \to \mathbb{R}$ be a continuously differentiable function such that*

$$\alpha_1(\|\boldsymbol{x}\|) \leq V(t, \boldsymbol{x}) \leq \alpha_2(\|\boldsymbol{x}\|)$$
$$\frac{\partial V}{\partial t} + \frac{\partial V}{\partial \boldsymbol{x}} \boldsymbol{f}(t, \boldsymbol{x}, \boldsymbol{x}) \leq -W_3(\boldsymbol{x}),\ \forall \|\boldsymbol{x}\| \geq \rho(\|\boldsymbol{x}\|) > 0$$

$\forall (t, \boldsymbol{x}, \boldsymbol{u}) \in [0, \infty) \times \mathbb{R}^n \times \mathbb{R}^m$, where α_1, α_2 are class-$\mathcal{K}_\infty$ functions, ρ is a class-$\mathcal{K}$ function and $W_3(\boldsymbol{x})$ is a continuous positive definite function on $\mathbb{R}^n$. Then, the system (III.4) *is input-to-state stable with $\gamma = \alpha_1^- \circ \alpha_2 \circ \rho$ (see Definition 10).*

Lemma ([128, Lem. 4.7, p. 180]). *Consider the system*

$$\dot{\boldsymbol{x}}_{\boldsymbol{1}} = \boldsymbol{f}_{\boldsymbol{1}}(t, \boldsymbol{x}_{\boldsymbol{1}}, \boldsymbol{x}_{\boldsymbol{2}}) \tag{III.6a}$$
$$\dot{\boldsymbol{x}}_{\boldsymbol{2}} = \boldsymbol{f}_{\boldsymbol{2}}(t, \boldsymbol{x}_{\boldsymbol{2}}) \tag{III.6b}$$

where $\boldsymbol{f}_{\boldsymbol{1}} : [0, \infty) \times \mathbb{R}^{n_1} \times \mathbb{R}^{n_2} \to \mathbb{R}^{n_1}$ and $\boldsymbol{f}_{\boldsymbol{2}} : [0, \infty) \times \mathbb{R}^{n_2} \to \mathbb{R}^{n_2}$ are piecewise continuous in t and locally Lipschitz in $\boldsymbol{x} \triangleq \begin{bmatrix} \boldsymbol{x}_{\boldsymbol{1}} & \boldsymbol{x}_{\boldsymbol{2}} \end{bmatrix}^T$. Suppose that both $\dot{\boldsymbol{x}}_{\boldsymbol{1}} = \boldsymbol{f}_{\boldsymbol{1}}(t, \boldsymbol{x}_{\boldsymbol{1}}, 0)$ has a globally uniformly asymptotically stable equilibrium point at its origin. Then, if the system (III.6a)*, with $\boldsymbol{x}_{\boldsymbol{2}}$ as input, is input-to-state stable and the origin of* (III.6b) *is globally uniformly asymptotically stable, the the origin of the cascade system* (III.6a) *and* (III.6b) *is globally uniformly asymptotically stable.*

IV Proof of ISS Property of e_θ (I&I-AC)

Define the continuously differentiable function $V_e(e_\omega) = \frac{1}{2} J_m e_\omega^2$ for which the following inequality holds:

$$\alpha_1(|e_\omega|) \leq V_e \leq \alpha_2(|e_\omega|)$$

with $\alpha_1(x) = \frac{1}{4}y^2$ and $\alpha_2(y) = x^2$ being class $\mathcal{K}_\infty$ functions. Taking the time derivative of V_e along the trajectories of the error system in (A.52) yields

$$\begin{aligned}\dot{V}_e &= -k_{II}e_\omega^2 - e_\omega \boldsymbol{\phi}(\omega_m)\boldsymbol{\phi}^T(\omega_m)\boldsymbol{z} \leq -k_{II}|e_\omega|^2 + |e_\omega| \cdot \lambda_{max}\left(\boldsymbol{\phi}(\omega_m)\boldsymbol{\phi}^T(\omega_m)\right)|\boldsymbol{z}| \\ &= -k_{II}(1-\lambda)|e_\omega|^2 - |e_\omega|\left[k_{II}\lambda|e_\omega| - \lambda_{max}\left(\boldsymbol{\phi}(\omega_m)\boldsymbol{\phi}^T(\omega_m)\right)|\boldsymbol{z}|\right] \\ &\leq -k_{II}(1-\lambda)|e_\omega|^2 \triangleq \alpha_4(|e_\omega|)\ ,\ \forall |e_\omega| \geq \frac{\lambda_{max}\left(\boldsymbol{\phi}(\omega_m)\boldsymbol{\phi}^T(\omega_m)\right)}{k_{II}\lambda}|\boldsymbol{z}| \triangleq \alpha_3(|\boldsymbol{z}|)\end{aligned}$$

where $\lambda_{max}(\cdot)$ denotes the largest eigenvalue of a real matrix, $0 < \lambda < 1$, $\alpha_4(\cdot)$ is a class $\mathcal{K}_\infty$ function and $\alpha_3(\cdot)$ is positive definite in $\mathbb{R}$. Then according to Theorem 4.19 in [128, p. 176] the system in (A.52) is ISS with respect to the input z.

V Proof of ISS Property of e_θ (ABSC)

Define the continuously differentiable function $V_e(e_\theta) = \frac{1}{2}e_\theta^2$ for which the following inequality holds:

$$\alpha_1(|e_\theta|) \leq V_e \leq \alpha_2(|e_\theta|)$$

with $\alpha_1(x) = \frac{1}{4}y^2$ and $\alpha_2(y) = x^2$ being class $\mathcal{K}_\infty$ functions. Taking the time derivative of V_e along the trajectories of the error system in (B.33) yields

$$\begin{aligned}\dot{V}_e &= -ce_\theta^2 - e_\theta z_1 \leq -c|e_\theta|^2 + |e_\theta| \cdot |z_1| = -c(1-q)|e_\theta|^2 - |e_\theta|\left(cq|e_\theta| - |z_1|\right) \\ &\leq -c(1-q)|e_\theta|^2 \triangleq \alpha_4(|e_\theta|)\ ,\ \forall |e_\theta| \geq \frac{1}{cq}|z_1| \triangleq \alpha_3(|z_1|)\end{aligned}$$

where $0 < q < 1$, $\alpha_4(\cdot)$ is a class $\mathcal{K}_\infty$ function and $\alpha_3(\cdot)$ is positive definite in $\mathbb{R}$. Then according to Theorem 4.19 in [128, p. 176] the system in (B.33) is ISS with respect to the input z_1.

VI Proof of BIBO Stability of χ With Respect to ω_m (SFL_1)

Define $\boldsymbol{\chi} \triangleq \begin{bmatrix}\Delta\theta & \omega_l\end{bmatrix}^T$. Considering ω_m as an input, the dynamics of $\boldsymbol{\chi}$ are written as:

$$\begin{aligned}\dot{\boldsymbol{\chi}} &= \underbrace{\begin{bmatrix}0 & -1 \\ K_S & -(D_S+\beta_l)\end{bmatrix}}_{-\boldsymbol{A}}\boldsymbol{\chi} - \begin{bmatrix}0 \\ T_{C,l}\text{sgn}(\omega_l)\end{bmatrix} + \underbrace{\frac{1}{N}\begin{bmatrix}1 \\ D_S\end{bmatrix}}_{\boldsymbol{B}}\omega_m \\ &= -\boldsymbol{A}\boldsymbol{\chi} - \begin{bmatrix}0 \\ T_{C,l}\text{sgn}(\omega_l)\end{bmatrix} + \boldsymbol{B}\omega_m\ .\end{aligned} \tag{VI.1}$$

Since both eigenvalues of $\boldsymbol{A}$ given by

$$\lambda_{1,2} = \frac{D_S + \beta_l \pm \sqrt{(D_S + \beta_l)^2 - 4K_S}}{2}$$

have positive real parts, $-A$ is Hurwitz. Define the continuously differentiable Lyapunov function candidate $V(\boldsymbol{\chi}) = \frac{1}{2}\boldsymbol{\chi}^T\boldsymbol{\chi}$ for which the following inequality holds:

$$\frac{1}{4}\|\boldsymbol{\chi}\|^2 \leq V \leq \|\boldsymbol{\chi}\|^2 .$$

Taking the time derivative of V along the trajectories of (VI.1) yields

$$\begin{aligned}
\dot{V} &= -\boldsymbol{\chi}^T\boldsymbol{A}\boldsymbol{\chi} - \boldsymbol{\chi}^T \begin{bmatrix} 0 \\ T_{C,l} \end{bmatrix} \operatorname{sgn}(\omega_l) + \boldsymbol{\chi}^T\boldsymbol{B}\omega_m \\
&\leq -|\boldsymbol{A}| \cdot \|\boldsymbol{\chi}\|^2 - T_{C,l}|\omega_l| + |\boldsymbol{B}| \cdot \|\boldsymbol{\chi}\| \cdot |\omega_m| \\
&\leq -\mu_{\boldsymbol{A}}\|\boldsymbol{\chi}\|^2 + |\boldsymbol{B}| \cdot \|\boldsymbol{\chi}\| \cdot |\omega_m| \\
&= -\mu_{\boldsymbol{A}}(1-w)\|\boldsymbol{\chi}\|^2 + \|\boldsymbol{\chi}\|\left(|\boldsymbol{B}| \cdot |\omega_m| - \mu_{\boldsymbol{A}} w\|\boldsymbol{\chi}\|\right) \\
&\leq -\mu_{\boldsymbol{A}}(1-w)\|\boldsymbol{\chi}\|^2 \triangleq \kappa_1(\|\boldsymbol{\chi}\|) \ , \ \forall \|\boldsymbol{\chi}\| \geq \frac{|\boldsymbol{B}|}{\mu_{\boldsymbol{A}} w}|\omega_m| \triangleq \kappa_2(|\omega_m|)
\end{aligned}$$

where $\mu_{\boldsymbol{A}}$ is the spectral radius of $\boldsymbol{A}$, $|\boldsymbol{B}|$ denotes any norm of $\boldsymbol{B}$, $0 < w < 1$, $\kappa_1(\cdot)$ is a class $\mathcal{K}_\infty$ function and $\kappa_2(\cdot)$ is positive definite in $\mathbb{R}$. Then according to Theorem 4.19 in [128, p. 176] the system in (VI.1) is ISS with respect to the input ω_m. Consequently, this implies the BIBO stability of $\boldsymbol{\chi}$ with ω_m taken as input.

VII Calculation of $\dot{a}$ (ABSC)

Differentiating α with respect to time gives:

$$\begin{aligned}
\dot{\alpha} &= \frac{d}{dt}\hat{\rho}\left[-\boldsymbol{\phi_2}^T(\boldsymbol{x})\hat{\boldsymbol{\vartheta}} + J_l\left(\ddot{\theta}_r - c\omega_l + c\dot{\theta}_r - k_1 z_1\right)\right] \\
&= \underbrace{\dot{\hat{\rho}}\left[J_l\left(\ddot{\theta}_r - c\omega_l + c\dot{\theta}_r - k_1 z_1\right) - \boldsymbol{\phi_2}^T(\boldsymbol{x})\hat{\boldsymbol{\vartheta}}\right]}_{\psi_1} + \hat{\rho}\frac{d}{dt}\left[J_l\left(\ddot{\theta}_r - c\omega_l + c\dot{\theta}_r - k_1 z_1\right) - \boldsymbol{\phi_2}^T(\boldsymbol{x})\hat{\boldsymbol{\vartheta}}\right] \\
&= \psi_1 + \hat{\rho}\left[-\frac{d}{dt}\left(\boldsymbol{\phi_2}^T(\boldsymbol{x})\hat{\boldsymbol{\vartheta}}\right) + J_l\left(\theta_r^{(3)} - c\ddot{\theta}_r\right)\right] + J_l\hat{\rho}\left[-\frac{c}{J_l}\left(\boldsymbol{\phi_2}^T(\boldsymbol{x})\boldsymbol{\vartheta} + b\omega_m\right) - k_1\dot{z}_1\right] \\
&= \psi_1 + \hat{\rho}\left[-\frac{d}{dt}\left(\boldsymbol{\phi_2}^T(\boldsymbol{x})\hat{\boldsymbol{\vartheta}}\right) + J_l\left(\theta_r^{(3)} - c\ddot{\theta}_r\right)\right] - c\hat{\rho}\left(\boldsymbol{\phi_2}^T(\boldsymbol{x})\boldsymbol{\vartheta} + b\omega_m\right) \\
&- J_l k_1\hat{\rho}\left(\frac{\boldsymbol{\phi_2}^T(\boldsymbol{x})\boldsymbol{\vartheta} + b\omega_m}{J_l} - \ddot{\theta}_r + c\omega_l - \dot{\theta}_r\right).
\end{aligned} \tag{VII.1}$$

Moreover, we have

$$\begin{aligned}\frac{d}{dt}\left(\boldsymbol{\phi_2}^T(\boldsymbol{x})\hat{\boldsymbol{\vartheta}}\right) &= \boldsymbol{\phi_2}^T(\boldsymbol{x})\dot{\hat{\boldsymbol{\vartheta}}} + \dot{\boldsymbol{x}}^T\frac{\partial \boldsymbol{\phi_2}^T(\boldsymbol{x})}{\partial \boldsymbol{x}}\hat{\boldsymbol{\vartheta}} \\ &= \boldsymbol{\phi_2}^T(\boldsymbol{x})\dot{\hat{\boldsymbol{\vartheta}}} + \left(\frac{\omega_m}{N} - \omega_l\right)\hat{K}_S - \left(\frac{\hat{D}_S + \hat{\beta}_m}{J_l}\right)\left(\boldsymbol{\phi_2}^T(\boldsymbol{x})\boldsymbol{\vartheta} + b\omega_m\right). \end{aligned} \tag{VII.2}$$

Substituting (VII.2) in (VII.1) and using (B.8) yields after some manipulation of the terms:

$$\begin{aligned}\dot{\alpha} &= \underbrace{\psi_1 + \hat{\rho}\Bigg[- \frac{d}{dt}\left(\boldsymbol{\phi_2}^T(\boldsymbol{x})\hat{\boldsymbol{\vartheta}}\right) - \left(\frac{\omega_m}{N} - \omega_l\right)\hat{K}_S + J_l\left(\theta_r^{(3)} - c\ddot{\theta}_r\right)}_{} \\ &\underbrace{+ \left(\frac{\hat{D}_S + \hat{\beta}_m}{J_l} - c - k_1\right)\left(\boldsymbol{\phi_2}^T(\boldsymbol{x})\hat{\boldsymbol{\vartheta}} + \hat{b}\omega_m\right) - J_l k_1\left(c\omega_l - \ddot{\theta}_r - \dot{\theta}_r\right)\Bigg]}_{\psi_2} \\ &+ \hat{\rho}\left(\frac{\hat{D}_S + \hat{\beta}_l}{J_l} - c - k_1\right)\boldsymbol{\phi_2}^T(\boldsymbol{x})\tilde{\boldsymbol{\vartheta}} + \hat{\rho}\left(\frac{\hat{D}_S + \hat{\beta}_l}{J_l} - c - k_1\right)\tilde{b}\omega_m \\ &= \psi_2 + \hat{\rho}\left(\frac{\hat{D}_S + \hat{\beta}_l}{J_l} - c - k_1\right)\boldsymbol{\phi_2}^T(\boldsymbol{x})\tilde{\boldsymbol{\vartheta}} + \hat{\rho}\left(\frac{\hat{D}_S + \hat{\beta}_l}{J_l} - c - k_1\right)\tilde{b}\omega_m\,. \end{aligned} \tag{VII.3}$$

Remark D.4. In the calculations above the derivative of the signum function with respect to the angular velocities shows up when evaluating the term $\frac{\partial \boldsymbol{\phi_2}^T(\boldsymbol{x})}{\partial \boldsymbol{x}}$. This derivative is everywhere 0 except at zero velocity, since $\text{sgn}(y)$ is not differentiable at $y = 0$. Introducing the approximation defined in Equation (B.34) suggests that the derivative of $\text{sgn}(\cdot)$ is given by

$$\frac{d}{dy}\left(\text{sgn}(y)\right) \approx \frac{2}{\pi}\frac{p}{1 + (py)^2} \tag{VII.4}$$

which is equal to $\frac{2p}{\pi}$ at $y = 0$ and vanishes when $|y| \to \infty$. This shows that for large values of the scaling factor p (e.g. $p \geq 100$), for which $\nu(p, y)$ approximates $\text{sgn}(y)$ with sufficient accuracy (one can easily see that $\lim_{p\to\infty} \nu(p, y) = \text{sgn}(y)$), the derivative with respect to y has a spike around $y = 0$, proportionally large to p. The larger the p factor is, however, the smaller the 0-neighbourhood in which the non-zero derivative exists is. In real-life applications the effect of measurement noise may introduce unwanted compensation terms at low (close to zero) speeds if the term in (VII.4) is included in the control design, even if the direction of motion has not changed (see Figure D.8). For this reason and without loss of generality, the derivative of $\text{sgn}(\cdot)$ is considered zero everywhere.

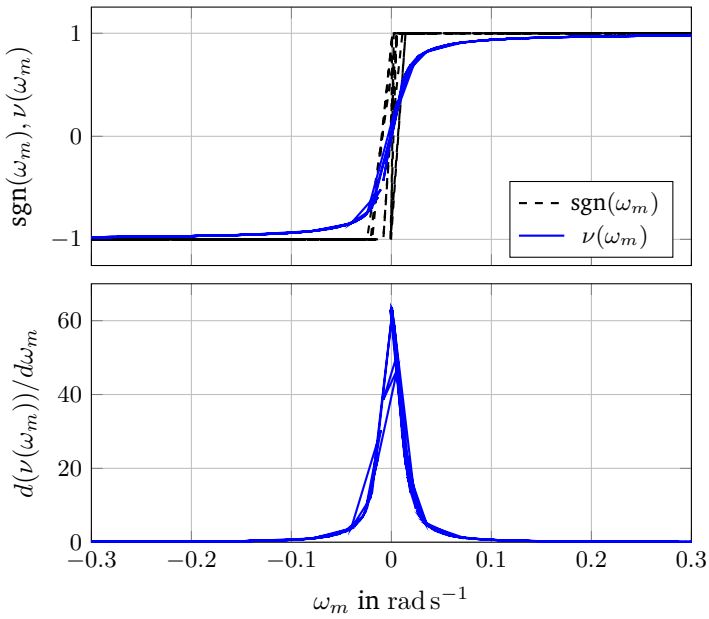

Figure D.8: (Top): Comparison of teh signum function and its approximation during a change of the drive motor motion. (Bottom): The derivative of the approximated signum function takes undesired non-zero values even before the direction of motion changes.

VIII Taylor Expansion Theorem

Theorem (11.1 [133]). *Suppose that* $\boldsymbol{r} : \mathbb{R}^n \to \mathbb{R}^n$ *is continuously differentiable in some convex open set* $\mathbb{D}$ *and that* $\boldsymbol{x}$ *and* $\boldsymbol{x} + \boldsymbol{p}$ *are vectors in* $\mathbb{D}$*. We then have that*

$$\boldsymbol{r}(\boldsymbol{x} + \boldsymbol{p}) = \boldsymbol{r}(\boldsymbol{x}) + \int_0^1 \frac{\partial \boldsymbol{r}}{\partial \boldsymbol{x}}(vx + t\boldsymbol{p})\boldsymbol{p}dt \ .$$

IX Proof of Property (C.34)

Since $\sigma(\boldsymbol{x}(t)) \geq 0, \forall t \geq 0$, it holds for $t, T \geq 0$:

$$\int_0^\infty e^{(t-\tau)}\sigma(\boldsymbol{x}(\tau))d\tau \geq \int_t^{t+T} e^{(t-\tau)}\sigma(\boldsymbol{x}(\tau))d\tau = e^{-T}\int_t^{t+T} e^{(t+T-\tau)}\sigma(\boldsymbol{x}(\tau))d\tau \ .$$

Moreover,

$$0 \leq t \leq \tau \leq T \Rightarrow t + T - \tau \geq 0 \Rightarrow e^{(t+T-\tau)} \geq 1$$

leading to

$$e^{-T}\int_t^{t+T} e^{(t+T-\tau)}\sigma(\boldsymbol{x}(\tau))d\tau \geq e^{-T}\int_t^{t+T} \sigma(\boldsymbol{x}(\tau))d\tau$$

which proves the property.

Bibliography

[1] D. Papageorgiou, M. Blanke, H. H. Niemann, and J. H. Richter. “Friction resilience of machine tool controls - Classic, sliding mode and nonlinear adaptive techniques compared”. *Control Engineering Practice* (2017). : Submitted paper under review.

[2] D. Papageorgiou, M. Blanke, H. H. Niemann, and J. H. Richter. “Friction-resilient position control for machine tools - Adaptive and sliding-mode methods compared”. *Control Engineering Practice* (2017). : Submitted paper under review.

[3] D. Papageorgiou, M. Blanke, H. H. Niemann, and J. H. Richter. “Robust backlash estimation for industrial drive-train systems - theory and validation”. *Transactions on Control Systems Technology* (2017). : Submitted paper under review.

[4] D. Papageorgiou, M. Blanke, H. H. Niemann, and J. H. Richter. “Backlash estimation for industrial drive-train systems” (July 2017). : To appear in IFAC-PapersOnLine.

[5] D. Papageorgiou, M. Blanke, H. H. Niemann, and J. H. Richter. “Fault tolerance for industrial actuators in absence of accurate models and hardware redundancy”. *2015 IEEE Conference on Control Applications (CCA)*. Sept. 2015, pp. 1887–1894. DOI: 10.1109/CCA.2015.7320885.

[6] *THE WORLD BANK - World Development Indicators*. Accessed: 2017-05-27.

[7] M. Maginness, E. Shehab, C. Beadle, and M. Carswell. “Principles for aerospace manufacturing engineering in integrated new product introduction”. *Proceedings of the Institution of Mechanical Engineers, Part B: Journal of Engineering Manufacture* 228.7 (2014), pp. 801–810.

[8] Y. Altintas. *Manufacturing automation: metal cutting mechanics, machine tool vibrations, and CNC design*. Cambridge university press, 2012.

[9] W. Tian, W. Gao, W. Chang, and Y. Nie. “Error modeling and sensitivity analysis of a five-axis machine tool”. *Mathematical Problems in Engineering* 2014 (2014).

[10] G. T. Smith. *Machine Tool Metrology: An Industrial Handbook*. Springer, 2016.

[11] A. Lamikiz, L. N. L. de Lacalle, and A. Celaya. “Machine tool performance and precision”. *Machine Tools for High Performance Machining*. Springer, 2009, pp. 219–260.

[12] H. Kagermann, W. Wahlster, and J. Helbig. *Recommendations for implementing the strategic initiative INDUSTRIE 4.0 - Final report of the Industrie 4.0 Working Group*. Ed. by A. Hellinger, V. Stumpf, and C. Kobsda. (Accessed on May 25, 2017). URL: http://www.acatech.de/fileadmin/user_upload/Baumstruktur_nach_Website/Acatech/root/de/Material_fuer_Sonderseiten/Industrie_4.0/Final_report__Industrie_4.0_accessible.pdf.

[13] X. Xu. "Machine Tool 4.0 for the new era of manufacturing". *The International Journal of Advanced Manufacturing Technology* (2017), pp. 1–8. DOI: 10.1007/s00170-017-0300-7.

[14] Y. Koren. "Control of machine tools". eng. *Transactions of the ASME, Journal of Manufacturing Science and Engineering* 119.4 (1997), pp. 749–755.

[15] Y. Koren. "Cross-Coupled Biaxial Computer Control for Manufacturing Systems". *Journal of Dynamic Systems, Measurement, and Control* 102.4 (Dec. 1980), 2731–2735 vol.5. DOI: 10.1115/1.3149612.

[16] G. T. C. Chiu and B. Yao. "Adaptive robust contour tracking of machine tool feed drive systems-a task coordinate frame approach". *American Control Conference, 1997. Proceedings of the 1997*. Vol. 5. June 1997, 2731–2735 vol.5. DOI: 10.1109/ACC.1997.611952.

[17] G. T. C. Chiu and M. Tomizuka. "Contouring control of machine tool feed drive systems: a task coordinate frame approach". *IEEE Transactions on Control Systems Technology* 9.1 (Jan. 2001), pp. 130–139. DOI: 10.1109/87.896754.

[18] H. Gross, J. Hamann, and G. Wiegärtner. *Electrical feed drives in automation: basics, computation, dimensioning*. Publicis MCD Corporate Pub., 2001.

[19] L. Settineri, P. Stavropoulos, D. Chantzis, C. Doukas, A. Papacharalampopoulos, and G. Chryssolouris. "Monitoring and Control of Manufacturing Processes: A Review". *Procedia CIRP* 8 (2013), pp. 421–425.

[20] Y. Koren. "Adaptive control systems for machining". *American Control Conference, 1988*. IEEE. 1988, pp. 1161–1167.

[21] C. M. G. Bort, M. Leonesio, and P. Bosetti. "A model-based adaptive controller for chatter mitigation and productivity enhancement in {CNC} milling machines". *Robotics and Computer-Integrated Manufacturing* 40 (2016), pp. 34–43. DOI: 10.1016/j.rcim.2016.01.006.

[22] C. Hu, B. Yao, and Q. Wang. “Coordinated Adaptive Robust Contouring Controller Design for an Industrial Biaxial Precision Gantry”. *IEEE/ASME Transactions on Mechatronics* 15.5 (Oct. 2010), pp. 728–735. DOI: 10.1109/TMECH.2009.2032292.

[23] J. Lee, W. E. Dixon, and J. C. Ziegert. “Adaptive nonlinear contour coupling control for a machine tool system”. *The International Journal of Advanced Manufacturing Technology* 61.9 (2012), pp. 1057–1065. DOI: 10.1007/s00170-011-3760-1.

[24] K. Khorasani. “Adaptive control of flexible-joint robots”. *IEEE Transactions on Robotics and Automation* 8.2 (Apr. 1992), pp. 250–267. DOI: 10.1109/70.134278.

[25] S. Avila-Becerril, A. Loría, and E. Panteley. “Global position-feedback tracking control of flexible-joint robots”. *American Control Conference (ACC), 2016*. IEEE. 2016, pp. 3008–3013.

[26] T. Wimböck, C. Ott, and G. Hirzinger. “Immersion and invariance control for an antagonistic joint with nonlinear mechanical stiffness”. *49th IEEE Conference on Decision and Control (CDC)*. Dec. 2010, pp. 1128–1135. DOI: 10.1109/CDC.2010.5717891.

[27] V. Utkin, J. Guldner, and J. Shi. *Sliding mode control in electro-mechanical systems*. Vol. 34. CRC press, 2009.

[28] J. Rivera, L. Garcia, C. Mora, J. J. Raygoza, and S. Ortega. “Super-Twisting Sliding Mode in Motion Control Systems”. 1993 (2008).

[29] B. Armstrong-Hélouvry, P. Dupont, and C. C. D. Wit. “A survey of models, analysis tools and compensation methods for the control of machines with friction”. *Automatica* 30.7 (1994), pp. 1083–1138. DOI: 10.1016/0005-1098(94)90209-7.

[30] O. Egeland and J. T. Gravdahl. *Modeling and simulation for automatic control*. Vol. 76. Marine Cybernetics Trondheim, Norway, 2002.

[31] P. R. Dahl. *Measurement of solid friction parameters of ball bearings*. Tech. rep. DTIC Document, 1977.

[32] C. C. De Wit, H. Olsson, K. J. Astrom, and P. Lischinsky. “A new model for control of systems with friction”. *IEEE Transactions on Automatic Control* 40.3 (1995), pp. 419–425.

[33] T. Piatkowski. “Dahl and LuGre dynamic friction models—The analysis of selected properties”. *Mechanism and Machine Theory* 73 (2014), pp. 91–100.

[34] P. Dupont, V. Hayward, B. Armstrong, and F. Altpeter. “Single state elastoplastic friction models”. *IEEE Transactions on automatic control* 47.5 (2002), pp. 787–792.

[35] V. Lampaert, J. Swevers, and F. Al-Bender. “Modification of the Leuven integrated friction model structure”. *IEEE transactions on Automatic Control* 47.4 (2002), pp. 683–687.

[36] T. Tjahjowidodo, F. Al-Bender, H. Van Brussel, and W. Symens. “Friction characterization and compensation in electro-mechanical systems”. *Journal of sound and vibration* 308.3 (2007), pp. 632–646.

[37] F. Al-Bender, V. Lampaert, and J. Swevers. “The generalized Maxwell-slip model: a novel model for friction simulation and compensation”. *IEEE Transactions on automatic control* 50.11 (2005), pp. 1883–1887.

[38] H. Olsson, K. J. Åström, C. C. De Wit, M. Gäfvert, and P. Lischinsky. “Friction models and friction compensation”. *European journal of control* 4.3 (1998), pp. 176–195.

[39] C. Rebelein and M. Zaeh. “Friction in feed drives of machine tools: investigation, modeling and validation”. *Production Engineering* (2016), pp. 1–11.

[40] L. R. Ray, A. Ramasubramanian, and J. Townsend. “Adaptive friction compensation using extended Kalmanan-Bucy filter friction estimation”. *Control Engineering Practice* 9.2 (2001), pp. 169–179. DOI: 10.1016/S0967-0661(00)00104-0.

[41] Y. Tan and I. Kanellakopoulos. “Adaptive nonlinear friction compensation with parametric uncertainties”. *American Control Conference, 1999. ...* June (1999), pp. 1–5.

[42] Y. Zhang and X. Ren. “Adaptive backstepping control of dual-motor driving servo systems with friction”. *Proceedings - 2014 6th International Conference on Intelligent Human-Machine Systems and Cybernetics, IHMSC 2014* 1.1 (2014), pp. 214–217. DOI: 10.1109/IHMSC.2014.60.

[43] E. Panteley, R. Ortega, and M. Gäfvert. “An adaptive friction compensator for global tracking in robot manipulators”. *Systems & Control Letters* 33.5 (1998), pp. 307–313.

[44] D. Garagić and K. Srinivasan. “Adaptive friction compensation for precision machine tool drive”. *Control Engineering Practice* 12.11 (2004), pp. 1451–1464.

[45] M. Nordin, J. Galic', and P.-O. Gutman. *New Models for Backlash and Gear Play*. 1997.

[46] R. Kalantari and M. Foomani. "Backlash Nonlinearity Modeling and Adaptive Controller Design for an Electromechanical Power Transmission System". *Scientia Iranica* 16.6 (2009).

[47] R. Merzouki and J. C. Cadiou. "Estimation of backlash phenomenon in the electromechanical actuator". *Control Engineering Practice* 13.8 (2005), pp. 973–983.

[48] J. C. Gerdes and V. Kumar. "An impact model of mechanical backlash for control system analysis". 5 (1995), pp. 3311–3315.

[49] M. Nordin and P. Gutman. "Controlling mechanical systems with backlash - a survey". und. *Automatica, Automatica, Automatica, Automatica Kidlington, Automatica J. Ifac, Automatica (oxf)* 38.10 (2002), pp. 1633–1649.

[50] J. A. de Marchi. "Modeling of dynamic friction, impact backlash and elastic compliance nonlinearities in machine tools, with applications to asymmetric viscous and kinetic friction identification" (1998).

[51] J. L. Stein and C.-H. Wang. "Estimation of Gear Backlash: Theory and Simulation". *Journal of Dynamic Systems, Measurement, and Control* 120.1 (1998), p. 74.

[52] G. Hovland, S. Hanssen, and E. Gallestey. "Nonlinear identification of backlash in robot transmissions". *Proceedings of the 33rd ISR (International Symposium on Robotics) October* 1 (2002), pp. 3–8.

[53] A. Lagerberg and B. S. Egardt. "Estimation of backlash with application to automotive powertrains". *Decision and Control, 2003. Proceedings. 42nd IEEE Conference on*. Vol. 5. Dec. 2003, 4521–4526 Vol.5.

[54] T. Hågglund. "Automatic on-line estimation of backlash in control loops". *Journal of Process Control* 17.6 (2007), pp. 489–499.

[55] J. Vörös. "Modeling and identification of systems with backlash". *Automatica* 46.2 (2010), pp. 369–374.

[56] P. Templin. "Simultaneous estimation of driveline dynamics and backlash size for control design". *Proceedings of the IEEE International Conference on Control Applications* (2008), pp. 13–18.

[57] R. Merzouki, J. A. Davila, L. Fridman, and J. C. Cadiou. "Backlash phenomenon observation and identification in electromechanical system". *Control Engineering Practice* 15.4 (2007), pp. 447–457.

[58] S. Emelyanov. “Variable structure control systems”. *Moscow, Nouka* (1967).

[59] V. Utkin. “Methods for constructing discontinuity planes in multidimensional variable structure systems”. *Automation and Remote Control* 39 (1978), pp. 1466–1470.

[60] C. Edwards and S. Spurgeon. *Sliding mode control: theory and applications*. Crc Press, 1998.

[61] Y. Shtessel, C. Edwards, L. Fridman, and A. Levant. *Sliding Mode Control and Observation*. New York, NY: Springer New York, 2014. DOI: 10.1007/978-0-8176-4893-0.

[62] H. Hakiki, B. Mazari, a. Liazid, and S. Djaber. “Fault reconstruction using sliding mode observers”. *American Journal of Applied Sciences* 3.1 (2006), pp. 1669–1674.

[63] C. Edwards, S. K. Spurgeon, and R. J. Patton. “Sliding mode observers for fault detection and isolation”. *Automatica* 36 (2000), pp. 541–553. DOI: 10.1016/S0005-1098(99)00177-6.

[64] C. P. Tan and C. Edwards. “Sliding mode observers for robust detection and reconstruction of actuator and sensor faults”. *International Journal of Robust and Nonlinear Control* 13.April 2002 (2003), pp. 443–463. DOI: 10.1002/rnc.723.

[65] X. Yan and C. Edwards. “Robust Sliding Mode Observer-Based Actuator Fault Detection and Isolation for a Class of Nonlinear Systems”. *44th IEEE Conference on Decision and Control, and the European Control Conference 2005*. Seville, Spain, 2005, pp. 987–992. DOI: 10.1080/00207720701778395.

[66] X.-G. Yan and C. Edwards. “Nonlinear robust fault reconstruction and estimation using a sliding mode observer”. *Automatica* 43 (2007), pp. 1605–1614. DOI: 10.1016/j.automatica.2007.02.008.

[67] C. Tan and C. Edwards. “Robust Fault Reconstruction in Uncertain Linear Systems Using Multiple Sliding Mode Observers in Cascade”. *IEEE Transactions on Automatic Control* 55.4 (2010), pp. 855–867. DOI: 10.1109/TAC.2010.2041996.

[68] H. Alwi, E. Christopher, and C. P. Tan. *Fault Detection and Fault-Tolerant Control Using Sliding Modes*. 2010, p. 338.

[69] G. Bartolini, A. Ferrara, E. Usai, and V. I. Utkin. “On multi-input chattering-free second-order sliding mode control”. *IEEE Transactions on Automatic Control* 45.9 (Sept. 2000), pp. 1711–1717. DOI: 10.1109/9.880629.

[70] A. Levant. “Sliding order and sliding accuracy in sliding mode control”. *International journal of control* 58.6 (1993), pp. 1247–1263.

[71] A. Levant. “Construction principles of output-feedback 2-sliding mode design”. *Decision and Control, 2002, Proceedings of the 41st IEEE Conference on*. Vol. 1. Dec. 2002, 317–322 vol.1. DOI: 10.1109/CDC.2002.1184511.

[72] A. Levant. “Principles of 2-sliding mode design”. *Automatica* 43.4 (2007), pp. 576–586. DOI: 10.1016/j.automatica.2006.10.008.

[73] J. a. Moreno and M. Osorio. “Strict lyapunov functions for the super-twisting algorithm”. *IEEE Transactions on Automatic Control* 57.4 (2012), pp. 1035–1040. DOI: 10.1109/TAC.2012.2186179.

[74] A. Levant. “Higher-order sliding modes, differentiation and output-feedback control”. *International Journal of Control* 76.9-10 (2003), pp. 924–941.

[75] Y. B. Shtessel, J. a. Moreno, F. Plestan, L. M. Fridman, and A. S. Poznyak. “Super-twisting adaptive sliding mode control: A Lyapunov design”. *49th IEEE Conference on Decision and Control (CDC)* (2010), pp. 5109–5113. DOI: 10.1109/CDC.2010.5717908.

[76] C. Edwards and Y. B. Shtessel. “Adaptive continuous higher order sliding mode control”. *Automatica* 65 (2016), pp. 183–190.

[77] C. Krimpmann, G. Schoppel, I. Glowatzky, and T. Bertram. “Lyapunov-Based Self-Tuning of Sliding Surfaces – Methodology And Application to Hydraulic Valves” (2016).

[78] G. Bartolini, L. Fridman, A. Pisano, and E. Usai, eds. *Modern Sliding Mode Control Theory: New Perspectives and Applications (Lecture Notes in Control and Information Sciences)*. 2008th ed. Springer, Apr. 2008.

[79] L. Fridman, J. Moreno, and R. Iriarte, eds. *Sliding Modes after the first Decade of the 21st Century: State of the Art (Lecture Notes in Control and Information Sciences)*. 2012th ed. Springer, Sept. 2011.

[80] X. Yu and M. Ö. Efe, eds. *Recent Advances in Sliding Modes: From Control to Intelligent Mechatronics (Studies in Systems, Decision and Control)*. 2015th ed. Springer, Apr. 2015.

[81] K. J. Åstrom. *Adaptive control (Addison-Wesley series in electrical and computer engineering)*. Addison-Wesley, 1989.

[82] P. Ioannou and J. Sun. *Robust Adaptive Control (Dover Books on Electrical Engineering) Paperback November 21, 2012*. dover publications (December 19, 2012), 1996.

[83] M. Krstic, I. Kanellakopoulos, and P. V. Kokotovic. *Nonlinear and Adaptive Control Design*. 1st ed. Wiley-Interscience, June 1995.

[84] A. Loria, T. I. Fossen, and A. Teel. "UGAS and ULES of nonautonomous systems: Applications to integral control of ships and manipulators". *Control Conference (ECC), 1999 European*. IEEE. 1999, pp. 1517–1522.

[85] A. Loría. "Uniform global position feedback tracking control of mechanical systems without friction". *American Control Conference (ACC), 2013*. IEEE. 2013, pp. 5722–5727.

[86] A. M. Annaswamy, F. P. Skantze, and A.-P. Loh. "Adaptive control of continuous time systems with convex/concave parametrization". *Automatica* 34.1 (1998), pp. 33–49.

[87] A. P. Loh, A. M. Annaswamy, and F. P. Skantze. "Adaptation in the presence of a general nonlinear parameterization: An error model approach". *IEEE Transactions on Automatic Control* 44.9 (1999), pp. 1634–1652. DOI: 10.1109/9.788531.

[88] C. Cao, A. M. Annaswamy, and A. Kojic. "Parameter Convergence in Nonlinearly Parameterized Systems". *IEEE Transactions on Automatic Control* 48.3 (2003), pp. 1–16.

[89] a. Kojic and a.M. Annaswamy. "Adaptive control of nonlinearly parametrized systems with a triangular structure". *Proceedings of the 38th IEEE Conference on Decision and Control (Cat. No.99CH36304)* 1999.December (1999), pp. 4754–4759. DOI: 10.1109/CDC.1999.833294.

[90] M. S. Netto, A. M. Annaswamy, R. Ortega, and P. Moya. "Adaptive control of a class of non-linearly parametrized systems using convexification". *International Journal of Control* 73.14 (2000), pp. 1312–1321. DOI: 10.1080/002071700421709.

[91] C. Cao and A. Annaswamy. "A Polynomial Adaptive Controller for Nonlinearly Parameterized Systems". *Proceedings of the 45th IEEE Conference on Decision and Control* (2006), pp. 1081–1086. DOI: 10.1109/CDC.2006.377009.

[92] W. Lin and C. Qian. "Adaptive control of nonlinearly parameterized systems: the smooth feedback case". *IEEE Transactions on Automatic Control* 47.8 (Aug. 2002), pp. 1249–1266. DOI: 10.1109/TAC.2002.800773.

[93] A. Astolfi and R. Ortega. "Immersion and invariance: a new tool for stabilization and adaptive control of nonlinear systems". *IEEE Transactions on Automatic Control* 48.4 (Apr. 2003), pp. 590–606. DOI: 10.1109/TAC.2003.809820.

[94] A. Astolfi, D. Karagiannis, and R. Ortega. *Nonlinear and Adaptive Control with Applications (Communications and Control Engineering)*. 2008th ed. Springer, Jan. 2008.

[95] A. Donaire, T. Perez, and Y. R. Teo. "Robust speed tracking control of synchronous motors using immersion and invariance". *2012 7th IEEE Conference on Industrial Electronics and Applications (ICIEA)*. July 2012, pp. 1482–1487. DOI: 10.1109/ICIEA.2012.6360958.

[96] I. Sarras, J. Á. Acosta, R. Ortega, and A. D. Mahindrakar. "Constructive immersion and invariance stabilization for a class of underactuated mechanical systems". *Automatica* 49.5 (2013), pp. 1442–1448.

[97] J. G. Romero, R. Ortega, and I. Sarras. "A globally exponentially stable tracking controller for mechanical systems using position feedback". *IEEE Transactions on Automatic Control* 60.3 (2015), pp. 818–823.

[98] X. Liu, R. Ortega, H. Su, and J. Chu. "Immersion and Invariance Adaptive Control of Nonlinearly Parameterized Nonlinear Systems ". *IEEE Transactions on Automatic Control* 55.9 (2010), pp. 2209–2214.

[99] N. Hovakimyan and C. Cao. *L1 Adaptive Control Theory: Guaranteed Robustness with Fast Adaptation (Advances in Design and Control)*. Society for Industrial and Applied Mathematics,U.S., Sept. 2010.

[100] C. Cao and N. Hovakimyan. "L1 adaptive controller for a class of systems with unknown nonlinearities: Part I". *2008 American Control Conference*. June 2008, pp. 4093–4098. DOI: 10.1109/ACC.2008.4587134.

[101] C. Cao and N. Hovakimyan. "L1 adaptive controller for nonlinear systems in the presence of unmodelled dynamics: Part II". *2008 American Control Conference*. June 2008, pp. 4099–4104. DOI: 10.1109/ACC.2008.4587135.

[102] X. Wang and N. Hovakimyan. "L1 Adaptive Controller for Nonlinear Reference Systems". *Proceedings of the 2011 American Control Conference* 5 (), pp. 594–599. DOI: 10.1016/j.sysconle.2012.01.010.

[103] R. Hindman, C. Cao, and N. Hovakimyan. "Designing a high performance, stable L1 adaptive output feedback controller". *Collection of Technical Papers - AIAA Guidance, Navigation, and Control Conference 2007*. Vol. 3. 2007, pp. 2799–2821.

[104] J. Wang, C. Cao, N. Hovakimyan, R. Hindman, and D. B. Ridgely. "L1 adaptive controller for a missile longitudinal autopilot design". *AIAA Guidance, Navigation and Control Conference*. 2008, pp. 18–21.

[105] P. Krause, O. Wasynczuk, S. Sudhoff, and I. P. E. Society. *Analysis of electric machinery and drive systems*. IEEE Press series on power engineering. IEEE Press, 2002.

[106] Siemens, ed. *SIMOTICS 1FT7 servomotors*. (2016, October 03). URL: http://w3.siemens.com/mcms/mc-solutions/en/motors/motion-control-motors/simotics-s-servomotors/simotics-s-1ft7/pages/simotics-s-1ft7.aspx.

[107] Siemens. *1FT7 synchronous motors SINAMICS S120 - Configuring Manual*. (2016, October 03). URL: http://www.industry.usa.siemens.com/drives/us/en/electric-motor/mc-motors/servo-motors/1ft7-servo-motors/pages/servo-motors-1ft7.aspx#Technical_20Data.

[108] H. Dyratok, ed. *Huco Vari-tork adjustable-friction clutches*. (Accessed on January 27, 2017). URL: http://www.huco.com/products.asp?p=true&cat=155.

[109] P. C. Krause, O. Wasynczuk, and S. D. Pekarek. *Electromechanical Motion Devices*. 2nd ed. Wiley-IEEE Press, Apr. 2012.

[110] T. H. G. Megson. *Structural and stress analysis*. Butterworth-Heinemann, 2005.

[111] G. Seber and C. Wild. *Nonlinear regression*. Wiley, 1989, 768 s.

[112] R. M. Prunescu, M. Blanke, and G. Sin. "Modelling and L1 Adaptive Control of pH in Bioethanol Enzymatic Process". *2013 American Control Conference*. 2013, pp. 1888–1895.

[113] A. Saltelli, M. Ratto, T. Andres, F. Campolongo, J. Cariboni, D. Gatelli, M. Saisana, and S. Tarantola. *Global Sensitivity Analysis: The Primer*. 1st ed. Wiley-Interscience, Feb. 2008.

[114] R. Brun, P. Reichert, and H. R. Künsch. "Practical identifiability analysis of large environmental simulation models". eng. *Water Resources Research* 37.4 (2001), pp. 1015–1030. DOI: 10.1029/2000wr900350.

[115] L. Ljung. *System Identification: Theory for the User (2nd Edition)*. 2nd ed. Prentice Hall, Jan. 1999.

[116] G. Straffelini. *Friction and Wear: Methodologies for Design and Control (Springer Tracts in Mechanical Engineering)*. 1st ed. Springer, Apr. 2015.

[117] H. F. Grip, A. Saberi, and T. A. Johansen. "Estimation of states and parameters for linear systems with nonlinearly parameterized perturbations". *Systems and Control Letters* 60.9 (2011), pp. 771–777. DOI: 10.1016/j.sysconle.2011.03.012.

[118] H. F. Grip, A. Saberi, and T. A. Johansen. “State and parameter estimation for nonlinearly parameterized systems: An H_∞-based approach”. eng. *Ifac Proceedings Volumes (ifac-papersonline)* 18.1 (2011), pp. 2997–3002.

[119] I. Y. Tyukin, D. V. Prokhorov, and C. van Leeuwen. “Adaptation and parameter estimation in systems with unstable target dynamics and nonlinear parametrization”. *IEEE Transactions on Automatic Control* 52.9 (2007), pp. 1543–1559. DOI: 10.1109/TAC.2007.904448.

[120] I. Y. Tyukin, E. Steur, H. Nijmeijer, and C. Van Leeuwen. “Adaptive observers and parameter estimation for a class of systems nonlinear in the parameters”. *Automatica* 49.8 (2013), pp. 2409–2423.

[121] I. Y. Tyukin, P. Rogachev, and H. Nijmeijer. “Adaptive observers for nonlinearly parameterized systems subjected to parametric constraints”. *IFAC Proceedings Volumes (IFAC-PapersOnline)* 19 (2014), pp. 10869–10874. DOI: 10.3182/20140824-6-ZA-1003.00807.

[122] H. F. Grip, T. A. Johansen, L. Imsland, and G.-o. Kaasa. “Parameter estimation and compensation in systems with nonlinearly parameterized perturbations”. *Automatica* 46.1 (2010), pp. 19–28. DOI: 10.1016/j.automatica.2009.10.013.

[123] S. Spurgeon. “Sliding Mode Observers - A Survey”. January 2015 (2008), pp. 37–41. DOI: 10.1080/00207720701847638.

[124] J. Davila, L. Fridman, and A. Levant. “Second-order sliding-mode observer for mechanical systems”. *IEEE Transactions on Automatic Control* 50.11 (Nov. 2005), pp. 1785–1789.

[125] W. Leonhard. *Control of Electrical Drives*. 3nd. Springer, Aug. 2001.

[126] C. Baratieri and H. Pinheiro. “New variable gain super-twisting sliding mode observer for sensorless vector control of nonsinusoidal back-EMF PMSM”. *Control Engineering Practice* 52 (2016). cited By 0, pp. 59–69. DOI: 10.1016/j.conengprac.2016.04.003.

[127] G. Bartolini, A. Ferrara, and E. Usai. “Chattering avoidance by second-order sliding mode control”. *IEEE Transactions on Automatic Control* 43.2 (Feb. 1998), pp. 241–246. DOI: 10.1109/9.661074.

[128] H. Khalil. *Nonlinear Systems*. Prentice Hall, 2002.

[129] R. Dorf and R. Bishop. *Modern Control Systems*. Pearson Prentice Hall, 2011.

[130] J. Zhou and Y. Wang. “Adaptive backstepping speed controller design for a permanent magnet synchronous motor”. *Electric Power Applications, IEE Proceedings-* 149.2 (2002), pp. 165–172. DOI: 10.1049/ip-epa:20020187.

[131] a. Levant. “Higher order sliding modes and arbitrary-order exact robust differentiation”. *Proceedings of the European Control Conference* (2001), pp. 996–1001.

[132] A. Loria and E. Panteley. “Cascaded nonlinear time-varying systems: Analysis and design”. eng. *Lecture Notes in Control and Information Sciences* 311 (2005), pp. 23–64. DOI: 10.1007/11334774_2.

[133] S. Wright and J. Nocedal. “Numerical optimization”. *Springer Science* 35 (1999), pp. 67–68.

[134] D. S. Watkins. *Fundamentals of matrix computations*. Vol. 64. John Wiley & Sons, 2004.

Technical University of Denmark
Automation and Control (AUT)
Elektrovej Building 326
DK-2800, Kgs. Lyngby
Denmark
Phone: (+45) 45 25 35 73
Email: info@elektro.dtu.dk
www.elektro.dtu.dk